Imperial College London

Triarylsilanols as Catalysts for Direct Amidation of Carboxylic Acids

A thesis submitted by

Rabia Qamar

in partial fulfilment of the requirements for the degree of

DOCTOR OF PHILOSOPHY

Department of Chemistry
Imperial College London
Molecular Sciences Research Hub
White City Campus
82 Wood Lane, London
W12 0BZ

August 2023

Did He not find you unaware of the Right Way, and then directed you to it?

(Quran 93:07)

Indeed, what is to come will be better for you than what has gone by.

(Quran 93:04)

Abstract

Triarylsilanols have been employed as the first silicon-based molecular catalysts for direct amidation of carboxylic acids. Tris(*p*-bromophenyl)silanol exhibited superior catalytic activity amongst tris(*p*-haloaryl)silanols selected for this study. Kinetic experiments revealed that Lewis acidic arylsilanol catalysts are sensitive to product inhibition, thus explaining the observed diminished catalytic efficiency in direct amidation reactions investigated. Tertiary amides proved to be more detrimental to the catalytic activity than secondary amides in the event of product inhibition. Accelerated catalyst deactivation in the presence of more basic secondary amines was evidenced by *ex situ* HPLC catalyst quantification. Computational studies uncovered the likelihood of a pentacoordinate silyl ester-amide complex as the possible mode of catalyst inhibition.

Table of Contents

Abstract 3

Acknowledgements 7

Declaration 8

Abbreviations 9

Chapter 1: Introduction 11

1.1 Arylsilanols in Organic Synthesis 12

1.1.1 Allylic Etherification 12

1.1.2 Cycloetherification 14

1.1.3 Hydrosilyloxylation 15

1.1.4 Enantioselective Stereogenic Silanols 20

1.2 Catalytic Amidations 23

Aims/Hypothesis 35

Chapter 2: Results & Discussion 36

2.1 Gram-Scale Synthesis of Selected Arylsilanols 36

2.2 Catalyst Loading Screening 38

2.3 Preparative Amidation Reactions 42

2.4 Kinetic Profiling 46

2.4.1 Time-Adjusted Analysis 49

2.4.2 Different Excess Experiments 53

2.4.3 Order in Catalyst 56

2.5 Mechanistic Considerations 58

2.6 Post Amidation Quantification of Catalyst Integrity by HPLC 61

2.7 X-Ray Crystal Structures 67

Conclusions 72

Outlook 72

Chapter 3: Experimental 73

General Experimental 73

3.1 Synthetic Procedures and Characterization Data for Compounds 74

3.2 General Procedure for Conversion vs Time Plots (Figures 8 & 9) 79

3.3 General Procedures for Triarylsilanols Catalyzed Direct Amidations 80

3.4 General Procedure for Tris(4-bromophenyl)silanol Catalyzed Concentration vs Time Plots (Figures 13 & 14) 83

3.5 General Procedure for Post Amidation Catalyst Integrity Quantification (Figure 22) 84

Table 3 Catalyst Loading Screening 85

Table 4 Catalyst Loading Screening 86

Table 5 Background Model Amidation Reaction at Different Concentrations 87

Table 6 Catalytic and Background Model Amidation Reactions for Concentration vs Time Plots 88

Table 7 Catalytic Model Amidation Reaction with Added Products 89

Table 8 Catalytic Model Amidation Reaction with Added 2^0 or 3^0 Amides 90

Table 9 Model Amidation Reaction with Different Stoichiometry of Acid/Amine 91

Table 10 Model Amidation Reaction with Different Concentrations of Catalyst [**62g**] 92

Table 11 Preparation of Calibration Solutions 93

Table 12 HPLC Calibration Data 94

HPLC Calibration Curves 96

Table 13 Quantification of [**62g**] and [**62e**] under Model Amidation Conditions 97

Table 14 Quantification of [**62g**] with Different Reaction Components of Model Amidation System 98

Table 15 Quantification of [**62g**] with Representative Primary, Secondary cyclic, Secondary acyclic and Aryl Amines 99

Table 16 Quantification of [**62g**] with Representative Amines under Catalytic Amidation Conditions 100

References 101

Supporting Information 121

Copies of ^{1}H, $^{13}C\{^{1}H\}$, $^{19}F\{^{1}H\}$ and $^{29}Si\{^{1}H\}$ NMR Spectra as appropriate for Synthesized Compounds 122

X-Ray Crystallographic Data 159

X-Ray Crystal Structure Figures 163

Appendices 166

Acknowledgments

I am truly grateful to Prof. Christopher Braddock and Prof. Paul Lickiss – without whom I wouldn't have been able to complete this journey – for their care and support over the past few years. Their wisdom and knowledge of the subject matter steered me throughout the PhD research. Indeed, it has been a great honour for me to work with them.

I reserve a special thanks to Dr. Mike Ray and Pete Haycock for all their unconditional support during these intense academic years.

I would like to acknowledge Dr. Andrew White and all technical staff for their excellent cooperation.

I owe a big thank you to Dr. Maariyah Suleman, Dr. Julian Becker, and Dr. Maryne Dubois for their friendship and support in difficult times.

Finally, but most importantly, I am deeply indebted to my Mother and Aunt for their constant love and exceptional dedication. I wouldn't have come this far without you!

Statement of Originality

I, Rabia Qamar, declare that the work presented herein is my own and has been generated as a result of my own original research. Where I've referred to published work of others, those sources are properly cited throughout the document.

Copyright Declaration

The copyright of this thesis rests with the author. Unless otherwise indicated, its contents are licensed under a Creative Commons Attribution-Non Commercial 4.0 International License (CC BY-NC).

Under this licence, you may copy and redistribute the material in any medium or format. You may also create and distribute modified versions of the work. This is on the condition that: you credit the author and do not use it, or any derivative works, for a commercial purpose.

When reusing or sharing this work, ensure you make the licence terms clear to others by naming the licence and linking to the licence text. Where a work has been adapted, you should indicate that the work has been changed and describe those changes.

Please seek permission from the copyright holder for uses of this work that are not included in this license or permitted under UK Copyright Law.

Rabia Qamar
August 2023

Abbreviations

Ar - aryl

Ac - acetyl

aq. - aqueous

Bu - butyl

Bn - Benzyl

Boc - *tert*-Butyloxycarbonyl

calcd. - calculated

cat. - catalyst

cm - Centimetre

Cy - cyclohexyl

DABCO - 1,4-Diazabicyclo[2.2.2]octane

DIBAL-H - Diisobutylaluminium hydride

DCM - Dichloromethane

DCE - Dichloroethane

DMF - *N,N*-dimethylformamide

dr - Diastereomeric ratio

equiv. - equivalent

EWD - Electron-withdrawing

EtOAc - Ethyl acetate

Et_2O - Diethyl ether

er - Enantiomeric ratio

ee - Enantiomeric excess

EI - Electron Ionization

Et - Ethyl

EtOH - Ethyl alcohol

Flu - Fluorenyl

g - gram

gem - geminal

h - hour

HPLC - High Performance Liquid Chromatography

HRMS - High Resolution Mass Spectrometry

*i*Pr - isopropyl

m - meta

M.p. - Melting point

mg - Milligram

μL - Microliter

mL - Millilitre

mmol - Millimole

mm - Millimetre

μm - Micron

min - minute

M - Molar

Me - Methyl

MeCN - Acetonitrile

MTBE - Methyl *tert*-butyl ether

MS - Mass Spectrometry

NMR - Nuclear Magnetic Resonance

NBE - Norbornene

NMP - *N*-methyl-2-pyrrolidone

nm - Nanometre

n - normal

OMe - Methoxy

OTf - Triflate (trifluoromethanesulfonate)

o - ortho

p - para

tert - Tertiary

ppm - parts per million

Pr - propyl

Ph - Phenyl

rt - room temperature

TLC - Thin Layer Chromatography

TM - Transition metal

THF - Tetrahydrofuran

TBAF - tetra-*n*-butylammonium fluoride

TBHP - *tert*-butyl hydroperoxide

Ts - Tosyl (toluenesulfonyl)

Chapter 1: Introduction

1.1 Arylsilanols in Organic Synthesis

Silanols – the silicon analogues of carbinols – generally exist as tetracoordinate species with a tetrahedral silicon centre (Figure 1). The average C–Si bond distance (1.863 Å) is around 20% longer than the corresponding C–C bond (1.530 Å), while the Si–O bond distance (1.631 Å) is about 15% longer than that of C–O (1.426 Å). These bond length variations are reflective of a larger atomic radius of silicon (117 pm) than carbon (77 pm). The enhanced acidity of silanols compared to their carbon counterparts fundamentally arises from the large electronegativity difference between carbon (2.55) and silicon (1.90), as more electropositive silicon is capable of stabilizing the anionic oxygen. It is quite obvious that the inherent properties of silicon impart unique physicochemical features to organosilanols, rendering them valuable structures in organic synthesis, pharmaceuticals, and polymeric materials.[1-5]



Figure 1. Chemical structures of carbinol and silanol.

The seminal work by Hiyama in 1988 acted as a gateway towards the application of organosilicon compounds as nucleophilic partners in Pd-catalyzed cross-couplings with electrophilic organic halides/pseudohalides.[3] Despite an extensive use of boron-, tin-, and zinc- derived organometallic variants in cross-coupling chemistry, organosilanes evolved as viable alternatives owing to their stability, low toxicity and easy-handling. However, fluoride-mediated activation of the stable C–Si bond to facilitate the transmetalation step undermined the synthetic utility of silicon-based cross-couplings. To bypass the requirement for a fluoride source, Denmark developed Pd-catalyzed cross-

coupling protocols which use organosilanols or their conjugate bases as potent coupling partners under mild conditions, thereby offering good functional group compatibility.[3]

Silicon-tethers bearing directing groups (DGs) have long been recognized for directed C–H functionalization in various processes such as cycloadditions, radical reactions, TM-catalyzed ring-closing metathesis (RCM), and cross-couplings.[4] However, the complications associated with the removal of directing groups considerably hampers the utility of this approach in organic synthesis. Thus, an easily removable and modifiable DG is highly desirable. Si-tethers, in particular, sufficiently fulfil these prerequisites, thereby justifying their widespread acceptance in C-H functionalization chemistry.[4]

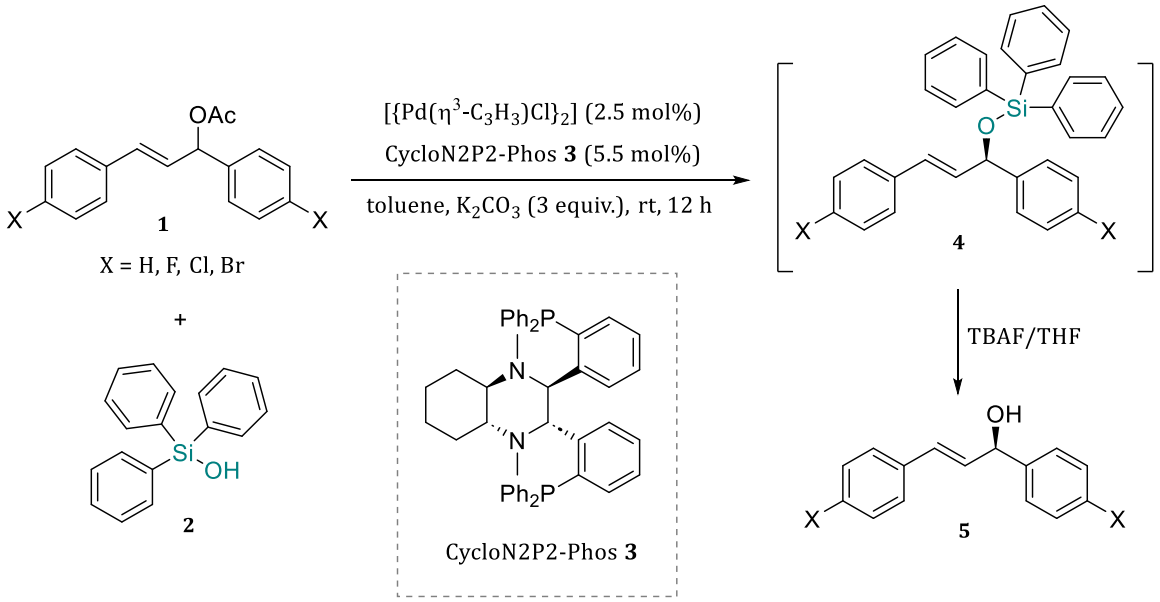
Since the employment of organosilanols in directed C–H functionalization and C–C cross-coupling reactions have been thoroughly reviewed previously[3,4] – and are indeed beyond the scope of the current discussion – these topics are not further detailed here. It is quite evident from literature that triarylsilanols have been solely engaged as substrates and/or reagents in synthetic transformations, however, their application as catalytic entities in contemporary organic synthesis is still non-existent.[1,3,4] The present discussion will deal with selected pertinent examples to showcase the practical value of arylsilanols in organic chemistry.[6-8]

1.1.1 Allylic Etherification

While organosilanols can efficiently participate in cross-coupling reactions,[3] their intrinsic potential as O-nucleophiles in asymmetric catalysis is largely unexplored. Over the last two decades, only a handful of catalytic methods involving the direct use of nucleophilic silanols have been developed, primarily to enable the construction of carbon-heteroatom bonds in chiral scaffolds.[6]

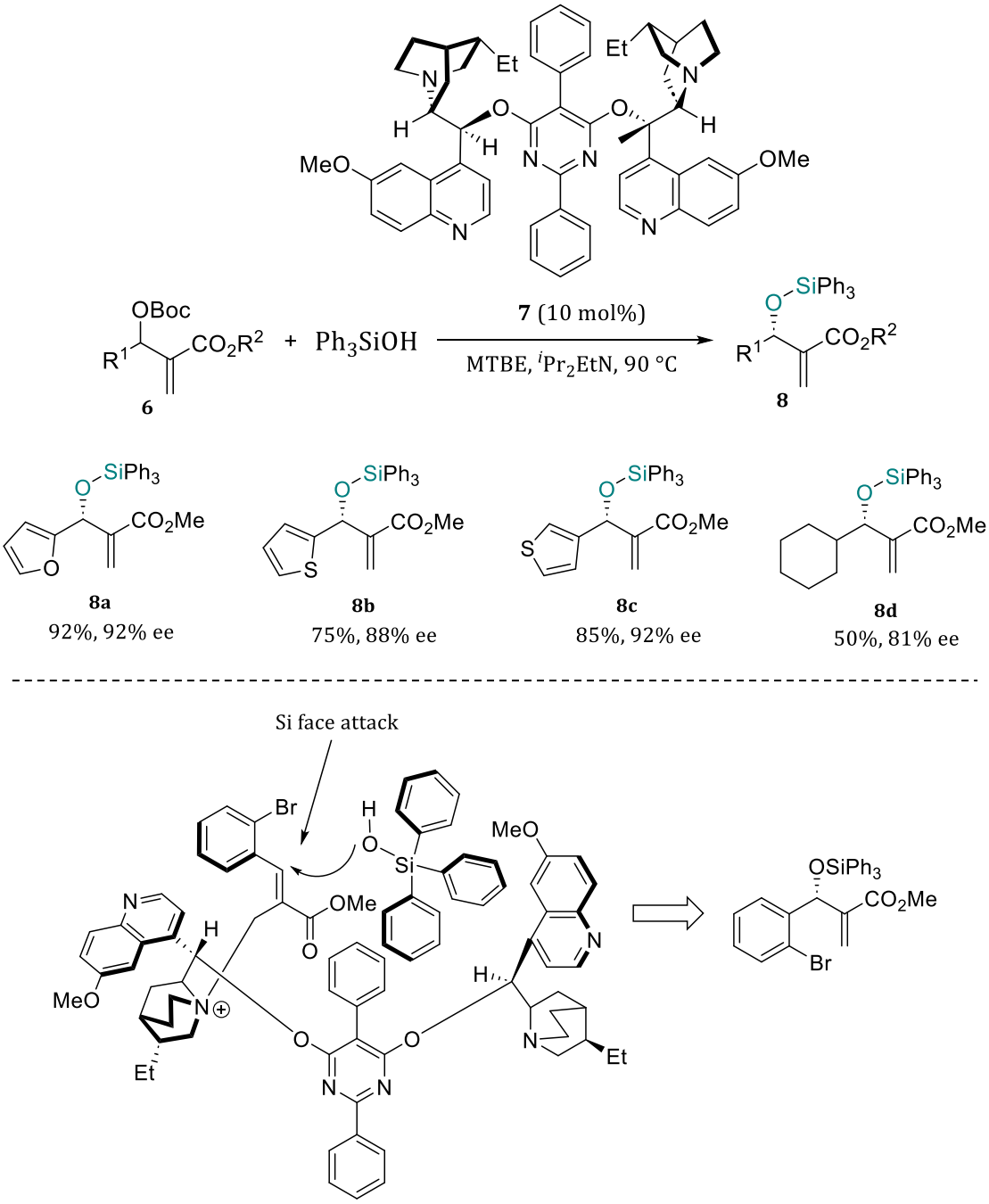
Xu *et al.* demonstrated the application of multifunctional *trans*-1,2-diaminocyclohexane-derived phosphine ligand CycloN2P2-Phos **3** in Pd-catalyzed reaction of allylic acetate **1** with triphenylsilanol

2 (Scheme 1).[6b] The desired chiral silyl ether **4** was obtained in excellent yields (> 90%), however, attempts to determine the enantioselectivity of **4** were unsuccessful due to poor resolution on chiral HPLC. Subsequently, TBAF-mediated desilylation was performed to obtain the corresponding allylic secondary alcohols **5** for an indirect determination of enantioselectivity.



Scheme 1. Pd/CycloN2P2-Phos-catalyzed asymmetric allylic etherification.

Later, a novel approach featuring (bis)*Cinchona* alkaloid $(DHQD)_2PYR$ **7** catalyzed allylic substitution reaction of Morita–Baylis–Hillman (MBH) carbonates **6** with Ph_3SiOH as O-nucleophile was developed (Scheme 2).[6d] To explore the generality of the protocol, various MBH carbonates including aromatic, heterocyclic, and aliphatic were reacted with **2** to afford the corresponding allylic etherification products **8** in moderate to good yields (58–98%) and respectable enantioselectivities. The reaction was proposed to proceed via formation of $(DHQD)_2PYR$–MBH adduct preferentially as *E*-isomer, where the sandwich-like geometry – stabilized by π-π interactions between quinoline moiety and phenyl rings – allows the attack of triphenylsilanol anion effectively from *Si* face to furnish the silyl ethers **8** with *R* configuration.

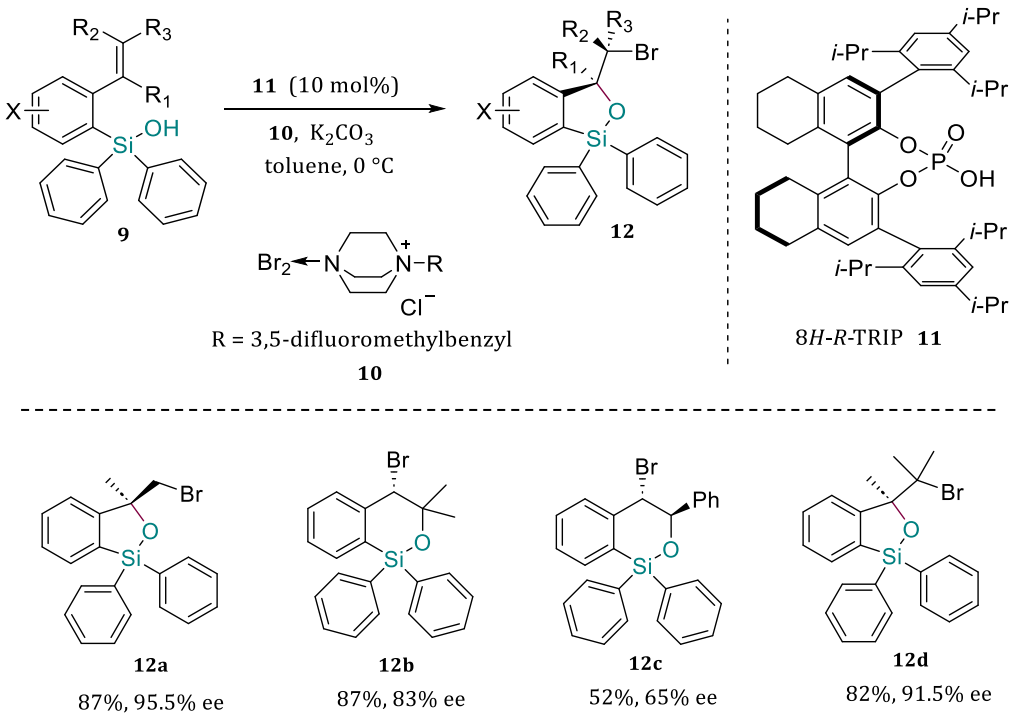


Scheme 2. Asymmetric allylic etherification of MBH carbonates and silanols.

1.1.2 Cycloetherification

To achieve the synthesis of structurally diverse enantiopure benzoxasiloles **9**, asymmetric halo-oxycyclization of olefinic silanols **9** in the presence of chiral phosphoric acid catalyst **11** (Scheme 3), was described by Xie and coworkers.[6e] The enantioselectivity of the reaction was found to be dependent on the counter anion of the brominating reagent, that is, bromine/*N*-benzyl-DABCO

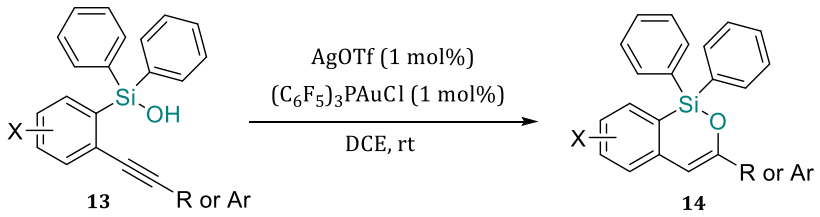
complex **10**. However, in terms of substrate scope, installation of olefinic alkyl substituents (Et, *i*-Pr) resulted in the erosion of enantioselectivities. Interestingly, removal of the Me group from the substrate led to the formation of only *6-endo*-bromo-oxycyclization products **12b** and **12c**. Moreover, the reaction worked well with tetra-substituted olefin delivering the corresponding benzoxasilole **12d** in 91.5% ee.



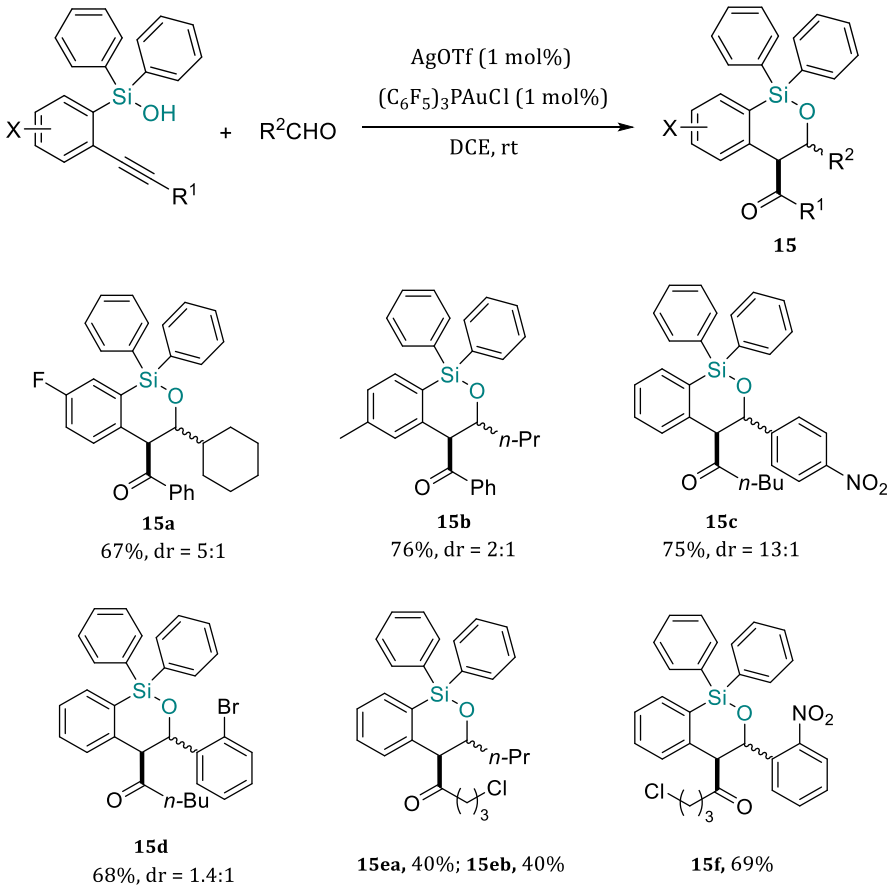
Scheme 3. Enantioselective bromo-cycloetherification of olefinic silanols.

1.1.3 Hydrosilyloxylation

In efforts to access synthetically useful enol silyl ethers from non-carbonyl precursors, a mild and convenient gold-catalyzed intramolecular cyclization of alkynyl silanols **13** was reported by Lee and coworkers (Scheme 4).[7a] The efficiency and robustness of this cyclization strategy was manifested by developing a one-pot tandem hydrosilyloxylation/aldol reaction, that involved the chemoselective *in situ* generation of an enol silyl ether, in the presence of an aldehyde. A range of alkynyl silanols and aldehydes were successfully subjected to intramolecular hydrosilyloxylation/aldol reaction conditions, giving the corresponding aldol products **15a-f** in a diastereoselective fashion (Scheme 5).

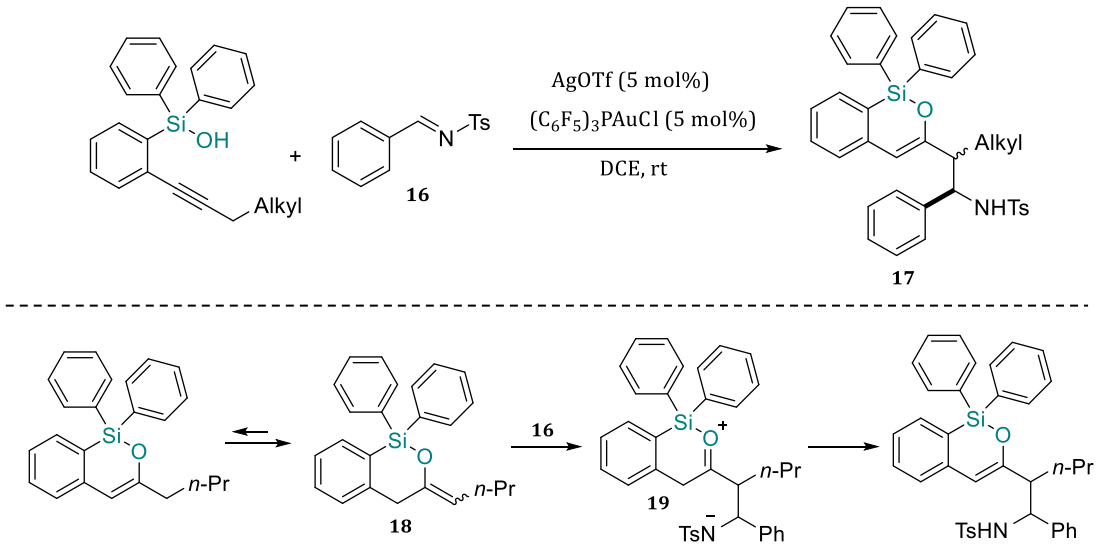


Scheme 4. Au-catalyzed intramolecular hydrosilyloxylation.



Scheme 5. Au-catalyzed intramolecular hydrosilyloxylation/aldol reaction.

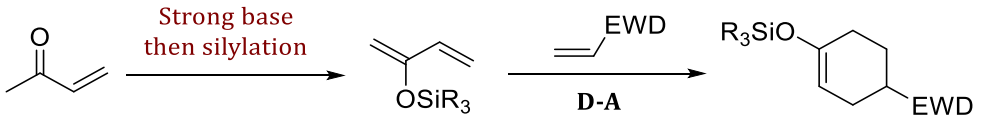
Additionally, the tandem hydrosilyloxylation/Mannich reaction was investigated by reacting alkynyl silanols bearing alkyl substituents, with (*E*)-*N*-benzylidene-4-methyl benzenesulfonamide **16** in the presence of a gold-catalyst system (Scheme 6).[7a] Unexpectedly, the installation of an imine moiety at *exo* position of the silicon ether products **17** was detected, thus, suggesting the isomerization of the enol double bond under the given conditions (*vide infra*). This was further corroborated by the fact that a non-isomerizable enol ether, generated from an alkynyl silanol having phenyl group *on sp*-hybridized carbon, did not react with imine **16** in this tandem one-pot process.



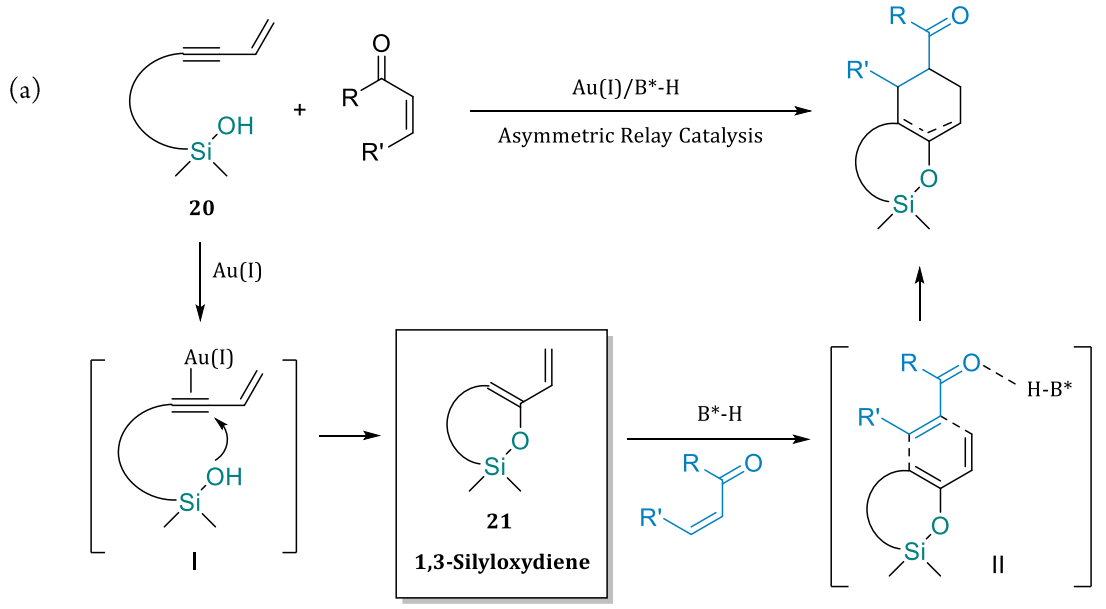
Scheme 6. Au-catalyzed hydrosilyloxylation/isomerization/Mannich reaction.

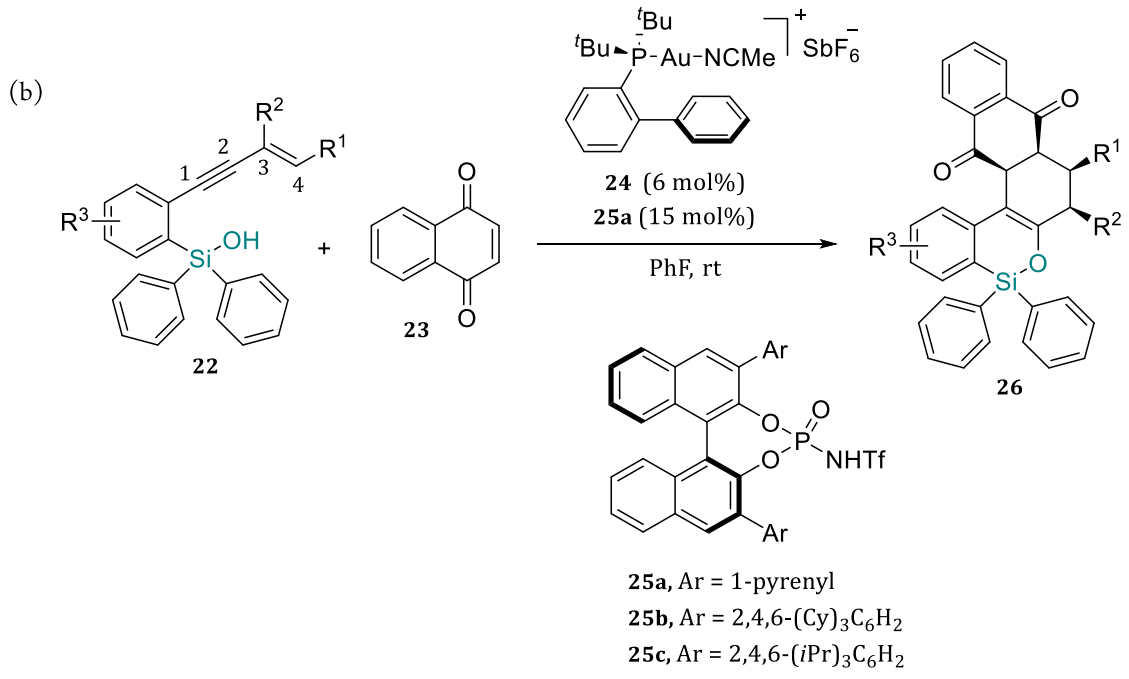
The frequently employed method to prepare 1,3-silyloxydienes for Diels–Alder reactions involve the silylation of carbonyl compounds, which requires stoichiometric amounts of strong bases (Scheme 7). In contrast to this traditional approach, Gong *et al.* reported the use of enynyl silanol **20** as latent 1,3-silyloxydiene **21** which is capable of reacting with an electron-deficient olefin in a catalytic asymmetric Diels–Alder reaction (Scheme 8a).[7b]

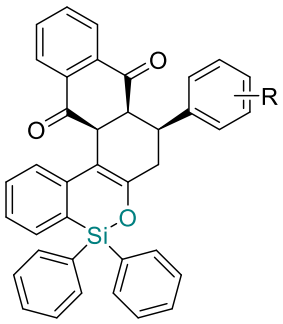
The protocol comprises a hybrid metal/organo catalyst system, where gold complex **24** facilitates the intramolecular hydrosilyloxylation of (2-(but-3-en-1-ynyl)phenyl)-diphenylsilanol derivatives **22** to yield the desired 1,3-silyloxydiene **21**, which subsequently participate in asymmetric relay Diels–Alder reaction with naphthoquinone under chiral Brønsted acid catalysis. Resultant polycyclic products **26** bearing multiple stereogenic centres were obtained in high yields and excellent enantioselectivities (Scheme 8b). It is worth noting that Diels–Alder reaction between enynyl silanols **22** and **23** using achiral gold complex **24** alone gave no desired product, thus, implying that Brønsted acid catalyst **25a** solely empowers the asymmetric Diels–Alder event in this cascade process.



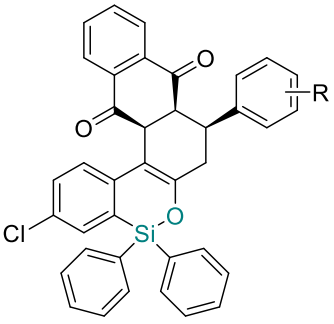
Scheme 7. Classical synthesis of 1,3-silyloxydienes for Diels–Alder reaction.



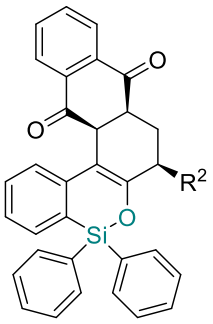




26a: R = H, 95%, 94% ee
26b: R = 4-Me, 70%, 96% ee
26c: R = 3-Me, 95%, 96% ee
26d: R = F, 98%, 95% ee
26e: R = Ph, 76%, 96% ee
26f: R = 2-OMe, 82%, 87% ee



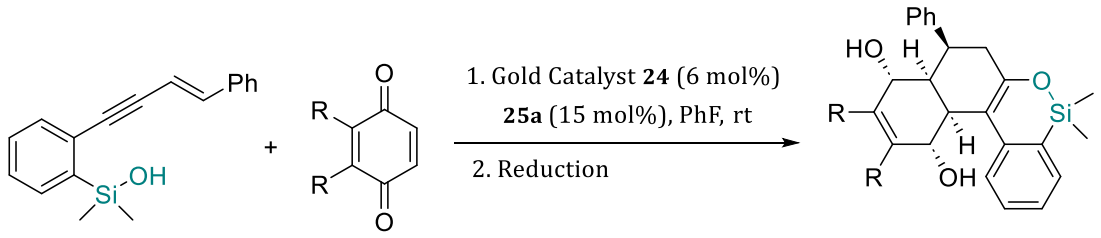
26g: R = H, 80%, 94% ee
26h: R = 3-Me, 95%, 96% ee



26i: R = Me, 67%, 91% ee
26j: R = n-C_4H_9, 94%, 91% ee
26k: R = n-C_5H_{11}, 94%, 91% ee

Scheme 8. Catalytic hydrosilyloxylation of enynyl silanol/asymmetric Diels–Alder reaction. (a) General strategy. (b) Substrate scope.

Furthermore, benzoquinone derivatives **27a-c** reacted well with 1,3-silyloxydiene generated from enynyl silanol **22a** bearing a phenyl group at C4, followed by a one-pot reduction using DIBAL-H, thus, furnishing the desired products **28a-c** with satisfactory results (Scheme 9).[7b]



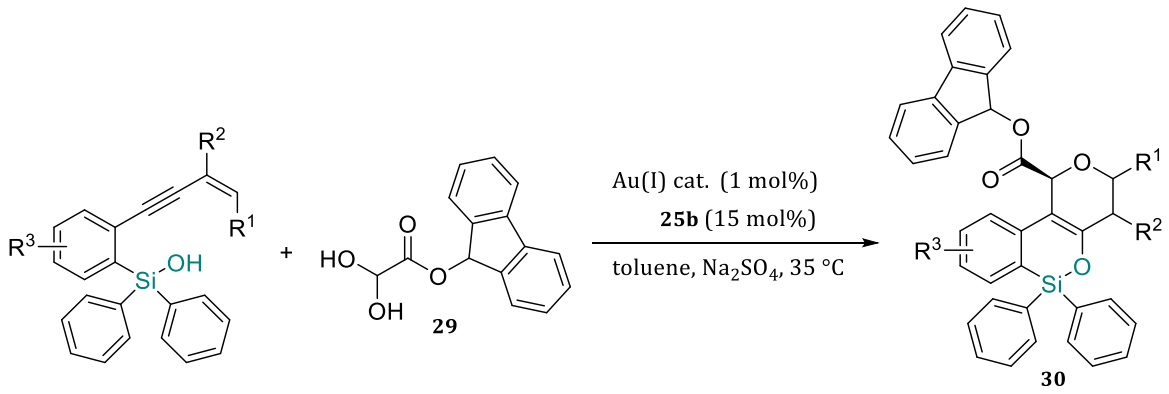
22a

27a: R = H
27b: R = Me
27c: R = Cl

28a: R = H, 82%, 93% ee
28b: R = Me, 81%, 94% ee
28c: R = Cl, 69%, 95% ee

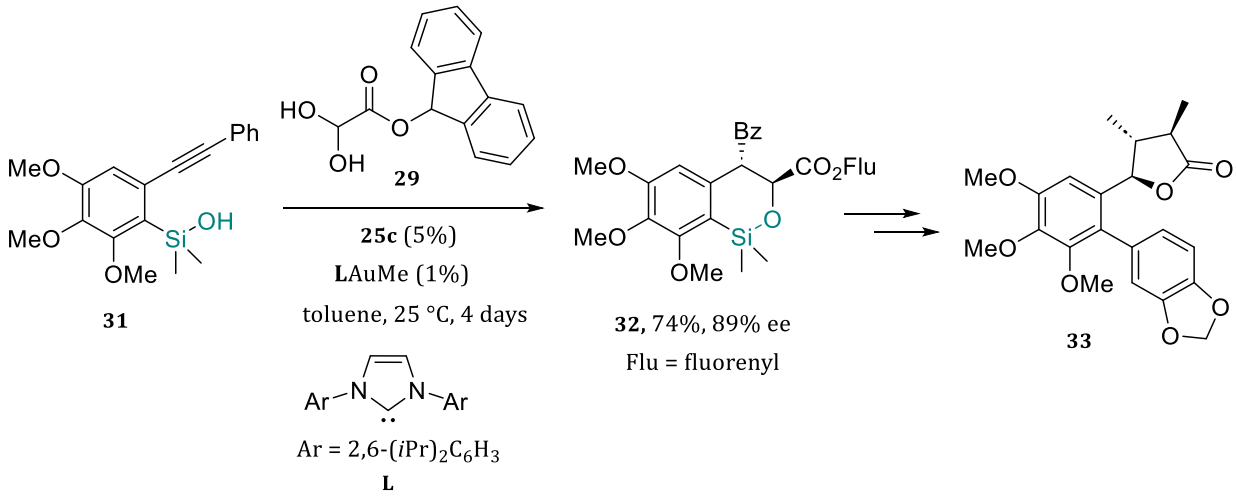
Scheme 9. Hydrosiloxylation/asymmetric Diels–Alder reaction using benzoquinones.

Au(I)/Brønsted acid binary catalyst system could be exploited to enable an asymmetric oxo–Diels–Alder reaction of enynyl diphenylsilanols with fluorenyl glyoxylate **29**, giving 3,6-dihydropyran derivatives **30** in good yields and with high stereo-control (Scheme 10). The reaction yields were enhanced by addition of anhydrous sodium sulphate.[7c]



Scheme 10. Catalytic hydrosiloxylation/asymmetric hetero–Diels–Alder reaction.

Likewise, the gold-catalyzed cyclization of 2,3,4-trimethoxy-6-(phenylethynyl)phenyl dimethylsilanol **31** generates silyl enol ether, which successfully undergoes chiral Brønsted acid induced asymmetric aldol reaction with **29**, thereby enabling the synthesis of key intermediate **32** en route to natural product eupomatilone-6 **33** (Scheme 11).[7d]

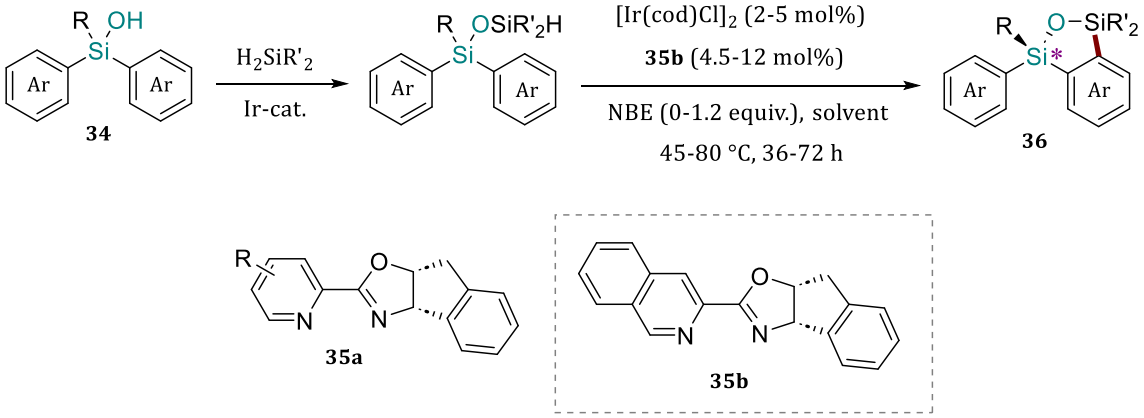


Scheme 11. Enantioselective synthesis of (−)-5-*epi*-eupomatilone-6.

1.1.4 Enantioselective Stereogenic Silanols

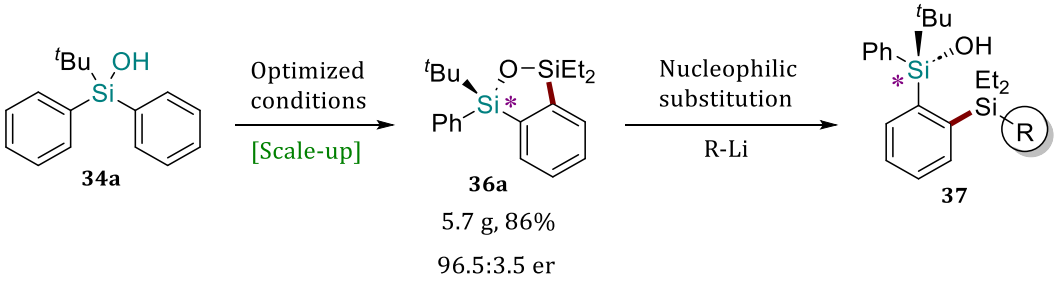
The intrinsic properties of silicon present substantial challenges to achieve the synthesis of enantioenriched silicon-stereogenic silanols in the domain of asymmetric catalysis.[8] Therefore, catalytic protocols capable of generating optically active silanols with high stereocontrol are of much interest. To this end, Zhao and coworkers established desymmetrization of prochiral diarylsilanols **34**

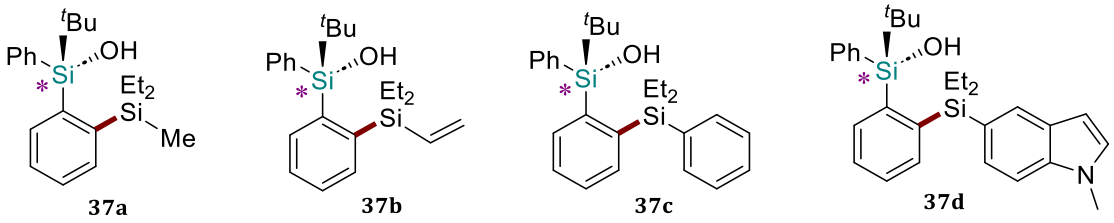
via Ir-catalyzed C–H silylation as a facile route to access silicon-stereogenic centres (Scheme 12).[8b] Notably, an extensive ligand screening revealed that the reaction efficiency with respect to reactivity and selectivity, could be enhanced by increasing the basicity of a pyridinyl group in the indane-fused ligand **35a**. Since the isoquinoline moiety is more basic than pyridine, subsequent employment of a novel isoquinoline-based oxazoline ligand **35b** delivered enantioenriched (95.5:4.5 er) silylated product **36** in excellent yields.



Scheme 12. Enantioselective desymmetrization of prochiral diarylsilanols.

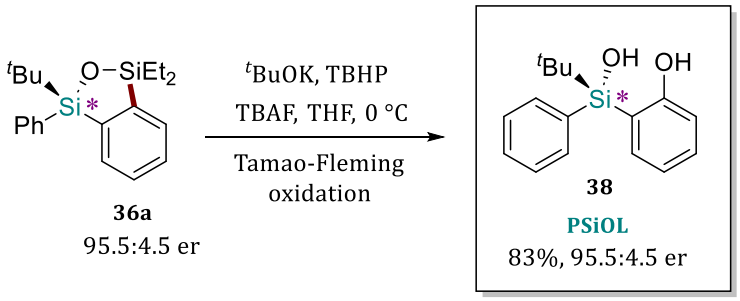
The practical value of this Ir-catalyzed C–H silylation was demonstrated by a gram-scale synthesis of **36a**, where the desired cyclic product was successfully obtained in 86% yield (Scheme 13). Following this enantioselective C–H silylation, cleavage of the sterically less demanding Si–O bond by various organolithium reagents (R–Li) resulted in a regiospecific ring-opening of diarylsilanol-derived silyl ether **36a** with retention of the enantioselectivity, thereby affording the enantiomerically enriched silanols **37a-d**.





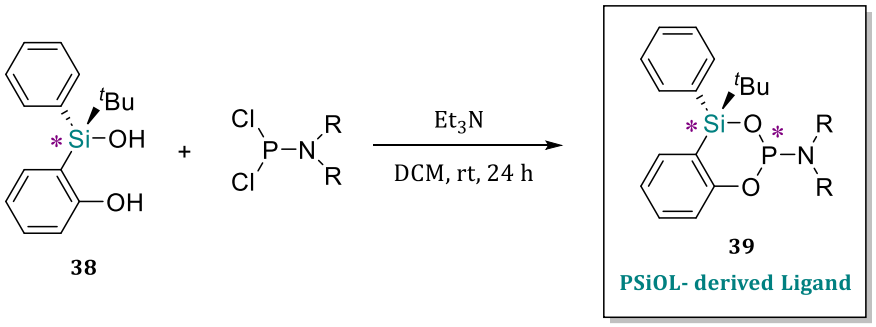
Scheme 13. Asymmetric synthesis of enantioenriched silicon-stereogenic silanols.

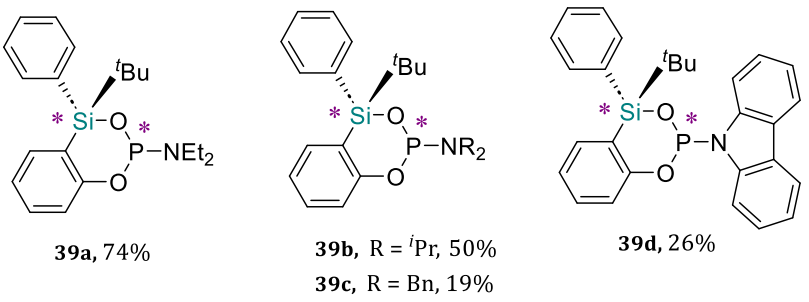
These authors further demonstrated the regioselective oxidation of two non-equivalent C–Si bonds in C–H silylation product **36a** under Fleming-Tamao oxidation conditions (Scheme 14). Treatment of **36a** with *t*-butyl hydroperoxide (TBHP) afforded the enantioenriched phenolic silanol (PSiOL) **38** in 83% yield without any loss of enantiomeric purity.



Scheme 14. Transformation of **36a** to PSiOL.

To demonstrate the synthetic utility of chiral diol scaffold **38**, enantiopure PSiOL (>99.5:0.5 er after recrystallization in toluene) was transformed into an array of monodentate PSiOL-derived phosphoramidite ligands **39a-d** (Scheme 15). The induction of chirality on the phosphine moiety was chiefly driven by the absence of C2-symmetry in **38**, thereby providing a novel chiral ligand bearing both Si and P-stereo centres.





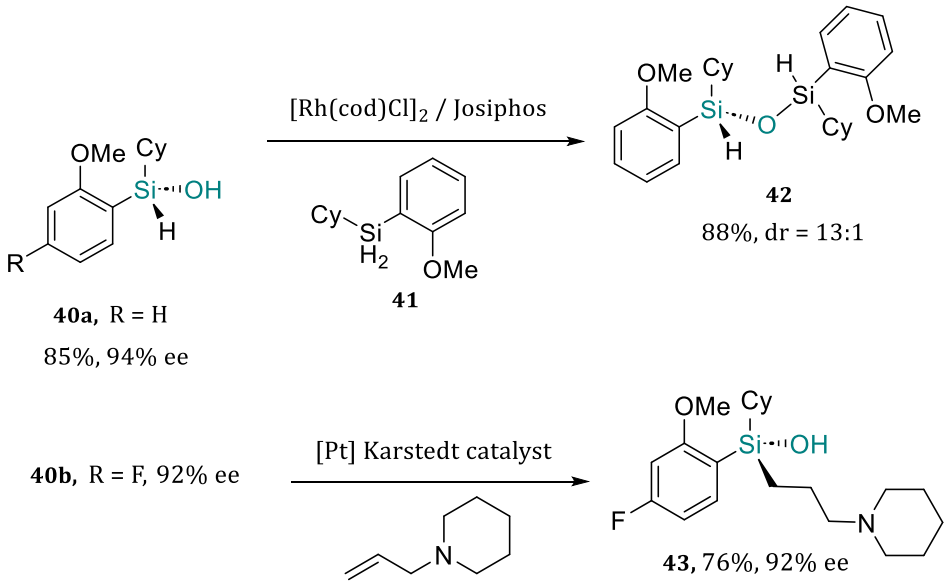
39a, 74%

39b, R = ^{i}Pr, 50%
39c, R = Bn, 19%

39d, 26%

Scheme 15. Transformation of PSiOL to a series of PSiOL-based phosphoramidite ligands.

He *et al.* exemplified the versatility of chiral silanols by carrying out a Rh-catalyzed coupling of cyclohexyl(2-methoxyphenyl)silanol **40a** with dihydrosilane **41**, generating disiloxane product **42** featuring two silicon stereo centres (Scheme 16).[8c] Furthermore, in order to obtain sila-substituted chiral drug **43** in a highly stereoselective manner, fluoro- derivative **40b** smoothly underwent Pt-catalyzed hydrosilylation with 1-allylpiperidine, delivering *p*-fluoro-hexahydro-sila-difenidol **43** in 92% ee.



Scheme 16. Stereospecific derivatization of silicon-stereogenic silanols.

1.2 Catalytic Direct Amidations

The classical methods for amide bond construction use stoichiometric amounts of coupling reagents (DCC (*N*,*N*′-dicyclohexylcarbodiimide), EDC (*N*-ethyl-*N*′-(3-

dimethylaminopropyl)carbodiimide), CDI (carbonyl diimidazole), HATU (*N*-[(dimethylamino)-1*H*-1,2,3-triazolo[4,5-*b*]pyridin-1-ylmethylene]-*N*-methylmethanaminium hexafluorophosphate *N*-oxide)), in conjunction with hazardous organic solvents (DCM, DMF, NMP), which pose serious environmental and safety concerns, thereby tremendously restricting the wider acceptance of these conventional approaches.[9] Hence, a call for the design and execution of safer, atom-economical protocols – with minimal waste production – for amide bond synthesis, is rational.[10,11]

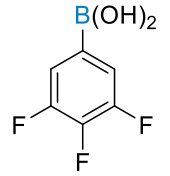
While boron-based catalysts,[12-15] group IV metal catalysts,[16] and other catalytic processes[17] have been established, a general and practical catalytic methodology for direct coupling of carboxylic acids and amines still remains daunting.[11] Several comprehensive reviews have summarized the developments in catalytic direct amide/peptide synthesis,[9,11] therefore, only selected recent organoboron catalysts will be discussed here.

Amongst boron-based catalysts for direct amidation of carboxylic acids,[12-15] DATB **55** and Pym-DATB **56** featuring B_3NO_2 heterocycle, deserve comment (Figure 2). Thermally and hydrolytically robust DATB exhibited excellent catalytic activity towards dehydrative condensation of structurally diverse carboxylic acids and amines (Figure 3).[15a] The promising catalytic efficiency has been postulated to arise from three Lewis acidic boron sites, where B^1 preferentially coordinates to Lewis-basic amines while the remaining two B^2 facilitate the complexation of carboxylic acid to B_3NO_2 core, thus permitting the substrate assembly by decreasing the entropic penalty.

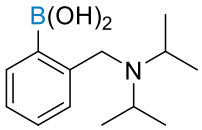
Despite the remarkable features of DATB mediated direct amidation protocol, this strategy suffers from tedious synthesis of **55**, subsequently hampering its broader utility. Therefore, the authors reported an alternative synthetic route to access DATBs by introducing 4,6-diarylpyrimidine scaffold.[15d] In sharp contrast to the stability of B_3NO_2 ring system in **55**, Pym-DATB was susceptible to undergo ring opening/closing dynamics in MeOH, which was attributed to the electron

withdrawing effect of pyrimidine moiety. To demonstrate the catalytic potential of Pym-DATB derivatives, **56** was successfully employed as amidation catalyst for direct coupling of various challenging carboxylic acid/amine substrates (Figure 4).

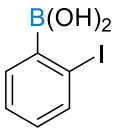
To deal with the downsides of organoboron catalysis in peptide synthesis, Takemoto and Shimada independently reported *gem*-DBA **57** and DBAA **58** as useful catalysts for dehydrative peptide formation with minimum loss of optical purity (Figure 2).[15f-g] DBAA enabled the conversion of serine and threonine derived *β*-hydroxy-*α*-amino acids into the corresponding dipeptides, whereas *gem*-DBA was found to be compatible with various functionalized *N*-protected *α*-amino acids. Hence, these boron-based catalysts (**57** & **58**) offer access to peptides in a highly chemoselective manner.



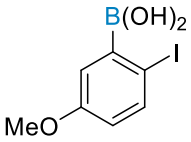
44
Yamamoto, **1996**[12a]



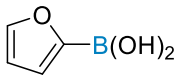
45
Whiting, **2008**[12c]



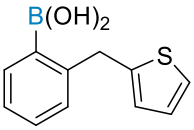
46
Hall, **2008**[12d]



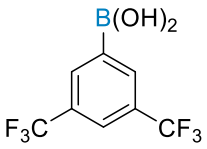
47, MIBA
Hall, **2012**[12e]



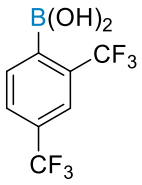
48
Tam & Chen, **2015**[12i]



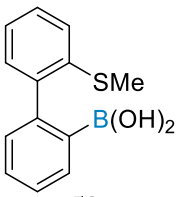
49
Blanchet, **2015**[12j]



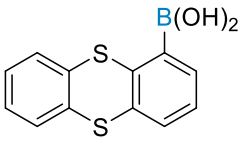
50 [a]
Ishihara, **2016**[12l]



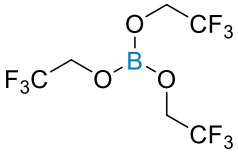
51
Ishihara, **2018**[12n]



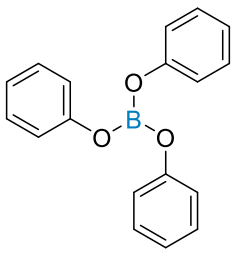
52
Hall, **2022**[12q]



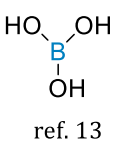
53
Su, **2023**[12r]



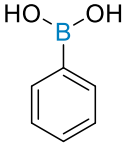
Sheppard, [b] **2017**[14a]
2018[14b], [c] **2019**[14d]



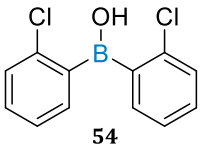
Sawant & Sekar, **2018**[14c]



ref. 13



Bandichhor, **2007**[13c]



54
Blanchet, **2015**[12k]

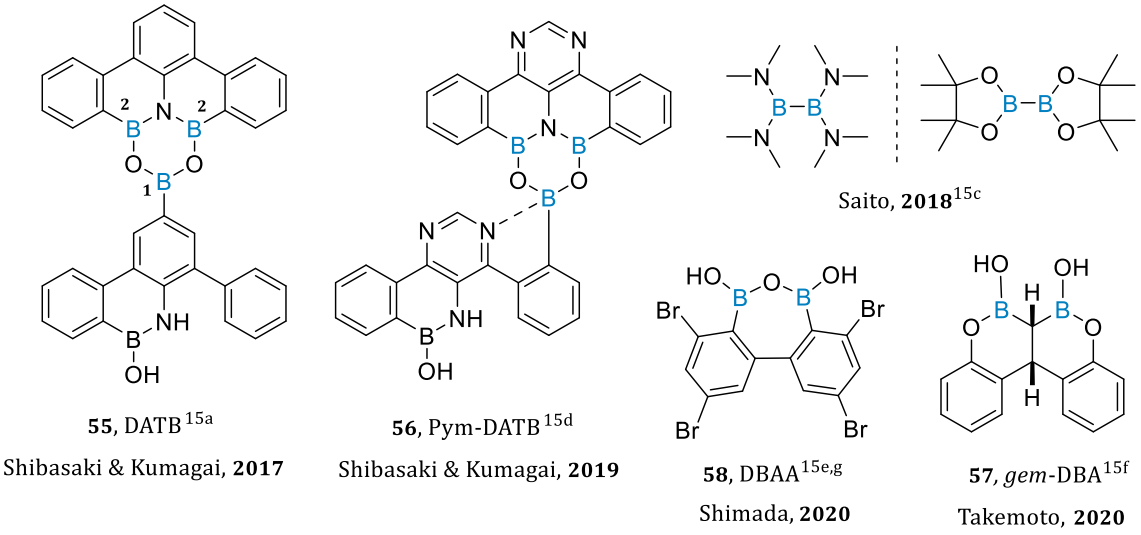


Figure 2. Previously employed boron catalysts. [a] DMAPO (4-(*N*,*N*-dimethylamino)pyridine *N*-oxide) was used as co-catalyst. [b] *tert*-Amyl methyl ether (TAME) was used as a solvent. [c] *tert*-Butyl acetate was used as a solvent. (MIBA = 5-Methoxy-2-iodophenylboronic acid; *gem*-DBA = *gem*-Diboronic acid; DBAA = Diboronic acid anhydride; DATB = 1,3-Dioxa-5-aza-2,4,6-triborinane; Pym-DATB = Pyrimidine-DATB).

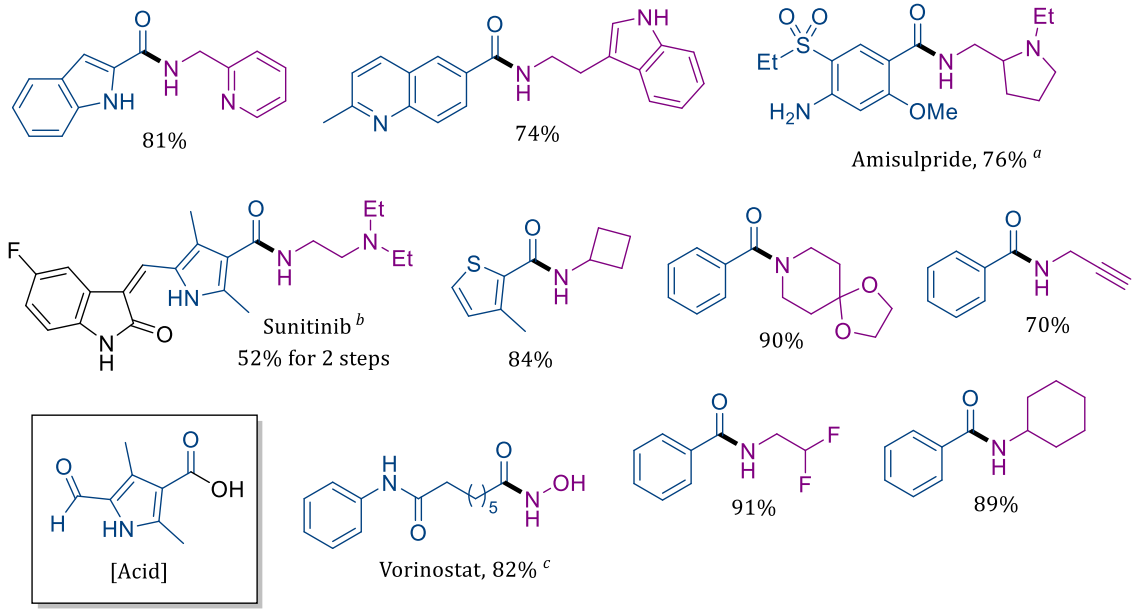


Figure 3. Scope of DATB catalyzed direct amidations (selected examples). Reaction conditions: Acid (0.30 mmol, 1.0 equiv.), Amine (0.30 mmol, 1.0 equiv.), DATB (5 mol%), toluene, MS4Å, 80 °C, 14 h. [a] Refluxing toluene. [b] Subsequent condensation with 5-fluoro-2-oxindole. [c] 1.0 equiv. Et_3N.

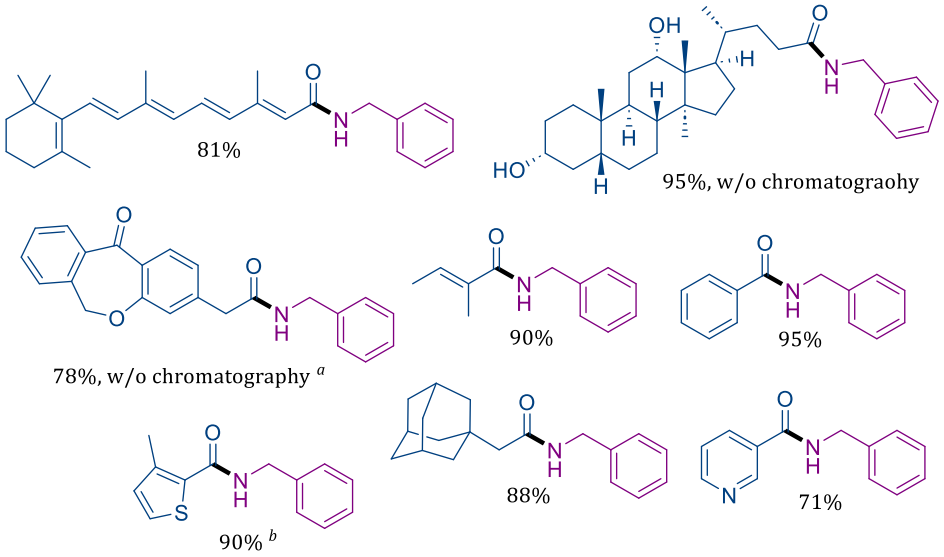
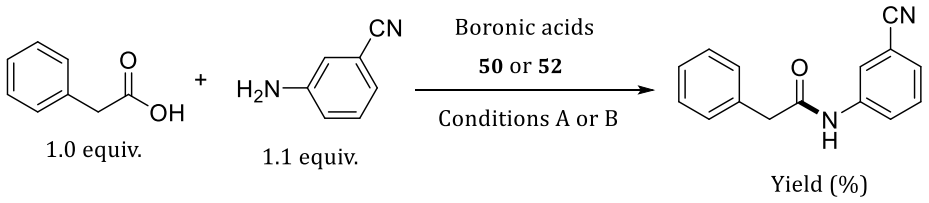


Figure 4. Scope of Pym-DATB catalyzed direct amidations (selected examples). Reaction conditions: Acid (0.25 mmol, 1.0 equiv.), Amine (0.25 mmol, 1.0 equiv.), Pym-DATB (5 mol%), PhF, MS4Å, 85 °C, ≤ 16 h. [a] **56** (0.5 mol%), gram-scale. [b] Refluxing toluene.

Considering the dual activation of carboxylic acid and amine, Hall and coworkers designed a bifunctional boronic acid catalyst **52** – comprising a biphenyl rigid core and a proximal hetero-atom functionality – to enable the dehydrative coupling of aliphatic carboxylic acids and anilines.[12q] A model reaction of phenylacetic acid and aniline was chosen to assess the catalytic potential of this new boronic acid derivative. Results revealed the superior catalytic efficiency of **52** in comparison to the previously reported catalysts **47** (MIBA) and **49**. Furthermore, in contrast to the preceding work by Ishihara, where the attempted amidation of phenylacetic acid with electron-deficient aniline under 3,5-(trifluoromethyl)phenylboronic acid **50**/ DMAPO cooperative catalysis afforded the corresponding anilide only in low yields,[12l] **52** was proved to be effective delivering the amide product in 82% yield (Scheme 17).

The subjection of an aliphatic carboxylic acid bearing an *α*-stereogenic centre and aniline to this boronic acid catalysis (MIBA or **52**) resulted in the erosion of enantioselectivity, as depicted in Scheme 18. In fact, lowering the reaction temperature from 85 °C to 65 °C did not ameliorate the

situation and traces of amide product were obtained, hence, this partial epimerization under the reaction conditions presents the limitation of the current catalytic protocol.



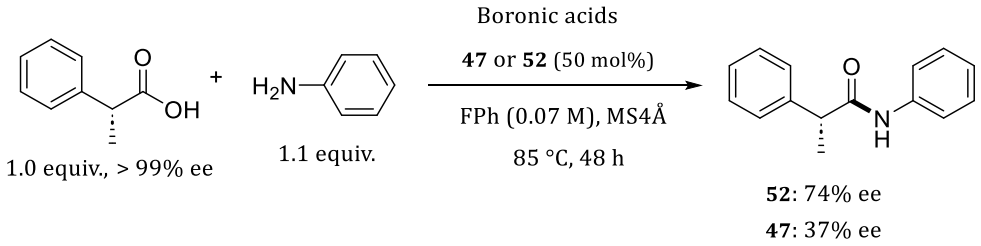
Conditions	Boronic acid:	**50**	**52**
A		34	82
B		15	64

Conditions:

A: **52** (50 mol%), DMAPO (5 mol%), FPh (0.07 M), MS4Å, 85 °C, 48 h

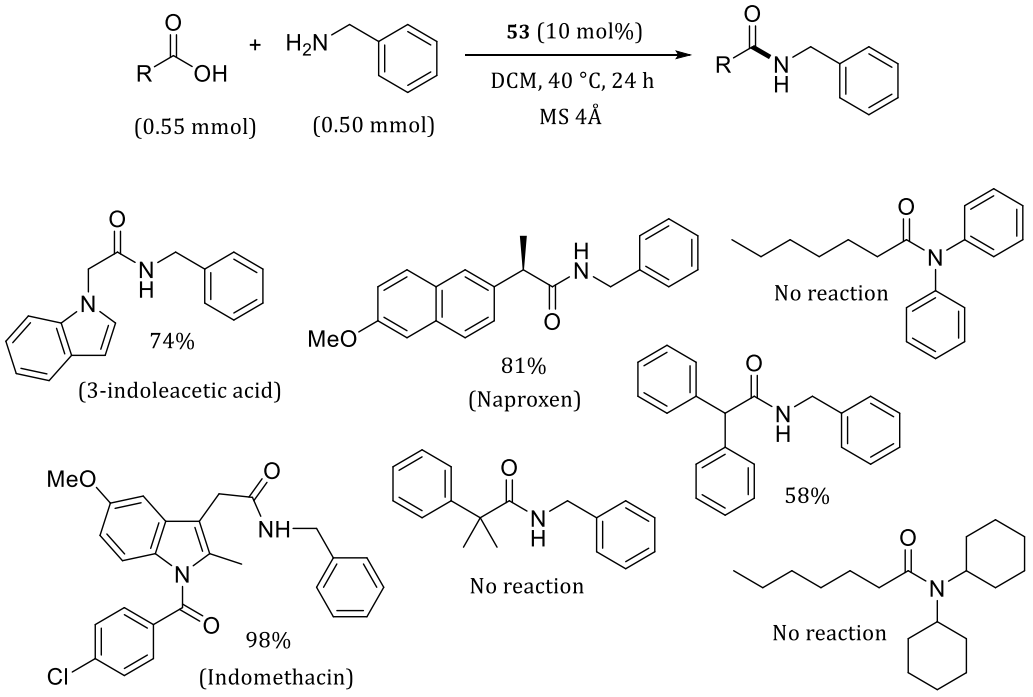
B: **50** (10 mol%), DMAPO (5 mol%), FPh (2 M), Dean-Stark, 85 °C, 48 h

Scheme 17. Comparison of boronic acids **50** and **52** under DMAPO co-catalysis.

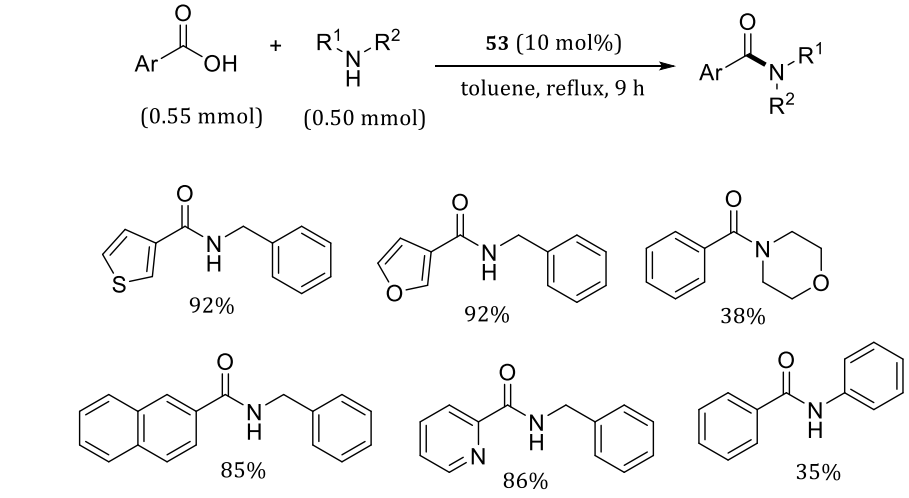


Scheme 18. Amidation of an optically enriched *α*-substituted carboxylic acid.

Very recently, Su *et al.* reported the first thianthrene based boronic acid catalyst **53** for direct amide bond synthesis.[12r] The heterocyclic catalyst was proven effective for catalytic dehydrative condensation of various aliphatic carboxylic acids and amines – except sterically cumbersome *α,α*-dimethylphenylacetic acid, diphenylamine and dicyclohexylamine coupling partners, which were found to be completely unreactive under the given conditions (Scheme 19). The less reactive aryl carboxylic acids were shown to react with different alkyl and aryl amines in refluxing toluene without employing molecular sieves (Scheme 20). However, diminished catalytic activity was observed in attempted amidations of benzoic acid with morpholine and aniline, thus affording the corresponding amides in relatively lower yields (38% & 35% respectively).

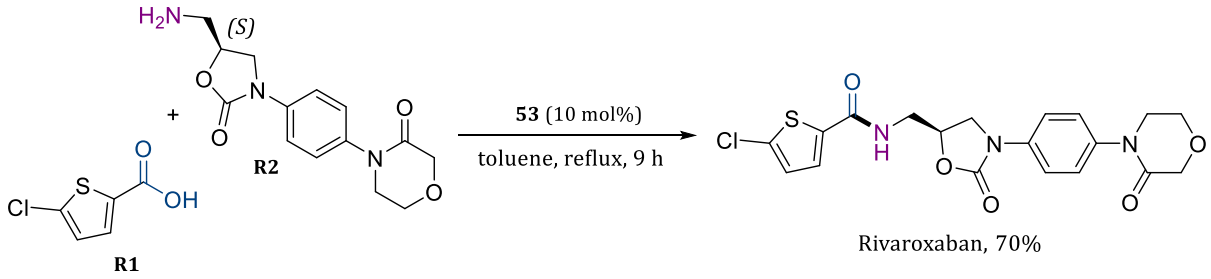


Scheme 19. Scope of 1-thianthrenylboronic acid catalyzed amidation of aliphatic carboxylic acids (selected examples).



Scheme 20. Scope of 1-thianthrenylboronic acid catalyzed amidation of aryl carboxylic acids (selected examples).

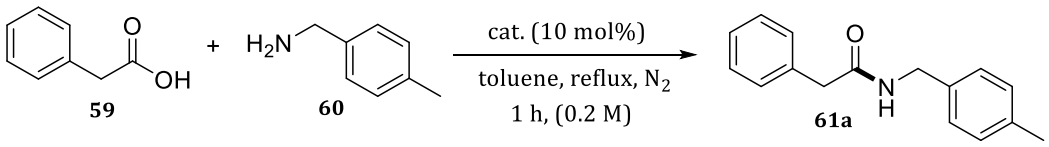
The practical value of 1-thianthrenylboronic acid catalysis was further demonstrated by carrying out the synthesis of a leading amide drug, rivaroxaban – from thienyl carboxylic acid and structurally complex amine fragment – in 70% yield (Scheme 21).[12r]

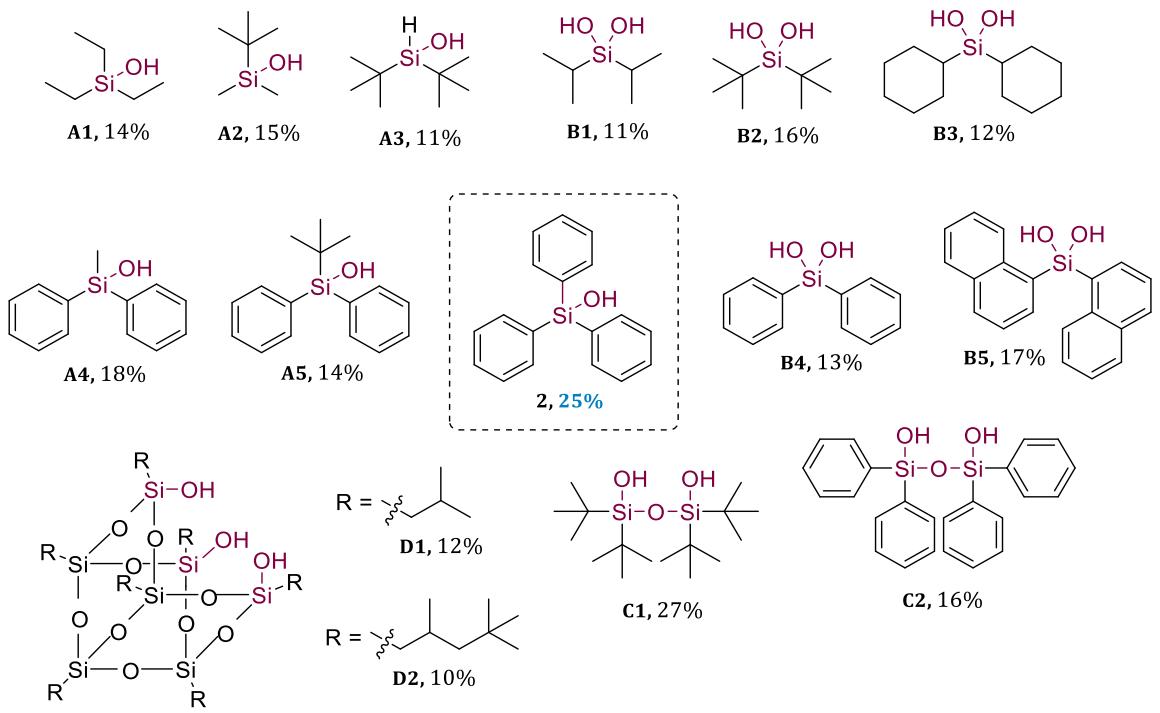


Scheme 21. Synthesis of anticoagulant amide drug.

Although silicon-based reagents[18] and silica gels[19] driven direct amidation protocols have been established, silicon-based amidation catalysts remain unreported in the literature.[20] To this end, we pursued the discovery of an organosilicon catalyst for direct coupling of carboxylic acids with amines and efforts towards this goal culminated in the identification of triarylsilanols as viable amidation catalysts under specified conditions (*vide infra*).[21]

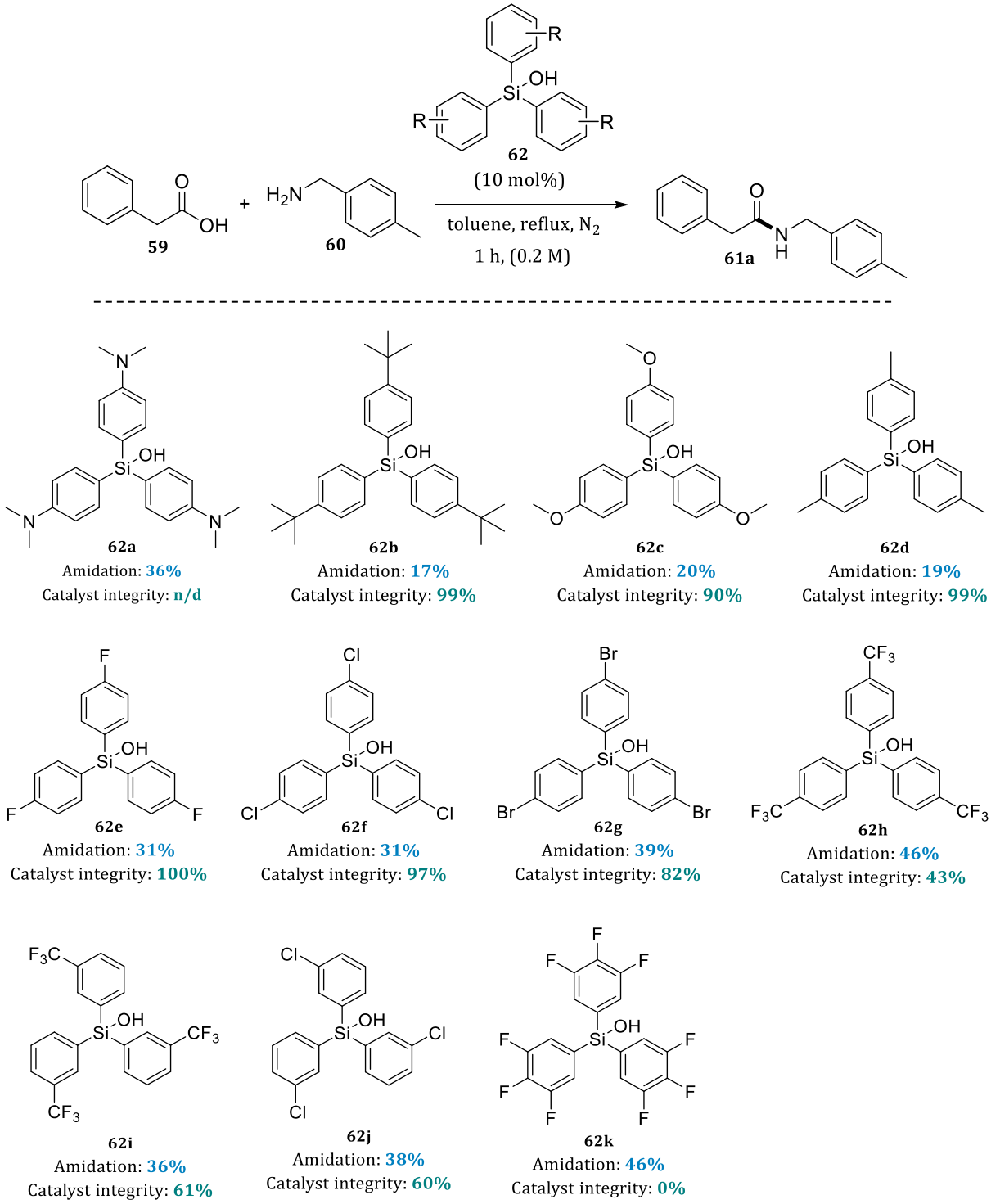
As the opening phase of the inquiry, silanols (**A1**-**A5**), silanediols (**B1**-**B5**), siloxane diols (**C1** & **C2**), and silsesquioxanes (**D1** & **D2**) were examined at 10 mol% loading, using a model amidation system of aliphatic carboxylic acid **59** and primary amine **60** in 1:1 stoichiometry to give the corresponding amide **61a**, in refluxing toluene for 1 h (Scheme 22). The 25% conversion to amide with triphenylsilanol **2** over background reaction (11%) in conjunction with chemical resistant towards the formation of catalytically inactive hexaphenyldisiloxane [$(Ph_3Si)_2O$], revealed **2** as the lead catalyst.[21a]





Scheme 22. Potential catalysts under model amidation conditions. Background reaction gives 11% amide conversion.[21a]

Having identified readily available Ph_3SiOH **2** as a practical choice, a series of known and new electronically differentiated triarylsilanols **62a-k** were synthesized, to conduct a systematic evaluation of their catalytic activity under model amidation conditions (Scheme 23). Electron-rich arylsilanols **62b-d** did not improve amide conversion over parent Ph_3SiOH; however, increased conversions were obtained with electron-deficient congeners. Furthermore, post-reaction catalyst quantification by ^1H NMR spectroscopy revealed the substantial loss of electron-deficient arylsilanols (**62h-k**) under the specified conditions, in contrast to the electron-rich analogues (**62b-d**) investigated. These preliminary findings pertaining to the catalyst stability led us to further comprehend the effect of substituents, as arylsilanols evaluated for their catalytic potential were found to be sensitive to the electronic characteristics of phenyl rings.



Scheme 23. Screening of the catalytic activity of triarylsilanols including the assessment of catalyst integrity post-reaction. **62a** could not be quantified due to signal overlapping in the ^{1}H NMR spectrum.[21a]

Hammett plot[22] ($\log(k_R/k_H)$ versus substituent constants $\sigma_{p/m}$) analysis revealed a linear correlation with slope or sensitivity constant of $\rho = 0.82$ (Figure 5). The increase in the rate of catalytic amidation

when triarylsilanols are substituted with electron-withdrawing groups is plausible, as the positive slope is indicative of a build-up of negative charge in the rate-determining step. Conversely, arylsilanols bearing electron-donating substituents somewhat decreased the reaction rate, presumably by increasing the electron density on silicon. Interestingly, *p*-dimethylamino silanol **62a** was found to be an evident outlier (not plotted), which stems from the fact that protonation of the amine centres under the reaction conditions significantly alter the electronic characteristics of this catalyst.

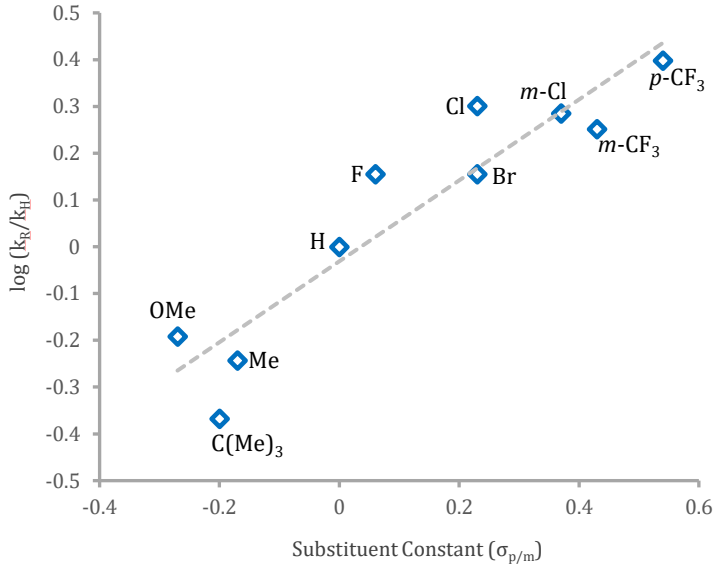


Figure 5. Hammett plot for catalytic amidation using catalysts **62b-j** and **2**.[21a]

Further analysis of catalyst integrity versus substituent constants $\sigma_{p/m}$ plot (Figure 6) led us to elucidate, that electron-deficient arylsilanols **62e-k** with enhanced catalytic performance, are susceptible to rapid decomposition, ranging from slight-to-moderate ($0.1 \geq \sigma_{p/m} \geq 0.3$) to severe ($0.4 \geq \sigma_{p/m} \geq 0.6$), under the given reaction conditions. Yet, no significant catalyst loss was observed for triphenylsilanol **2** itself ($\sigma_p = 0$) and electron-rich arylsilanols **62b-d** (σ_p *ca.* -0.2). These findings are consistent with preceding literature where the occurrence of aryl-silicon bond cleavage of electron-rich arylsilanes is observed under strongly acidic conditions; in contrast, arylsilanes bearing electron-withdrawing groups, suffer accelerated decomposition in the presence of a base.[23]

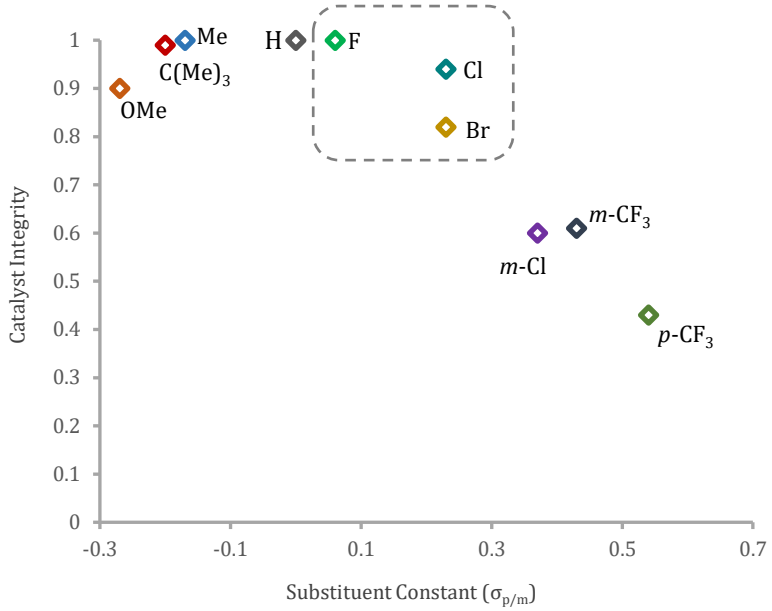


Figure 6. Post amidation catalyst integrity vs substituent constants ($\sigma_{p/m}$). Grey box denotes the catalysts selected for further study.[21a]

These results suggest that two counteracting factors, reactivity and stability, are at play – which must be considered for the design and execution of an efficient arylsilanol mediated catalytic direct amidation protocol.

Aims/Hypothesis

At this juncture, electron-deficient arylsilanol catalysts with improved amide conversions and seemingly less prone to bimolecular catalyst decomposition ($0.1 \geq \sigma_{p/m} \geq 0.3$) were chosen for further interrogation. Thus, tris(*p*-haloaryl)silanols **62e** (*p*-F), **62f** (*p*-Cl), and **62g** (*p*-Br) emerged as the selected catalysts. We intended to identify the most active halo-substituted catalyst by carrying out a catalyst loading screen, under the given reaction conditions, followed by a substrate scope of catalytic amidation reactions.[21b]

We also envisioned the implementation of 'Reaction Progress Kinetic Analysis (RPKA)' to evaluate the behaviour of arylsilanols as amidation catalysts. The kinetic profiling – by obtaining sufficient good-quality data over the reaction course – will provide valuable clues to the two most likely events, i.e., catalyst deactivation and/or product inhibition, accompanying the main reaction. Subsequently, the mechanistic insights gained through this kinetic analysis will inform our decision to fine-tune the catalyst system from the viewpoint of reactivity, stability, and substrate scope.

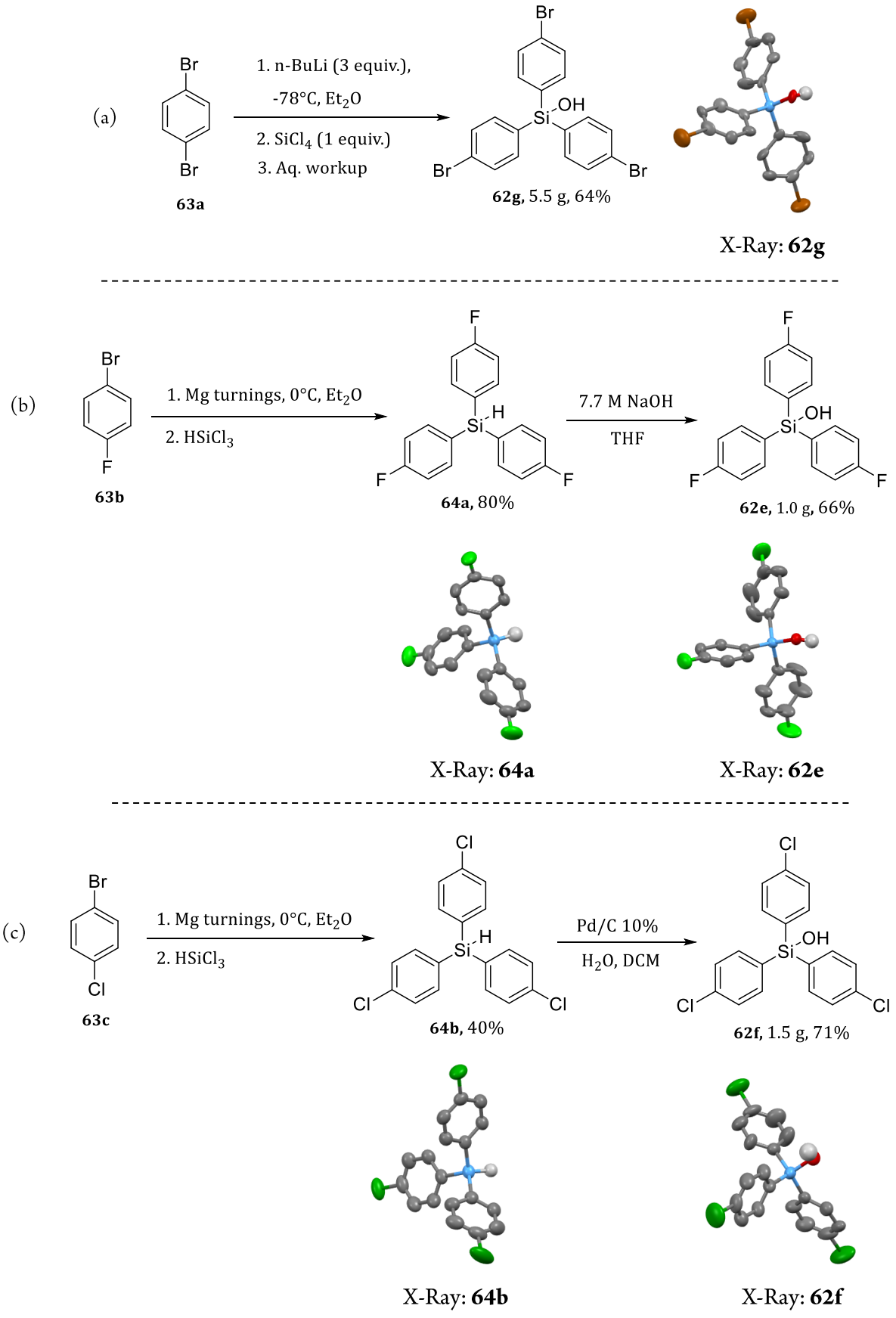
Chapter 2: Results & Discussion

2.1 Gram-Scale Synthesis of Selected Arylsilanols

Initially, we decided to synthesize known tris(*p*-haloaryl)silanols **62e-g** according to the published literature procedures.[21a,24]

In order to achieve the gram-scale synthesis of tris(*p*-bromophenyl)silanol **62g**, the preparative route described by Blatov and Sun was taken into consideration.[24a] Accordingly, 1,4-dibromobenzene **63a** was treated with *n*-BuLi in an equimolar ratio to access the desired metalated substrate, by lithium-halogen exchange. Upon the addition of $SiCl_4$, *in situ* generated ArLi successively attacked the electrophilic silicon centre to yield Ar_3SiCl intermediate. Subsequent aqueous workup led to the rapid hydrolysis of this intermediate, thereby affording the corresponding triarylsilanol **62g** (Scheme 24a) in a slightly higher yield (64%), than that (59%) reported by the authors.

Next, we performed the syntheses of fluoro- and chloro- congeners by following a two-step protocol. Appropriate aryl halides (**63b** or **63c**) smoothly underwent metalation with activated magnesium (vigorously stirred under N_2)[25] to generate the respective Grignard reagents, which further participated in the reaction with the silicon electrophile $HSiCl_3$ to give tris(*p*-haloaryl)silanes **64a** and **64b**. This transformation furnished arylsilane products in yields (80% and 40% respectively) comparable to those reported by our laboratory and Cossairt *et al.*.[21a, 24b] Subsequently, base and/or Pd-C mediated hydrolysis converted triarylsilanes into the desired halogenated triarylsilanols **62e** and **62f** in respectable yields (66% and 71%) (Scheme 24b & 24c).[21a,24c] Notably, we report the first X-ray crystal structures for all these organosilicon compounds, as part of this project.[21b]



Scheme 24. Preparative routes to selected tris(*p*-haloaryl)silanols **62e-g**.

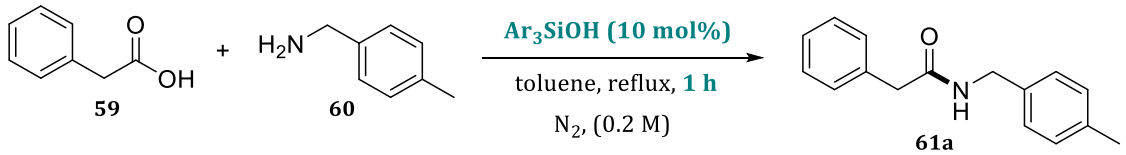
2.2 Catalyst Loading Screening

Previously in our laboratory, the catalytic activity of electronically differentiated arylsilanols was assessed at 10 mol% loading using a model reaction of aliphatic carboxylic acid **59** and primary amine **60** in a 1:1 stoichiometry to give the corresponding amide **61a**, in refluxing toluene for 1 h (Figure 7. A). Thus, we commenced our inquiry by carrying forward these standard conditions, with an aim to gain insight into the catalyst system by decoding the following two features (Figure 7. B).

Relative reactivities of chosen tris(*p*-haloaryl)silanols (**62e-g**):

- over an extended reaction time
- at different catalyst loadings

A. *Prior work from our laboratory:*[21a]



B. *This work:*[21b]

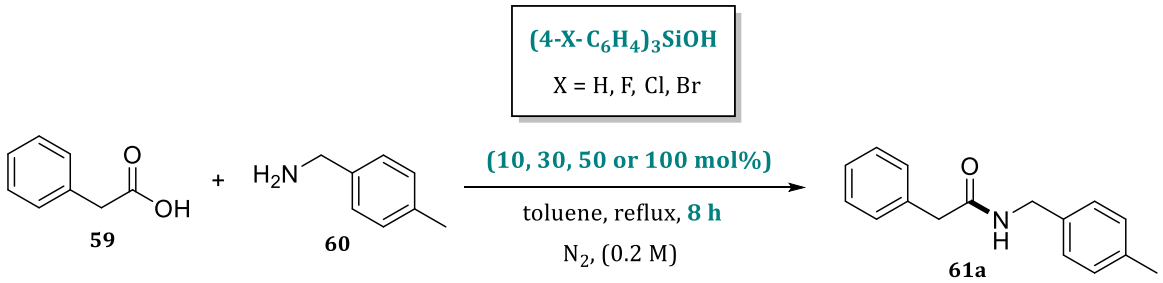
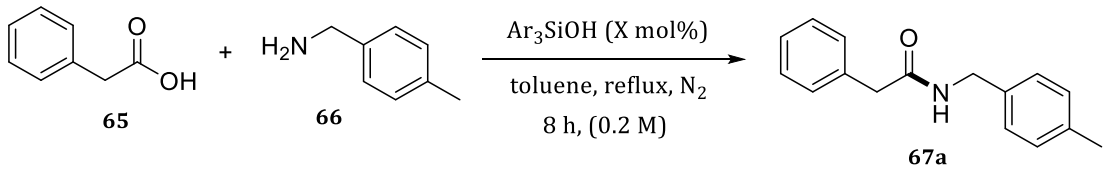


Figure 7.

Accordingly, phenylacetic acid **59** and 4-methylbenzylamine **60** were allowed to react in equimolar quantities to furnish the amide **61a** in refluxing toluene for 11 h, at first, without adding a catalyst. Reaction progression was monitored by ^{1}H NMR spectroscopy with the use of tetrakis(trimethylsilyl)methane (TTMSM) as an internal standard. In a related fashion, we proceeded

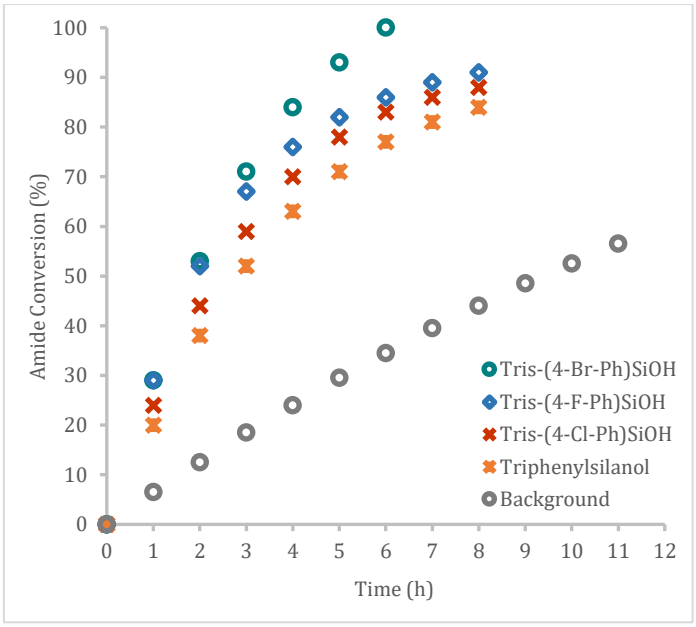
to inspect the model amidation system by employing Ph_3SiOH **2** and tris(*p*-haloaryl)silanols **62e-g**, initially, at 10 and 30 mol% loadings. Plotting the reaction progress data as conversion vs time (Figure 8) explicitly indicated the superior catalytic performance of triarylsilanols (**2** & **62e-g**) relative to the background reaction under the given set of conditions.

Among the arylsilanols examined, halogenated derivatives **62e-g** exhibited increased initial rates in comparison to the parent silanol **2**, suggesting that the catalytic efficiencies of these Lewis acidic catalysts are governed by electron-withdrawing halo-substituents.[26] Interestingly, fluoro- and chloro-congeners displayed somewhat similar efficiencies, while the bromo- derivative emerged as the most promising catalyst under the model conditions, where, at the given loadings the initial reaction rate was found to be ca. 5 and 8 times faster respectively, compared to the background run (Figure 8). These results, indeed, established that overall, augmented initial rates were substantiated for all catalyzed reactions, however, the origin of non-linear responses on increase of catalyst loading from 10 to 30 mol% presumably points towards the underlying complex kinetic behaviour. A similar qualitative interpretation was drawn when analogous model reactions were conducted to investigate the relative reactivities of arylsilanols (**2** & **62e-g**) at 50 and 100 mol% loadings (Figure 9) in the amidation process.



65 **66** **67a**

(a)



(b)

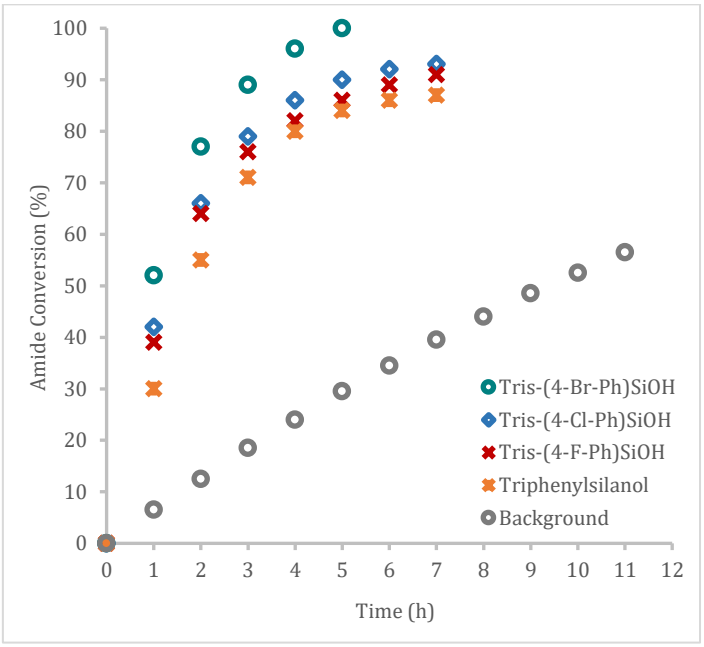
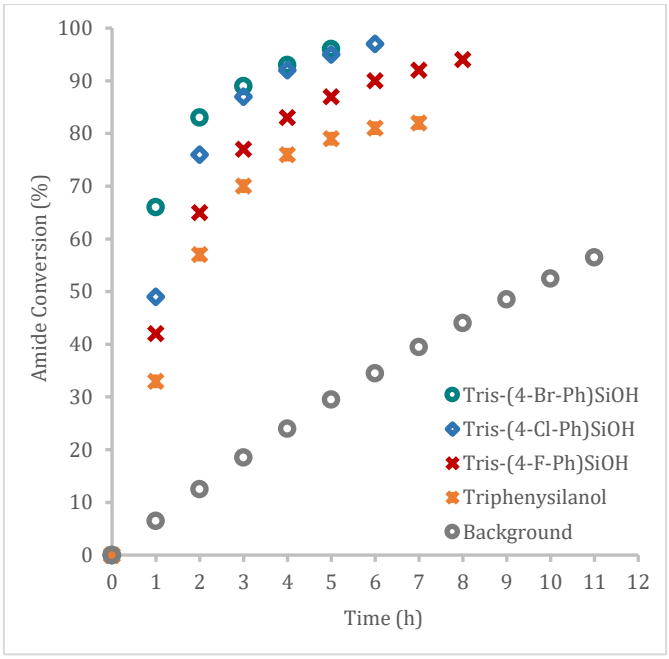


Figure 8. Conversion vs time plots. (a) 10 mol% (b) 30 mol%. Reactions were performed in triplicate and average conversions are reported. The variation in observed percentage conversions is ±2%. The grey profile shows the background reaction. (see Chapter 3, pp. 85-86)

(a)



(b)

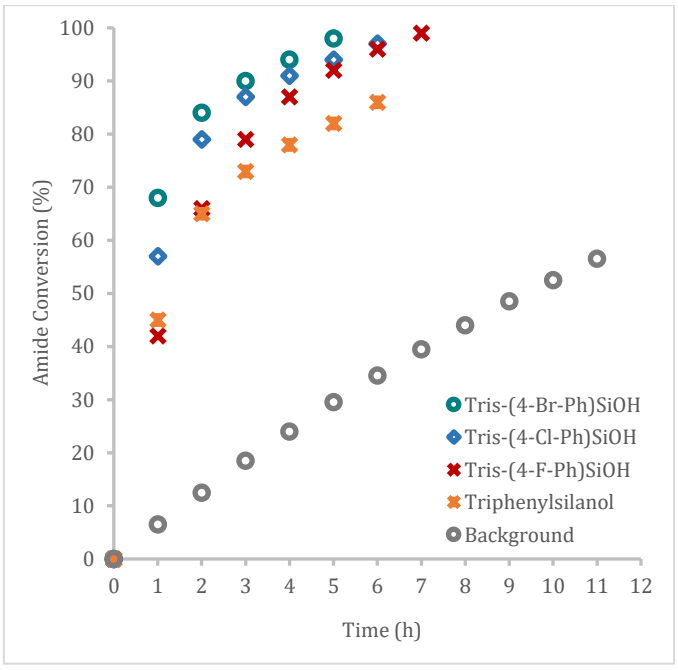


Figure 9. Conversion vs time plots. (a) 50 mol% (b) 100 mol%. Reactions were performed in triplicate and average conversions are reported. The variation in observed percentage conversions is ±2%. The grey profile shows the background reaction. (see Chapter 3, pp. 85-86)

2.3 Preparative Amidation Reactions

Having established tris(*p*-bromophenyl)silanol **62g** as the most effective catalyst under the model conditions of catalysis, we were intrigued to explore the substrate scope of this catalytic direct amidation protocol. In this context, phenylacetic acid and benzoic acid were chosen as representative aliphatic and aromatic carboxylic acids, respectively. The latter is of particular interest since the low reactivity of benzoic acid renders its amidation challenging. On the other hand, 4-methylbenzylamine, morpholine, *N*-methylbenzylamine, and aniline were employed as representative primary, secondary cyclic, secondary acyclic, and aromatic amine counterparts respectively, to investigate amidations of increasing difficulty.

Equimolar quantities of representative acid and amine were combined, using a catalyst loading of 30 mol%, in refluxing toluene for 24 h (Scheme 25). A higher catalyst loading (30 mol% rather than 10 mol%) in conjunction with a prolonged reaction timescale (24 h) was chosen to promote the coupling of intrinsically less reactive acid/amine substrates. Furthermore, corresponding background runs were conducted in parallel to ensure the judicious comparison of isolated yields from arylsilanol-mediated catalysis.

The purification of resultant amide products was accomplished by an extractive acid-base work-up and subsequent dry column vacuum chromatography (DCVC).[27] Any unreacted carboxylic acid and unreacted amine were removed in the former, whereas the removal of residual Ar_3SiOH and any disiloxane by-products was achieved in the latter.

The high affinity of fluorine to react with neutral tetracoordinate silanes,[28] prompted us to also explore the use of KF or TBAF as fluoride ion sources, which may facilitate the removal of aforementioned silicon-based impurities, perhaps as hypercoordinated silicates, thereby enabling the isolation of pure amide products, without the need for chromatography. However, attempts to devise an extractive

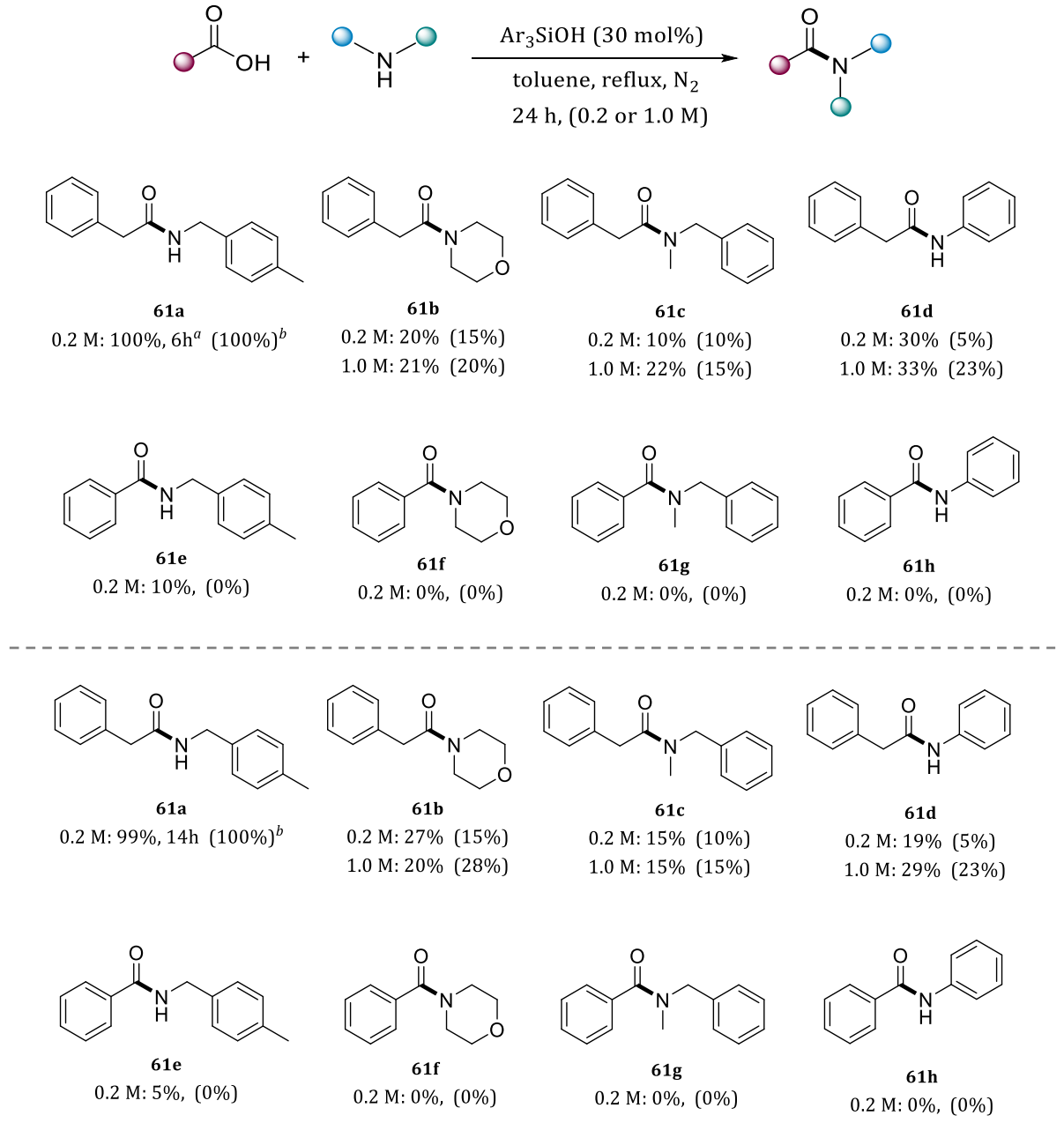
workup by exploiting Si-F chemistry were unsuccessful, presumably due to the poor solubilization of poly-aromatic arylsilanols (**2** or **62g**) and their corresponding disiloxanes (Ar_3-Si-O-Si-Ar_3) in the aqueous phase (Table 1, entry 1-4). Additionally, the extraction of these bulky organic compounds from the less polar organic medium into the aqueous phase was investigated with KF/18-crown-6 (Table 1, entry 5).[26] Unfortunately, this phase-transfer catalyst approach did not perform well and failed to provide pure amide products. Subsequently, purification was achieved by dry column vacuum chromatography (DCVC).

Table 1. Development of fluoride ion source-mediated work-up procedure

Entry	F^- ion source	Volume (mL)	Wash time	Extraction solvent	Purity
1	1 M KF soln.	45	1 min	Toluene	impure
2	1 M KF soln.	45	60 min	Toluene	impure
3	[a] 1 M KF soln.	45	120 min	Toluene	impure
4	1 M KF soln. / [b] TBAF.$3H_2O$	-	60 min	Toluene	impure
5	[c] KF / 18-crown-6	-	60 min	Toluene	impure

[a] Mixture was heated at 55 °C. [b] TBAF.$3H_2O$ was added as a solid. [c] KF and crown ether were added as solids.

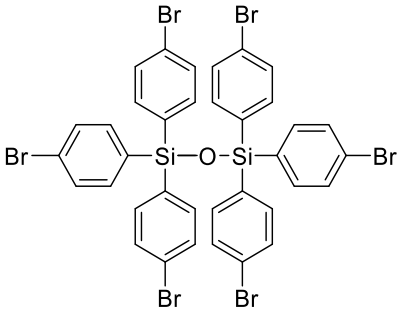
Our efforts to explore the generality of the reaction system (Scheme 25) revealed that the sub-stoichiometric quantities of Ph_3SiOH **2** and tris(*p*-bromophenyl)silanol **62g** were found to be ineffective in catalysing the amidations of less reactive benzoic acid, providing the benzamide **61e** from primary amine in poor yields, whereas no catalytic activity was observed for the formation of amides **61f-h** from secondary or aryl amines, under the given reaction conditions. This is perhaps unsurprising as only a few successful examples of *catalytic* amidations for these acid-amine combinations have previously been documented in the literature.[12-17]



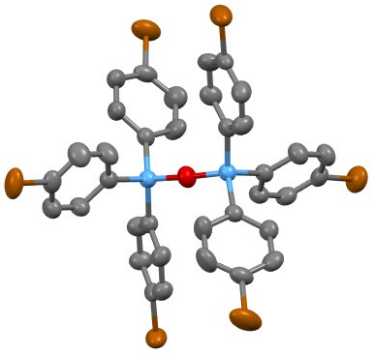
Scheme 25. Substrate scope of catalytic amidation with tris(*p*-bromophenyl)silanol **62g** (top) and Ph_3SiOH **2** (bottom) at 0.2 or 1.0 M concentration in both acid and amine with isolated yields after acid-base work-up and dry column vacuum chromatography. Percentages in parentheses are the isolated yields of background reactions without added catalysts **2** or **62g**, where the amide products were pure after acid-base work-up. [a] ^{1}H NMR yield. [b] Amide **61a** precipitated from the reaction mixture on cooling and could be collected by filtration. [c] Amide **61d** was triturated with *n*-hexane to remove unreacted aniline.

Phenylacetic acid underwent successful direct amidation with the chosen primary amine, furnishing the corresponding amide **61a** in quantitative yield within 6 h, in comparison to the background reaction that reached completion in 24 h. Under identical conditions, attempts to couple this aliphatic carboxylic acid with the chosen cyclic and acyclic secondary amines gave tertiary amides **61b-c** albeit in only unsatisfactory yields. In fact, increasing the molar concentration – from 0.2 M to 1.0 M – only barely affected the reaction outcome compared to the background run. It must be noted, in both these instances, upon removal of toluene and/or dilution with EtOAc in the workup procedure, white precipitates were observed, which, when collected were identified as hexa(4-bromophenyl)disiloxane **65**,[29] thus, implying the deactivation of catalyst *via* bimolecular condensation (ca. 15% catalyst loss observed for reactions conducted at 1.0 M concentration and 5 mmol reaction scale). Attempted recrystallization from hot toluene afforded single crystals of disiloxane **65**, yielding the first X-ray crystal structure of this organosiloxane.

On the contrary, enhanced catalyst performance over background reaction was detected for the transformation of phenylacetic acid into anilide **67d**. In fact, these results led us to deduce a correlation between amine basicity, catalyst stability, and amide product yield. We postulated that the less nucleophilic – yet more basic – secondary amines (4-methylbenzylamine pK_a = 9.21; *N*-methylbenzylamine pK_a = 9.58; morpholine pK_a = 8.36) presumably induce less product formation, thus [amine] remains high in the reaction system, thereby resulting in the catalyst decomposition. Consequently, the tertiary amides **67b-c** are less accessible under the model conditions of catalysis. In contrast, the base-driven catalyst deactivation is expected to be negligible in the case of aniline, as its reduced basicity (aniline pK_a = 4.63) serves to prevent the catalyst loss, so enabling the formation of secondary amide **67d** albeit in moderate yields.



65



X-Ray: **65**

Regrettably, the substrate scope of this catalytic direct amidation protocol is limited, so, we set out to conduct a systematic kinetic analysis by employing the "Reaction Progress Kinetic Analysis (RPKA)" to probe the factors adversely affecting the catalysis.

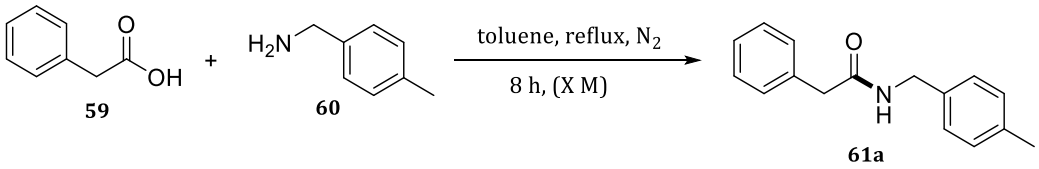
2.4 Kinetic Profiling

Reaction progress kinetic analysis (RPKA) pioneered by Blackmond *et al.*, is a powerful tool to illuminate the kinetic information of a complex catalytic system from a limited number of experiments executed under synthetically relevant conditions.[30] This methodology has progressively been implemented in a diverse range of catalytic transformations to model kinetics-based mechanistic investigations.[31] RPKA introduces two key experimental protocols (a) "Same excess" which informs whether the catalyst concentration remains constant over the entire reaction course (b) "Different excess" to extract reaction order in a given substrate. Nevertheless, standard RPKA entails the mathematical manipulation of experimental concentration data to obtain the reaction rate, which impedes the wider application of this method. To deal with this conundrum, Blackmond et al. reported a "Time-Adjusted" graphical analysis, which allows the comparison of two reaction profiles using concentration parameter without prior conversion to rate.[31d] This viable approach could be exploited by non-experts in kinetics to extract meaningful information concerning catalyst stability and product inhibition from accessible concentration vs time profiles.

Later, Jordi Burés established "Variable Time Normalization Analysis (VTNA)" – which in contrast to RPKA which relies on *rate profiles* – enables the determination of order in any reaction component by manipulating the reaction *concentration profiles* against a normalized time scale.[32]

On account of the powerful aspects of RPKA, we were drawn to decrypt the kinetic features – encompassing the reaction rate dependence on the concentrations of [acid]/[amine] and determination of catalyst order by employing VTNA – of arylsilanol-catalyzed amidation system from reaction progress experiments, with the goal of supplementing our mechanistic information related to this transformation.

Typically, visual graphical interrogation of kinetic data necessitates a reasonable overlay of the two concentration profiles,[30c] therefore, in the first instance, a set of background experiments was conducted, where the initial concentration of carboxylic acid **65** and amine **66** was varied to probe the best working concentrations for the same excess protocol (Figure 10). After interrogating the concentration data presented in Figure 10, graphical manipulation allowed us to deduce the 0.3 M versus 0.2 M regime as a rational choice, exhibiting an adequate overlay of two curves as illustrated in Figure 11.



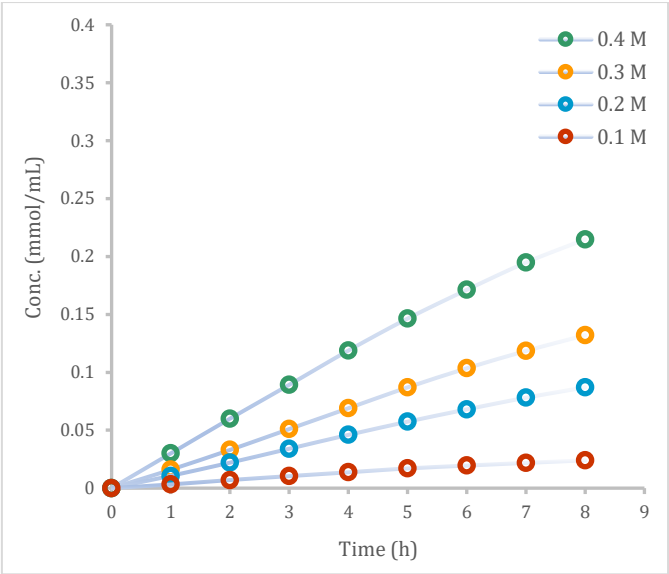


Figure 10. Concentration of amide **61a** as a function of time with varying [**59**] and [**60**] for background reaction. Reactions were performed in triplicate or more. The variation in observed concentrations is ±1%. (see Chapter 3, p. 87)

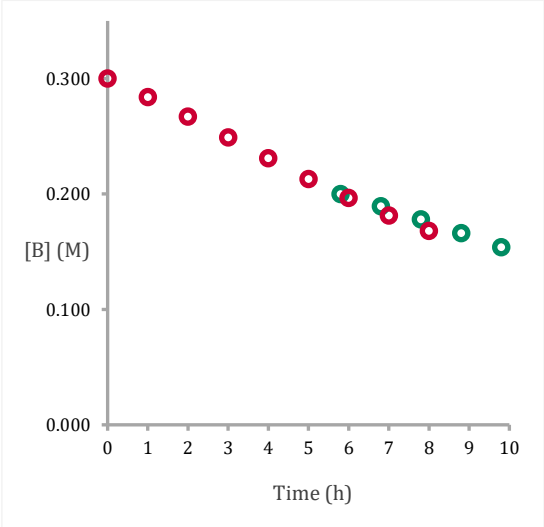


Figure 11. 'Same excess' concentration vs time plots for background reaction. Red circles t_0 = 0.3 M [**59**], 0.3 M [**60**], and time-adjusted green circles $t_{5.8}$ = 0.2 M [**59**], 0.2 M [**60**]. (see Chapter 3, p. 87)

While exploring the kinetic behaviour of tris(*p*-bromophenyl)silanol (30 mol%) catalyzed model amidation reaction, observed catalytic conversions were adjusted with respect to the pre-determined background reaction profile, as illustrated in Figure 12.

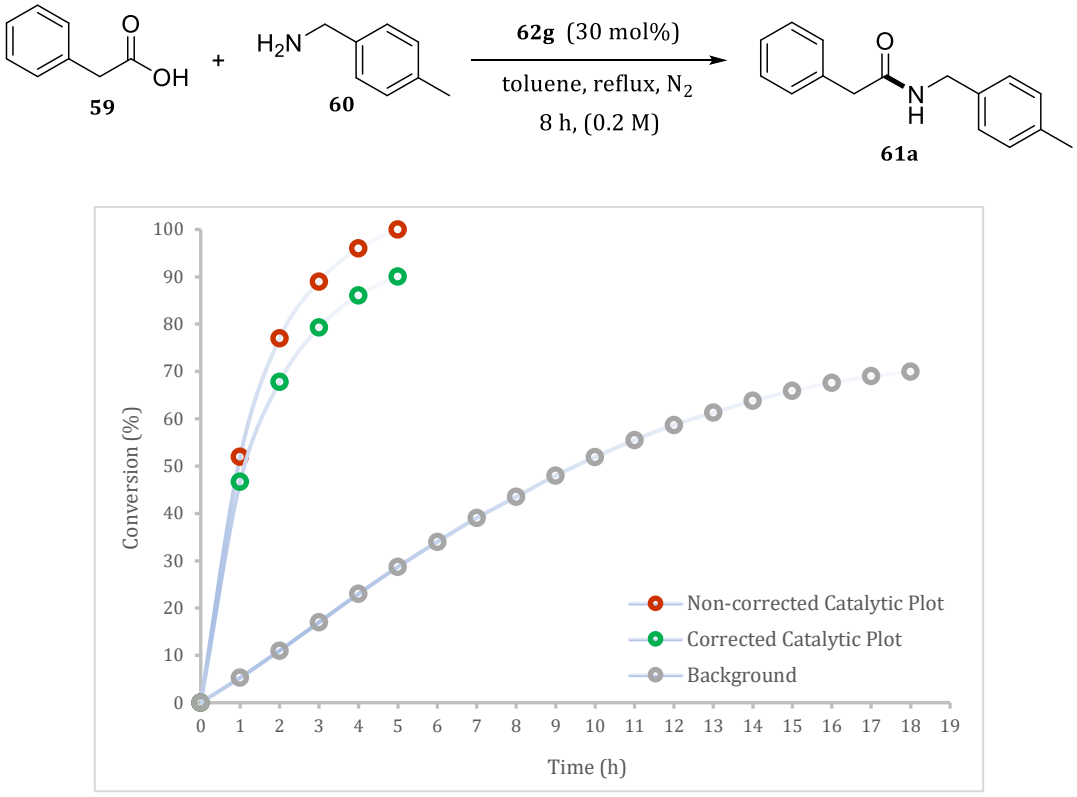


Figure 12. Correction of catalytic conversions by subtracting the background contribution.

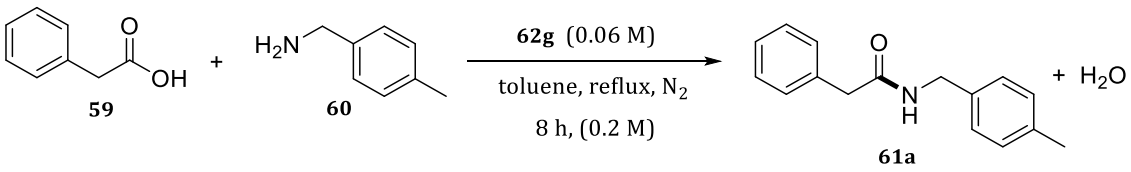
2.4.1 Time-Adjusted Analysis

We continued with the catalytic coupling of phenylacetic acid **59** and 4-methylbenzylamine **60** using tris(*p*-bromophenyl)silanol **62g** at 30 mol% loading, by employing the 'same excess' protocol. To address the question of catalyst robustness, four kinetic experiments were designed and performed under the model conditions of catalysis. Figure 13a shows the plot of [substrate] vs time for two reactions, where the difference in the initial concentrations of carboxylic acid **59** and amine **60**, is defined by the parameter excess (where [excess] = 0.1 M). It can be easily seen, the 'time-adjusted' profile shows a clear lack of overlay between the two curves from the point onward, where the two reactions have identical concentration, thus, suggestive of either catalyst deactivation or product inhibition (Figure 13a). To distinguish between these two possibilities, a further kinetic experiment with the addition of an appropriate quantity of amide product **61a** was carried out. The graphical manipulation of reaction progress data resulted in a nearly perfect overlay as illustrated in Figure 13b.

This demonstrates that the amide product interacts with the catalyst or catalytic intermediates in an unproductive manner presumably taking one of these off-cycle, resulting in a slower reaction rate with increasing reaction progress.

Having established that the catalyst system is subject to inhibition by the amide product under the given set of conditions, we turned to investigate the possibility of product inhibition by H_2O, the other condensation product of the reaction. Hence, a third kinetic experiment with the addition of an appropriate quantity of H_2O was conducted. The kinetic profile in Figure 13c implies that H_2O contributes to suppress the rate, however, the effect minimizes over the course of the reaction. This behaviour could be rationalized by the fact that H_2O is expected to be lost from the reacting system in refluxing toluene.

Lastly, in this series of kinetic experiments, Figure 13d manifests the case where both reaction products, amide **61a** and H_2O were added at the outset of the reaction, giving rise to a plot that illustrates an essentially exact overlay of two curves, providing unequivocal evidence that the catalyst system suffers from product inhibition in these catalytic amidation reactions by both the amide product and H_2O.



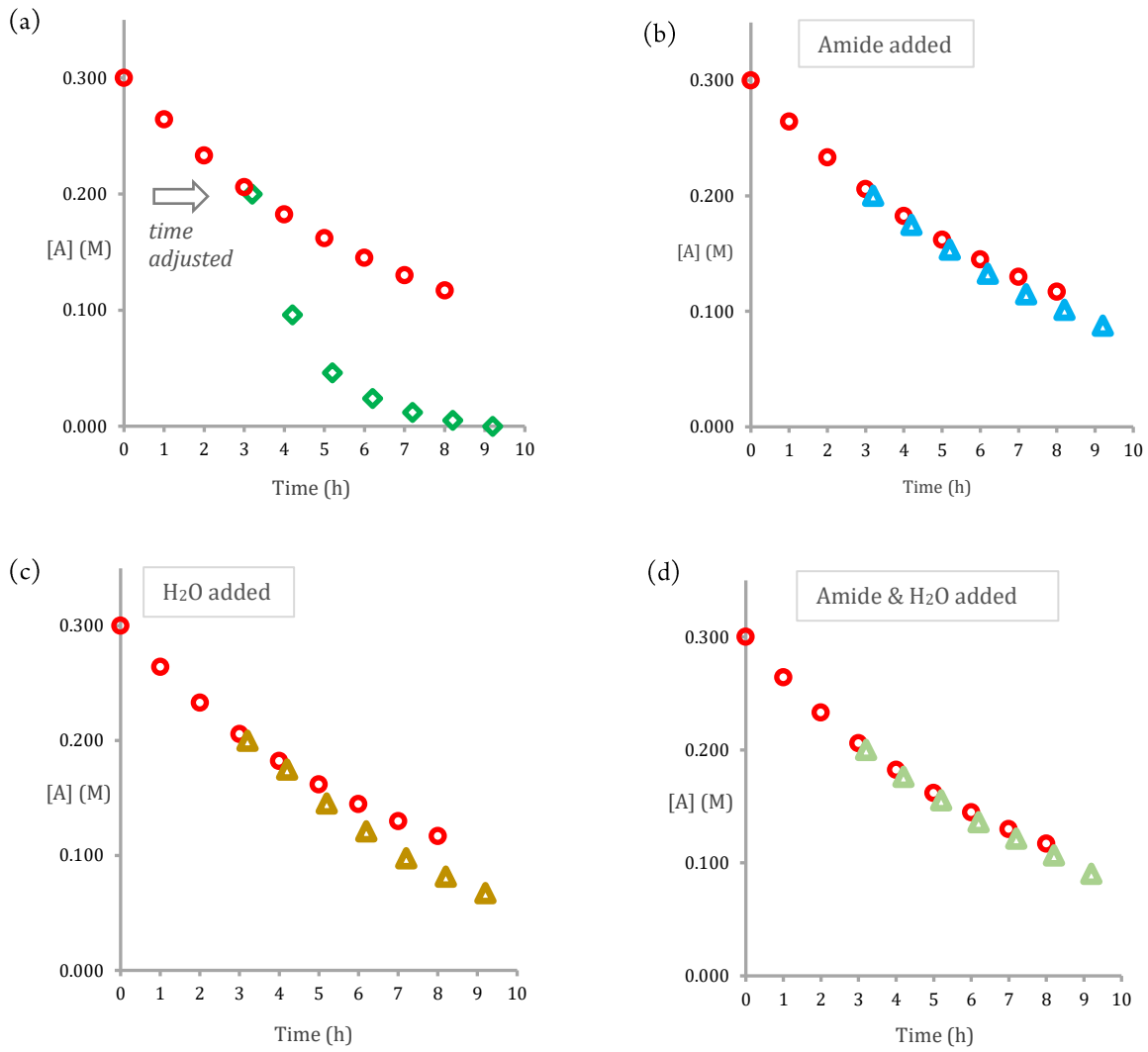
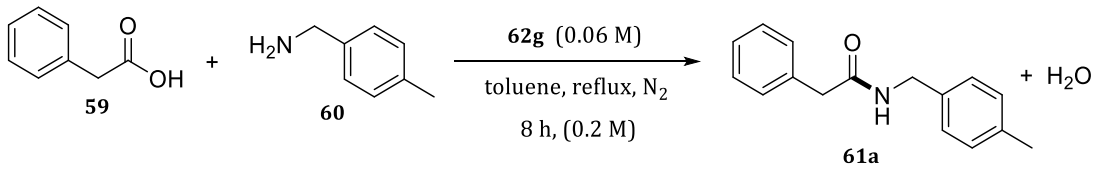


Figure 13. 'Same excess' concentration vs time plots. (a) Red circles t_0 = 0.3 M [**59**], 0.3 M [**60**], 0.06 M [**62g**] and time-adjusted green diamonds $t_{3.2}$ = 0.2 M [**59**], 0.2 M [**60**], 0.06 M [**62g**]; (b) Blue triangles 0.2 M [**59**], 0.2 M [**60**], 0.06 M [**62g**], 0.1 M [**61a**]; (c) Dark golden triangles 0.2 M [**59**], 0.2 M [**60**], 0.06 M [**62g**], 0.1 M [H_2O]; (d) Light green triangles with added 0.1 M [**61a**] amide and 0.1 M [H_2O]. (see Chapter 3, p. 89)

At this juncture, we chose to utilize this RPKA methodology to investigate the effect of secondary and tertiary amide products on catalytic activity during the course of the reaction. In this scenario, we set out to obtain the reaction progress data under the same excess regime by carrying out three individual kinetic experiments of our standard amidation reaction with appropriate quantities of amide products **61b-d** added, notably, without any substantial modification of the experimental protocol. The

resultant time course profiles (Figure 14) reveal that tertiary amide products markedly reduced the catalytic activity in comparison to the secondary amides, consequently, the product inhibition induced rate suppression was pronounced as depicted in Figure 14c & 14d. This trend, indeed, sheds light on the likely cause for the inferior results obtained in preparative amidation reactions, whereby synthesis of tertiary amides is less feasible under the given conditions of catalysis.



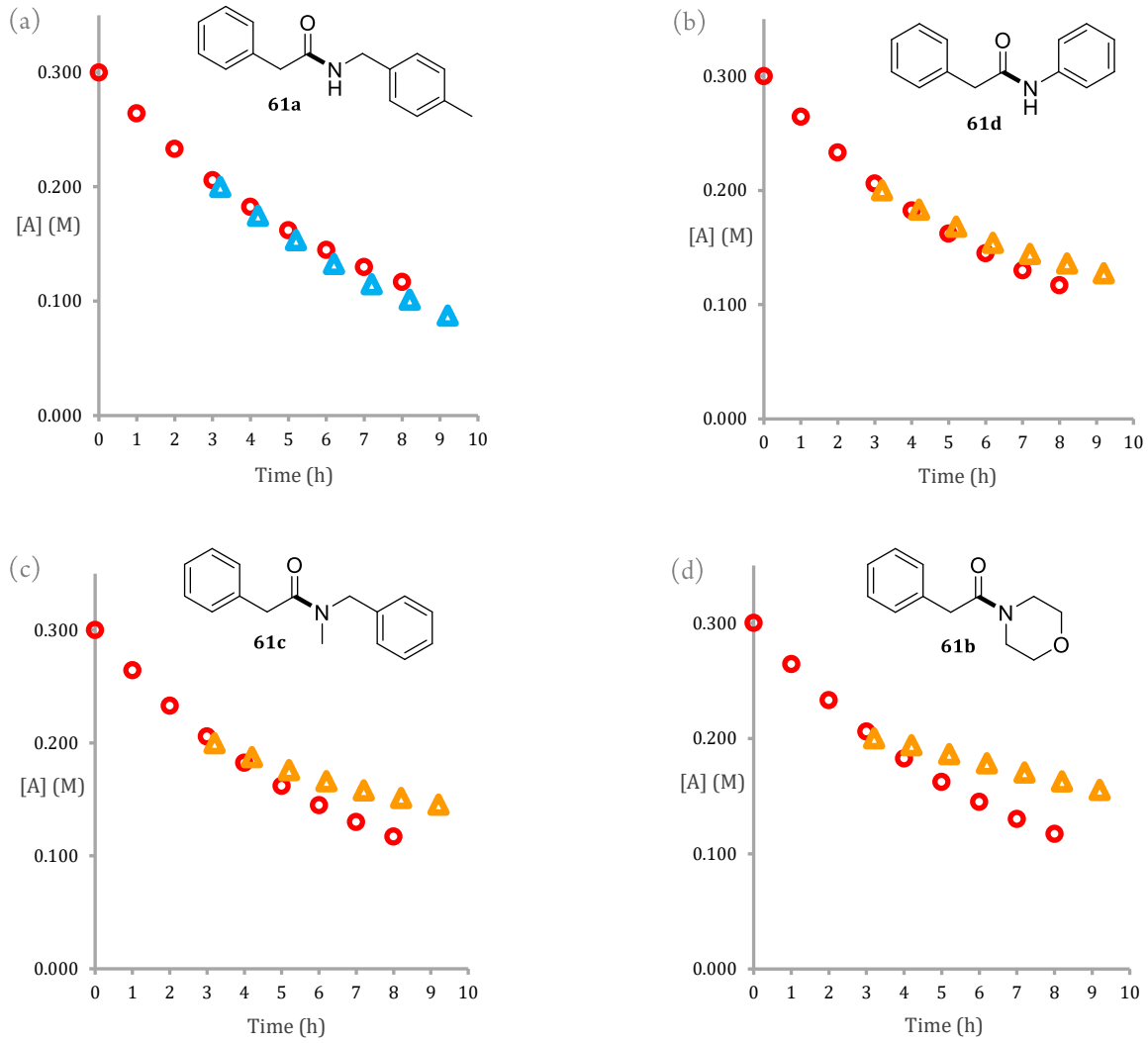


Figure 14. 'Same excess' concentration vs time plots. (a) Red circles t_0 = 0.3 M [**59**], 0.3 M [**60**], 0.06 M [**62g**] and time-adjusted blue triangles $t_{3.2}$ = 0.2 M [**59**], 0.2 M [**60**], 0.06 M [**62g**], with added 0.1

M [**61a**]; (b) Orange triangles with added 0.1 M [**61d**]; (c) Orange triangles with added 0.1 M [**61c**]; (d) Orange triangles with added 0.1 M [**61b**]. (see Chapter 3, p. 90)

Having realized the deleterious effects of product inhibition on reaction rate under model amidation conditions, we next sought to comprehend the dependence of reaction rate on the concentrations of reactants by employing the different excess protocol.

2.4.2 Different Excess Experiments

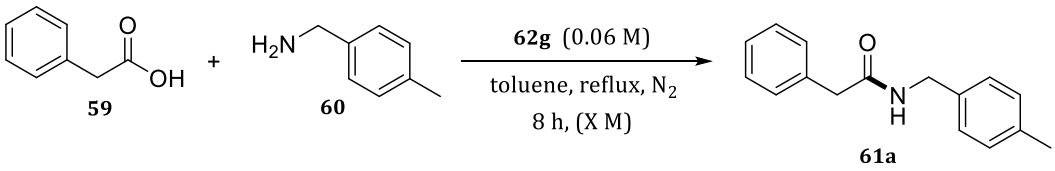
To examine the model reaction between phenylacetic acid **59** and 4-methylbenzylamine **60** using tris(*p*-bromophenyl)silanol **62g**, under 'different excess' conditions, a set of experiments was performed by varying the initial concentration of either [acid] or [amine] under the specified conditions of catalysis, and the corresponding [product] vs time plots were constructed (Figures 15 & 16).

An enhanced reaction rate at higher substrate concentration was anticipated, conversely, preliminary results presented a rather complicated picture. Figure 15 shows overall sluggish rates for reactions carried out with an excess of either carboxylic acid **59** or primary amine **60**, in comparison to those conducted in equimolar conditions ([excess] = 0). This behaviour suggests that 1:1 stoichiometry of acid/amine components is crucial for optimal reaction outcome under the given conditions, whereas an excess of either substrate has a detrimental effect on the reaction rate. Thus, the following trend was deduced for observed rates:

Reaction rate with excess amine < reaction rate with excess acid < reaction rate with 1:1 acid/amine

To elucidate the reaction orders in substrates [**59**] and [**60**], variable time normalization analysis (VTNA) was performed on the reaction progress data obtained from different excess experiments.[31] Figure 17a demonstrates the VTNA plot for two experiments carried out with identical $[\mathbf{60}]_0$ and different initial concentrations of $[\mathbf{59}]_0$, whereas, Figure 17b illustrates the inverse scenario, that is,

identical $[\mathbf{59}]_0$ and different initial concentrations of $[\mathbf{60}]_0$. The graphical overlays are complicated and reveal overall negative order dependences in both [acid] and [amine]. This complexity in reaction kinetics arises presumably due to the protonation of amine **60** by a surplus amount of carboxylic acid **59** present in the former (Scheme 26), whereas the latter accelerates the counterproductive catalyst dimerization, thereby conducive to effectively decreasing the active catalyst concentration in the process (Scheme 27).



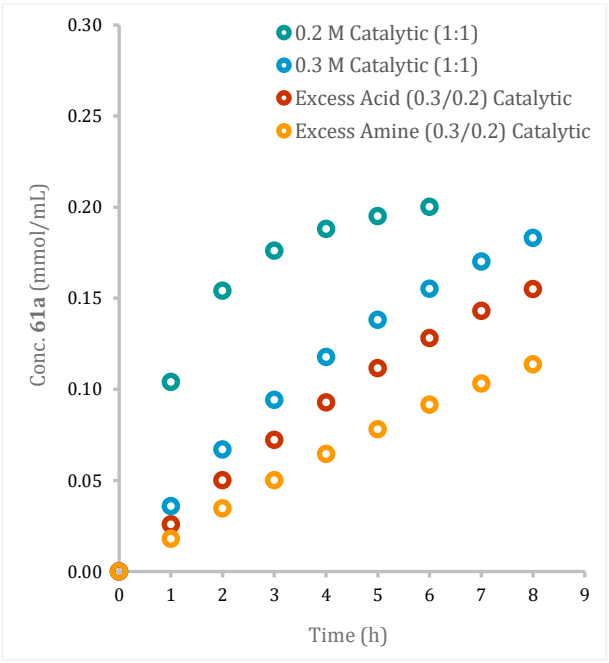


Figure 15. Concentration of amide **61a** as a function of time. Comparison of catalytic 1:1 acid/amine reaction rates with catalytic 'excess acid' and 'excess amine' reaction rates. Reactions were performed in triplicate or more. The variation in observed percentage conversions is ±1 or ±2%. (see Chapter 3, pp. 88, 91)

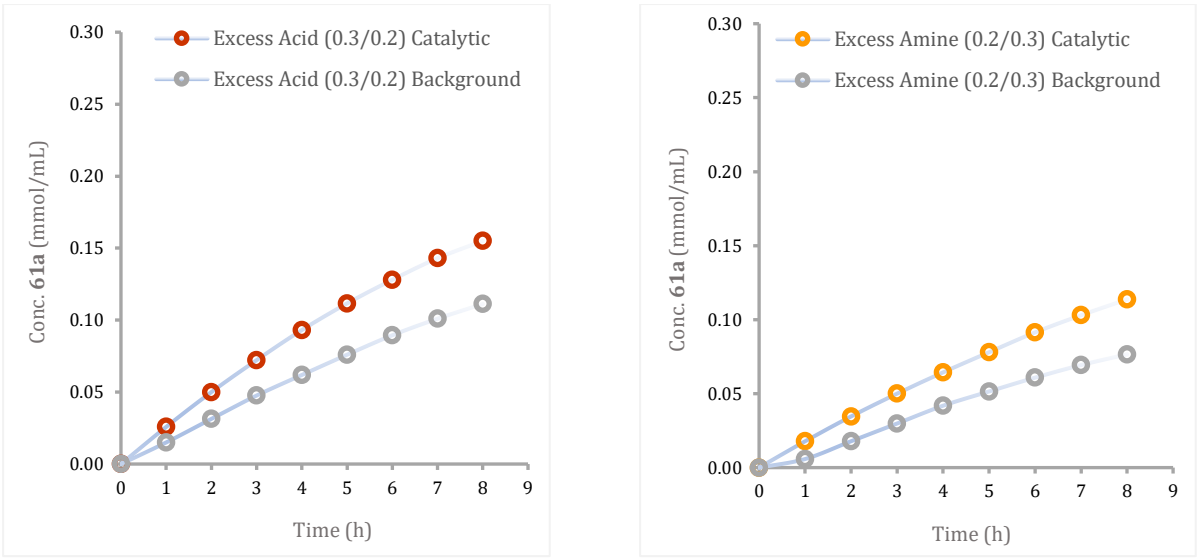


Figure 16. Concentration of amide **61a** as a function of time. (Left) Catalytic reaction with excess acid. (Right) Catalytic reaction with excess amine. The grey profiles show respective background runs. Reactions were performed in triplicate or more. The variation in observed percentage conversions is ±1 and ±2% respectively. (see Chapter 3, p. 91)

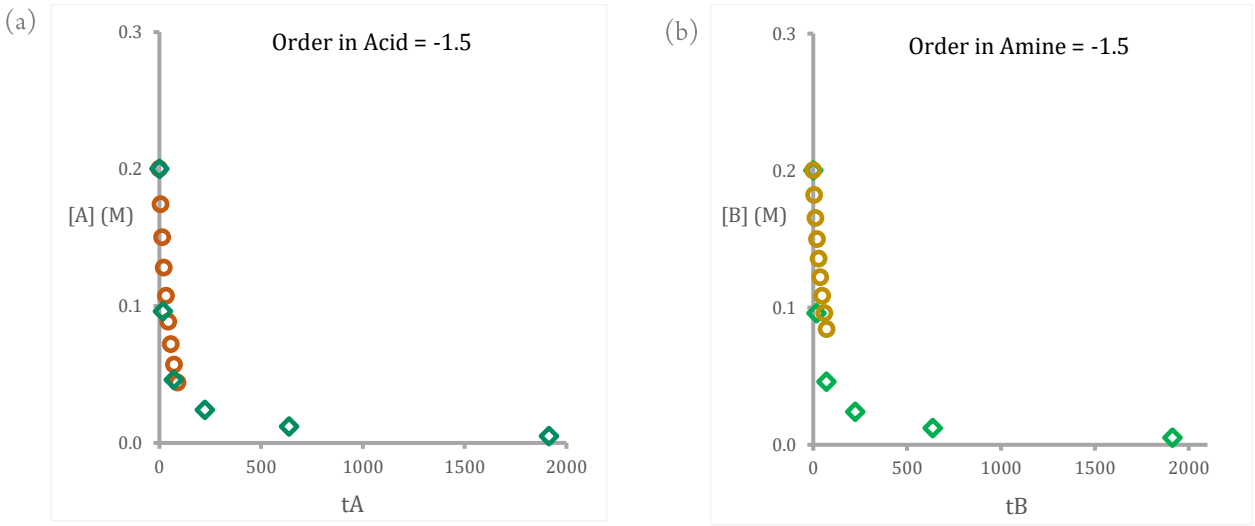
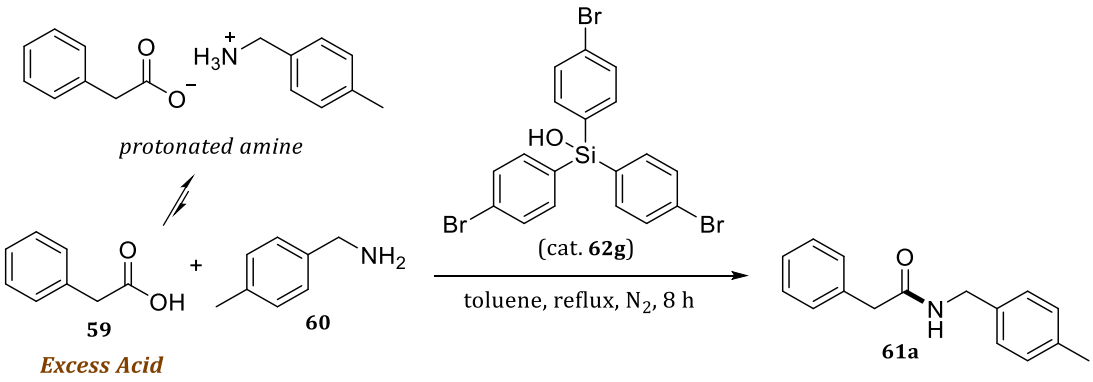
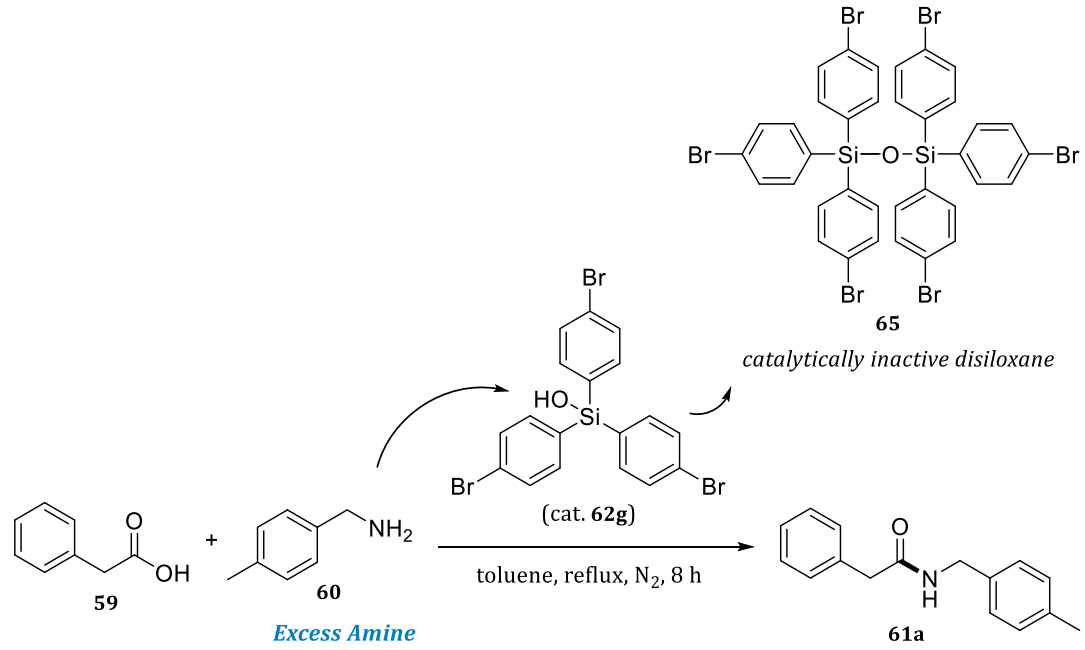


Figure 17. VTNA plots of concentration vs normalized timescale. (a) Excess acid experiment to determine 'order in acid': green diamonds [**59**] = [**60**] = 0.2 M, [**62g**] = 0.06 M and orange circles 0.3 M [**59**], 0.2 M [**60**], [**62g**] = 0.06 M; (b) Excess amine experiment to determine 'order in amine': golden circles 0.2 M [**59**], 0.3 M [**60**], [**62g**] = 0.06 M. (see Chapter 3, pp. 88, 91)



Scheme 26. Plausible reaction pathway operating in case of excess acid.

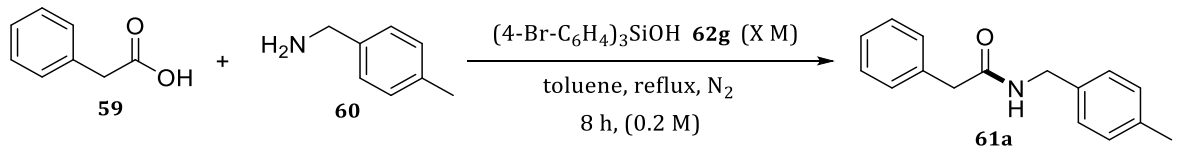


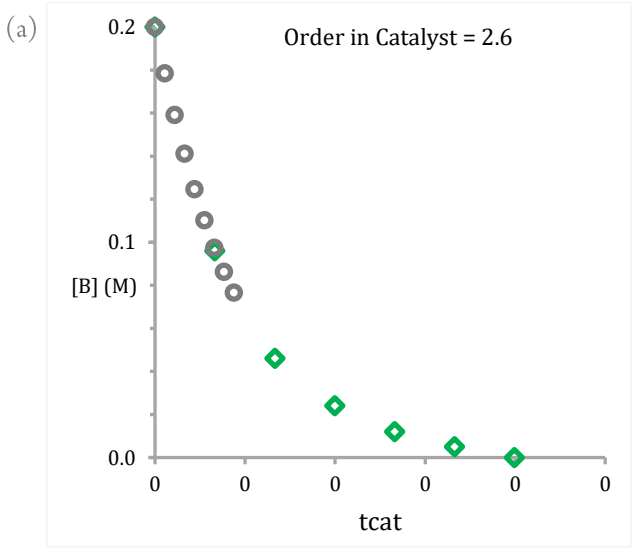
Scheme 27. Plausible reaction pathway operating in case of excess amine.

2.4.3 Order in Catalyst

With an eye towards elucidating the order in catalyst under the given set of conditions by exploiting the normalized time scale method, kinetic experiments were conducted by varying the catalyst concentration to collect reaction progress data over the reaction course.[32] Figure 18 shows the evolution of concentration profiles and orders in catalyst determined across all concentrations studied (0.06, 0.045 & 0.03 M).

In our exploration of the reaction network, the core insight obtained from time-adjusted analysis helped us to establish definitively that the catalytic system is susceptible to interact with reaction products in an unproductive manner, under the model conditions of amidation (*vide supra*). Thus, one must consider that the reaction kinetics in the existing experimental setting is intricate on the account of product inhibition, as a result, extraction of the correct order in catalyst is rather complicated. Prior studies from our laboratory to propose a mechanism of these triarylsilanol catalyzed direct amidations, established the intermediacy of silyl ester in the catalytic cycle,[21a,33] which renders first-order dependence in catalyst concentration, thus, a catalyst order of 1 is conceivable (Figure 18c). However, the apparent orders greater than one ostensibly refer to the event of product inhibition (Figure 18a & 18b), which is in line with the precedent literature.[32c]





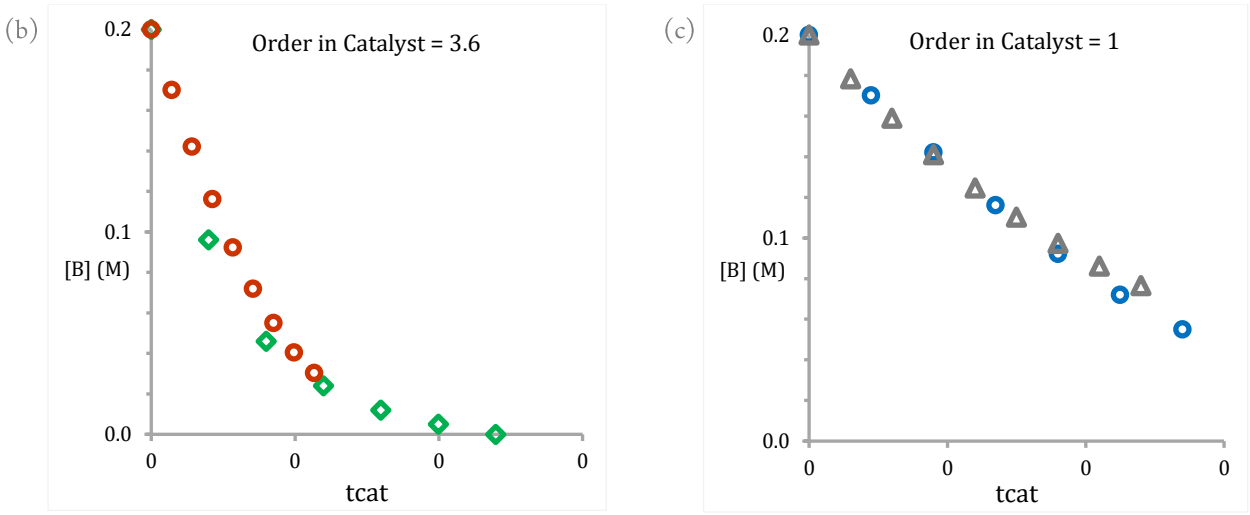


Figure 18. VTNA plots of concentration vs normalized timescale with varying [**62g**] to determine 'order in catalyst'. [**59**] = [**60**] = 0.2 M in all experiments. (a) Green diamonds $[\mathbf{62g}]_0$ = 0.06 M and grey circles $[\mathbf{62g}]_0$ = 0.03 M; (b) Red circles $[\mathbf{62g}]_0$ = 0.045 M; (**c**) Grey triangles $[\mathbf{62g}]_0$ = 0.03 M and blue circles $[\mathbf{62g}]_0$ = 0.045 M. (see Chapter 3, p. 92)

2.5 Mechanistic Considerations

Given the fact that product inhibition drastically impacts the catalytic efficiency in the amidation process, the understanding of the inhibition mechanism is likely to be of vital importance to overcome this limitation in due course. Initially, intermolecular hydrogen-bonding between arylsilanol catalyst and amide product was speculated to play a decisive role in the event of non-productive catalyst inhibition (Figure 19). To test this premise, ^{1}H NMR titration experiments were carried out in $CDCl_3$ at room temperature, thus probing the binding ability of arylsilanol/amide in 1:1 stoichiometry (**I, II**). A distinct broad singlet at 5.67 ppm for amide -NH (in the case of secondary amide - **I**) was monitored to observe the effect of complexation, however, the amide resonance remained unchanged at this chemical shift. We reasoned that silanol catalyst does not sufficiently interact with the amide product, which might stem from the fact that organosilanols are known to possess a strong affinity for hydrogen-bonding derived self-assembly.[34] Furthermore, the coordination behaviour of tertiary amide/arylsilanol (**II**) was studied by following the signal corresponding to Si-OH (2.82 ppm), where

the labile proton was not detected in the spectrum. Similarly, attempts to crystallize any H-bonded adducts of tris(*p*-bromophenyl)silanol with either 2° or 3° amides in 1:1 or 1:2 ratios by crystallization (EtOH, Et_2O/*n*-hexane), proved to be futile.[34]

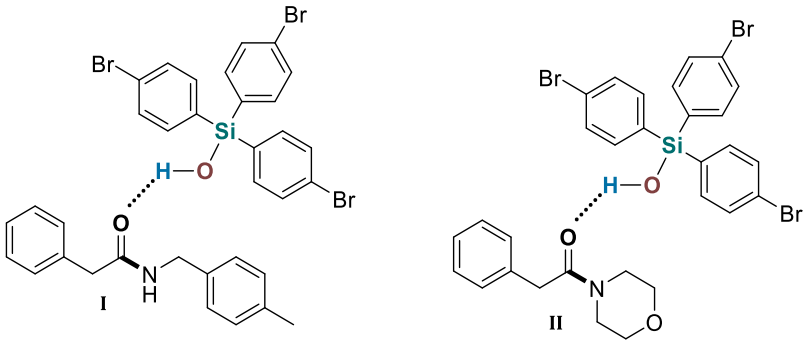
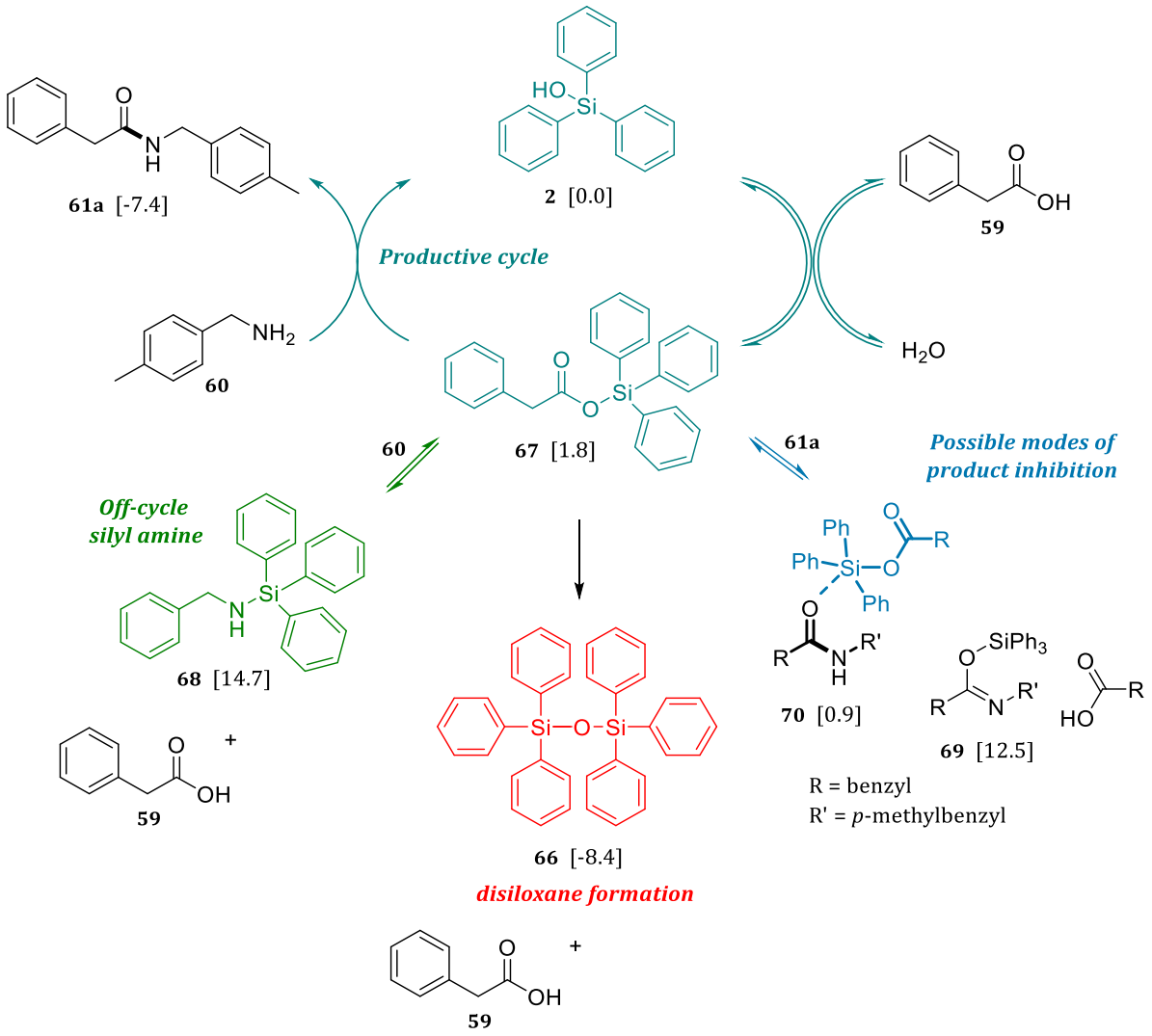


Figure 19. Proposed hydrogen-bonded structures.

With no experimental evidence for arylsilanol/amide interaction through hydrogen-bonding, we conjectured that the catalyst inhibition *via* formation of silyl imidate **69** is reasonable to consider.[35a] However, in efforts to ascertain the basis of this possibility computationally, the viability of **69** was calculated to be unfavourable (Scheme 28), which consequently led us to rule out this explanation.[21b] Since silyl ester acts as a putative mediator en route to amide synthesis,[21a,33] along with the preceding work by Dilman and Korlyukov,[35b] prompted us to formulate that the complexion of Lewis basic amide product with silyl ester to be considered as an accessible pathway in the inhibition mechanism. Thus, to elucidate this specific interaction between amide **61a** and silyl ester **67**, density functional calculations were performed by our colleague Henry Rzepa,[21b] where the resultant computed free energy values supported the possible intervention of pentacoordinate amide-silyl ester complex **70** (Scheme 28).

The catalytic cycle involves the generation of **67** *via* nucleophilic attack by carboxylate anion at Si of Ph_3SiOH, where the productive attack by amine **60** at acyl carbon leads to amide formation, while attack at Si generates silyl amine **68**. Taken together with above mentioned experimental observations,

we proposed the feasibility of attack by any Lewis basic lone pair, at either acyl carbon or silicon centre of silyl ester. Attack by H_2O at either carbonyl carbon or Si releases silanol **2** and carboxylic acid **59**; attack by silanol **2** at Si irreversibly produces disiloxane **66** while attack at C is a degenerate process. Indeed, these mechanistic studies enabled us to delineate various events potentially at play in arylsilanol mediated catalysis.



Scheme 28. Plausible catalytic cycle. Numbers in square brackets are computed relative free energies ΔG_{384} in kcal/mol @ 4 atm. standard state (~ 0.13 M) for discrete species involved in the catalytic cycle using the B3LYP+GD3+BJ/Def-TZVPP/SCRF = toluene density functional procedure.[21b]

2.6 Post Amidation Quantification of Catalyst Integrity by HPLC

As addressed in Section 2.3, the likelihood of change in the active catalyst concentration during the reaction course – culminating in a buildup of catalytically inactive disiloxane – was corroborated by the experimental observations (isolation and identification of degradation by-product hexa(4-bromophenyl)disiloxane **65** during the work-up procedure of preparative amidation reactions). The propensity of arylsilanols to self-dimerize under the model conditions of catalysis prompted us to monitor the catalyst integrity. At the outset, ^{1}H NMR spectral analysis was the method of choice for the quantification of catalyst decomposition, however, heavy signal overlapping of arylsilanols and the corresponding disiloxane side products, in the aromatic region of the spectrum remained a key issue, thus, preventing accurate quantification. To circumvent this problem, we developed *ex situ* HPLC methods for the quantitative determination of catalyst, leading to the collection of time course data. Initially, a series of experiments was conducted to probe the catalyst stability in the presence of individual reaction components of the model amidation system, that is, toluene, acid **59**, amine **60**, and amide product **61a**. The catalyst concentration was monitored by analysing the reaction aliquots drawn periodically over the course of 8 h and the plots of [**62g**] as a function of time were generated (Figure 20). It was found that, tris(*p*-bromophenyl)silanol (0.06 M in toluene) was thermally robust and showed good tolerance to carboxylic acid **59** and amide **61a** reaction components, hence, catalyst [**62g**] remains constant over the reaction course. However, catalyst decomposition to a certain degree (0.049 M, ca. 20%) was observed in the case of primary amine **60** (Figure 20c), which can be attributed to the base mediated biomolecular condensation of arylsilanol species.

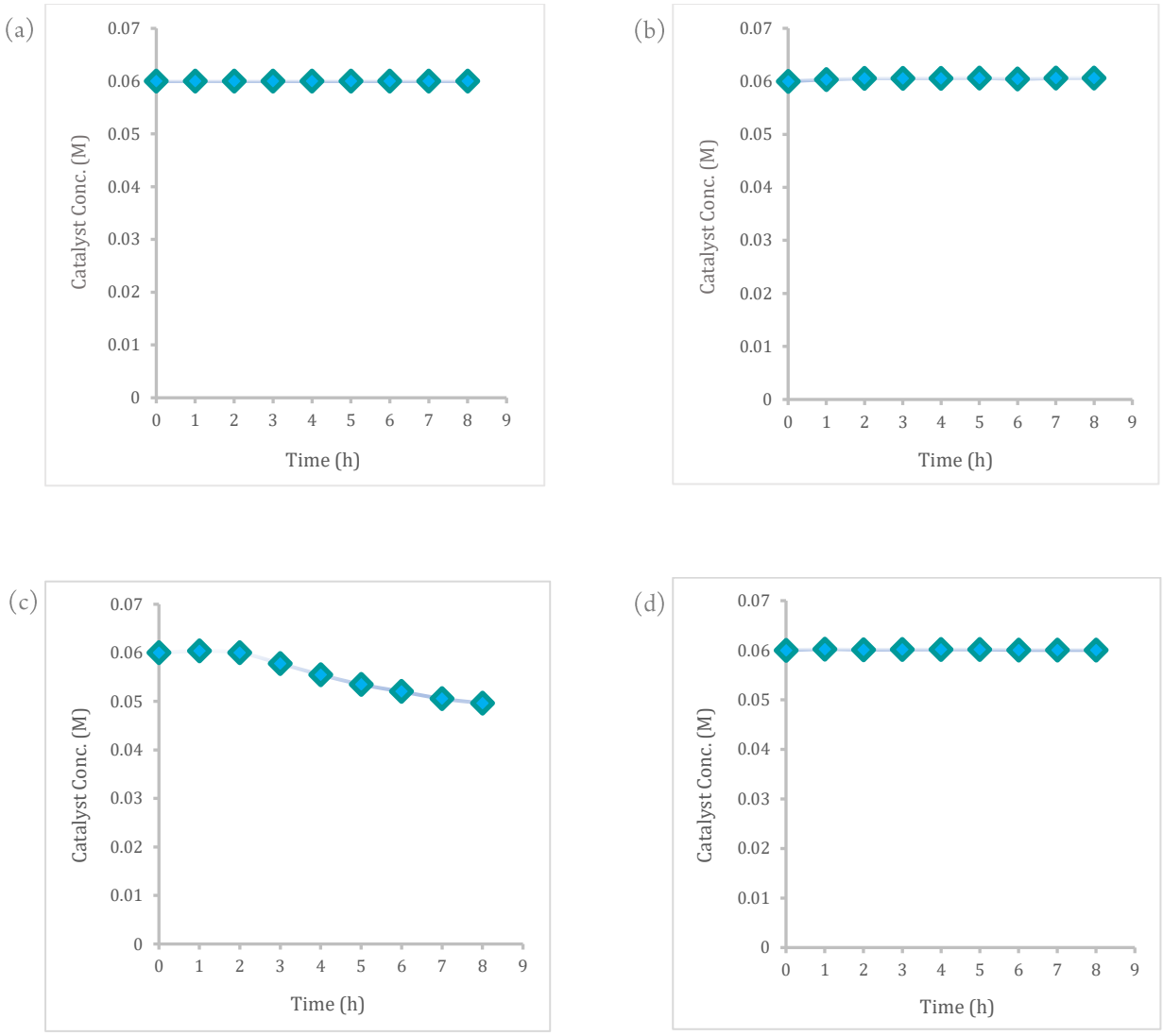
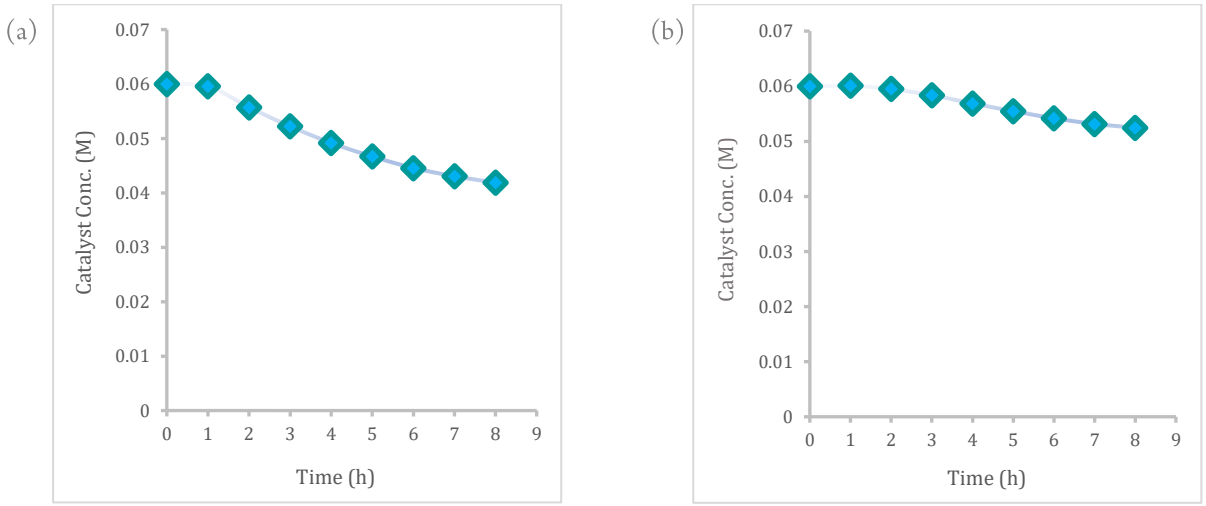


Figure 20. Catalyst integrity plots of [**62g**] vs time in refluxing toluene: (a) catalyst alone [**62g**] = 0.06 M; (b) with added acid **59** [0.2 M]; (c) with added amine **60** [0.2 M]; (d) with added amide **61a** [0.2 M]. (see Chapter 3, p. 98)

Likewise, to determine the magnitude of catalyst degradation in the presence of representative secondary and aryl amines independently, **62g** was treated with *N*-methylbenzylamine, morpholine, and aniline in refluxing toluene respectively. The resulting concentration profiles (Figure 21) revealed further catalyst loss (0.041 M, ca. 30%) under the action of *N*-methylbenzylamine, which appears to be associated with the enhanced basicity of acyclic alkyl amines with increased alkyl-substitution (4-methylbenzylamine pK_a = 9.21; *N*-methylbenzylamine pK_a = 9.58). In contrast, somewhat less

catalyst depletion (0.052 M, ca. 13%) was witnessed in the case of morpholine, where the diminished electronic contribution to the basicity centre (morpholine pK_a = 8.36) account for the effect. However, aniline marginally influenced the catalyst stability (0.058 M, ca. 3%), which is consistent with its reduced intrinsic basic character (aniline pK_a = 4.63).

Thus, the time course reaction profiles (Figure 21) imply that the relative strengths of examined amines exerted a profound effect on the catalyst integrity under the given conditions, thereby, providing further rationale for complications encountered in catalytic amidation reactions (Section 2.3). We reasoned that the secondary alkyl amines – more basic than primary alkyl amines – tend to promote catalyst decomposition, thus seemingly contributing to the decay in catalytic activity and hindering the formation of tertiary amides **61b-c**. Whereas, aniline is less likely to initiate the catalyst deactivation, hence, enabling the catalytic amidation to furnish the amide product **61d** despite its poor nucleophilicity.



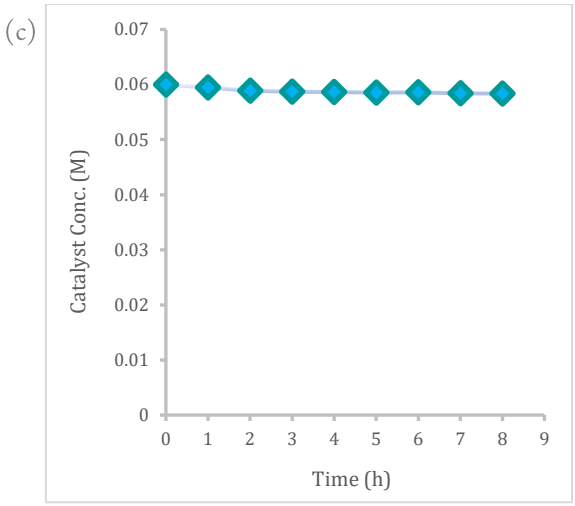


Figure 21. Catalyst integrity plots of [**62g**] vs time in refluxing toluene. $[\mathbf{62g}]_0$ = 0.06 M (a) with added *N*-methylbenzylamine [0.2 M]; (b) with added morpholine [0.2 M]; (c) with added aniline [0.2 M]. (see Chapter 3, p. 99)

Having realized the impact of various reaction components, particularly amine coupling partners, upon the catalyst integrity, we proceeded to monitor and quantify [**62g**] by conducting a set of tris(*p*-bromophenyl)silanol catalyzed amidation reactions. In this context, phenylacetic acid **59** was treated with representative primary, cyclic/acyclic secondary, and aryl amines in refluxing toluene to afford the corresponding amides **61a-d**. The quantification of catalyst over the course of reaction resulted in [**62g**] vs time plot depicted in Figure 22. Evidently, the catalyst degradation was found to be more drastic under the actual amidation conditions, where the onset of stability loss leads to 39, 49, 52, and 13% catalyst depletion respectively over a reaction time of 8 h. As can be seen, the catalyst suffers more significant biomolecular decomposition in these catalytic runs than under the action of each individual amine reaction component. This can possibly be explained as the carboxylic acid and amine may act in a synergistic way to induce catalyst deactivation, where extended reaction period in conjunction with higher concentration of secondary amines (less nucleophilic secondary alkyl amines react slowly, subsequently less amide product forms, thus [amine] remains high in the reaction system leading to catalyst decomposition) further facilitate the process.

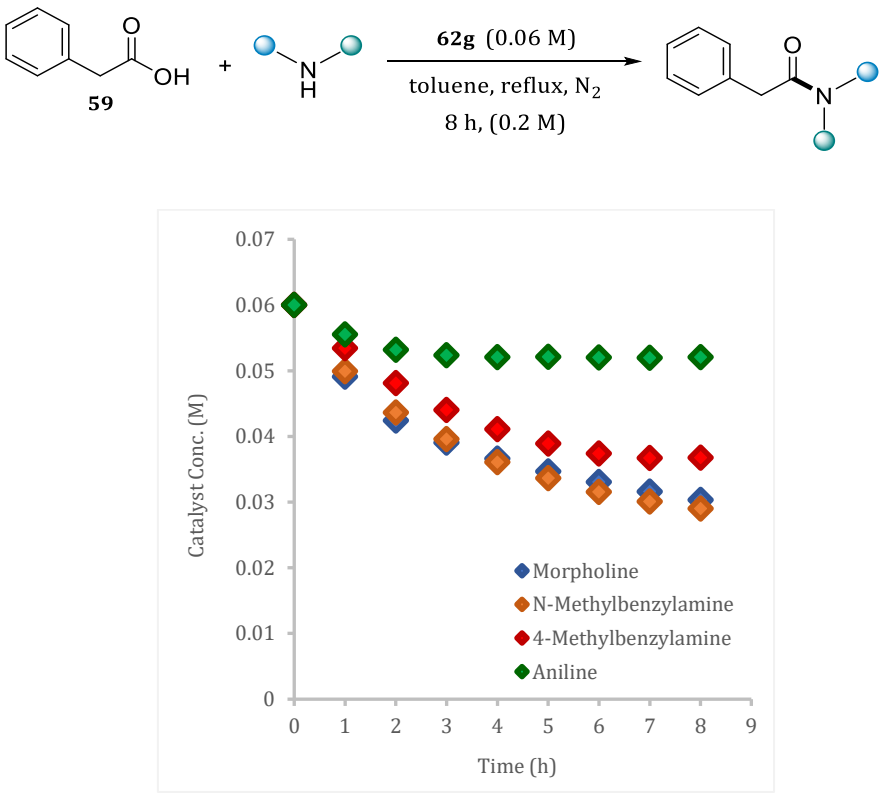
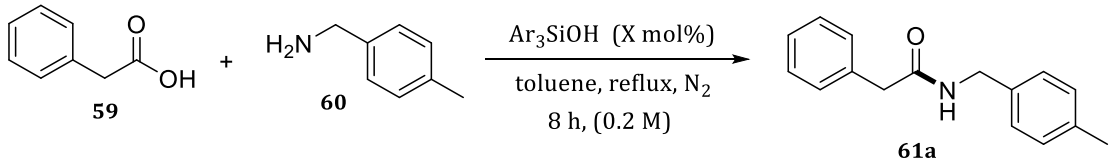


Figure 22. Catalyst integrity plot of [**62g**] vs time in catalytic amidations of phenyl acetic acid **59** with 4-methylbenzylamine **60**, *N*-methylbenzylamine, morpholine and aniline. (see Chapter 3, p. 100)

Having identified the pronounced catalyst depletion in tris(*p*-bromophenyl)silanol (30 mol%, 0.06 M) catalyzed direct amidations, we sought to mitigate this deleterious effect by decreasing the catalyst loading to 10 mol% (0.02 M). Thus, a model amidation reaction between carboxylic acid **59** and primary amine **60** using arylsilanol **62g** at 10 mol% loading was conducted to further probe the catalyst stability. By the comparison of the concentration profiles (Figure 23), it is immediately apparent that catalyst degradation is less severe (25%) at reduced concentration (0.02 M) as compared to 40% depletion observed at 0.06 M over 8 h in refluxing toluene. These results present a correlation between catalyst stability and concentration in these amidation reactions, as arylsilanol catalyst is susceptible to rapid decomposition at higher loading, whereas the opposite scenario was observed at reduced loading, where the rate of catalyst decomposition is somewhat suppressed.

A similar outcome was derived when tris(*p*-fluorophenyl)silanol **62e** was quantified under identical conditions (Figure 23), as can be seen, even though the catalyst deactivation necessarily manifests itself (5 and 23% depletion at 0.02 & 0.06 M respectively), the loss of catalyst stability seems to be less drastic in comparison to bromo- congener **62g**.



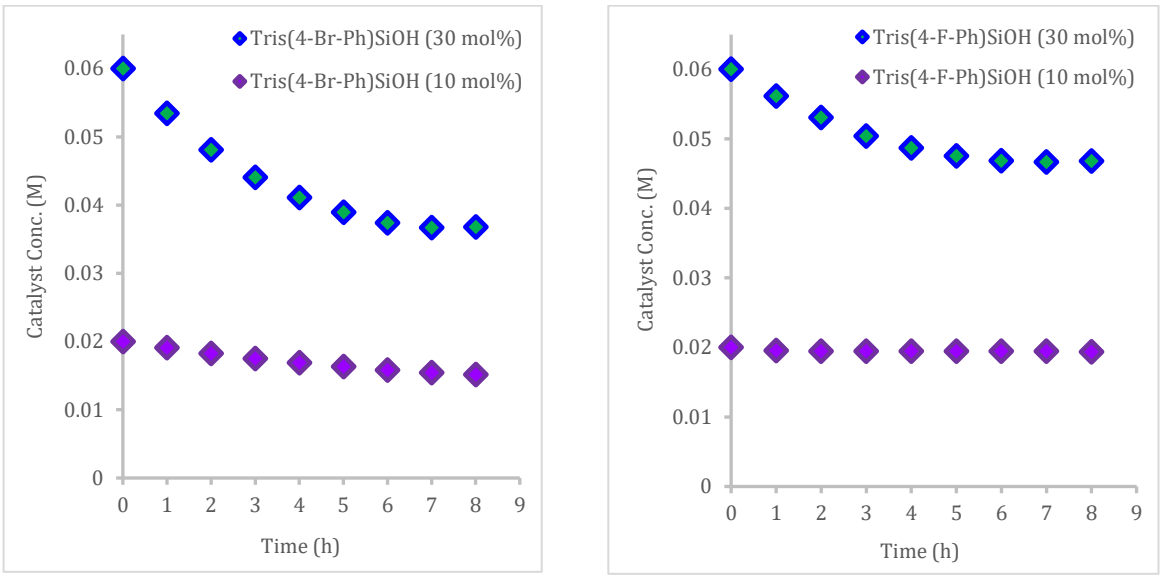


Figure 23. Catalyst integrity plots of [**62g**] and [**62e**] vs time. (see Chapter 3, p. 97)

To improve the catalyst system, catalyst stability over the reaction course is of paramount importance. The factors primarily impacting the catalyst integrity in the present experimental setting could be summarized as: (1) Relatively more basic secondary alkyl amines were found to be incompatible with arylsilanol catalyst. (2) Rapid loss of catalyst integrity at increased catalyst loadings was identified, which can be attributed to the rate acceleration of disiloxane formation.

2.7 X-ray Crystal Structures

The tris(*p*-haloaryl)silanes (**64a** & **64b**) crystallized in space group *Pbca* with $Z = 8$, and space group $P2_12_12_1$ with $Z = 4$, respectively. The crystal structures of **64a** (*p*-F) and **64b** (*p*-Cl) did not display atypical features (Figures S1 & S2). Si–C bond lengths and C–Si–C bond angles were found to be in agreement with those reported for $Ph_3Si–H$ (Table 2a).[36a]

Likewise, observed Si–O(H), Si–C bond lengths and O–Si–C, C–Si–C bond angles in the structures of tris(*p*-haloaryl)silanols **62e-g** were almost identical to those found in Ph_3SiOH (Table 2b-c).[36b] Bromo- and fluoro- compounds crystallized in triclinic (space group *P*1 with $Z = 4$) and monoclinic (space group *C*2/*c* with $Z = 16$) systems, respectively. The crystal structures of **62e-g** consist of hydrogen-bonded tetramers as shown in Figures 24-26. Four molecules – two of each type – hydrogen bond to form a non-planar 'square' or butterfly arrangement with fold angles given in Table 2b-c. O–H hydrogen atoms were reliably refined for the fluoro-analogue only, with an O–H bond distance of 0.900 (1) Å. Hydrogen atoms alternate between both possible ways around the 'square', that is, ...O–H...O–H... and –O...H–O...H–, where the relative occupancy of two sequences was about 50:50. Six crystallographically independent molecules were identified in the crystal structure of the chloro-analogue **62f**, and all were found to be distorted.

The crystals of disiloxane **65** crystallized in an orthorhombic (space group $P2_12_12_1$ with $Z = 8$) unit cell, containing two crystallographically distinct molecules. The principal bond distances (Si–O, Si–C) and bond angles (O–Si–C, C–Si–C, Si–O–Si) were comparable to those determined for hexaphenyldisiloxane (Table 2d).[36c]

Table 2(a). Selected distances and angles in the crystal structures of tris(*p*-haloaryl)silanes **64a-b**.[a,c]

Bond length (Å)	(*p*-F) **64a**	(*p*-Cl) **64b**	Ph_3Si–H [b]
Si–C	1.866 (2) – 1.874 (2)	1.860 (4) – 1.868 (4)	1.867 (8) – 1.876 (9)
Bond angle (°)			
C–Si–C	109.08 (9) – 110.41 (9)	109.72 (17) – 109.98 (18)	111.0 (4) – 111.9 (4)

Table 2(b). Selected distances and angles in the crystal structures of tris(*p*-haloaryl)silanols **62g** & **62e**.[a,c]

Bond length (Å)	(*p*-Br) **62g**	(*p*-F) **62e**	Ph_3Si–OH [b]
Si–O(H)	1.634 (11) – 1.674 (10)	1.6459 (15) – 1.6464 (14)	1.633 (5) – 1.651 (5)
Si–C	1.838 (16) – 1.899 (15)	1.860 (2) – 1.8652 (19)	1.843 (6) – 1.871 (5)
Bond angle (°)			
O–Si–C	105.2 (6) – 111.3 (6)	106.92 (8) – 110.02 (9)	105.7 (3) – 110.0 (3)
C–Si–C	108.0 (7) – 114.0 (7)	109.3 (6) – 111.6 (5)	108.0 (3) – 113.3 (3)
Fold angle (°)	46.9 (6)	32.8	35.8

Table 2(c). Selected distances and angles in the crystal structure of tris(*p*-chlorophenyl)silanol **62f**.[a,c]

Bond length (Å)	(*p*-Cl) **62f**	Ph_3Si–OH [b]
Si–O(H)	1.63 (3) – 1.65 (2)	1.633 (5) – 1.651 (5)
Si–C	1.846 (11) – 1.92 (2)	1.843 (6) – 1.871 (5)
Bond angle (°)		
O–Si–C	104.6 (4) – 114 (3)	105.7 (3) – 110.0 (3)
C–Si–C	103.1 (6) – 118.2 (8)	108.0 (3) – 113.3 (3)
Fold angle (°)	48.4 (5)	35.8

Table 2(d). Selected distances and angles in the crystal structure of 1,1,1,3,3,3-hexakis(*p*-bromophenyl)disiloxane **65**.[a,c]

Bond length (Å)	**65**	Ph_3–Si–O–Si–Ph_3 [b]
Si–O	1.615 (4) – 1.623 (4)	1.616 (1)
Si–C	1.860 (6) – 1.871 (6)	1.860 (2) – 1.870 (2)
Bond angle (°)		
O–Si–C	107.0 (2) – 108.3 (2)	108.4 (1) – 109.7 (1)
C–Si–C	109.8 (2) – 112.5 (2)	109.9 (1) – 110.1 (1)
Si–O–Si	174.1 (3) – 179.2 (4)	176.8 (7)

[a] E.s.d's are given in parentheses. [b] See ref. 36. [c] Full crystallographic data for all the structures described above have been deposited at Cambridge Structural Database (CSD) and can be retrieved here: https://www.ccdc.cam.ac.uk/structures Accession codes: CCDC 2247808, 2247809, 2247756, 2247757, 2247811 – 2247813, 2247765.

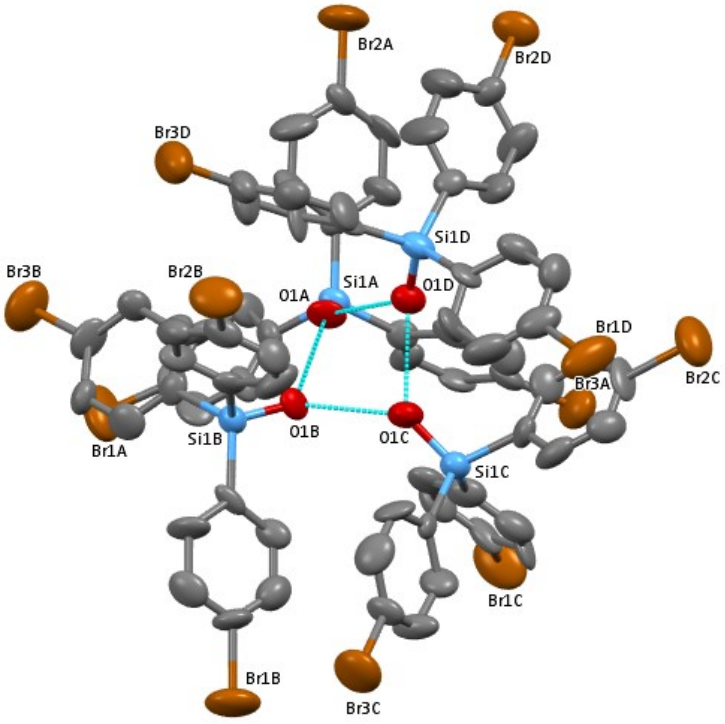


Figure 24. Molecular structure of **62g**. Hydrogen atoms are omitted for clarity. Thermal ellipsoids are shown at 70% probability.[21b]

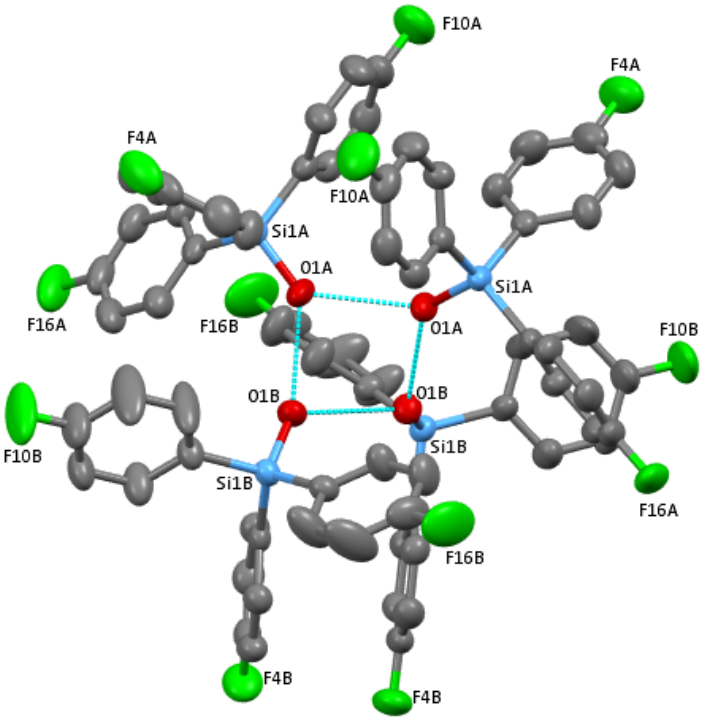


Figure 25. Molecular structure of **62e**. Hydrogen atoms are omitted for clarity. Thermal ellipsoids are shown at 70% probability.[21b]

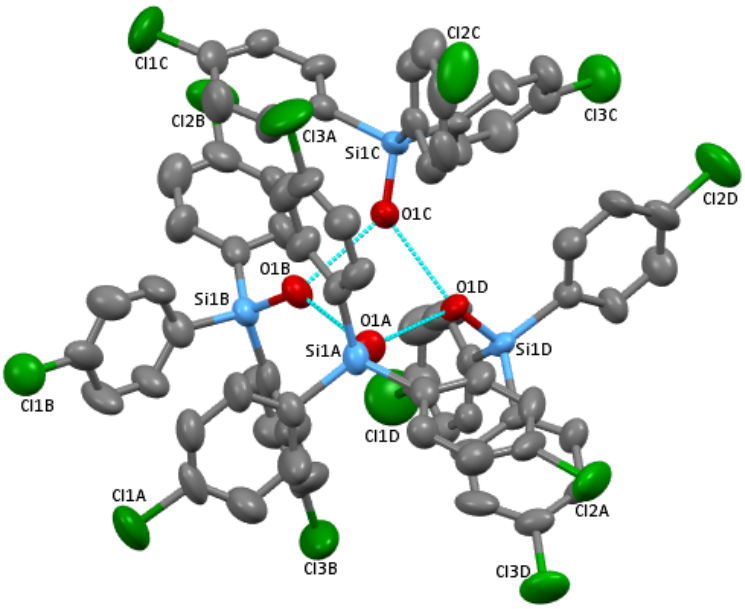


Figure 26. Molecular structure of **62f**. Hydrogen atoms are omitted for clarity. Thermal ellipsoids are shown at 70% probability.[21b]

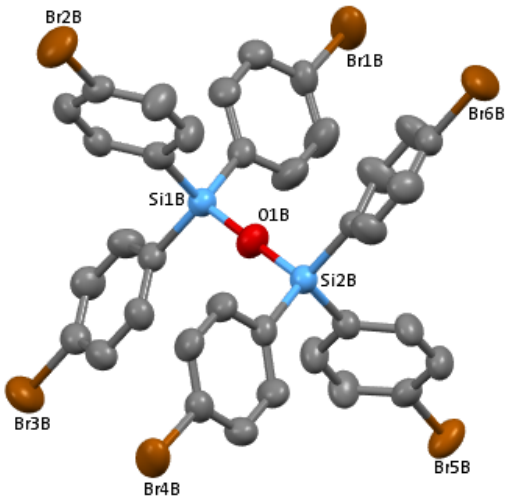


Figure 27. Molecular structure of **65**. Hydrogen atoms are omitted for clarity. Thermal ellipsoids are shown at 70% probability.[21b]

Conclusions

An unprecedented approach featuring triarylsilanols as catalysts for the direct amidation of carboxylic acids with amines is demonstrated. However, the protocol presented substantial constraints in terms of substrate scope and catalytic efficiency. RPKA unequivocally established product inhibition as the governing factor for diminished catalytic efficiency in the amidation reactions. Tertiary amide products were found to be more inhibitory than secondary amides. The origin of catalyst order greater than one further endorsed the occurrence of product inhibition. The findings pertaining to the catalyst quantification uncovered a correlation between amine basicity, catalyst stability, and reaction yields. Mechanistically, the viability of amide-silyl ester complex in catalyst inhibition is proposed computationally. This work demonstrates that Lewis acidic amidation catalysts are sensitive to the Lewis basicity of the amide moiety, thereby limiting the scope of catalytic direct amidations with these particular triarylsilanols.

Outlook

Further investigations to gain a complete understanding of this newly developed arylsilanol-catalyzed amidation system are ongoing in our laboratory. We anticipate that these findings will help (1) design a streamlined catalytic protocol, capable of catalyzing inherently difficult acid/amine combinations and (2) fine tune the structural topology of arylsilanols as amidation catalysts, thus enabling the development of robust silicon-centered catalytic processes for direct dehydrative coupling of carboxylic acids and amines.

Chapter 3: Experimental

General Experimental

Experimental Techniques: All reactions were carried out in oven-dried glassware under an N_2 atmosphere. Reaction temperatures other than ambient temperature were achieved with a DrySyn, ice/water bath (0 °C), or dry ice/acetone bath (-78 °C). Volatiles were removed *in vacuo* by rotary evaporation. Analytical TLC was performed on Silica gel 60 F254 pre-coated aluminium-backed plates and visualized by irradiation with UV light (254 or 350 nm). Brine refers to a saturated aqueous NaCl solution. Work-up solutions are aqueous solutions unless otherwise stated.

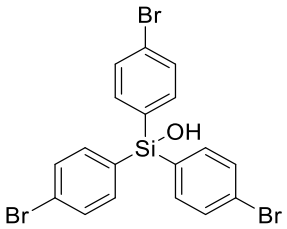
Reagents and Solvents: All organometallic and amidation reactions were carried out in anhydrous solvents obtained from Imperial College solvent towers. Unless otherwise noted, reagents were purchased from commercial sources and used without further purification. Previously synthesized tetrakis(trimethylsilyl)methane (TTMSM) was available as a legacy chemical from the Lickiss group. All extraction and chromatography solvents (EtOAc, Et_2O, *n*-hexane, petroleum ether) were purchased from commercial suppliers and used as received. HPLC grade solvents (MeCN and *i*PrOH) were used for HPLC separations.

Characterization: ^{1}H NMR (400 MHz), ^{13}C NMR (101 MHz), ^{29}Si NMR (80 MHz), and ^{19}F NMR (377 MHz) spectra were recorded in $CDCl_3$ at 298K on a Bruker AV-400 spectrometer. Chemical shifts (δ) are reported in ppm relative to the residual solvent peaks (δ = 7.26, 77.16 ppm for $CDCl_3$). Abbreviations for peak multiplicity are as follows: s - singlet, d - doublet, t - triplet, br - broad, m - multiplet. Coupling constants (J) are reported in Hertz (Hz). Melting points were measured using a Stuart SMP10 melting point apparatus and are uncorrected. Fourier-transform infrared (IR) spectra were recorded neat using an ATR-FTIR spectrometer. High resolution mass spectra (HRMS) were recorded by Thermo Q-Exactive Orbitrap Mass Spectrometer using atmospheric pressure chemical

ionization (APCI) in positive or negative mode. X-ray crystal structures were determined by Agilent Xcalibur 3E diffractometer (for details see supporting information). Reverse phase HPLC was performed on a SUPELCOSIL™ LC-18 column (25 cm × 4.6 mm, 5 μm) with UV detection at 222/230 nm, flow rate of 2 mL/min, and an injection volume of 1.0 μL. The mobile phase consisted of various combinations of MeCN and H_2O.

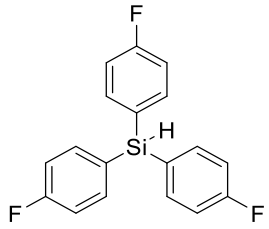
3.1 Synthetic Procedures and Characterization Data for Compounds

3.1.1 Tris(4-bromophenyl)silanol (62g)[24a]



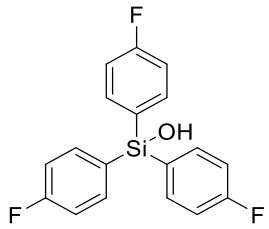
A solution of *n*-BuLi (20 mL, 50 mmol, 2.5 M in hexanes) in Et_2O (100 mL) was added to a solution of 1,4-dibromobenzene (11.8 g, 50 mmol) in Et_2O (100 mL) at -78 °C and the resulting mixture allowed to stir for 2 h. $SiCl_4$ (1.9 mL, 16.7 mmol) was then added dropwise, and the reaction mixture was heated at reflux for 2 h. After being quenched with H_2O (50 mL), the organic layer was separated, washed with brine, dried over $MgSO_4$, and evaporated to yield a yellow oil. The crude oil was purified by crystallization from hot *n*-hexane to give tris(4-bromophenyl)silanol **62g** (5.5 g, 10.7 mmol, 64%) as a white crystalline solid: M.p. 125.9 - 126.5 °C (lit.[37a] M.p. 126 - 127 °C); ATR-FTIR ν_{max}/cm^{-1}: 3028 (Si-OH); ^1H NMR (400 MHz, $CDCl_3$): δ 7.55 – 7.53 (m, 6H, Ar-H), 7.44 – 7.41 (m, 6H, Ar-H), 2.68 (s, 1H, Si-OH); ^{13}C NMR (101 MHz, $CDCl_3$): δ 136.5, 133.0, 131.5, 125.8; $^{29}Si\{^1H\}$ NMR (80 MHz, $CDCl_3$): δ -12.5; HRMS (APCI) *m/z*: $[M-H]^-$ calcd. for $C_{18}H_{12}OSi\ ^{79}Br_2\ ^{81}Br$ 510.8182, Found 510.8189.

3.1.2 Tris(4-fluorophenyl)silane (64a)[21a]



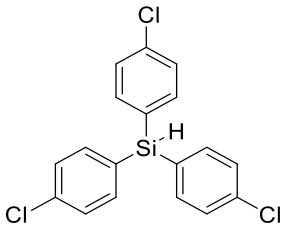
Magnesium turnings (1.3 g, 54 mmol) were vigorously stirred under N_2 for 45 min, and a solution of 1-bromo-4-fluorobenzene (5.9 mL, 54 mmol) in Et_2O (60 mL) was added over 15 min at 0 °C. The reaction was held at 0 °C until the magnesium was consumed resulting in a brown solution. The mixture was gently heated for 1 h and then cooled to -78 °C whereupon trichlorosilane (1.36 mL, 13.5 mmol) was added dropwise over 20 min. After complete addition, the mixture was allowed to stir overnight at room temperature. Aqueous HCl solution (1.0 M, 20 mL) was added, and the aqueous phase was extracted with diethyl ether (2 × 15 mL). The ether layers were combined and washed with brine, separated, dried over $MgSO_4$, filtered, and evaporated to yield a pale-yellow oil. The crude oil was purified by silica plug eluting with *n*-hexane to give tris(4-fluorophenyl)silane **64a** (3.4 g, 10.8 mmol, 80%) as a colourless crystalline solid: M.p. 43 - 44 °C (lit.[37b] M.p. 42 - 44 °C); ATR-FTIR ν_{max}/cm^{-1}: 2144 (Si-H); ^1H NMR (400 MHz, $CDCl_3$): δ 7.54 - 7.49 (m, 6H, Ar-H), 7.13 - 7.09 (m, 6H, Ar-H), 5.45 (s, $^1J_{Si-H}$ = 201.9 Hz, 1H, Si-H); ^{13}C NMR (101 MHz, $CDCl_3$): δ 165.7 (d, $^1J_{C-F}$ = 250.2 Hz), 137.8 (d, $^3J_{C-F}$ = 7.7 Hz), 128.5 (d, $^4J_{C-F}$ = 3.6 Hz), 115.7 (d, $^2J_{C-F}$ = 20.2 Hz); $^{19}F\{^1H\}$ NMR (377 MHz, $CDCl_3$): δ -109.9 (s, 3F, $^1J_{F-C}$ = 250.0 Hz); $^{29}Si\{^1H\}$ NMR (80 MHz, $CDCl_3$): δ -18.9; HRMS (APCI) *m/z*: $[M-H]^-$ calcd. for $C_{18}H_{12}F_3Si$ 313.0655, Found 313.0651.

3.1.3 Tris(4-fluorophenyl)silanol (62e)[21a]



A solution of silane **64a** (1.0 g, 3.2 mmol) in THF (26 mL) was added dropwise over 10 min to an aqueous solution of NaOH (1.3 mL, 7.7 M) whilst vigorously stirring in open air allowing the escape of generated H_2. Upon reaction completion, the solvent was evaporated and an aqueous HCl solution (1.0 M, 10 mL) was added to the resulting emulsion. Diethyl ether (25 mL) was added, the layers were separated, and the aqueous phase was extracted with Et_2O (2 × 10 mL). The organics were combined and washed with brine, separated, dried over $MgSO_4$, filtered, and evaporated to yield a colourless solid. The crude solid was purified by silica plug eluting with *n*-hexane and, then diethyl ether to give tris(4-fluorophenyl)silanol **62e** (0.7 g, 2.1 mmol, 66%) as a colourless crystalline solid: M.p. 89 - 90 °C (lit.[37a] M.p. 90 °C); ATR-FTIR ν_{max}/cm^{-1}: 3026 (Si-OH); ^1H NMR (400 MHz, $CDCl_3$): δ 7.59 – 7.54 (m, 6H, Ar-H), 7.12 – 7.06 (m, 6H, Ar-H), 2.82 (s, 1H, Si-OH); ^{13}C NMR (101 MHz, $CDCl_3$): δ 165.8 (d, $^1J_{C\text{-}F}$ = 250.6 Hz), 137.2 (d, $^3J_{C\text{-}F}$ = 7.9 Hz), 130.5 (d, $^4J_{C\text{-}F}$ = 3.5 Hz), 115.6 (d, $^2J_{C\text{-}F}$ = 20.0 Hz); $^{19}F\{^1H\}$ NMR (377 MHz, $CDCl_3$): δ -109.5 (s, 3F, $^1J_{F\text{-}C}$ = 250.1 Hz); $^{29}Si\{^1H\}$ NMR (80 MHz, $CDCl_3$): δ -12.8; HRMS (APCI) *m/z*: $[M+H]^+$ calcd. for $C_{18}H_{14}F_3SiO$ 331.0761, Found 331.0751.

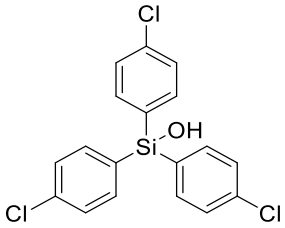
3.1.4 Tris(4-chlorophenyl)silane (64b)[24b]



Magnesium turnings (4.3 g, 176 mmol) were vigorously stirred under N_2 for 45 min, and a solution of 1-bromo-4-chlorobenzene (30 g, 157 mmol) in Et_2O (60 mL) was added. The solution started refluxing on its own after 15 min and turned brown. After 40 min, the mixture was cooled to 0 °C whereupon $HSiCl_3$ (5.2 mL, 51 mmol) was added dropwise. After complete addition, the reaction mixture was refluxed for 4 h. The reaction was quenched by pouring the solution into an ice/5% HCl mixture and the aqueous layer was extracted with Et_2O (3 × 20 mL). The organic layers were

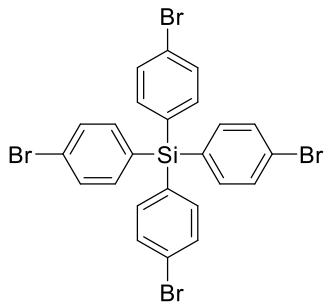
combined and washed with brine, separated, dried over $MgSO_4$, filtered, and evaporated to yield an oil. Upon the addition of *n*-pentane to crude oil, white precipitates were formed. The solution was left overnight in a fridge to encourage further precipitation. The white precipitates were collected and recrystallized from EtOH/*n*-pentane to give tris(4-chlorophenyl)silane **64b** (7.5 g, 20.6 mmol, 40%) as a white crystalline solid: M.p. 74.6 - 75.3 °C (lit.[37c] M.p. 74 - 76 °C); ATR-FTIR ν_{max}/cm^{-1}: 2137 (Si-H); ^1H NMR (400 MHz, $CDCl_3$): δ 7.47 – 7.42 (m, 6H, Ar-H), 7.37 (d, J = 8.3 Hz, 6H, Ar-H), 5.42 (s, $^1J_{Si-H}$ = 203.5 Hz, 1H, Si-H); ^{13}C NMR (101 MHz, $CDCl_3$): δ 136.9, 136.8, 130.6, 128.6; $^{29}Si\{^1H\}$ NMR (80 MHz, $CDCl_3$): δ -18.6; HRMS (APCI) *m/z*: $[M]^{+\bullet}$ calcd. for $C_{18}H_{13}Cl_3Si$ 361.9852, Found 361.9845.

3.1.5 Tris(4-chlorophenyl)silanol (62f)[21a, 24c]



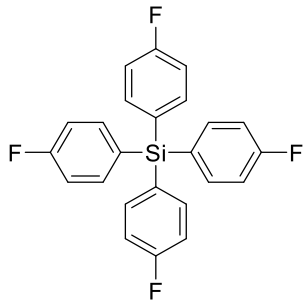
10% Pd-C (60 mg, 0.6 mmol) was added to a solution of silane **64b** (0.9 g, 2.5 mmol) in anhydrous CH_2Cl_2 (6 mL). An equimolar amount of H_2O was added (50 µL, 2.5 mmol), and immediate bubbling occurred. The reaction mixture was allowed to stir at room temperature for 1 h, the solution was filtered, and concentrated *in vacuo* to give a yellow oil. The crude oil was purified by silica plug eluting with *n*-hexane and, then diethyl ether to yield tris(4-chlorophenyl)silanol **62f** (0.67 g, 1.76 mmol, 70%) as a white crystalline solid: M.p. 120.3 - 120.9 °C (lit.[37d] M.p. 121 °C); ATR-FTIR ν_{max}/cm^{-1}: 3024 (Si-OH); ^1H NMR (400 MHz, $CDCl_3$): δ 7.51 – 7.48 (m, 6H, Ar-H), 7.39 – 7.36 (m, 6H, Ar-H), 2.82 (s, 1H, Si-OH); ^{13}C NMR (101 MHz, $CDCl_3$): δ 137.1, 136.3, 132.6, 128.5; $^{29}Si\{^1H\}$ NMR (80 MHz, $CDCl_3$): δ -12.9; HRMS (APCI) *m/z*: $[M-H]^-$ calcd. for $C_{18}H_{12}Cl_3SiO$ 376.9801, Found 376.9701.

3.1.6 Tetrakis(4-bromophenyl)silane (71a)[38a]



To a solution of 1,4-dibromobenzene (11.8 g, 50 mmol) in THF (60 mL) at -78 °C, *n*-BuLi (20 mL, 50 mmol, 2.5 M in hexanes) was added dropwise and the resulting mixture allowed to stir for 2 h. $SiCl_4$ (1.9 mL, 16.7 mmol) was then added dropwise, and the reaction mixture was left to stir overnight at -78 °C. The reaction was quenched with H_2O (50 mL) and the organic layer separated. The aqueous phase was extracted with Et_2O (3 × 20 mL), combined organics were dried over $MgSO_4$ and concentrated to yield a colourless oil. The oil was solidified on standing to give tetrakis(4-bromophenyl)silane **71a** (7.5 g, 11.5 mmol, 66%) as a colourless crystalline solid; M.p. 242.5 - 243 °C (lit.[38a] M.p. 242 - 243 °C); ^{1}H NMR (400 MHz, $CDCl_3$): δ 7.56 – 7.52 (m, 8H, Ar-H), 7.36 – 7.33 (m, 8H, Ar-H); ^{13}C NMR (101 MHz, $CDCl_3$): δ 137.7, 131.6, 125.5; ^{29}Si{^{1}H} NMR (80 MHz, $CDCl_3$): δ -13.5; HRMS (APCI) *m/z*: $[M]^{+\cdot}$ calcd. for $C_{24}H_{16}Si^{79}Br_2{}^{81}Br_2$ 651.7708, Found 651.7717.

3.1.7 Tetrakis(4-fluorophenyl)silane (71b)[38b]



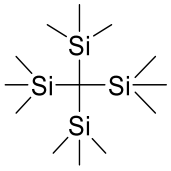
To a solution of 1-bromo-4-fluorobenzene (5.5 mL, 50 mmol) in THF (60 mL) at -78 °C, *n*-BuLi (20 mL, 50 mmol, 2.5 M in hexanes) was added dropwise and the resulting mixture stirred for 2 h. $SiCl_4$ (1.9 mL, 16.7 mmol) was then added dropwise, and the mixture was allowed to stir overnight at -78

°C. The reaction was quenched with water (50 mL) and the organic layer separated. The aqueous layer was extracted with Et_2O (3 × 20 mL), combined organic extracts were dried over $MgSO_4$, and volatiles were removed. The residual oil was solidified on standing to give tetrakis(4-fluorophenyl)silane **71b** (0.8 g, 2 mmol, 12%) as colourless needles; M.p. 131.4 – 131.8 °C (lit.[38b] M.p. 131 - 132 °C); ^{1}H NMR (400 MHz, $CDCl_3$): δ 7.51 - 7.46 (m, 8H, Ar-H), 7.13 - 7.07 (m, 8H, Ar-H); ^{13}C NMR (101 MHz, $CDCl_3$): δ 165.4 (d, $^1J_{C\text{-}F}$ = 250.3 Hz), 138.2 (d, $^3J_{C\text{-}F}$ = 7.7 Hz), 129.1 (d, $^4J_{C\text{-}F}$ = 3.7 Hz), 115.3 (d, $^2J_{C\text{-}F}$ = 20.1 Hz); ^{19}F{^{1}H} NMR (377 MHz, $CDCl_3$): -110.1 (s, 4F, $^1J_{F\text{-}C}$ = 249.8 Hz); ^{29}Si{^{1}H} NMR (80 MHz, $CDCl_3$): δ -14.6; HRMS (APCI) *m/z*: $[M]^{+\bullet}$ calcd. for $C_{24}H_{16}F_4Si$ 408.0952, Found 408.0945.

3.2 General Procedure for Conversion vs Time Plots (Figures 8 & 9)

Phenylacetic acid (0.41 g, 3.0 mmol, 1 equiv.), 4-methylbenzylamine (0.38 mL, 3.0 mmol, 1 equiv.), appropriate triarylsilanol **2**, **62e-g** (10, 30, 50, or 100 mol%), tetrakis(trimethylsilyl)methane (30 mg, 0.098 mmol) as internal standard, and toluene (15 mL, 0.2 M) were placed within a 100 mL two neck round bottomed flask. The mixture was purged under a flow of N_2 for 5 min before bringing to reflux. After the elapsed time, an aliquot (0.1 mL) from the reaction mixture was removed and transferred to a glass vial. Chloroform-*d* was added until a homogenous solution was observed at which point ^{1}H NMR spectra were recorded, and conversions were calculated from the crude reaction mixture against internal standard. Reactions were conducted in triplicate, and the average conversions are reported. Characteristic data for internal standard TTMSM is provided.

3.2.1 Tetrakis(trimethylsilyl)methane[39]



White solid; M.p. 132 - 133 °C (lit.[40b] M.p. 129 - 135 °C); ^{1}H NMR (400 MHz, $CDCl_3$): δ 0.26 (s, 36H); ^{13}C NMR (101 MHz, $CDCl_3$): δ 5.4 (12C, 12 × CH_3), -1.74 (CSi_4); ^{29}Si{^{1}H} NMR (80 MHz, $CDCl_3$): δ -1.5; HRMS (APCI) *m/z*: $[M+H]^+$ calcd. for $C_{13}H_{37}Si_4$ 305.1967, Found 305.1552.

3.3 General Procedures for Triarylsilanols Catalyzed Direct Amidations

3.3.1 General procedure 1 (GP1: tris(*p*-bromophenyl)silanol (30 mol%) catalyzed amidations at 0.2 M)

Carboxylic acid (5.0 mmol, 1 equiv.), amine (5.0 mmol, 1 equiv.), **62g** (0.76 g, 1.5 mmol, 30 mol%) and toluene (25 mL) were charged into a 100 mL round bottomed flask. This mixture was purged under a flow of N_2 for 5 min and heated to reflux for 24 h. After the reaction time, the mixture was allowed to cool to room temperature and concentrated *in vacuo*. The yellow oily residue was diluted with EtOAc (20 mL), and the resulting solution was washed with the aqueous NaOH (25 mL, 0.4 M) and aqueous HCl (25 mL, 1.0 M) solutions. The organic layer was dried over $MgSO_4$, filtered, and evaporated. The residue was further purified by dry column vacuum chromatography (2-8% EtOAc) to yield amide products.

3.3.2 General procedure 2 (GP2: Ph_3SiOH (30 mol%) catalyzed amidations at 0.2 M)

Carboxylic acid (5.0 mmol, 1 equiv.), amine (5.0 mmol, 1 equiv.), **2** (0.41 g, 1.5 mmol, 30 mol%), and toluene (25 mL) were charged into a 100 mL round bottomed flask. This mixture was purged under a flow of N_2 for 5 min and heated to reflux for 24 h. After the reaction time, the mixture was allowed to cool to room temperature and concentrated *in vacuo*. The yellow oily residue was diluted with EtOAc (20 mL), and the resulting solution was washed with the aqueous NaOH (25 mL, 0.4 M) and aqueous HCl (25 mL, 1.0 M) solutions. The organic layer was dried over $MgSO_4$, filtered and evaporated. The residue was further purified by dry column vacuum chromatography (EtOAc, 2-8%) to yield amide products.

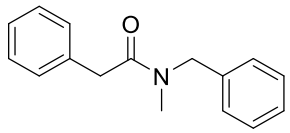
Modified work-up procedure A (W/U A)

Following either GP1 or GP2, after evaporation, the amide was triturated with *n*-hexane (2 × 10 mL) for the removal of aniline.

Modified work-up procedure B (W/U B)

Following either GP1 or GP2, after the reaction time, the mixture was allowed to cool to room temperature and the precipitated ammonium carboxylate salt was filtered. Toluene solution was concentrated *in vacuo* and the yellow residue was diluted with EtOAc (20 mL).

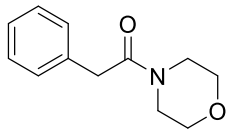
3.3.3 *N*-Benzyl-*N*-methyl-2-phenylacetamide (61c)[18j]



Following GP1, amide **61c** (0.12 g, 0.5 mmol, 10%) was isolated as a colourless oil: ^{1}H NMR (400 MHz, $CDCl_3$) (Mixture of two rotamers): δ (Major rotamer) 7.40 – 7.15 (m, 9H, Ar-H), 7.10 (d, *J* = 7.3 Hz, 1H, Ar-H), 4.65 (s, 2H), 3.82 (s, 2H), 2.93 (s, 3H). (Minor rotamer) 7.40 – 7.15 (m, 9H, Ar-H), 7.10 (d, *J* = 7.3 Hz, 1H, Ar-H), 4.56 (s, 2H), 3.79 (s, 2H), 2.99 (s, 3H); ^{13}C NMR(101 MHz, $CDCl_3$): δ 171.5, 171.1, 137.3, 136.5, 135.1, 134.9, 128.9, 128.8, 128.7, 128.6, 128.0, 127.6, 127.3, 126.8, 126.4, 53.6, 50.9, 41.2, 40.9, 35.2, 34.0.

Following GP2, amide **61c** (0.19 g, 0.79 mmol, 16%) was isolated as a colourless oil.

3.3.4 1-Morpholino-2-phenylethan-1-one (61b)[18j]

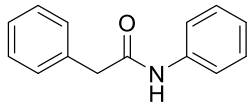


Following GP1, amide **61b** (0.21 g, 1.0 mmol, 20%) was isolated as a yellowish crystalline solid: M.p. 65.8 – 66.8 °C (lit.[18j] M.p. 65 - 67 °C); ^{1}H NMR (400 MHz, $CDCl_3$): δ 7.36 (dd, *J* = 8.3, 6.1 Hz, 2H,

Ar-H), 7.30 – 7.27 (m, 3H, Ar-H), 3.76 (s, 2H), 3.67 (s, 4H), 3.52 – 3.49 (m, 2H), 3.47 – 3.45 (m, 2H); ^{13}C NMR (101 MHz, $CDCl_3$): δ 169.6, 134.8, 128.8, 128.5, 126.9, 66.8, 66.4, 46.5, 42.1, 40.8.

Following GP2, amide **61b** (0.28 g, 1.36 mmol, 27%) was isolated as a yellowish crystalline solid.

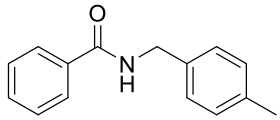
3.3.5 *N*,2-Diphenylacetamide (61d)[18n]



Following GP1 and W/U A, amide **61d** (0.35 g, 1.64 mmol, 33%) was isolated as a white solid: M.p. 113.4 – 114.8 °C (lit.[18n] M.p. 113 - 115 °C); ^{1}H NMR (400 MHz, $CDCl_3$): δ 7.43 – 7.39 (m, 4H, Ar-H), 7.36 – 7.33 (m, 3H, Ar-H), 7.30 -7.28 (m, 2H, Ar-H), 7.09 (t, J = 7.4 Hz, 1H, Ar-H), 7.03 (br s, 1H, N-H), 3.74 (s, 2H); ^{13}C NMR (101 MHz, $CDCl_3$): δ 169.2, 137.7, 134.6, 129.6, 129.4, 129.0, 127.8, 124.6, 119.9, 45.0.

Following GP2 and W/U A, amide **61d** (0.2 g, 0.95 mmol, 19%) was isolated as a white solid.

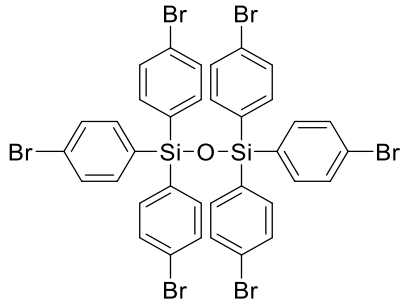
3.3.6 *N*-(4-Methylbenzyl)benzamide (61e)[18j]



Following GP1, compound **61e** (90 mg, 0.4 mmol, 8%) was isolated as a white solid: M.p. 140.3 – 141°C (lit.[18j] M.p. 140 - 141 °C); ^{1}H NMR (400 MHz, $CDCl_3$): δ 7.80 (dd, J = 7.1, 1.7 Hz, 2H, Ar-H), 7.55 – 7.49 (m, 1H, Ar-H), 7.48 – 7.41 (m, 2H, Ar-H), 7.30 – 7.25 (m, 2H, Ar-H), 7.19 (d, J = 7.8 Hz, 2H, Ar-H), 6.40 (br s, 1H, N-H), 4.63 (d, J = 5.6 Hz, 2H), 2.37 (s, 3H); ^{13}C NMR (101 MHz, $CDCl_3$): δ 167.4, 137.5, 135.3, 134.6, 131.5, 129.5, 128.6, 128.0, 127.1, 44.0, 21.2.

Following GP2 and W/U B, amide **61e** (34 mg, 0.15 mmol, 3%) was isolated as a white solid.

3.3.7 1,1,1,3,3,3-Hexakis(4-bromophenyl)disiloxane (65)[29]



During work-up of tris(*p*-bromophenyl)silanol catalyzed amidations of phenylacetic acid with morpholine and *N*-methylbenzylamine, upon evaporation of toluene and/or dilution with EtOAc, disiloxane **65** was isolated as a white solid; M.p. 295.3 - 295.9 °C (lit.[29] M.p. 294.5 - 296 °C); ^{1}H NMR (400 MHz, $CDCl_3$): δ 7.44 (d, *J* = 7.7 Hz, 12H, Ar-H), 7.21 (d, *J* = 7.7 Hz, 12H, Ar-H); ^{13}C NMR (101 MHz, $CDCl_3$): δ 136.4, 132.7, 131.5, 125.9; ^{29}Si{^{1}H} NMR (80 MHz, $CDCl_3$): δ -17.4; HRMS (APCI) *m/z*: calcd. for $C_{36}H_{24}OSi_2{}^{79}Br_4{}^{81}Br_2$ 1006.6332, Found [M+ Cl +H]$^-$ 1042.6108.

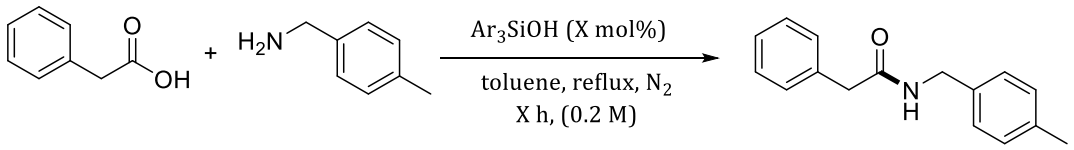
3.4 General Procedure for Tris(4-bromophenyl)silanol Catalyzed Concentration vs Time Plots (Figures 13 & 14)

Phenylacetic acid (0.41g, 3.0 mmol, 1 equiv.), 4-methylbenzylamine (0.38 mL, 3.0 mmol, 1 equiv.), tris(4-bromophenyl)silanol (0.46 g, 0.9 mmol, 30 mol%), tetrakis(trimethylsilyl)methane (30 mg, 0.098 mmol) as internal standard, and toluene (15 mL, 0.2 M) were charged into a 100 mL two-neck round bottomed flask. *N*-(4-methylbenzyl)-2-phenylacetamide **61a** (0.36 g, 1.5 mmol, 0.1 M) and/or H_2O (27 μL, 1.5 mmol, 0.1 M) or amides **61b-d** (1.5 mmol, 0.1 M) were added, and the mixture was purged under a flow of N_2 for 5 min before bringing to reflux. After the elapsed time, an aliquot (0.1 mL) from the reaction mixture was removed and transferred to a glass vial. Chloroform-*d* was added until a homogenous solution was observed at which point ^{1}H NMR spectra were recorded. Concentrations were calculated by integration against the internal standard. Reactions were conducted in triplicate and the average concentrations are reported.

3.5 **General Procedure for Post Amidation Catalyst Integrity Quantification** (Figure 22)

Phenylacetic acid (0.41 g, 3.0 mmol, 1 equiv.), amine (3.0 mmol, 1 equiv.), triarylsilanols **62e** or **62g** (10 or 30 mol%), durene (30 mg, 0.2 mmol) as internal standard, and toluene (15 mL, 0.2 M) were placed within a 100 mL two neck round bottomed flask. The mixture was purged under a flow of N_2 for 5 min before bringing to reflux for the required time. After the elapsed time, an aliquot (100 μL) from the reaction mixture was removed and transferred to a glass vial. *i*PrOH (1000 μL) was added to give a homogenous solution. Samples were analysed on a reverse phase SUPELCOSIL™ LC-18 HPLC column (25 cm × 4.6 mm, 5 μm) @ 222/230 nm, using MeCN/H_2O mobile phase. Catalyst integrity was determined by integration against the internal standard and by reference to a pre-determined calibration curve. Stock solutions of catalysts (**62e**, **62g**) and internal standard were prepared in MeCN at 1.82 mM concentration. (For details of calibration solutions see Table 11)

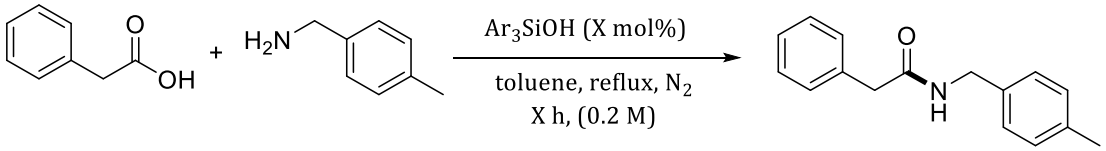
Table 3. Catalyst Loading Screening



Entry	Time (h)	Amide Conversion (%) [a]								
			Triphenylsilanol (**2**)				Tris(*p*-bromophenyl)silanol (**62g**)			
		Background	10 mol%	30 mol%	50 mol%	100 mol%	10 mol%	30 mol%	50 mol%	100 mol%
1	1	7	20	30	33	45	29	52	66	68
2	2	13	38	55	57	65	53	77	83	84
3	3	19	52	71	70	73	71	89	89	90
4	4	25	63	80	76	78	84	96	93	94
5	5	30	71	84	79	82	93	100	97	98
6	6	35	77	86	81	86	100			
7	7	40	81	87	82					
8	8	44	84							
9	9	48								
10	10	52								
11	11	56								

[a] Conversions were determined by analysing ^{1}H NMR spectra of crude reaction mixture relative to the internal standard TTMSM. The variation in observed percentage conversions is ±2%.

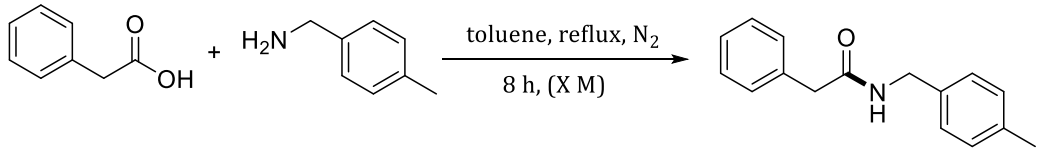
Table 4. Catalyst Loading Screening



Entry	Time (h)	Amide Conversion (%) [a]								
			Tris(*p*-fluorophenyl)silanol (**62e**)				Tris(*p*-chlorophenyl)silanol (**62f**)			
		Background	10 mol%	30 mol%	50 mol%	100 mol%	10 mol%	30 mol%	50 mol%	100 mol%
1	1	7	29	39	42	42	24	42	49	57
2	2	13	52	64	65	66	44	66	76	79
3	3	19	67	76	77	79	59	79	87	87
4	4	25	76	82	83	87	70	86	92	91
5	5	30	82	86	87	92	78	90	95	94
6	6	35	86	89	90	96	83	92	97	97
7	7	40	89	91	92	99	86	93		
8	8	44	91		94		87			
9	9	48								
10	10	52								
11	11	56								

[a] Conversions were determined by analysing ^{1}H NMR spectra of crude reaction mixture relative to the internal standard TTMSM. The variation in observed percentage conversions is ±2%.

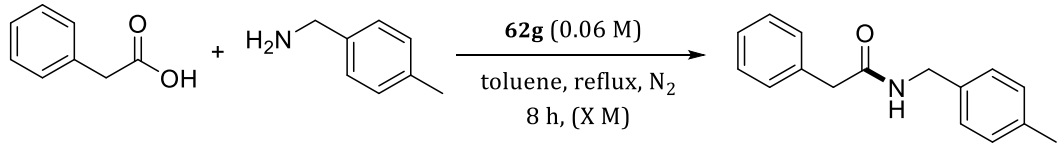
Table 5. Background Model Amidation Reaction at Different Concentrations



Entry	Time (h)	Concentration of Amide (M) [a]			
		[Acid]	0.4 M	0.3 M	0.2 M	0.1 M
		[Amine]	0.4 M	0.3 M	0.2 M	0.1 M
1	1		0.030	0.016	0.011	0.003
2	2		0.060	0.033	0.022	0.007
3	3		0.089	0.051	0.034	0.010
4	4		0.119	0.069	0.046	0.014
5	5		0.146	0.087	0.057	0.017
6	6		0.171	0.104	0.068	0.020
7	7		0.195	0.119	0.078	0.022
8	8		0.215	0.132	0.087	0.024

[a] Concentrations were determined by analysing ^{1}H NMR spectra of crude reaction mixture relative to the internal standard TTMSM. The variation in observed concentrations is ±1%. Concentration (M) = mmol/ mL unless otherwise stated.

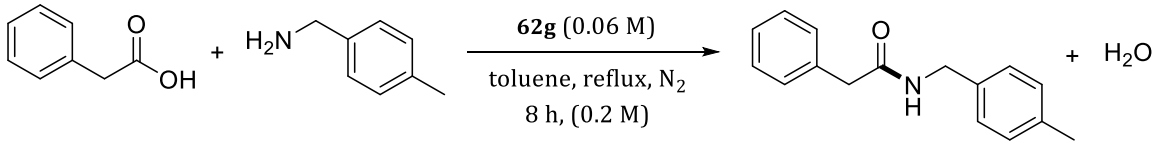
Table 6. Catalytic/Background Model Amidation Reactions for Concentration vs Time Plots



Entry	Time (h)	Concentration of Amide (M) [a]			
		1:1 Background		**1:1 Catalytic**	
		[Acid]	0.3 M	0.2 M	0.3 M	0.2 M
		[Amine]	0.3 M	0.2 M	0.3 M	0.2 M
		[**62g**]			0.06 M	0.06 M
1	1		0.016	0.011	0.036	0.104
2	2		0.033	0.022	0.067	0.154
3	3		0.051	0.034	0.094	0.176
4	4		0.069	0.046	0.118	0.188
5	5		0.087	0.057	0.138	0.195
6	6		0.104	0.068	0.155	0.200
7	7		0.119	0.078	0.170	
8	8		0.132	0.087	0.183	

[a] Concentrations were determined by analysing ^{1}H NMR spectra of crude reaction mixture relative to the internal standard TTMSM. The variation in observed concentrations is ±2%. Concentration (M) = mmol/ mL unless otherwise stated.

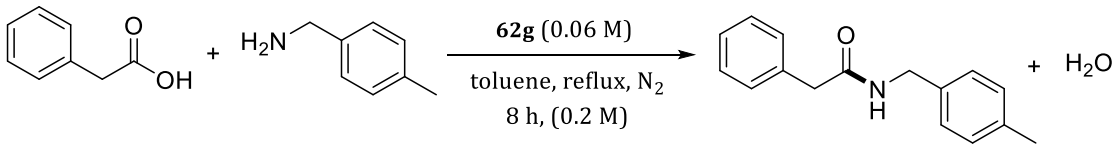
Table 7. Catalytic Model Amidation Reaction with Added Products

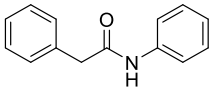
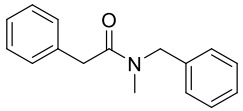
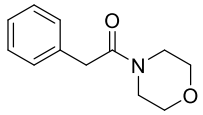


Entry	Time (h)	Concentration of Amide (M) [a]		
		Amide Added	**H_2O Added**	**Amide & H_2O Added**
		[Acid] 0.2 M	[Acid] 0.2 M	[Acid] 0.2 M
		[Amine] 0.2 M	[Amine] 0.2 M	[Amine] 0.2 M
		[**62g**] 0.06 M	[**62g**] 0.06 M	[**62g**] 0.06 M
		[Amide] 0.1 M	H_2O 0.1 M	H_2O 0.1 M
				[Amide] 0.1 M
1	1	0.125	0.025	0.122
2	2	0.144	0.055	0.140
3	3	0.161	0.079	0.160
4	4	0.181	0.102	0.176
5	5	0.199	0.118	0.196
6	6	0.214	0.133	0.210
7	7	0.228	0.144	0.222
8	8	0.238	0.155	0.231

[a] Concentrations were determined by analysing ^{1}H NMR spectra of crude reaction mixture relative to the internal standard TTMSM. The variation in observed concentrations is ±2%. Concentration (M) = mmol/ mL unless otherwise stated.

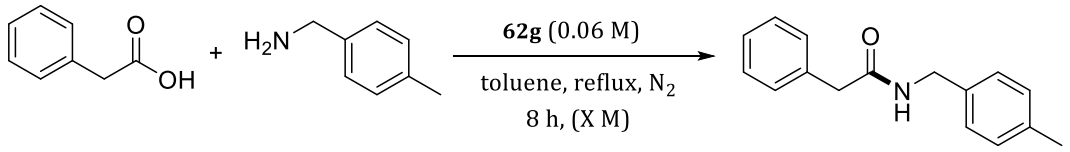
Table 8. Catalytic Model Amidation Reaction with Added 2^0 or 3^0 Amides



Entry	Time (h)	Concentration of Amide (M)					
		[Acid]	0.2 M	[Acid]	0.2 M	[Acid]	0.2 M
		[Amine]	0.2 M	[Amine]	0.2 M	[Amine]	0.2 M
		[**62g**]	0.06 M	[**62g**]	0.06 M	[**62g**]	0.06 M
		 [Amide]	0.1 M	 [Amide]	0.1 M	 [Amide]	0.1 M
1	1		0.017		0.013		0.006
2	2		0.032		0.024		0.014
3	3		0.046		0.034		0.022
4	4		0.056		0.042		0.030
5	5		0.064		0.049		0.037
6	6		0.073		0.055		0.044
7	7		0.079		0.059		0.052
8	8		0.084		0.063		0.058

[a] Concentrations were determined by analysing ^{1}H NMR spectra of crude reaction mixture relative to the internal standard TTMSM. The variation in observed concentrations is ±2%. Concentration (M) = mmol/ mL unless otherwise stated.

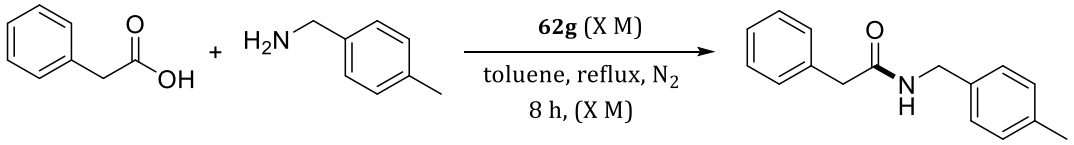
Table 9. Model Amidation Reaction with Different Stoichiometry of Acid/Amine



Entry	Time (h)	Concentration of Amide (M) [a]					
		Excess Acid			**Excess Amine**		
	[Acid]	0.3 M	0.3 M	0.25 M	0.2 M	0.2 M	0.15 M
	[Amine]	0.2 M	0.2 M	0.15 M	0.3 M	0.3 M	0.25 M
	[**62g**]		0.06 M	0.06 M		0.06 M	0.06 M
1	1	0.015	0.026	0.022	0.006	0.018	0.019
2	2	0.031	0.050	0.046	0.018	0.035	0.038
3	3	0.048	0.072	0.066	0.030	0.050	0.054
4	4	0.062	0.093	0.085	0.041	0.064	0.070
5	5	0.076	0.112	0.100	0.051	0.078	0.082
6	6	0.089	0.128	0.112	0.061	0.091	0.093
7	7	0.101	0.143	0.120	0.069	0.103	0.099
8	8	0.112	0.156	0.126	0.077	0.114	0.103

[a] Concentrations were determined by analysing ^{1}H NMR spectra of crude reaction mixture relative to the internal standard TTMSM. The variation in observed concentrations is ±1% for 'excess acid' and ±3% for 'excess amine' experiments. Concentration (M) = mmol/ mL unless otherwise stated.

Table 10. Model Amidation Reaction with Different Concentrations of Catalyst [62g]



Entry	Time (h)	Concentration of Amide (M) [a]		
		[Acid]	0.2 M	0.2 M	0.2 M
		[Amine]	0.2 M	0.2 M	0.2 M
		[**62g**]	0.06 M	0.03 M	0.045 M
1	1		0.104	0.022	0.030
2	2		0.154	0.041	0.058
3	3		0.176	0.059	0.084
4	4		0.188	0.075	0.108
5	5		0.195	0.090	0.128
6	6		0.200	0.103	0.145
7	7			0.114	0.160
8	8			0.123	0.170

[a] Concentrations were determined by analysing ^{1}H NMR spectra of crude reaction mixture relative to the internal standard TTMSM. The variation in observed concentrations is ±2%. Concentration (M) = mmol/ mL unless otherwise stated.

Table 11. Preparation of Calibration Solutions*

a) Catalyst **62g** or **62e** (30 mol%)/Durene

Entry	Catalyst remaining	part IS	part catalyst	vol (mL) IS	vol (mL) cat.	Conc. IS (mM)	Conc. cat. (mM)	Conc. ratio
1	100%	1	3	0.5	1.5	0.4545	1.3636	3
2	80%	1	2.4	0.5	1.2	0.5348	1.2834	2.4
3	60%	1	1.8	0.5	0.9	0.6494	1.1688	1.8
4	40%	1	1.2	0.5	0.6	0.8264	0.9917	1.2
5	20%	1	0.6	0.5	0.3	1.1364	0.6818	0.6

b) Catalyst **62g** or **62e** (10 mol%)/Durene

Entry	Catalyst remaining	part IS	part catalyst	vol (mL) IS	vol (mL) cat.	Conc. IS (mM)	Conc. cat. (mM)	Conc. ratio
1	100%	1	1	0.5	0.5	0.9091	0.9090	1
2	80%	1	0.8	0.5	0.4	1.0101	0.8080	0.8
3	60%	1	0.6	0.5	0.3	1.1364	0.6818	0.6
4	40%	1	0.4	0.5	0.2	1.2987	0.5194	0.4
5	20%	1	0.2	0.5	0.1	1.5152	0.3030	0.2

* All calibration solutions were prepared in MeCN and *i*PrOH.

Table 12. HPLC Calibration Data

a) Tris(*p*-bromophenyl)silanol **62g** (30 mol%)/Durene

Entry	Catalyst remaining	Conc. Ratio	Peak Area [a]		Peak Area Ratio
			Analyte (**62g**)	IS (Durene)	
1	20%	0.6	589701.06	206770.96	2.85195
2	40%	1.2	873429.19	150229.4	5.81396
3	60%	1.8	1041286.17	118688.08	8.77330
4	80%	2.4	1156628.33	100451.36	11.51431
5	100%	3	1239433.37	85486.47	14.49859

b) Tris(*p*-bromophenyl)silanol **62g** (10 mol%)/Durene

Entry	Catalyst remaining	Conc. Ratio	Peak Area [a]		Peak Area Ratio
			Analyte (**62g**)	IS (Durene)	
1	20%	0.2	307338.22	268795.06	1.14339
2	40%	0.4	512771.7	231889.36	2.21127
3	60%	0.6	653277.8	202722.39	3.22252
4	80%	0.8	742153.31	179957.49	4.12404
5	100%	1	838124.59	162890.44	5.14532

[a] Mobile phase: MeCN/H_2O 85 : 15, λ = 222 nm

c) Tris(*p*-fluorophenyl)silanol **62e** (30 mol%)/Durene

Entry	Catalyst remaining	Conc. Ratio	Peak Area [b]		Peak Area Ratio
			Analyte (**62e**)	IS (Durene)	
1	20%	0.6	343122.22	214173.43	1.60207
2	40%	1.2	486556.22	151626.74	3.20890
3	60%	1.8	578545.06	121961.53	4.74366
4	80%	2.4	652324.2	100786.72	6.47232
5	100%	3	694899.12	88751.56	7.82971

d) Tris(*p*-fluorophenyl)silanol **62e** (10 mol%)/Durene

Entry	Catalyst remaining	Conc. Ratio	Peak Area [b]		Peak Area Ratio
			Analyte (**62e**)	IS (Durene)	
1	20%	0.2	152658.22	291086.41	0.52444
2	40%	0.4	266701.23	259996.07	1.02578
3	60%	0.6	342007.04	223242.94	1.53199
4	80%	0.8	402657.52	196193.89	2.05234
5	100%	1	447204.85	174964.65	2.55597

[b] Mobile phase: MeCN/H_2O 70 : 30, λ = 222 nm

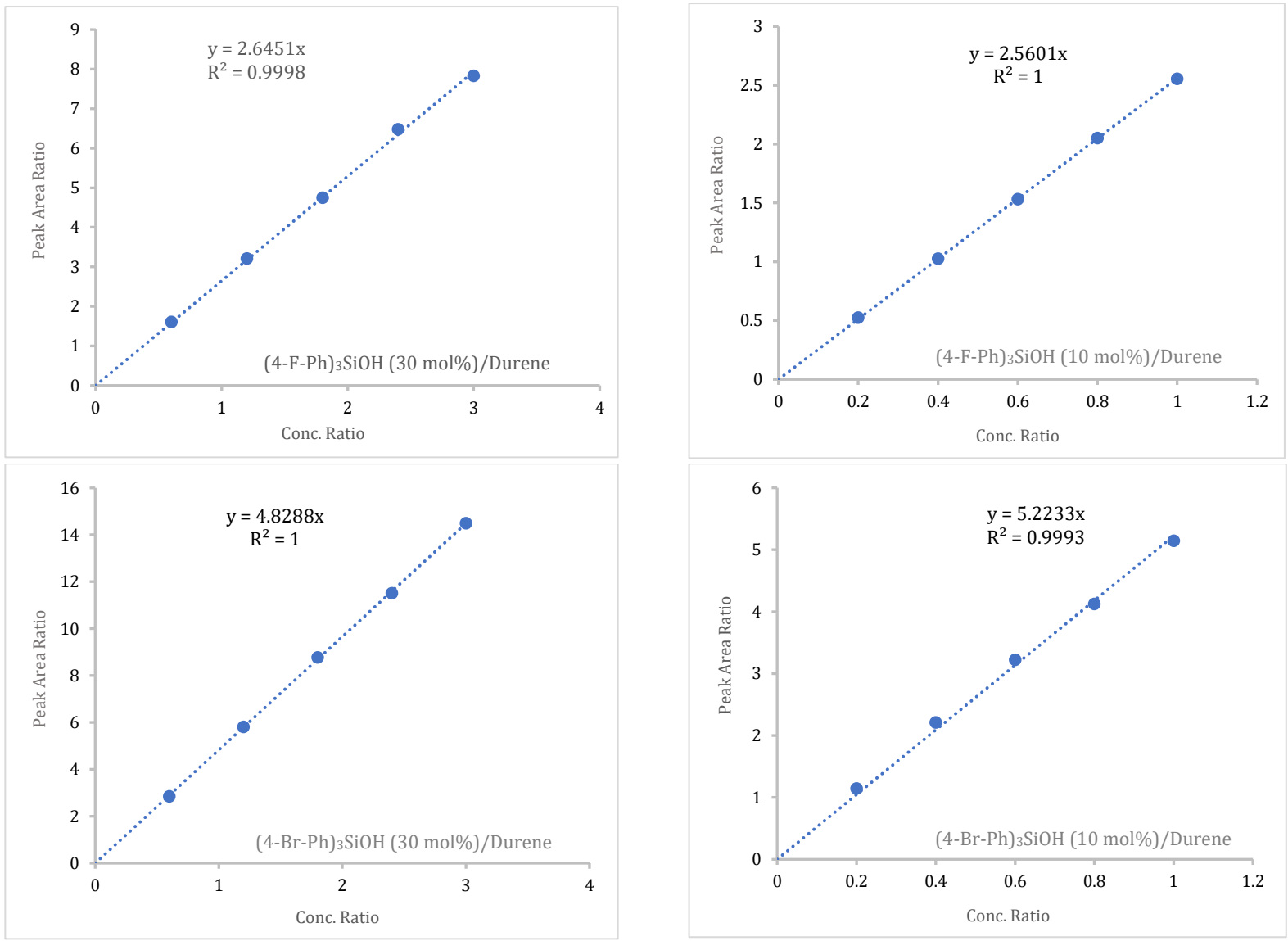
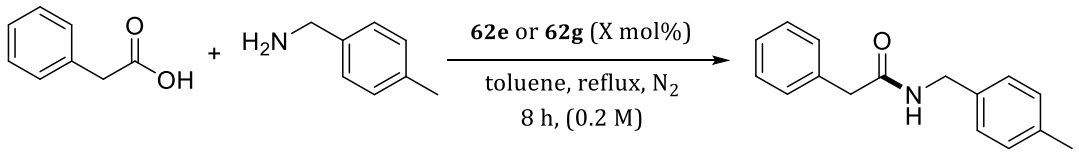


Figure 28. HPLC calibration curves.

Table 13. Quantification of [62e] and [62g] under Model Amidation Conditions



Entry	Time (h)	Catalyst Concentration (M) [a]					
		[Acid]	0.2 M	0.2 M	[Acid]	0.2 M	0.2 M
		[Amine]	0.2 M	0.2 M	[Amine]	0.2 M	0.2 M
		[**62e**]	30 mol%	10 mol%	[**62g**]	30 mol%	10 mol%
1	0		0.06	0.02		0.06	0.02
2	1		0.056	0.02		0.053	0.019
3	2		0.053	0.019		0.048	0.018
4	3		0.050	0.019		0.044	0.017
5	4		0.048	0.019		0.041	0.017
6	5		0.047	0.019		0.039	0.016
7	6		0.046	0.019		0.037	0.016
8	7		0.046	0.019		0.037	0.015
9	8		0.046	0.019		0.037	0.015

[a] Concentrations were determined by integrating peak area against the internal standard durene and by reference to a pre-determined calibration curve. The variation in observed concentrations is ±2%. Concentration (M) = mmol/ mL unless otherwise stated.

Table 14. Quantification of [62g] with Different Reaction Components of Model Amidation System

Entry	Time (h)	Concentration of [**62g**] (M) [a]			
		[Toluene]	0.2 M	0.2 M	0.2 M	0.2 M
		[Acid]		0.2 M		
		[Amine]			0.2 M	
		[Amide]				0.2 M
		[**62g**]	30 mol%	30 mol%	30 mol%	30 mol%
1	0		0.06 M	0.06 M	0.06 M	0.06 M
2	1		0.060	0.060	0.060	0.060
3	2		0.060	0.060	0.060	0.060
4	3		0.060	0.060	0.057	0.060
5	4		0.060	0.060	0.055	0.060
6	5		0.060	0.060	0.053	0.060
7	6		0.060	0.060	0.052	0.060
8	7		0.060	0.060	0.050	0.060
9	8		0.060	0.060	0.049	0.060

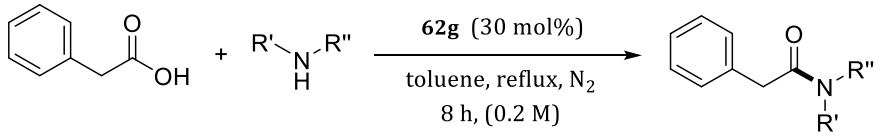
[a] Concentrations were determined by integrating peak area against the internal standard durene and by reference to a pre-determined calibration curve. The variation in observed concentrations is ±2%. Concentration (M) = mmol/ mL unless otherwise stated.

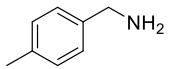
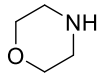
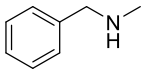
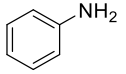
Table 15. Quantification of [62g] with Representative Primary, Secondary cyclic, Secondary acyclic and Aryl Amines

Entry	Time (h)	Concentration of [**62g**] (M) [a]			
		[Toluene]	0.2 M	0.2 M	0.2 M	0.2 M
		[4-Methylbenzylamine]	0.2 M			
		[Morpholine]		0.2 M		
		[*N*-Methylbenzylamine]			0.2 M	
		[Aniline]				0.2 M
		[**62g**]	30 mol%	30 mol%	30 mol%	30 mol%
1	0		0.06 M	0.06 M	0.06 M	0.06 M
2	1		0.060	0.060	0.059	0.059
3	2		0.060	0.059	0.055	0.058
4	3		0.057	0.058	0.052	0.058
5	4		0.055	0.056	0.049	0.058
6	5		0.053	0.055	0.046	0.058
7	6		0.052	0.054	0.044	0.058
8	7		0.050	0.053	0.043	0.058
9	8		0.049	0.052	0.041	0.058

[a] Concentrations were determined by integrating peak area against the internal standard durene and by reference to a pre-determined calibration curve. The variation in observed concentrations is ±2%. Concentration (M) = mmol/ mL unless otherwise stated.

Table 16. Quantification of [62g] with Representative Amines under Catalytic Amidation Conditions



Entry	Time (h)	Concentration of [**62g**] (M) [a]							
		[Acid]	0.2 M	[Acid]	0.2 M	[Acid]	0.2 M	[Acid]	0.2 M
		 [Amine]	0.2 M	 [Amine]	0.2 M	 [Amine]	0.2 M	 [Amine]	0.2 M
		[**62g**]	30 mol%	[**62g**]	30 mol%	[**62g**]	30 mol%	[**62g**]	30 mol%
1	0		0.06		0.06		0.06		0.06
2	1		0.053		0.049		0.049		0.055
3	2		0.048		0.042		0.043		0.053
4	3		0.044		0.039		0.039		0.052
5	4		0.041		0.036		0.036		0.052
6	5		0.038		0.034		0.033		0.052
7	6		0.037		0.033		0.031		0.052
8	7		0.036		0.031		0.030		0.052
9	8		0.036		0.030		0.029		0.052

[a] Concentrations were determined by integrating peak area against the internal standard durene and by reference to a pre-determined calibration curve. The variation in observed concentrations is ±2%. Concentration (M) = mmol/ mL unless otherwise stated.

References

1. (a) Chandrasekhar, V.; Boomishankar, R.; Nagendran, S. Recent Developments in the Synthesis and Structure of Organosilanols. *Chem. Rev.* **2004,** *104,* 5847-5910. DOI: 10.1021/cr0306135 (b) Jeon, M.; Han, J.; Park, J. Catalytic Synthesis of Silanols from Hydrosilanes and Applications. *ACS Catal.* **2012,** *2,* 1539-1549. DOI: 10.1021/cs300296x (c) Komiyama, T.; Minami, Y.; Hiyama, T. Recent Advances in Transition-Metal-Catalyzed Synthetic Transformations of Organosilicon Reagents. *ACS Catal.* **2017,** *7,* 631-651. DOI: 10.1021/acscatal.6b02374 (d) Boer, S. A.; Foyle, E. M.; Thomas, C. M.; White, N. G. Anion Coordination Chemistry using O–H Groups. *Chem. Soc. Rev.* **2019,** *48,* 2596-2614. DOI: 10.1039/C8CS00828K (e) Li, L.; Wei, Y.-L.; Xu, L.-W. Organosilicon-Mediated Organic Synthesis (SiMOS): A Personal Account. *Synlett* **2020,** *31,* 21-34. DOI: 10.1055/s-0039-1691496 (f) Yamagishi, H.; Shimokawa, J.; Yorimitsu, H. Utilization of Silanols in Transition Metal-Catalyzed Organic Synthesis. *ACS Catal.* **2023,** *13,* 7472-7487. DOI: 10.1021/acscatal.3c01504

2. (a) Tran, N. T.; Min, T.; Franz, A. K. Silanediol Hydrogen Bonding Activation of Carbonyl Compounds. *Chem. Eur. J.* **2011,** *17,* 9897-9900. DOI: 10.1002/chem.201101492 (b) Schafer, A. G.; Wieting, J. M.; Mattson, A. E. Silanediols: A New Class of Hydrogen Bond Donor Catalysts. *Org. Lett.* **2011,** *13,* 5228-5231. DOI: 10.1021/ol2021115 (c) Tran, N. T.; Wilson, S. O.; Franz, A. K. Cooperative Hydrogen-Bonding Effects in Silanediol Catalysis. *Org. Lett.* **2012,** *14,* 186-189. DOI: 10.1021/ol202971m (d) Min, T.; Fettinger, J. C.; Franz, A. K. Enantiocontrol with a Hydrogen-Bond Directing Pyrrolidinylsilanol Catalyst. *ACS Catal.* **2012,** *2,* 1661-1666. DOI: 10.1021/cs300290j (e) Schafer, A. G.; Wieting, J. M.; Fisher, T. J.; Mattson, A. E. Chiral Silanediols in Anion-Binding Catalysis. *Angew. Chem. Int. Ed.* **2013,** *52,* 11321-11324. DOI: 10.1002/ange.201305496 (f) Diemoz, K. M.; Wilson, S. O.; Franz, A. K. Synthesis of Structurally Varied 1,3-

Disiloxanediols and Their Activity as Anion-Binding Catalysts. *Chem. Eur. J.* **2016,** *22,* 18349-18353. DOI: 10.1002/chem.201604103

3. (a) Denmark, S. E.; Regens, C. S. Palladium-Catalyzed Cross-Coupling Reactions of Organosilanols and Their Salts: Practical Alternatives to Boron- and Tin-Based Methods. *Acc. Chem. Res.* **2008,** *41,* 1486-1499. DOI: 10.1021/ar800037p (b) Denmark, S. E. The Interplay of Invention, Discovery, Development, and Application in Organic Synthetic Methodology: A Case Study. *J. Org. Chem.* **2009,** *74,* 2915-2927. DOI: 10.1021/jo900032x (c) Nakao, Y.; Hiyama, T. Silicon-based Cross-Coupling Reaction: An Environmentally Benign Version. *Chem. Soc. Rev.* **2011,** *40,* 4893-4901. DOI: 10.1039/C1CS15122C (d) Sore, H. F.; Galloway, W. R.; Spring, D. R. Palladium-Catalysed Cross-Coupling of Organosilicon Reagents. *Chem. Soc. Rev.* **2012,** *41,* 1845-1866. DOI: 10.1039/C1CS15181A (e) Denmark, S. E.; Ambrosi, A. Why You Really Should Consider using Palladium-Catalyzed Cross-Coupling of Silanols and Silanolates. *Org. Process Res. Dev.* **2015,** *19,* 982-994. DOI: 10.1021/acs.oprd.5b00201

4. (a) Parasram, M.; Gevorgyan, V. Silicon-Tethered Strategies for C–H Functionalization Reactions. *Acc. Chem. Res.* **2017,** *50,* 2038-2053. DOI: 10.1021/acs.accounts.7b00306 (b) Sambiagio, C.; Schönbauer, D.; Blieck, R.; Dao-Huy, T.; Pototschnig, G.; Schaaf, P.; Wiesinger, T.; Zia, M. F.; Wencel-Delord, J.; Besset, T. A Comprehensive Overview of Directing Groups Applied in Metal-Catalysed C–H Functionalisation Chemistry. *Chem. Soc. Rev.* **2018,** *47,* 6603-6743. DOI: 10.1039/C8CS00201K (c) Usman, M.; Zhang, X.-W.; Liu, W.-B. Silicon-Tethered Frameworks as Directing Groups for Carbon–Carbon and Carbon–Heteroatom Bond Formation. *Synthesis* **2019,** *51,* 1529-1544. DOI: 10.1055/s-0037-1612123

5. (a) Franz, A. K.; Wilson, S. O. Organosilicon Molecules with Medicinal Applications. *J. Med. Chem.* **2013,** *56,* 388-405. DOI: 10.1021/jm3010114 (b) Ramesh, R.; Reddy, D. S. Quest for Novel Chemical Entities through

Incorporation of Silicon in Drug Scaffolds. *J. Med. Chem.* **2017,** *61,* 3779-3798. DOI: 10.1021/acs.jmedchem.7b00718

6. (a) Ueno, S.; Hartwig, J. F. Direct, Iridium-Catalyzed Enantioselective and Regioselective Allylic Etherification with Aliphatic Alcohols. *Angew. Chem. Int. Ed.* **2008,** *47,* 1928-1931. DOI: 10.1002/anie.200705267 (b) Ye, F.; Zheng, Z. J.; Li, L.; Yang, K. F.; Xia, C. G.; Xu, L. W. Development of a Novel Multifunctional N, P Ligand for Highly Enantioselective Palladium-Catalyzed Asymmetric Allylic Etherification of Alcohols and Silanols. *Chem. Eur. J.* **2013,** *19,* 15452-15457. DOI: 10.1002/chem.201303233 (c) Bellini, R.; Magre, M.; Biosca, M.; Norrby, P.-O.; Pamies, O.; Dieguez, M.; Moberg, C. Conformational Preferences of a Tropos Biphenyl Phosphinooxazoline–a Ligand with Wide Substrate Scope. *ACS Catal.* **2016,** *6,* 1701-1712. DOI: 10.1021/acscatal.5b02766 (d) Liu, H.-L.; Xie, M.-S.; Qu, G.-R.; Guo, H.-M. Organocatalytic Enantioselective Allylic Etherification of Morita–Baylis–Hillman Carbonates and Silanols. *J. Org. Chem.* **2016,** *81,* 10035-10042. DOI: 10.1021/acs.joc.6b01931 (e) Xia, Z.; Hu, J.; Shen, Z.; Wan, X.; Yao, Q.; Lai, Y.; Gao, J.-M.; Xie, W. Enantioselective Bromo-oxycyclization of Silanol. *Org. Lett.* **2016,** *18,* 80-83. DOI: 10.1021/acs.orglett.5b03303

7. (a) Kang, D.; Park, S.; Ryu, T.; Lee, P. H. Gold-Catalyzed Hydrosilyloxylation Driving Tandem Aldol and Mannich Reactions. *Org. Lett.* **2012,** *14,* 3912-3915. DOI: 10.1021/ol301660f (b) Han, Z.-Y.; Chen, D.-F.; Wang, Y.-Y.; Guo, R.; Wang, P.-S.; Wang, C.; Gong, L.-Z. Hybrid Metal/Organo Relay Catalysis Enables Enynes to be Latent Dienes for Asymmetric Diels–Alder Reaction. *J. Am. Chem. Soc.* **2012,** *134,* 6532-6535. DOI: 10.1021/ja3007148 (c) Li, N.; Chen, D.-F.; Wang, P.-S.; Han, Z.-Y.; Gong, L.-Z. Relay Catalytic Cascade Hydrosiloxylation and Asymmetric Hetero-Diels–Alder Reaction. *Synthesis* **2014,** *46,* 1355-1361. DOI: 10.1055/s-0033-1340905 (d) Wu, X.; Li, M.-L.; Wang, P.-S. Hybrid Gold/Chiral Brønsted Acid Relay

Catalysis Allows an Enantioselective Synthesis of (−)-5-*epi*-Eupomatilone-6. *J. Org. Chem.* **2014,** *79*, 419-425. DOI: 10.1021/jo4024232

8. (a) Guo, Y.; Liu, M.-M.; Zhu, X.; Zhu, L.; He, C. Catalytic Asymmetric Synthesis of Silicon-Stereogenic Dihydrodibenzosilines: Silicon Central-to-Axial Chirality Relay. *Angew. Chem. Int. Ed.* **2021**, *60*, 13887–13891. DOI: 10.1002/anie.202103748 (b) Zhang, H.; Zhao, D. Synthesis of Silicon-Stereogenic Silanols Involving Iridium-Catalyzed Enantioselective C–H Silylation Leading to a New Ligand Scaffold. *ACS Catal.* **2021,** *11*, 10748-10753. DOI: 10.1021/acscatal.1c03112 (c) Yuan, W.; Zhu, X.; Xu, Y.; He, C. Synthesis of Si-Stereogenic Silanols by Catalytic Asymmetric Hydrolytic Oxidation. *Angew. Chem. Int. Ed.* **2022,** *61*, e202204912. DOI: 10.1002/anie.202204912 (d) Gao, J.; He, C. Chiral Silanols: Strategies and Tactics for Their Synthesis. *Chem. Eur. J.* **2023,** *29*, e202203475. DOI: 10.1002/chem.202203475

9. For selected recent reviews see: (a) Lanigan, R. M.; Sheppard, T. D. Recent Developments in Amide Synthesis: Direct Amidation of Carboxylic Acids and Transamidation Reactions. *Eur. J. Org. Chem.* **2013,** 7453-7465. DOI: 10.1002/ejoc.201300573 (b) de Figueiredo, R. M.; Suppo, J.-S.; Campagne, J.-M. Nonclassical Routes for Amide Bond Formation. *Chem. Rev.* **2016,** *116*, 12029-12122. DOI: 10.1021/acs.chemrev.6b00237 (c) Ojeda-Porras, A.; Gamba-Sanchez, D. Recent Developments in Amide Synthesis using Nonactivated Starting Materials. *J. Org. Chem.* **2016,** *81*, 11548-11555. DOI: 10.1021/acs.joc.6b02358 (d) Muramatsu, W.; Hattori, T.; Yamamoto, H. Game Change from Reagent-To Substrate-Controlled Peptide Synthesis. *Bull. Chem. Soc. Jpn.* **2020,** *93*, 759-767. DOI: 10.1246/bcsj.20200057 (e) Santos, A. S.; Silva, A. M.; Marques, M. M. B. Sustainable Amidation Reactions – Recent Advances. *Eur. J. Org. Chem.* **2020,** *2020*, 2501-2516. DOI: 10.1002/ejoc.202000106 (f) Massolo, E.; Pirola, M.; Benaglia, M. Amide bond formation strategies: Latest Advances on a Dateless Transformation. *Eur. J. Org. Chem.* **2020,** *2020*, 4641-4651. DOI: 10.1002/ejoc.202000080 (g) Pedrood, K.; Bahadorikhalili,

S.; Lotfi, V.; Larijani, B.; Mahdavi, M. Catalytic and Non-Catalytic Amidation of Carboxylic Acid Substrates. *Mol. Divers.* **2021**, *26*, 1311-1344. DOI: 10.1007/s11030-021-10252-0 (h) Muramatsu, W.; Hattori, T.; Yamamoto, H. Amide Bond Formation: Beyond the Dilemma between Activation and Racemisation. *Chem. Commun.* **2021,** *57*, 6346-6359. DOI: 10.1039/D1CC01795K

10. (a) Constable, D. J.; Dunn, P. J.; Hayler, J. D.; Humphrey, G. R.; Leazer Jr, J. L.; Linderman, R. J.; Lorenz, K.; Manley, J.; Pearlman, B. A.; Wells, A. Key Green Chemistry Research Areas—A Perspective From Pharmaceutical Manufacturers. *Green Chem.* **2007,** *9*, 411-420. DOI: 10.1039/B703488C (b) Bryan, M. C.; Dunn, P. J.; Entwistle, D.; Gallou, F.; Koenig, S. G.; Hayler, J. D.; Hickey, M. R.; Hughes, S.; Kopach, M. E.; Moine, G. Key Green Chemistry Research Areas From A Pharmaceutical Manufacturers' Perspective Revisited. *Green Chem.* **2018,** *20*, 5082-5103. DOI: 10.1039/C8GC01276H

11. (a) Allen, C. L.; Williams, J. M. Metal-Catalysed Approaches to Amide Bond Formation. *Chem. Soc. Rev.* **2011,** *40*, 3405-3415. DOI: 10.1039/C0CS00196A (b) Pattabiraman, V. R.; Bode, J. W. Rethinking Amide Bond Synthesis. *Nature* **2011,** *480*, 471-479. DOI: 10.1038/nature10702 (c) Lundberg, H.; Tinnis, F.; Selander, N.; Adolfsson, H. Catalytic Amide Formation from Non-Activated Carboxylic Acids and Amines. *Chem. Soc. Rev.* **2014,** *43*, 2714-2742. DOI: 10.1039/C3CS60345H (d) Sabatini, M. T.; Boulton, L.; Sneddon, H. F.; Sheppard, T. D. A Green Chemistry Perspective on Catalytic Amide Bond Formation. *Nat. Catal.* **2019,** *2*, 10-17. DOI: 10.1038/s41929-018-0211-5 (e) Wang, X. Challenges and Outlook for Catalytic Direct Amidation Reactions. *Nature Catal.* **2019,** *2*, 98-102. DOI: 10.1038/s41929-018-0215-1 (f) Todorovic, M.; Perrin, D. M. Recent Developments in Catalytic Amide Bond Formation. *Peptide Science* **2020,** *112*, e24210. DOI: 10.1002/pep2.24210 (g) Taussat, A.; de Figueiredo, R.M.; Campagne, J.-M. Direct Catalytic

Amidations from Carboxylic Acid and Ester Derivatives: A Review. *Catalysts* **2023**, *13*, 366. DOI: 10.3390/catal13020366

12. Aryl and alkyl boronic and borinic acids, representative examples: (a) Ishihara, K.; Ohara, S.; Yamamoto, H. 3, 4, 5-Trifluorobenzeneboronic Acid as an Extremely Active Amidation Catalyst. *J. Org. Chem.* **1996,** *61*, 4196-4197. DOI: 10.1021/jo9606564 (b) Maki, T.; Ishihara, K.; Yamamoto, H. New Boron(III)-Catalyzed Amide and Ester Condensation Reactions. *Tetrahedron* **2007,** *63*, 8645-8657. DOI: 10.1016/j.tet.2007.03.157 (c) Arnold, K.; Batsanov, A. S.; Davies, B.; Whiting, A. Synthesis, Evaluation and Application of Novel Bifunctional *N,N*-di-isopropylbenzylamineboronic Acid Catalysts for Direct Amide Formation between Carboxylic Acids and Amines. *Green Chem.* **2008,** *10*, 124-134. DOI: 10.1039/B712008G (d) Al-Zoubi, R. M.; Marion, O.; Hall, D. G. Direct and Waste-Free Amidations and Cycloadditions by Organocatalytic Activation of Carboxylic Acids at Room Temperature. *Angew. Chem., Int. Ed.* **2008,** *47*, 2876-2879. DOI: 10.1002/anie.200705468 (e) Gernigon, N.; Al-Zoubi, R. M.; Hall, D. G. Direct Amidation of Carboxylic Acids Catalyzed by *ortho*-iodo Arylboronic Acids: Catalyst Optimization, Scope, and Preliminary Mechanistic Study Supporting a Peculiar Halogen Acceleration Effect. *J. Org. Chem.* **2012,** *77*, 8386-8400. DOI: 10.1021/jo3013258 (f) Gernigon, N.; Zheng, H.; Hall, D. G. Solid-Supported *ortho*-iodoarylboronic Acid Catalyst for Direct Amidation of Carboxylic Acids. *Tetrahedron Lett.* **2013,** *54*, 4475-4478. DOI: 10.1016/j.tetlet.2013.06.043 (g) Yamashita, R.; Sakakura, A.; Ishihara, K. Primary Alkylboronic Acids as Highly Active Catalysts for the Dehydrative Amide Condensation of α-Hydroxycarboxylic Acids. *Org. Lett.* **2013,** *15*, 3654-3657. DOI: 10.1021/ol401537f (h) Fatemi, S.; Gernigon, N.; Hall, D. G. A Multigram-Scale Lower E-Factor Procedure for MIBA-Catalyzed Direct Amidation and its Application to the Coupling of Alpha and Beta Aminoacids. *Green Chem.* **2015,** *17*, 4016-4028. DOI: 10.1039/C5GC00659G (i) Tam, E. K. W.; Liu, L. Y.; Chen, A. 2-Furanylboronic Acid as an Effective Catalyst

for the Direct Amidation of Carboxylic Acids at Room Temperature. *Eur. J. Org. Chem.* **2015,** *2015,* 1100-1107. DOI: 10.1002/ejoc.201403468 (j) Mohy El Dine, T.; Erb, W.; Berhault, Y.; Rouden, J.; Blanchet, J. Catalytic Chemical Amide Synthesis at Room Temperature: One more Step toward Peptide Synthesis. *J. Org. Chem.* **2015,** *80,* 4532-4544. DOI: 10.1021/acs.joc.5b00378 (k) El Dine, T. M.; Rouden, J.; Blanchet, J. Borinic acid Catalysed Peptide Synthesis. *Chem. Commun.* **2015,** *51,* 16084-16087. DOI: 10.1039/C5CC06177F (l) Ishihara, K.; Lu, Y. Boronic Acid–DMAPO Cooperative Catalysis for Dehydrative Condensation between Carboxylic Acids and Amines. *Chem. Sci.* **2016,** *7,* 1276-1280. DOI: 10.1039/C5SC03761A (m) Lu, Y.; Wang, K.; Ishihara, K. Design of Boronic Acid–Base Complexes as Reusable Homogeneous Catalysts in Dehydrative Condensations between Carboxylic Acids and Amines. *Asian J. Org. Chem.* **2017,** *6,* 1191-1194. DOI: 10.1002/ajoc.201700194 (n) Wang, K.; Lu, Y.; Ishihara, K. The *ortho*-Substituent on 2,4-bis(trifluoromethyl)phenylboronic Acid Catalyzed Dehydrative Condensation between Carboxylic Acids and Amines. *Chem. Commun.* **2018,** *54,* 5410-5413. DOI: 10.1039/C8CC02558D (o) Du, Y.; Barber, T.; Lim, S. E.; Rzepa, H. S.; Baxendale, I. R.; Whiting, A. A Solid-Supported Arylboronic Acid Catalyst for Direct Amidation. *Chem. Commun.* **2019,** *55,* 2916-2919. DOI: 10.1039/C8CC09913H (p) Al-Zoubi, R. M.; Al-Jammal, W. K.; McDonald, R. Regioselective Synthesis of *ortho*-iodobiphenylboronic Acid Derivatives: A Superior Catalyst for Carboxylic Acid Activation. *New J. Chem.* **2020,** *44,* 3612-3623. DOI: 10.1039/C9NJ05708K (q) Zhou, J.; Paladino, M. Hall, D. G. Direct Boronic Acid Promoted Amidation of Carboxylic Acids with Poorly Nucleophilic Amines. *Eur. J. Org. Chem.* **2022,** e202201050. DOI: 10.1002/ejoc.202201050 (r) Pan, B.; Huang, D.-M; Sun, H.-T.; Song, S.-N. Su, X.-B. Heterocyclic Boron Acid Catalyzed Dehydrative Amidation of Aliphatic/Aromatic Carboxylic Acids with Amines. *J. Org. Chem.* **2023,** *88,* 2832-2840. DOI: 10.1021/acs.joc.2c02515

13. Boric acid, representative examples: (a) Tang, P. Boric Acid Catalyzed Amide Formation from Carboxylic Acids and Amines: N-Benzyl-4-phenylbutyramide. *Org. Synth.* **2003,** *81,* 262-272. DOI: 10.1002/0471264229.os081.28 (b) Anderson, J. E.; Davis, R.; Fitzgerald, R. N.; Haberman, J. M. Selective Phenol Alkylation: An Improved Preparation of Efaproxiral. *Synth. Commun.* **2006,** *36,* 2129-2133. DOI: 10.1080/00397910600636527 (c) Mylavarapu, R. K.; Gcm, K.; Kolla, N.; Veeramalla, R.; Koilkonda, P.; Bhattacharya, A.; Bandichhor, R. Boric acid Catalyzed Amidation in the Synthesis of Active Pharmaceutical Ingredients. *Org. Process Res. Dev.* **2007,** *11,* 1065-1068. DOI: 10.1021/op700098w (d) Janvier, M.; Moebs-Sanchez, S.; Popowycz, F. Bio-Based Amides from Renewable Isosorbide by a Direct and Atom-Economic Boric Acid Amidation Methodology. *Eur. J. Org. Chem.* **2016,** *2016,* 2308-2318. DOI: 10.1002/ejoc.201600186 (e) Yun, F.; Cheng, C.; Zhang, J.; Li, J.; Liu, X.; Xie, R.; Tang, P.; Yuan, Q. Boric Acid Catalyzed Direct Amidation between Amino-Azaarenes and Carboxylic Acids. *Synthesis* **2017,** *49* , 1583-1596. DOI: 10.1055/s-0036-1588126

14. Boronates, recent representative examples: (a) Sabatini, M. T.; Boulton, L. T.; Sheppard, T. D. Borate Esters: Simple Catalysts for the Sustainable Synthesis of Complex Amides. *Sci. Adv.* **2017,** *3,* e1701028. DOI: 10.1126/sciadv.1701028 (b) Sabatini, M. T.; Karaluka, V.; Lanigan, R. M.; Boulton, L. T.; Badland, M.; Sheppard, T. D. Protecting-Group-Free Amidation of Amino Acids Using Lewis Acid Catalysts. *Chem. Eur. J.* **2018,** *24,* 7033-7043. DOI: 10.1002/chem.201800372 (c) Ghorpade, S. A.; Sawant, D. N.; Sekar, N. Triphenyl Borate Catalyzed Synthesis of Amides from Carboxylic Acids and Amines. *Tetrahedron* **2018,** *74,* 6954-6958. DOI: 10.1016/j.tet.2018.10.030 (d) Coomber, C. E.; Laserna, V.; Martin, L. T.; Smith, P. D.; Hailes, H. C.; Porter, M. J.; Sheppard, T. D. Catalytic Direct Amidations in tert-Butyl Acetate Using $B(OCH_2CF_3)_3$. *Org. Biomol. Chem.* **2019,** *17,* 6465-6469. DOI: 10.1039/C9OB01012B

15. B_3NO_2 heterocycles, diborons, diboronic acids and anhydrides, representative examples: (a) Noda, H.; Furutachi, M.; Asada, Y.; Shibasaki, M.; Kumagai, N. Unique Physicochemical and Catalytic Properties Dictated by the B_3NO_2 Ring System. *Nat. Chem.* **2017,** *9,* 571-577. DOI: 10.1038/nchem.2708 (b) Liu, Z.; Noda, H.; Shibasaki, M.; Kumagai, N. Catalytic Oligopeptide Synthesis. *Org. Lett.* **2018,** *20,* 612-615. DOI: 10.1021/acs.orglett.7b03735 (c) Sawant, D. N.; Bagal, D. B.; Ogawa, S.; Selvam, K.; Saito, S. Diboron-Catalyzed Dehydrative Amidation of Aromatic Carboxylic Acids with Amines. *Org. Lett.* **2018,** *20,* 4397-4400. DOI: 10.1021/acs.orglett.8b01480 (d) Opie, C. R.; Noda, H.; Shibasaki, M.; Kumagai, N. All Non-Carbon B_3NO_2 Exotic Heterocycles: Synthesis, Dynamics, and Catalysis. *Chem. Eur. J.* **2019,** *25,* 4648-4653. DOI: 10.1002/chem.201900715 (e) Shimada, N.; Hirata, M.; Koshizuka, M.; Ohse, N.; Kaito, R.; Makino, K. Diboronic Acid Anhydrides as Effective Catalysts for the Hydroxy-Directed Dehydrative Amidation of Carboxylic Acids. *Org. Lett.* **2019,** *21,* 4303-4308. DOI: 10.1021/acs.orglett.9b01484 (f) Michigami, K.; Sakaguchi, T.; Takemoto, Y. Catalytic Dehydrative Peptide Synthesis with *gem*-Diboronic Acids. *ACS Catal.* **2020,** *10,* 683-688. DOI: 10.1021/acscatal.9b03894 (g) Koshizuka, M.; Makino, K.; Shimada, N. Diboronic Acid Anhydride-Catalyzed Direct Peptide Bond Formation enabled by Hydroxy-Directed Dehydrative Condensation. *Org. Lett.* **2020,** *22,* 8658-8664. DOI: 10.1021/acs.orglett.0c03252

16. (a) Terada, Y.; Ieda, N.; Komura, K.; Sugi, Y. Multivalent Metal Salts as Versatile Catalysts for the Amidation of Long-Chain Aliphatic Acids with Aliphatic Amines. *Synthesis* **2008,** 2318-2320. DOI: 10.1055/s-2008-1067168 (b) Allen, C. L.; Chhatwal, A. R.; Williams, J. M. Direct Amide Formation from Unactivated Carboxylic Acids and Amines. *Chem. Commun.* **2012,** *48,* 666-668. DOI: 10.1039/C1CC15210F (c) Lundberg, H.; Tinnis, F.; Adolfsson, H. Titanium(IV) Isopropoxide as an Efficient Catalyst for Direct Amidation of Nonactivated Carboxylic Acids. *Synlett* **2012,** *23,* 2201-2204. DOI: 10.1055/s-0032-1316993 (d) Lundberg, H.; Tinnis, F.; Adolfsson, H. Direct Amide Coupling of Non-activated Carboxylic Acids and

Amines Catalysed by Zirconium(IV) Chloride. *Chem. Eur. J.* **2012,** *18,* 3822-3826. DOI: 10.1002/chem.201104055 (e) Tinnis, F.; Lundberg, H.; Adolfsson, H. Direct Catalytic Formation of Primary and Tertiary Amides from Non-Activated Carboxylic Acids, Employing Carbamates as Amine Source. *Adv. Synth. Catal.* **2012,** *354,* 2531-2536. DOI: 10.1002/adsc.201200436 (f) Lundberg, H.; Adolfsson, H. Hafnium-Catalyzed Direct Amide Formation at Room Temperature. *ACS Catal.* **2015,** *5,* 3271-3277. DOI: 10.1021/acscatal.5b00385 (g) Wang, Z.; Bao, X.; Xu, M.; Deng, Z.; Han, Y.; Wang, N. Direct Formation of Amides from Carboxylic Acids and Amines Catalyzed by Niobium(V) Oxalate Hydrate. *Chem. Select* **2018,** *3,* 2599-2603. DOI: 10.1002/slct.201800204 (h) Cheng, L.; Ge, X.; Huang, L. Direct amidation of Non-Activated Phenylacetic Acid and Benzylamine Derivatives Catalysed by $NiCl_2$. *R. Soc. Open Sci.* **2018,** *5,* 171870. DOI: 10.1098/rsos.171870 (i) Li, N.; Wang, L.; Zhang, L.; Zhao, W.; Qiao, J.; Xu, X.; Liang, Z. Air stable Bis(pentamethylcyclopentadienyl) Zirconium Perfluorooctanesulfonate as an Efficient and Recyclable Catalyst for the Synthesis of N-substituted Amides. *ChemCatChem* **2018,** *10,* 3532-3538. DOI: 10.1002/cctc.201800590 (j) De Azambuja, F.; Parac-Vogt, T. N. Water-tolerant and Atom Economical Amide Bond Formation by Metal-Substituted Polyoxometalate Catalysts. *ACS Catal.* **2019,** *9,* 10245-10252. DOI: 10.1021/acscatal.9b03415 (k) Lundberg, H.; Tinnis, F.; Adolfsson, H. Zirconium Catalyzed Amide Formation without Water Scavenging. *Appl. Organomet. Chem.* **2019,** *33,* e5062. DOI: 10.1002/aoc.5062 (l) Muramatsu, W.; Yamamoto, H. Tantalum-Catalyzed Amidation of Amino Acid Homologues. *J. Am. Chem. Soc.* **2019,** *141,* 18926-18931. DOI: 10.1021/jacs.9b08415 (m) Muramatsu, W.; Hattori, T.; Yamamoto, H. Substrate-Directed Lewis-Acid Catalysis for Peptide Synthesis. *J. Am. Chem. Soc.* **2019,** *141,* 12288-12295. DOI: 10.1021/jacs.9b03850 (n) Wang, H.; Dong, W.; Hou, Z.; Cheng, L.; Li, X.; Huang, L. Direct Amidation of Non-Activated Carboxylic Acid and Amine Derivatives Catalyzed by $TiCp_2Cl_2$. *Appl. Organomet. Chem.*

2020, *34*, e5568. DOI: 10.1002/aoc.5568 (o) Ali, M. A.; Nath, A.; Jannat, M.; Islam, M. M. Direct Synthesis of Diamides from Dicarboxylic Acids with Amines Using Nb_2O_5 as a Lewis Acid Catalyst and Molecular Docking Studies as Anticancer Agents. *ACS Omega* **2021,** *6*, 25002-25009. DOI: 10.1021/acsomega.1c04069 (p) Zhang, Y.; de Azambuja, F.; Parac-Vogt, T. N. Zirconium Oxo Clusters as Discrete Molecular Catalysts for the Direct Amide Bond Formation. *Catal. Sci. Technol.* **2022,** *12*, 3190-3201. DOI: 10.1039/D2CY00421F (q) Wang, A.; Xie, Y.; Wang, J.; Shi, D.; Yu, H. Atom-Economic Amide Synthesis by Using an Iron-substituted Polyoxometalate Catalyst. *Chem. Commun.* **2022,** *58*, 1127-1130. DOI: 10.1039/D1CC05417A

17. For recent representative examples see: (a) Lenstra, D. C.; Rutjes, F. P.; Mecinović, J. Triphenylphosphine-Catalysed Amide Bond Formation between Carboxylic Acids and Amines. *Chem. Commun.* **2014,** *50*, 5763-5766. DOI: 10.1039/C4CC01861C (b) Krause, T.; Baader, S.; Erb, B.; Goosen, L. J. Atom-Economic Catalytic Amide Synthesis from Amines and Carboxylic Acids Activated *in situ* with Acetylenes. *Nat. Commun.* **2016,** *7*, 1-7. DOI: 10.1038/ncomms11732 (c) Kothandapani, J.; Ganesan, A.; Ganesan, S. S. Nano-Magnetic Sulfonic Acid Catalyzed Facile Synthesis of Diverse Amide Derivatives. *Synthesis* **2017,** *49*, 685-692. DOI: 10.1055/s-0036-1588319 (d) Philpott, H. K.; Thomas, P. J.; Tew, D.; Fuerst, D. E.; Lovelock, S. L. A Versatile Biosynthetic Approach to Amide Bond Formation. *Green Chem.* **2018,** *20*, 3426-3431. DOI: 10.1039/C8GC01697F (e) Manova, D.; Gallier, F.; Tak-Tak, L.; Yotava, L.; Lubin-Germain, N. Lipase-Catalyzed Amidation of Carboxylic Acid and Amines. *Tetrahedron Lett.* **2018,** *59*, 2086-2090. DOI: 10.1016/j.tetlet.2018.04.049 (f) Potadar, S. M.; Mali, A. S.; Waghmode, K. T.; Chaturbhuj, G. U. Repurposing *n*-Butyl Stannoic Acid as Highly Efficient Catalyst for Direct Amidation of Carboxylic Acids with Amines. *Tetrahedron Lett.* **2018,** *59*, 4582-4586. DOI: 10.1016/j.tetlet.2018.11.036 (g) Srivastava, V.; Singh, P. K.; Singh, P. P. Visible Light Photoredox Catalysed Amidation of Carboxylic Acids with Amines. *Tetrahedron Lett.* **2019,** *60*, 40-43. DOI: 10.1016/j.tetlet.2018.11.050 (h) Handoko; Satishkumar, S.;

Panigrahi, N. R.; Arora, P. S. Rational Design of an Organocatalyst for Peptide Bond Formation. *J. Am. Chem. Soc.* **2019,** *141,* 15977-15985. DOI: 10.1021/jacs.9b07742 (i) Zarecki, A. P.; Kolanowski, J. L.; Markiewicz, W. T. Microwave-Assisted Catalytic Method for a Green Synthesis of Amides Directly from Amines and Carboxylic Acids. *Molecules* **2020,** *25,* 1761. DOI: 10.3390/molecules25081761 (j) Li, Z.; Liu, L.; Xu, K.; Huang, T.; Li, X.; Song, B.; Chen, T. Palladium-Catalyzed N-Acylation of Tertiary Amines by Carboxylic Acids: A Method for the Synthesis of Amides. *Org. Lett.* **2020,** *22,* 5517-5521. DOI: 10.1021/acs.orglett.0c01869 (k) Movahed, F. S.; Sawant, D. N.; Bagal, D. B.; Saito, S. Tris(*o*-phenylenedioxy)cyclotriphosphazene as a Promoter for the Formation of Amide Bonds between Aromatic Acids and Amines. *Synthesis* **2020,** *52,* 3253-3262. DOI: 10.1055/s-0040-1707174 (l) Wang, J.; Hou, H.; Hu, Y.; Lin, J.; Wu, M.; Zheng, Z.; Xu, X. Visible-Light-Induced Direct Construction of Amide Bond from Carboxylic Acids with Amines in Aqueous Solution. *Tetrahedron Lett.* **2021,** *65,* 152801. DOI: 10.1016/j.tetlet.2020.152801 (m) de Azambuja, F.; Loosen, A.; Conic, D.; van den Besselaar, M.; Harvey, J. N.; Parac-Vogt, T. N. En Route to a Heterogeneous Catalytic Direct Peptide Bond Formation by Zr-Based Metal–Organic Framework Catalysts. *ACS Catal.* **2021,** *11* , 7647-7658. DOI: 10.1021/acscatal.1c01782 (n) Handoko; Panigrahi, N. R.; Arora, P. S. Two-Component Redox Organocatalyst for Peptide Bond Formation. *J. Am. Chem. Soc.* **2022,** *144,* 3637-3643. DOI: 10.1021/jacs.1c12798 (o) Zhang, L.; Jiang, J.; Li, L.; Chen, Q.; Zhang, L.; Sun, H.; Li, C. Sustainable Synthesis of Amides from Carboxylic Acids and Equivalent Amounts of Amines Using a Reusable Bronsted Acidic Ionic Liquid as a Catalyst and a Solvent. *ACS Sustain. Chem. Eng.* **2022,** *10,* 8433-8442. DOI: 10.1021/acssuschemeng.2c01434 (p) Su, J.; Mo, J. N.; Chen, X.; Umanzor, A.; Zhang, Z.; Houk, K. N.; Zhao, J. Generation of Oxyphosphonium Ions by Photoredox/Cobaloxime Catalysis for Scalable Amide and Peptide Synthesis in Batch and Continuous-Flow. *Angew. Chem. Int. Ed.* **2022,** *134,* e202112668. DOI: 10.1002/anie.202112668

18. For representative examples see: (a) Chan, T. H.; Wong, L. T. L. Silicon Tetrachloride as a Coupling Reagent for Amide Formation. *J. Org. Chem.* **1969**, *34*, 2766-2767. DOI: 10.1021/jo01261a064 (b) Chou, W.-C.; Chou, M.-C.; Lu, Y.-Y.; Chen, S.-F. HMDS-Promoted *in situ* Amidation Reactions of Carboxylic Acids and Amines. *Tetrahedron Lett.* **1999**, *40*, 3419– 3422. DOI: 10.1016/S0040-4039(99)00505-5 (c) van Leeuwen, S. H.; Quaedflieg, P. J. L. M.; Broxterman, Q. B.; Liskamp, R. M. J. Synthesis of Amides from Unprotected Amino Acids by a Simultaneous Protection–Activation Strategy using Dichlorodialkyl Silanes. *Tetrahedron Lett.* **2002**, *43*, 9203-9207. DOI: 10.1016/S0040-4039(02)02275-X (d) Tozawa, T.; Yamane, Y.; Mukaiyama, T. A Convenient Method for Preparations of 1-Acylimidazoles and Carboxamides by using Novel Imidazolylsilane Derivatives. *Chem. Lett.* **2005**, *34*, 734-735. DOI: 10.1246/cl.2005.734 (e) Tozawa, T.; Yamane, Y.; Mukaiyama, T. An Effective Method for the Synthesis of Carboxamides by using Tetrakis(pyridine-2-yloxy)silane as a Mild Coupling Reagent. *Chem. Lett.* **2005**, *34*, 1334-1335. DOI: 10.1246/cl.2005.1334 (f) Tozawa, T.; Yamane, Y.; Mukaiyama, T. An Efficient Method for the Preparation of Carboxamides by Dehydration Condensation using Tetrakis(1,1,1,3,3,3-hexafluoro-2-propoxy)silane. *Chem. Lett.* **2005**, *34*, 1586-1587. DOI: 10.1246/cl.2005.1586 (g) Ruan, Z.; Lawrence, R. M.; Cooper, C. B. Phenylsilane as an Active Amidation Reagent for the Preparation of Carboxamides and Peptides. *Tetrahedron Lett.* **2006**, *47*, 7649-7651. DOI: 10.1016/j.tetlet.2006.08.024 (h) Aspin, S. J.; Taillemaud, S.; Cyr, P.; Charette, A. B. 9-Silafluorenyl Dichlorides as Chemically Ligating Coupling Agents and Their Application in Peptide Synthesis. *Angew. Chem., Int. Ed.* **2016**, *55*, 13833-13837. DOI: 10.1002/anie.201606120 (i) Sayes, M.; Charette, A. B. Diphenylsilane as a Coupling Reagent for Amide Bond Formation. *Green Chem.* **2017**, *19*, 5060-5064. DOI: 10.1039/C7GC02643A (j) Braddock, D. C.; Lickiss, P. D.; Rowley, B. C.; Pugh, D.; Purnomo, T.; Santhakumar, G.; Fussell, S. J. Tetramethyl Orthosilicate (TMOS) as a Reagent for Direct Amidation of Carboxylic Acids. *Org. Lett.* **2018**, *20*, 950-953. DOI: 10.1021/acs.orglett.7b03841 (k)

Morisset, E.; Chardon, A.; Rouden, J.; Blanchet, J. Phenysilane and Silicon Tetraacetate: Versatile Promotors for Amide Synthesis. *Eur. J. Org. Chem.* **2020,** 388-392. DOI: 10.1002/ejoc.201901660 (l) D'Amaral, M. C.; Jamkhou, N.; Adler, M. J. Efficient and Accessible Silane-Mediated Direct Amide Coupling of Carboxylic Acids and Amines. *Green Chem.* **2021,** *23,* 288-295. DOI: 10.1039/D0GC02833A (m) Muramatsu, W.; Yamamoto, H. Peptide Bond Formation of Amino Acids by Transient Masking with Silylating Reagents. *J. Am. Chem. Soc.* **2021,** *143,* 6792-6797. DOI: 10.1021/jacs.1c02600 (n) Braddock, D. C.; Davies, J. J.; Lickiss, P. D. Methyltrimethoxysilane (MTM) as a Reagent for Direct Amidation of Carboxylic Acids. *Org. Lett.* **2022,** *24,* 1175-1179. DOI: 10.1021/acs.orglett.1c04265 (o) Lainer, T.; Czerny, F.; Haas, M. Solvent-Free Amide Bond Formation Using a Variety of Methoxysilanes as Coupling Agent. *Org. Biomol. Chem.* **2022**, *20,* 3717. DOI: 10.1039/D2OB00589A

19. For representative examples see: (a) Comerford, J. W.; Clark, J. H.; Macquarrie, D. J.; Breeden, S. W. Clean, Reusable and Low Cost Heterogeneous Catalyst for Amide Synthesis. *Chem. Commun.* **2009**, 2562-2564. DOI: 10.1039/B901581G (b) Yang, X.-D.; Zeng, X.-H.; Zhao, Y.-H.; Wang, X.-Q.; Pan, Z.-Q.; Li, L.; Zhang, H.-B. Silica Gel-Mediated Amide Bond Formation: An Environmentally Benign Method for Liquid-Phase Synthesis and Cytotoxic Activities of Amides. *J. Comb. Chem.* **2010**, *12,* 307-310. DOI: 10.1021/cc900135f (c) Komura, K.; Nakano, Y.; Koketsu, M. Mesoporous Silica MCM-41 as a Highly Active, Recoverable and Reusable Catalyst for Direct Amidation of Fatty Acids and Long-Chain Amines. *Green Chem.* **2011**, *13,* 828-831. DOI: 10.1039/C0GC00673D (d) Ojeda-Porras, A.; Hernandez-Santana, A.; Gamba-Sanchez, D. Direct Amidation of Carboxylic Acids with Amines under Microwave Irradiation using Silica Gel as a Solid Support. *Green Chem.* **2015**, *17,* 3157-3163. DOI: 10.1039/C5GC00189G (e) Tamura, M.; Murase, D.; Komura, K. Direct Amide Synthesis from Equimolar Amounts of Carboxylic Acid and Amine Catalyzed by Mesoporous Silica SBA-15. *Synthesis* **2015**, *47,* 769-776. DOI: 10.1055/s-0034-1379966 (f) Tamura, M.; Murase, D.;

Komura, K. Mesoporous Silica Catalyzed the Direct Amidation of Palmitic Acid and Hexylamine and Unique Dependence of Reaction Rate on Pore Size with *p6mm* Topological Catalyst. *Chem. Lett.* **2016**, *45*, 451-453. DOI: 10.1246/cl.160049 (g) Zakharova, M. V.; Kleitz, F.; Fontaine, F.-G. Lewis Acidity Quantification and Catalytic Activity of Ti, Zr and Al-Supported Mesoporous Silica. *Dalton Trans.* **2017**, *46*, 3864-3876. DOI: 10.1039/C7DT00035A

20. For the use of a catalytic silicon entity used in conjunction with a stoichiometric silicon reagent see: (a) Muramatsu, W.; Manthena, C.; Nakashima, E.; Yamamoto, H. Peptide Bond-Forming Reaction via Amino Acid Silyl Esters: New Catalytic Reactivity of an Aminosilane. *ACS Catal.* **2020**, *10*, 9594-9603. DOI: 10.1021/acscatal.0c02512 (b) Muramatsu, W.; Yamamoto, H. Organocatalytic Activation of Inert Hydrosilane for Peptide Bond Formation. *Org. Lett.* **2022,** *24*, 7194-7199. DOI: 10.1021/acs.orglett.2c02947. For a review on stoichiometric silicon reagents for direct amidation see: (c) Davies, J. J.; Braddock, D. C.; Lickiss, P. D. Silicon Compounds as Stoichiometric Coupling Reagents for Direct Amidation. *Org. Biomol. Chem.* **2021**, *19*, 6746-6760. DOI: 10.1039/D1OB01003D

21. (a) Rowley, C. B. Silicon-containing Catalysts and Reagents for the Direct Amidation of Carboxylic acids. *Ph.D. Thesis,* Imperial College London, **2017**. DOI: 10.25560/78224 (b) Braddock, D. C.; Rowley, B. C.; Lickiss, P. D.; Fussell, S. J.; Qamar, R.; Pugh, D.; Rzepa, H. S.; White, A. J. On the Use of Triarylsilanols as Catalysts for Direct Amidation of Carboxylic Acids. *J. Org. Chem.* **2023,** *88*, 9853-9869. DOI: 10.1021/acs.joc.3c00585

22. Hansch, C.; Leo, A.; Taft, R. W. A Survey of Hammett Substituent Constants and Resonance and Field Parameters. *Chem. Rev.* **1991**, *91*, 165-195. DOI: 10.1021/cr00002a004

23. (a) Eaborn, C. Cleavages of Aryl-Silicon and Related Bonds by Electrophiles. *J. Organomet. Chem.* **1975**, *100*, 43-57. DOI: 10.1016/S0022-328X(00)88933-0 (b) Brook, M. A. Cleavage of Si-C Bonds. In *Silicon in*

Organic, Organometallic and Polymer Chemistry, ed.; Wiley, **2000**; pp 552-607. (c) Shirai, S.; Goto, Y., Mizoshita, N.; Ohashi, M.; Tani, T.; Shimada, T.; Hyodo, S.; Inagaki, S. Th eoretical Studies on Si−C Bond Cleavage in Organosilane Precursors during Polycondensation to Organosilica Hybrids. *J. Phys. Chem. A*, **2010**, *114*, 6047–6054. DOI: 10.1021/jp101242g (d) Reich, H. J. Mechanism of C-Si Bond Cleavage using Lewis Bases (n → σ*). In *Lewis Base Catalysis in Organic Synthesis*, ed.; Vol 1, Eds. Vedejs, E.; Denmark, S. E., **2016**, Chapter 8, pp. 233-280. DOI: 10.1002/9783527675142.ch8

24. (a) Ma, H.; Sun, D.; Zhang, L.; Wang, R.; Blatov, V. A.; Guo, J.; Sun, D. A "Strongly" Self-Catenated Metal–Organic Framework with the Highest Topological Density Among 3, 4-Coordinated Nets. *Inorg. Chem.* **2013,** *52*, 10732-10734. DOI: 10.1021/ic4018757 (b) Gary, D. C.; Glassy, B. A.; Cossairt, B. M. Investigation of Indium Phosphide Quantum Dot Nucleation and Growth Utilizing Triarylsilylphosphine Precursors. *Chem. Mater.* **2014,** *26*, 1734-1744. DOI: 10.1021/cm500102q (c) Sommer, L. H.; Lyons, J.-E. Stereochemistry of Asymmetric Silicon. XVI. Transition Metal Catalyzed Substitution Reactions of Optically Active Organosilicon Hydrides. *J. Am. Chem. Soc.* **1969,** *91*, 7061-7067. DOI: 10.1021/ja01053a028

25. Baker, K. V.; Brown, J. M.; Hughes, N.; Skarnulis, A. J.; Sexton, A. Mechanical Activation of Magnesium Turnings for the Preparation of Reactive Grignard Reagents. *J. Org. Chem.* **1991,** *56*, 698-703. DOI: 10.1021/jo00002a039

26. Hartmann, D.; Schädler, M.; Greb, L. Bis(catecholato)silanes: Assessing, Rationalizing and Increasing Silicon's Lewis Superacidity. *Chem. Sci.* **2019,** *10*, 7379-7388. DOI: 10.1039/C9SC02167A

27. Pedersen, D. S.; Rosenbohm, C. Dry Column Vacuum Chromatography. *Synthesis* **2001,** *2001*, 2431-2434. DOI: 10.1055/s-2001-18722

28. Chuit, C.; Corriu, R. J.; Reye, C.; Young, J. C. Reactivity of Penta- and Hexacoordinate Silicon Compounds and their Role as Reaction Intermediates. *Chem. Rev.* **1993,** *93,* 1371-1448. DOI: 10.1021/cr00020a003

29. Delmas, L. C.; Horton, P. N.; White, A. J.; Coles, S. J.; Lickiss, P. D.; Davies, R. P. Siloxane-Based Linkers in the Construction of Hydrogen Bonded Assemblies and Porous 3D MOFs. *Chem. Comm.* **2017,** *53,* 12524-12527. DOI: 10.1039/C7CC06022J

30. (a) Blackmond, D. G. Reaction Progress Kinetic Analysis: A Powerful Methodology for Mechanistic Studies of Complex Reactions. *Angew. Chem., Int. Ed.* **2005**, *44,* 4302-4320. DOI: 10.1002/anie.200462544 (b) Blackmond, D. G. Kinetic Profiling of Catalytic Organic Reactions as a Mechanistic Tool. *J. Am. Chem. Soc.* **2015,** *137,* 10852-10866. DOI: 10.1021/jacs.5b05841 (c) Nielsen, C. D.-T.; Burés, J. Visual Kinetic Analysis. *Chem. Sci.* **2019**, *10,* 348-353. DOI: 10.1039/C8SC04698K

31. (a) Mathew, J. S.; Klussmann, M.; Iwamura, H.; Valera, F.; Futran, A.; Emanuelsson, E. A.; Blackmond, D. G. Investigations of Pd-catalyzed ArX Coupling Reactions Informed by Reaction Progress Kinetic Analysis. *J. Org. Chem.* **2006,** *71,* 4711-4722. DOI: 10.1021/jo052409i (b) Zuend, S. J.; Jacobsen, E. N. Mechanism of Amido-Thiourea Catalyzed Enantioselective Imine Hydrocyanation: Transition State Stabilization via Multiple Non-Covalent Interactions. *J. Am. Chem. Soc.* **2009,** *131,* 15358-15374. DOI: 10.1021/ja9058958 (c) Devery III, J. J.; Conrad, J. C.; MacMillan, D. W.; Flowers, R. A. Mechanistic Complexity in Organo–SOMO Activation. *Angew. Chem. Int. Ed.* **2010,** *49,* 6106-6110. DOI: 10.1002/anie.201001673 (d) Baxter, R. D.; Sale, D.; Engle, K. M; Yu, J.-Q.; Blackmond, D. G. Mechanistic Rationalization of Unusual Kinetics in Pd-Catalyzed C–H Olefination. *J. Am. Chem. Soc.* **2012,** *134,* 10, 4600-4606. DOI: 10.1021/ja207634t (e) Ruiz-Castillo, P.; Blackmond, D. G.; Buchwald, S. L. Rational Ligand Design for the Arylation of Hindered Primary Amines Guided by Reaction Progress Kinetic Analysis. *J. Am. Chem. Soc.* **2015,** *137,* 3085-3092. DOI: 10.1021/ja512903g (f) Klausen, R. S.; Kennedy, C. R.; Hyde, A. M.; Jacobsen, E. N. Chiral Thioureas

Promote Enantioselective Pictet–Spengler Cyclization by Stabilizing Every Intermediate and Transition State in the Carboxylic Acid-Catalyzed Reaction. *J. Am. Chem. Soc.* **2017,** *139,* 12299-12309. DOI: 10.1021/jacs.7b06811 (g) Diemoz, K. M.; Hein, J. E.; Wilson, S. O.; Fettinger, J. C.; Franz, A. K. Reaction Progress Kinetics Analysis of 1,3-Disiloxanediols as Hydrogen-Bonding Catalysts. *J. Org. Chem.* **2017,** *82,* 6738-6747. DOI: 10.1021/acs.joc.7b00875 (h) Wendlandt, A. E.; Vangal, P.; Jacobsen, E. N. Quaternary Stereocentres via an Enantioconvergent Catalytic S_N1 Reaction. *Nature* **2018,** *556,* 447-451. DOI: 10.1038/s41586-018-0042-1 (i) Swords, W. B.; Chapman, S. J.; Hofstetter, H.; Dunn, A. L.; Yoon, T. P. Variable Temperature LED–NMR: Rapid Insights into a Photocatalytic Mechanism from Reaction Progress Kinetic Analysis. *J. Org. Chem.* **2022,** *87,* 11776-11782. DOI: 10.1021/acs.joc.2c01479

32. (a) Burés, J. Variable Time Normalization Analysis: General Graphical Elucidation of Reaction Orders from Concentration Profiles. *Angew. Chem. Int. Ed.* **2016**, *55,* 16084-16087. DOI: 10.1002/anie.201609757 (b) Burés, J. A Simple Graphical Method to Determine the Order in Catalyst. *Angew. Chem. Int. Ed.* **2016**, *55,* 2028-2031. DOI: 10.1002/anie.201508983 (c) Alamillo-Ferrer, C.; Hutchinson. G.; Bures, J. Mechanistic Interpretation of Orders in Catalyst Greater than One. *Nat. Rev. Chem.* **2023**, *7*, 26-34. DOI: 10.1038/s41570-022-00447-w

33. D'Amaral, M. C.; Andrews, K. G.; Denton, R. Silyl Esters as Reactive Intermediates in Organic Synthesis. *Synthesis* **2023**. DOI: 10.1055/a-2083-8591

34. (a) Cypryk, M. Ab initio Study of the Basicity and Propensity of Siloxanols towards Hydrogen Bond Formation. *J. Organomet. Chem.* **1997,** *545,* 483-493. DOI: 10.1016/S0022-328X(97)00374-4 (b) Martin-Fernandez, C.; Montero-Campillo, M. M.; Alkorta, I.; Elguero, J. Modulating the Proton Affinity of Silanol and Siloxane Derivatives by Tetrel Bonds. *J. Phys. Chem. A* **2017,** *121,* 7424-7431. DOI: 10.1021/acs.jpca.7b07886

35. (a) Downey, C. W.; Fleisher, A. S.; Rague, J. T.; Safran, C. L.; Venable, M. E.; Pike, R. D. Synthesis of *N*-acyl-*N,O*-acetals from *N*-aryl Amides and Acetals in the Presence of TMSOTf. *Tetrahedron Lett.* **2011,** *52*, 4756-4759. DOI: 10.1016/j.tetlet.2011.07.023 (b) Dilman, A. D.; Levin, V. V.; Korlyukov, A. A.; Belyakov, P. A.; Struchkova, M. I.; Antipin, M. Y.; Tartakovsky, V. A. Complexation of Tris(pentafluorophenyl)silanes with Neutral Lewis Bases. *J. Organomet. Chem.* **2008,** *693*, 1005-1019. DOI: 10.1016/j.jorganchem.2007.12.022

36. (a) Allemand, J.; Gerdil, R. *Cryst. Struct. Commun.* **1979,** *8*, 927-932. (b) Puff, H.; Braun, K.; Reuter, H. Molecular and Crystal-Structure of Triphenylsilanol. *J. Organomet. Chem.* **1991,** *409*, 119-129. DOI: 10.1016/0022-328X(91)86137-F (c) Bowes, K. F.; Glidewell, C.; Low, J. N. Tetrameric Triphenylsilanol, $(Ph_3SiOH)_4$, and the Adduct $(Ph_3SiOH)_2$–Dimethyl sulfoxide, both at 120 K, and the Adduct $(Ph_3SiOH)_3$–1,4-Dioxan at 150 K: Interplay of O—H··· O and C—H··· π(Arene) Interactions. *Acta Cryst. C,* **2002,** *58*, o409-o415. DOI: 10.1107/S0108270102009381 (d) Glidewell, C.; Liles, D. C. The Crystal and Molecular Structure of Oxobis[triphenylsilicon(IV)]. *Acta Cryst. B,* **1978,** *34*, 124-128. DOI: 10.1107/S0567740878002435

37. (a) Pauling, H.; Andrews, D. A.; Hindley, N. C. The Rearrangement of *α*-Acetylenic Alcohols to *α, β*-Unsaturated Carbonyl Compounds by Silylvanadate Catalysts. *Helv. Chim. Acta* **1976,** *59*, 1233-1243. DOI: 10.1002/hlca.19760590426 (b) Prince, P. D.; Bearpark, M. J.; McGrady, G. S.; Steed, J. W. Hypervalent Hydridosilicates: Synthesis, Structure and Hydride Bridging. *Dalton Trans.* **2008,** 271-282. DOI: 10.1039/B713427D (c) Akhani, R. K.; Moore, M. I.; Pribyl, J. G.; Wiskur, S. L. Linear Free-Energy Relationship and Rate Study on a Silylation-Based Kinetic Resolution: Mechanistic Insights. *J. Org. Chem.* **2014,** *79*, 2384-2396. DOI: 10.1021/jo402569h (d) Gilman, H.; Miller, L. S. The Preparation of Some

Chlorinated Aryl Silanes for the Examination of their Insecticidal Properties. *J. Am. Chem. Soc.* **1951,** *73,* 968-970. DOI: 10.1021/ja01147a023

38. (a) Guijarro, A.; Yus, M. Polychlorinated Materials as a Source of Polyanionic Synthons. *Tetrahedron* **1996,** *52,* 1797-1810. DOI: 10.1016/0040-4020(95)01014-9 (b) Zhang, B.; Wang, Z. Building Ultramicropores within Organic Polymers Based on a Thermosetting Cyanate Ester Resin. *Chem. Comm.* **2009,** 5027-5029. DOI: 10.1039/B909424E (c) Pombrik, S.; Kravtsov, D.; Peregudov, A.; Fedin, E.; Nesmeyanov, A. A ^{19}F NMR Investigation of the Transmission of Electronic Effects in Triaryl(4-fluorophenyl)silanes. *J. Organomet. Chem.* **1977,** *131,* 355-363. DOI: 10.1016/S0022-328X(00)84411-3

39. Schmohl, K.; Reinke, H.; Oehme, H. Reaction of the (Dichloromethyl)oligosilanes R(Me$_3$Si)$_2$Si-CHCl$_2$ (R = Me, Ph, Me$_3$Si) with Organolithium Reagents and the Synthesis of Novel Kinetically Stabilized Silenes. *Eur. J. Inorg. Chem.* **2001,** *2001,* 481-489. DOI: 10.1002/1099-0682(200102)2001:2<481::AID-EJIC481>3.0.CO;2-6

Imperial College London

Triarylsilanols as Catalysts for Direct Amidation of Carboxylic Acids

Electronic Supporting Information

A thesis submitted by

Rabia Qamar

in partial fulfilment of the requirements for the degree of

DOCTOR OF PHILOSOPHY

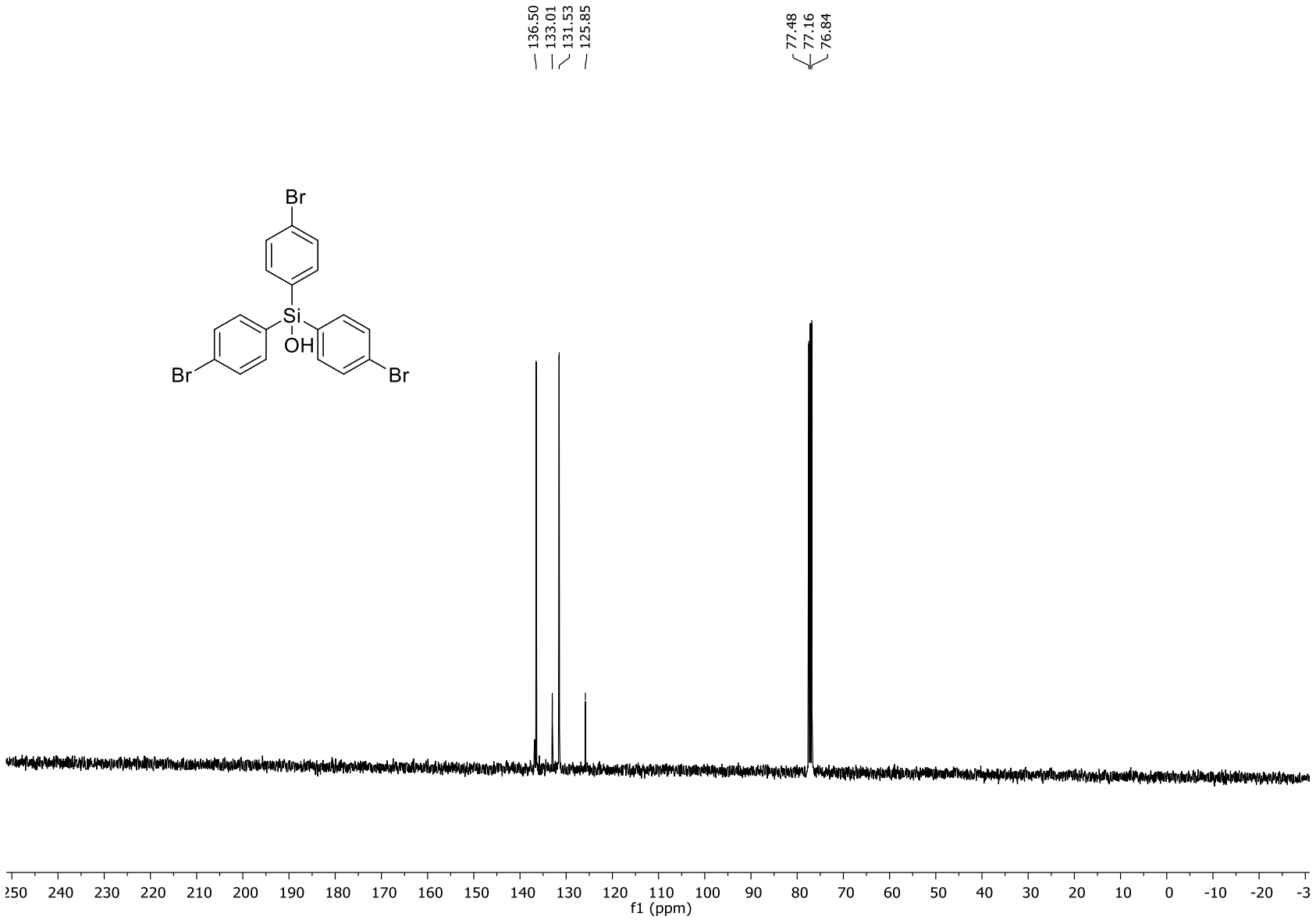
Department of Chemistry
Imperial College London
Molecular Sciences Research Hub
White City Campus
82 Wood Lane, London
W12 0BZ

August 2023

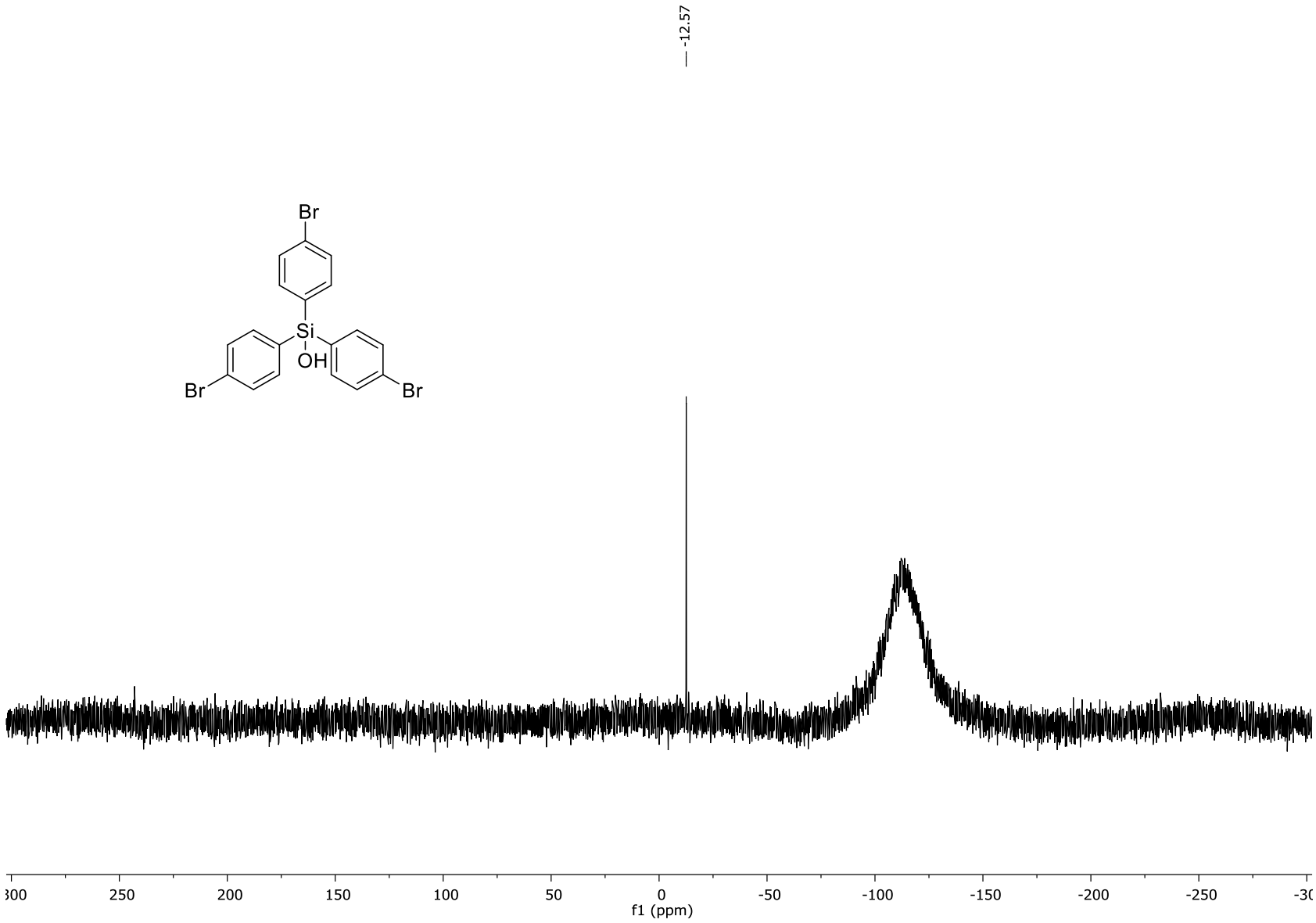
^{1}H NMR spectrum of tris(*p*-bromophenyl)silanol **(62g)** (400 MHz, $CDCl_3$)



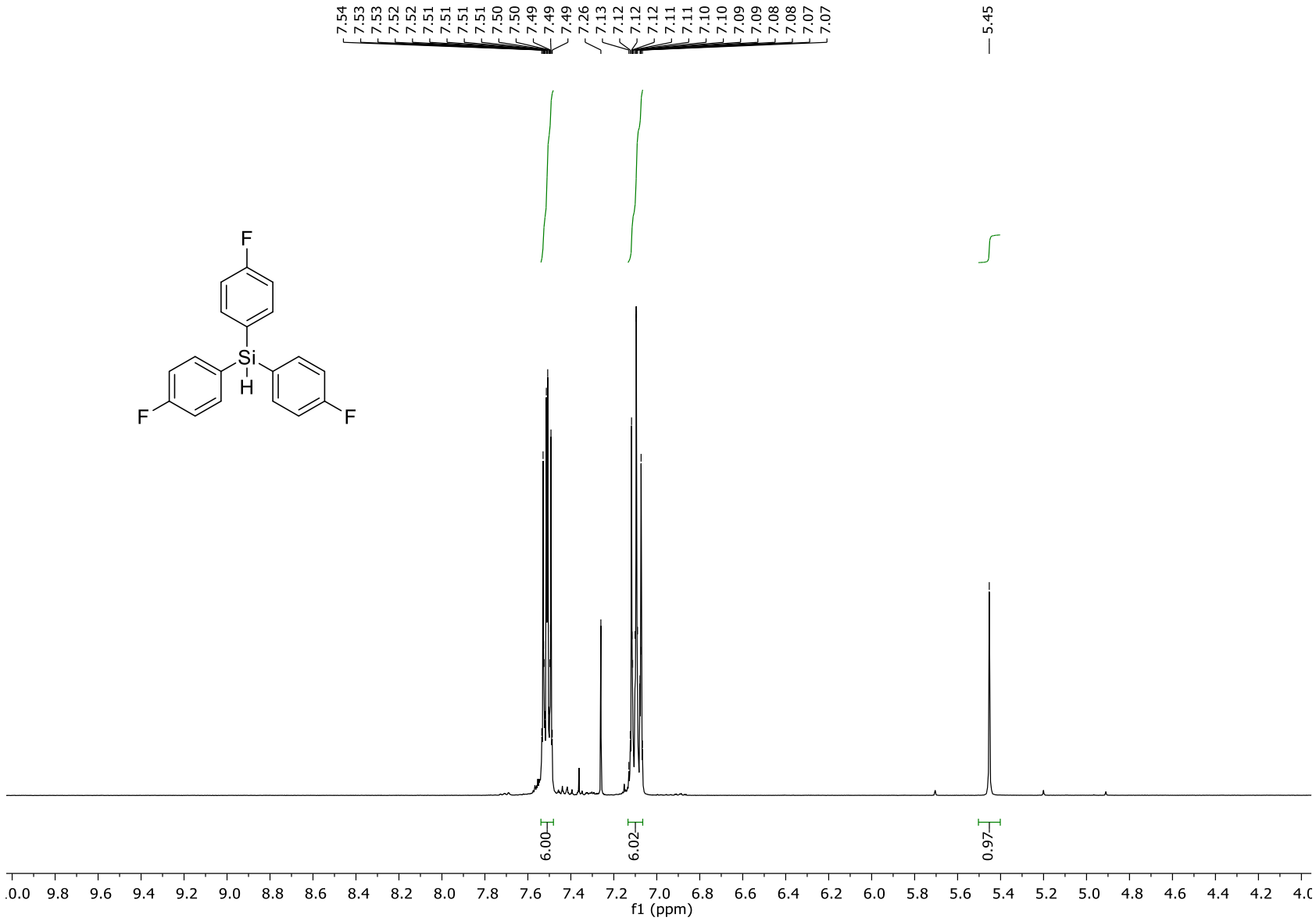
^{13}C NMR spectrum of tris(*p*-bromophenyl)silanol **(62g)** (101 MHz, $CDCl_3$)



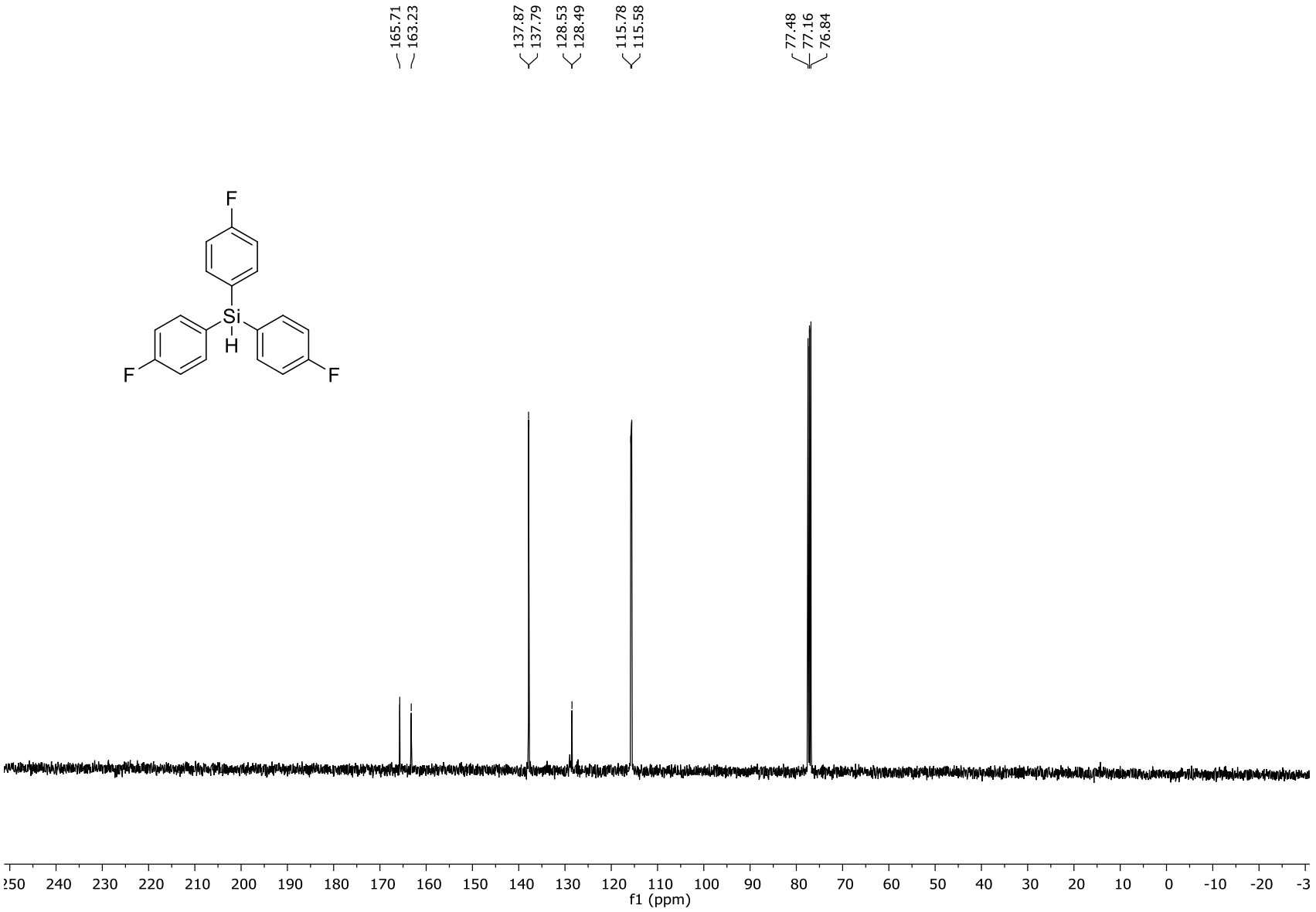
$^{29}Si\{^{1}H\}$ NMR spectrum of tris(*p*-bromophenyl)silanol **(62g)** (80 MHz, $CDCl_3$)



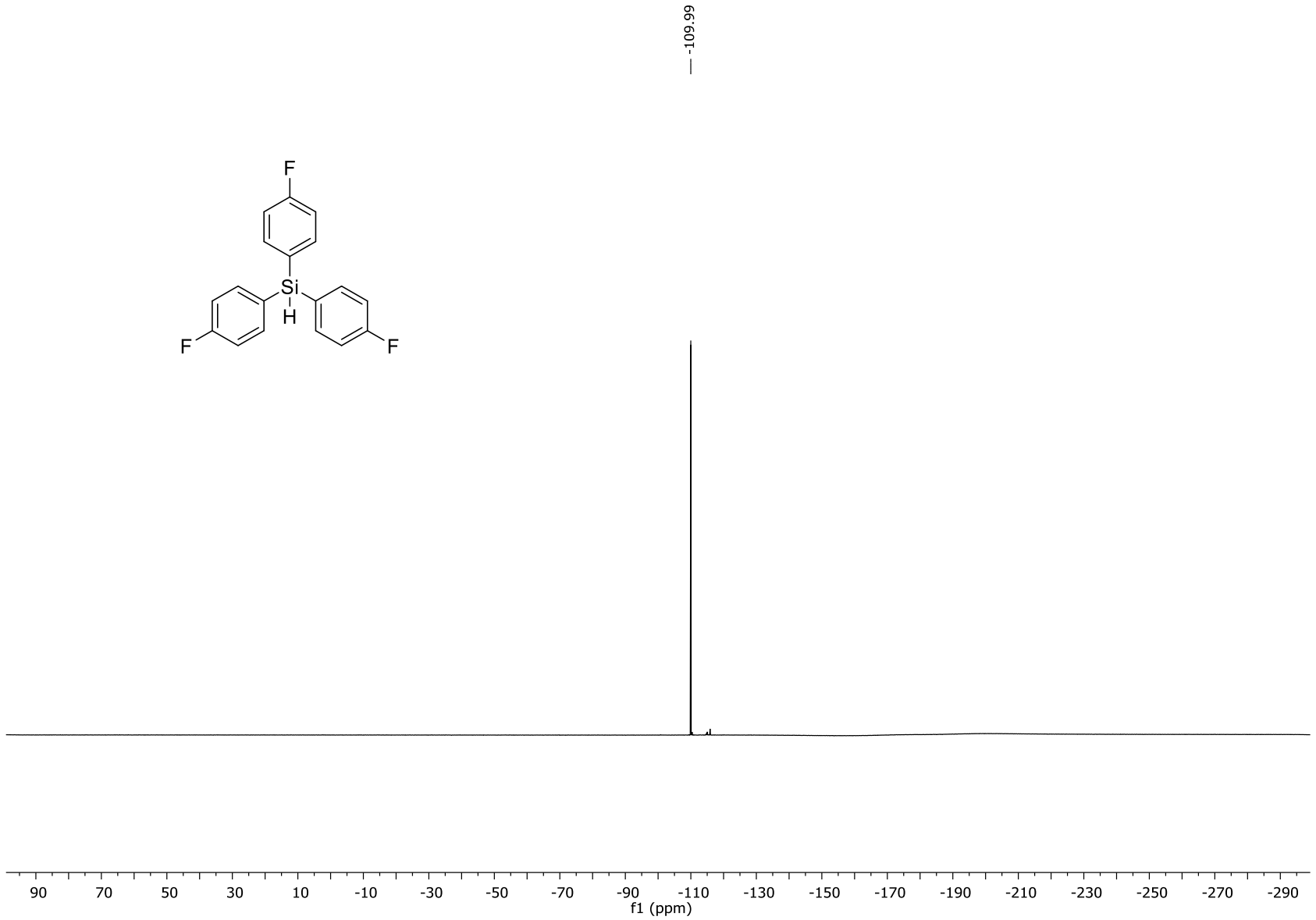
^{1}H NMR spectrum of tris(*p*-fluorophenyl)silane **(64a)** (400 MHz, $CDCl_3$)



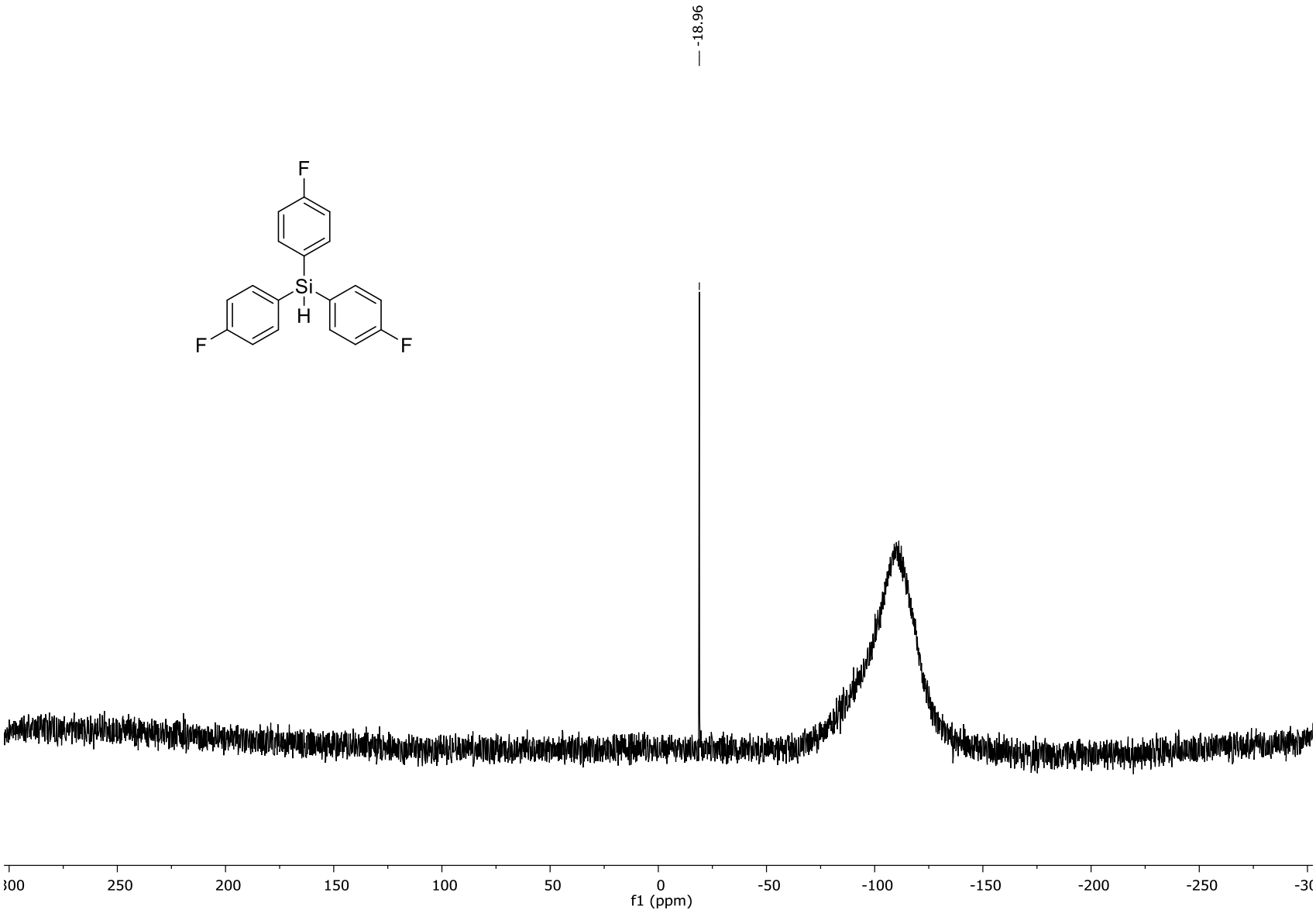
^{13}C NMR spectrum of tris(*p*-fluorophenyl)silane **(64a)** (101 MHz, $CDCl_3$)



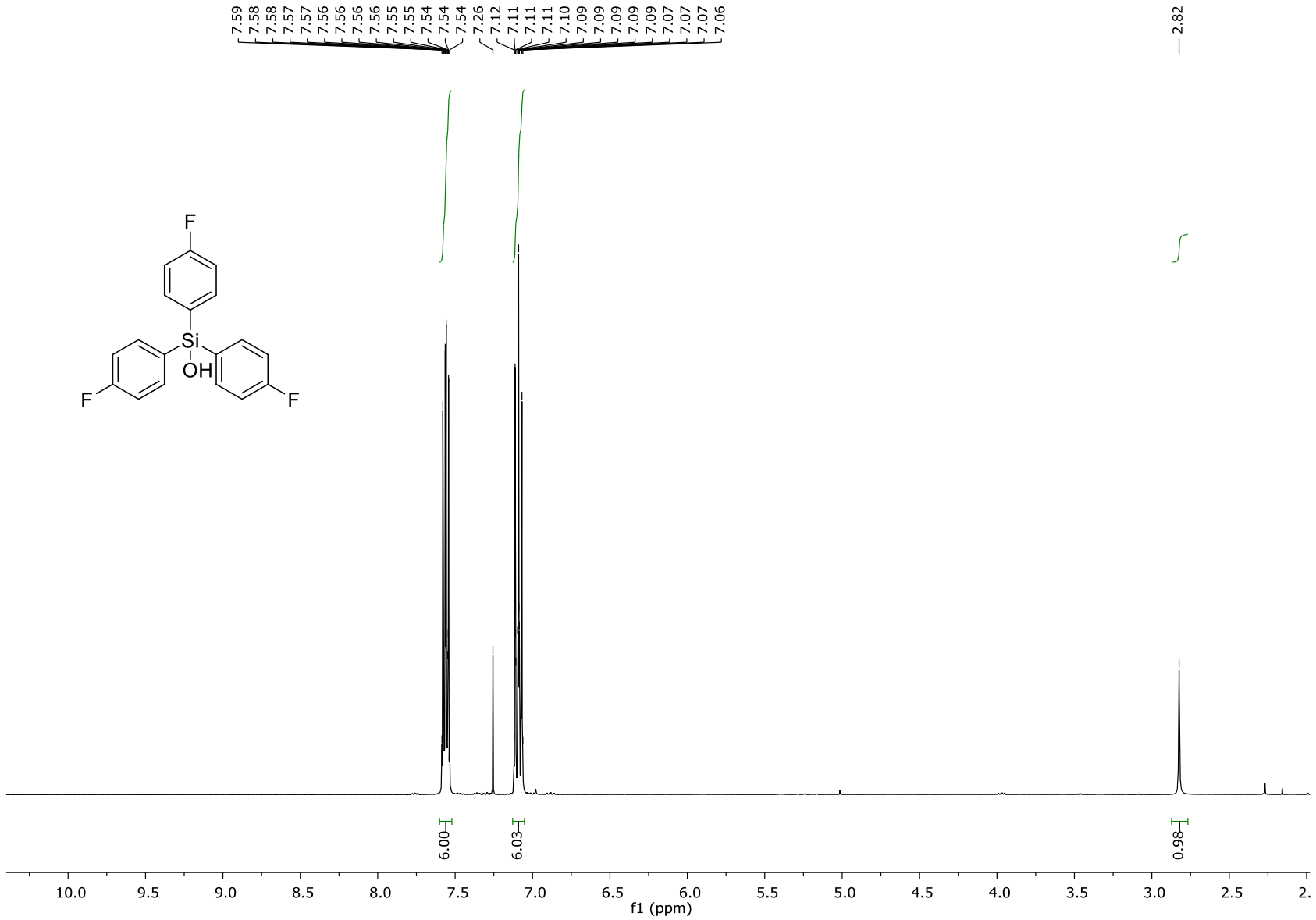
$^{19}F\{^{1}H\}$ NMR spectrum of tris(*p*-fluorophenyl)silane **(64a)** (377 MHz, $CDCl_3$)



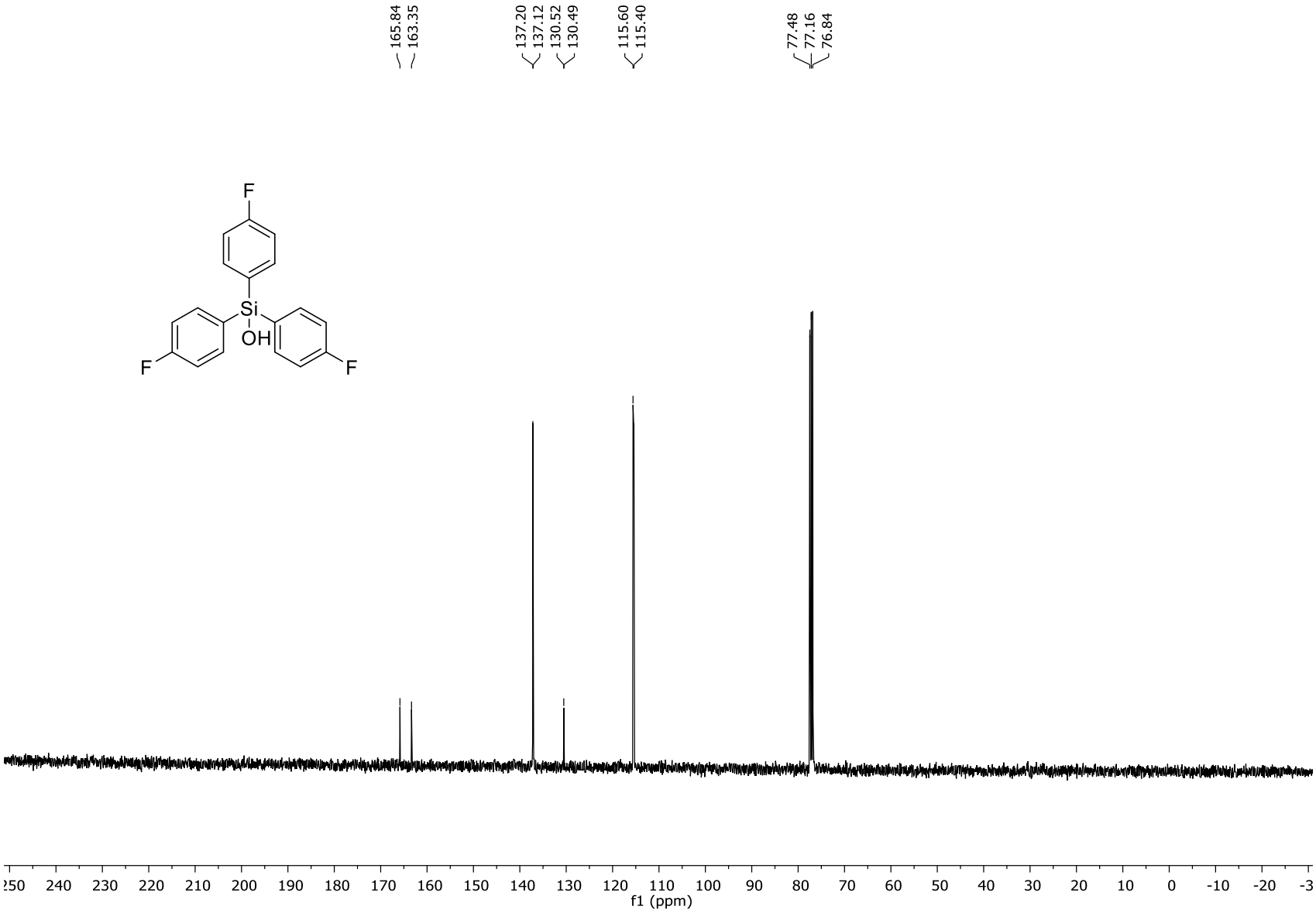
$^{29}Si\{^{1}H\}$ NMR spectrum of tris(*p*-fluorophenyl)silane **(64a)** (80 MHz, $CDCl_3$)



^{1}H NMR spectrum of tris(*p*-fluorophenyl)silanol **(62e)** (400 MHz, $CDCl_3$)



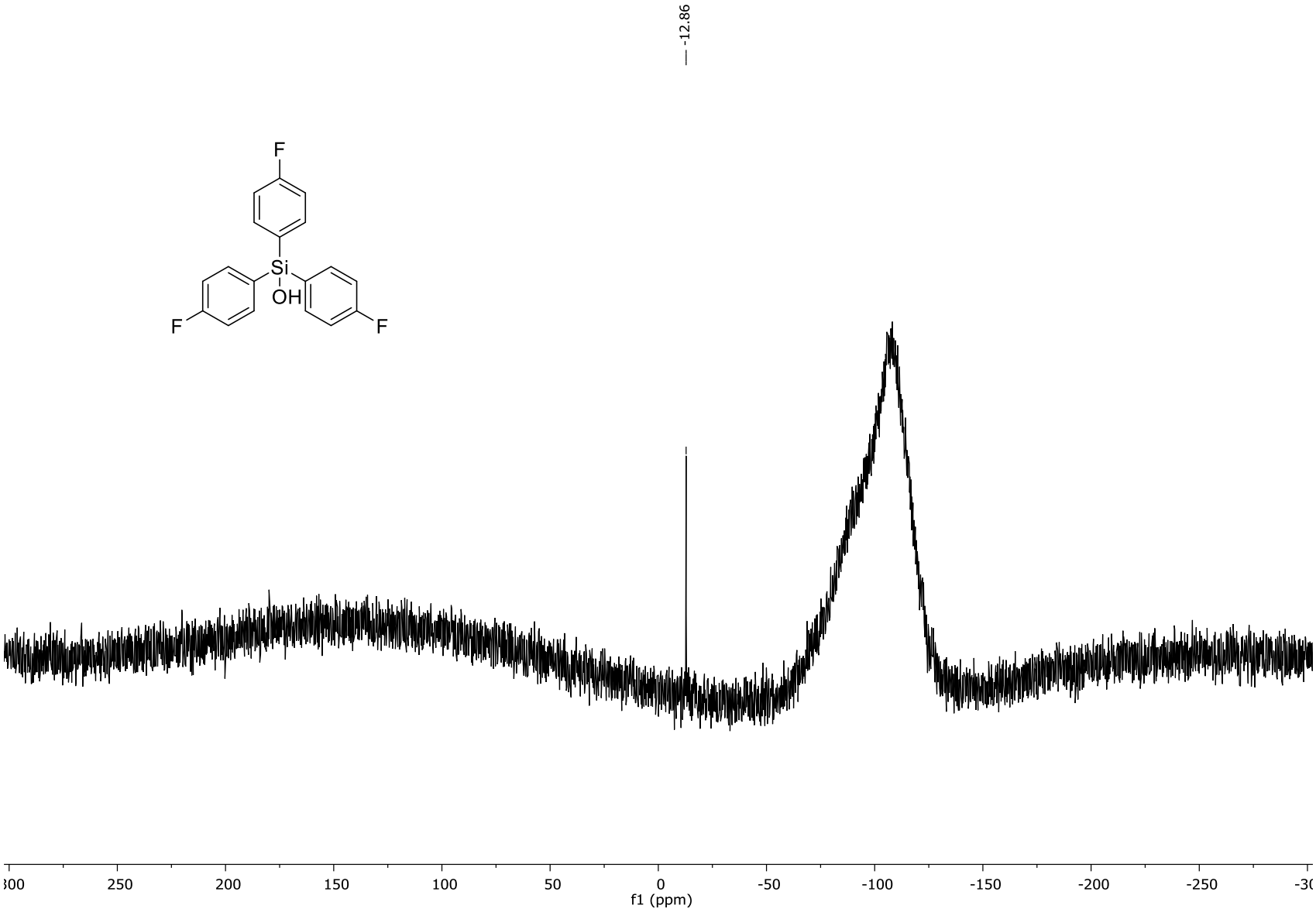
^{13}C NMR spectrum of tris(*p*-fluorophenyl)silanol **(62e)** (101 MHz, $CDCl_3$)



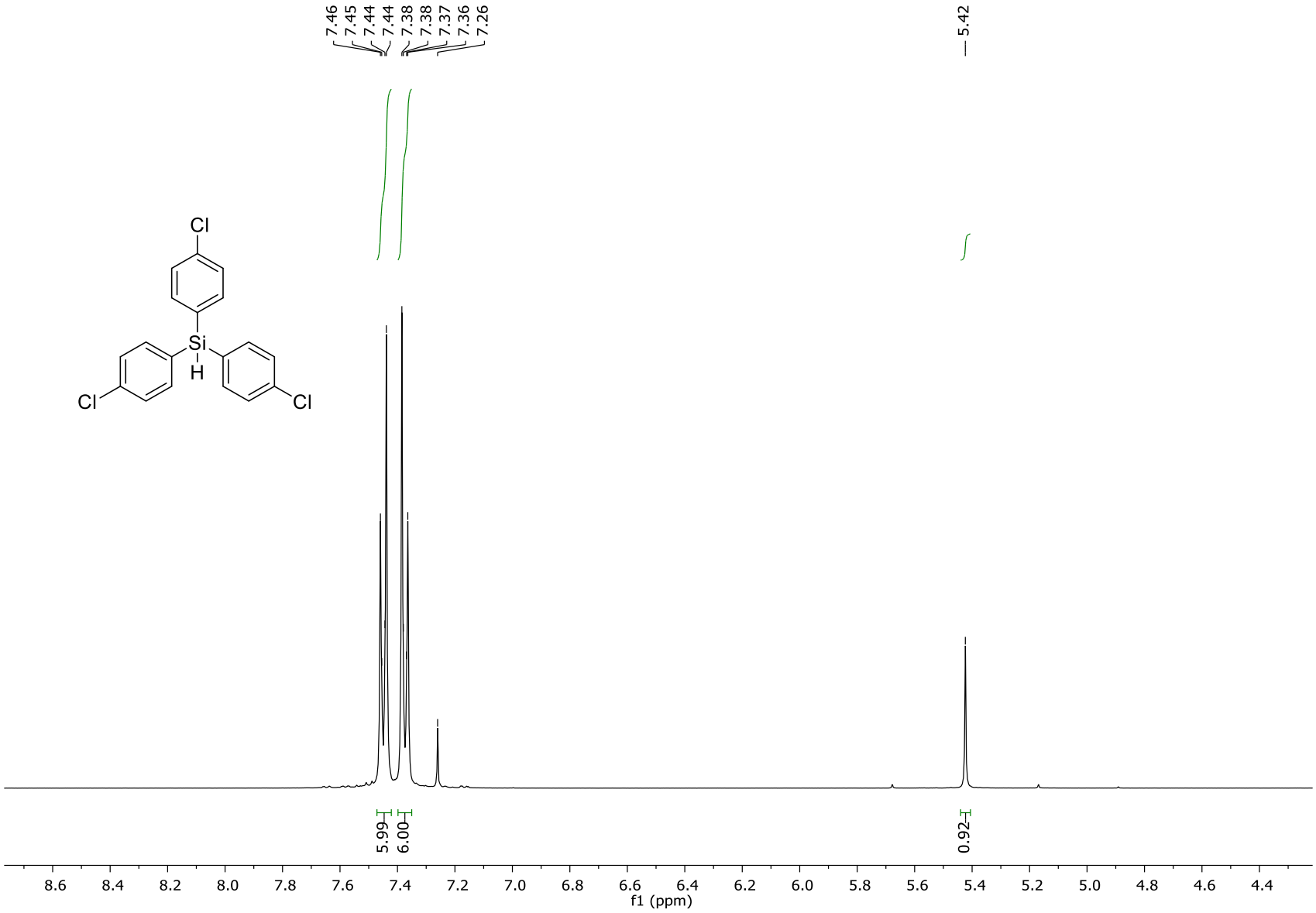
$^{19}F\{^{1}H\}$ NMR spectrum of tris(*p*-fluorophenyl)silane **(62e)** (377 MHz, $CDCl_3$)



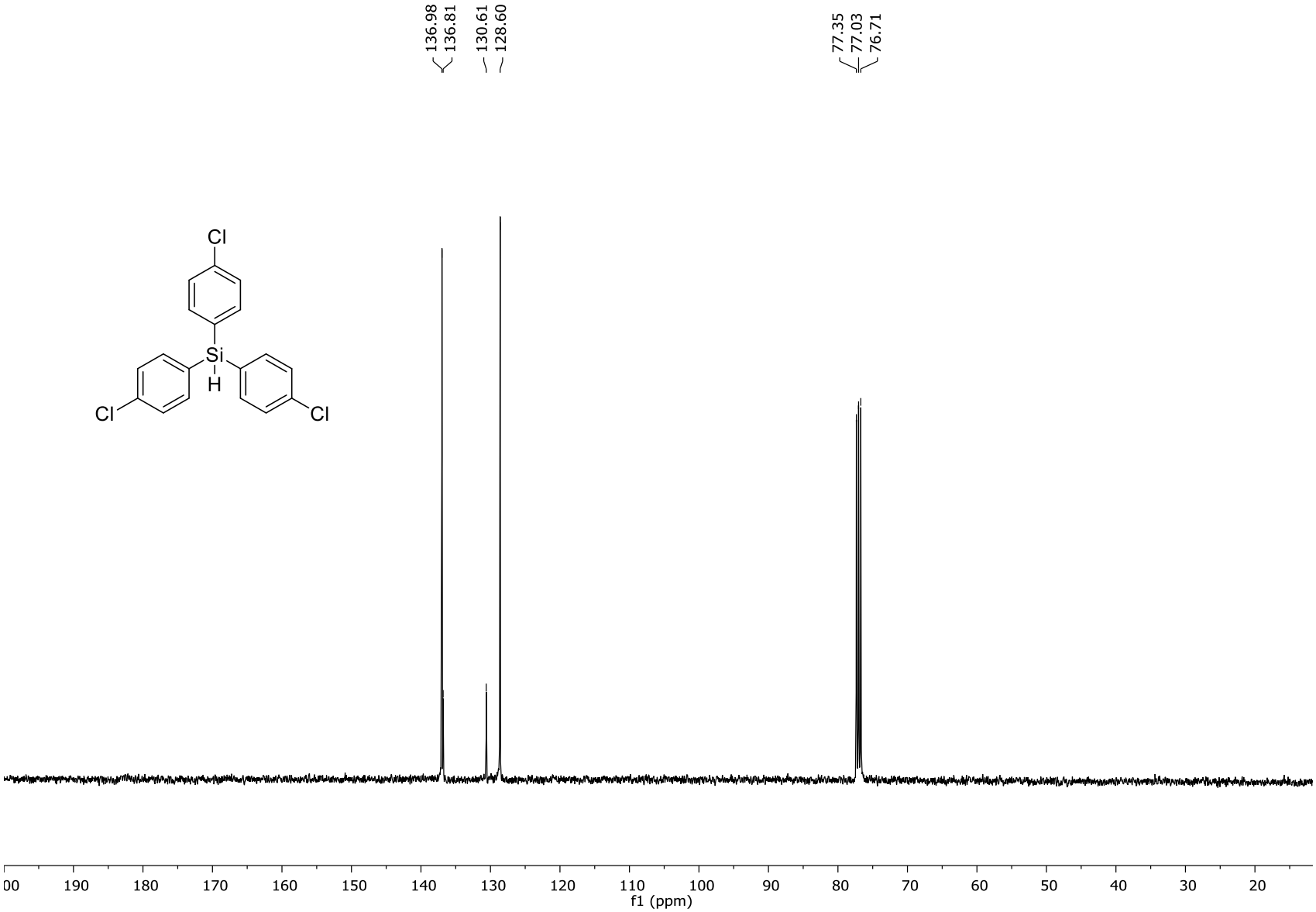
$^{29}Si\{^{1}H\}$ NMR spectrum of tris(*p*-fluorophenyl)silanol **(62e)** (80 MHz, $CDCl_3$)



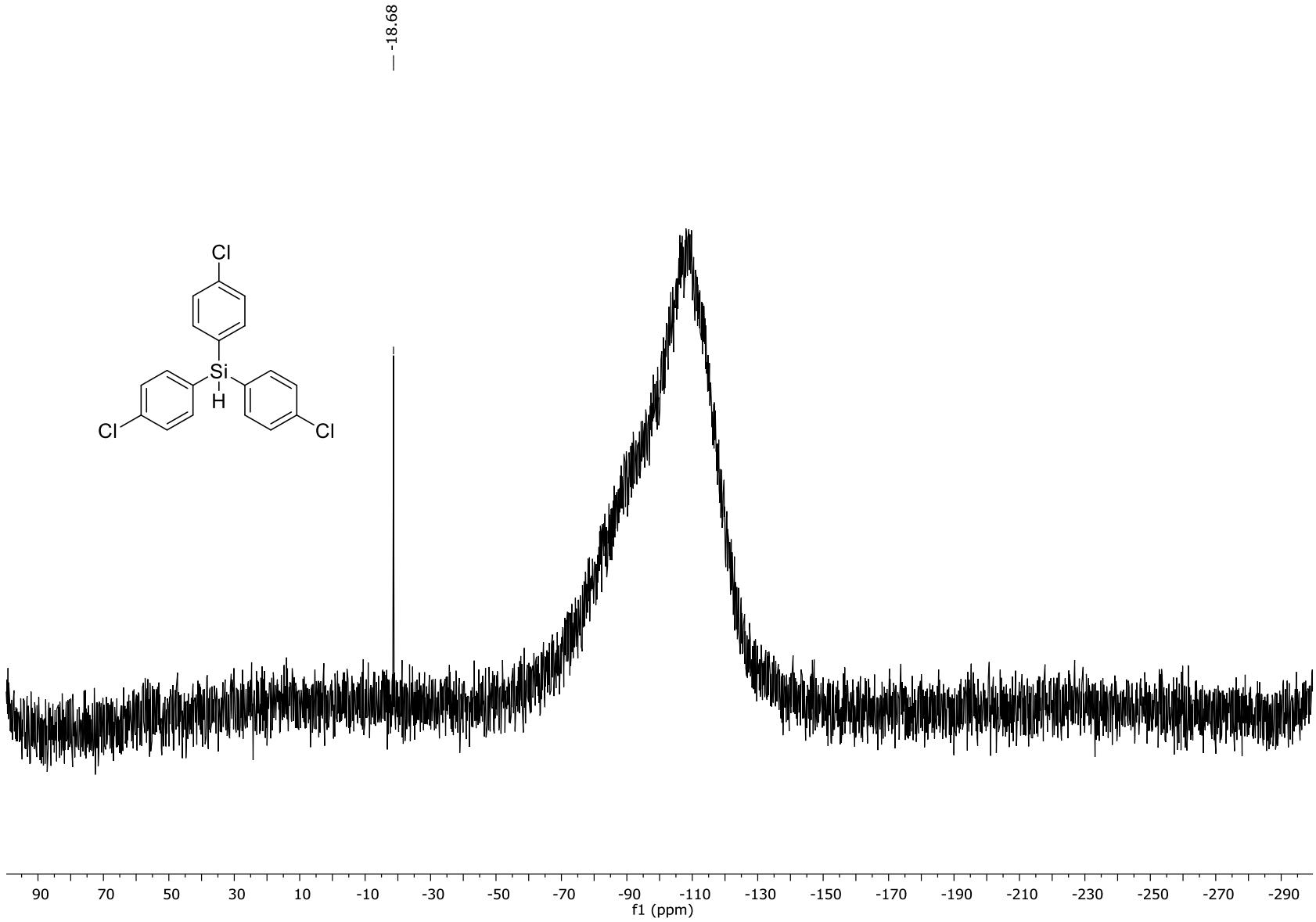
^{1}H NMR spectrum of tris(*p*-chlorophenyl)silane **(64b)** (400 MHz, $CDCl_3$)



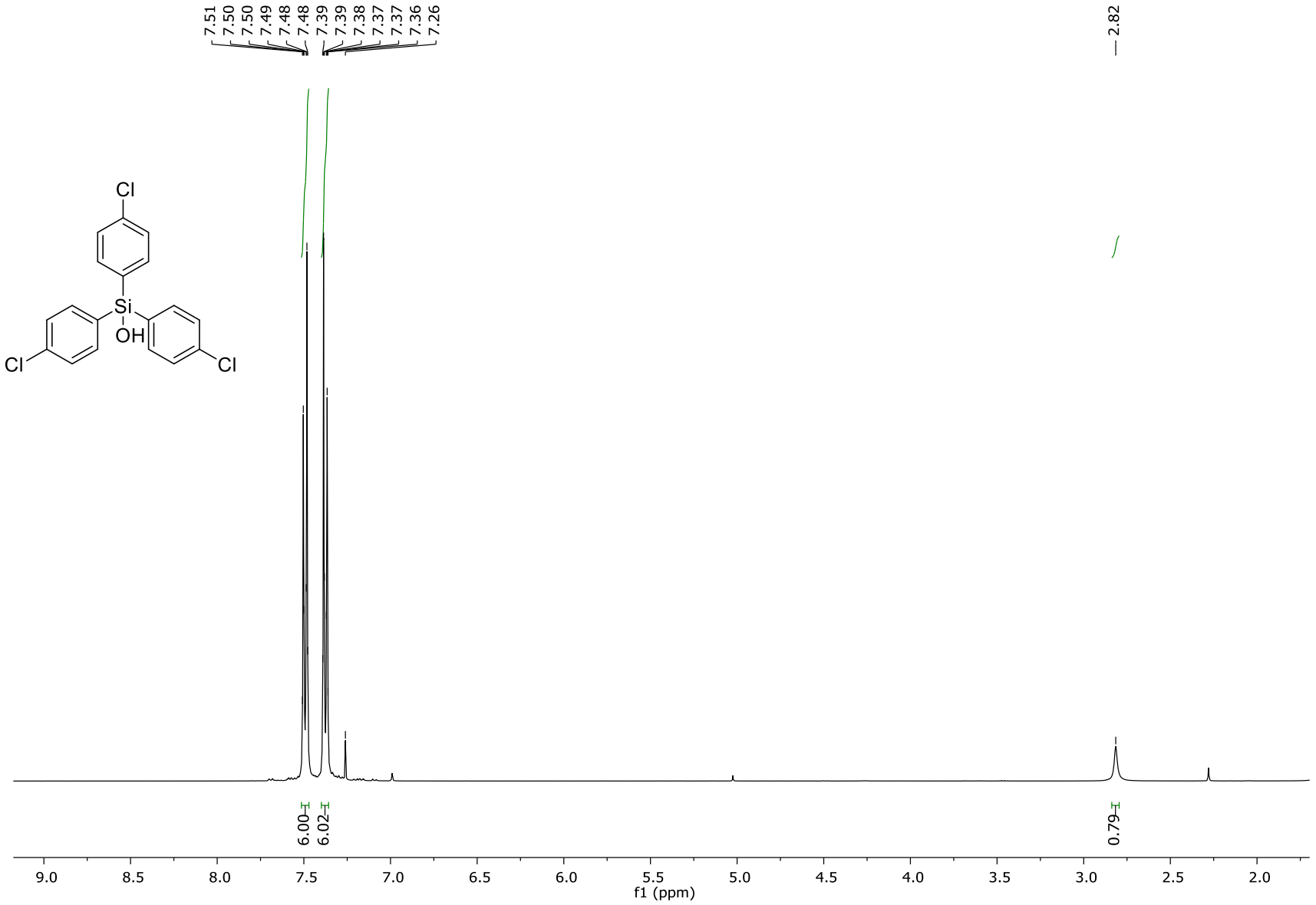
^{13}C NMR spectrum of tris(*p*-chlorophenyl)silane **(64b)** (101 MHz, $CDCl_3$)



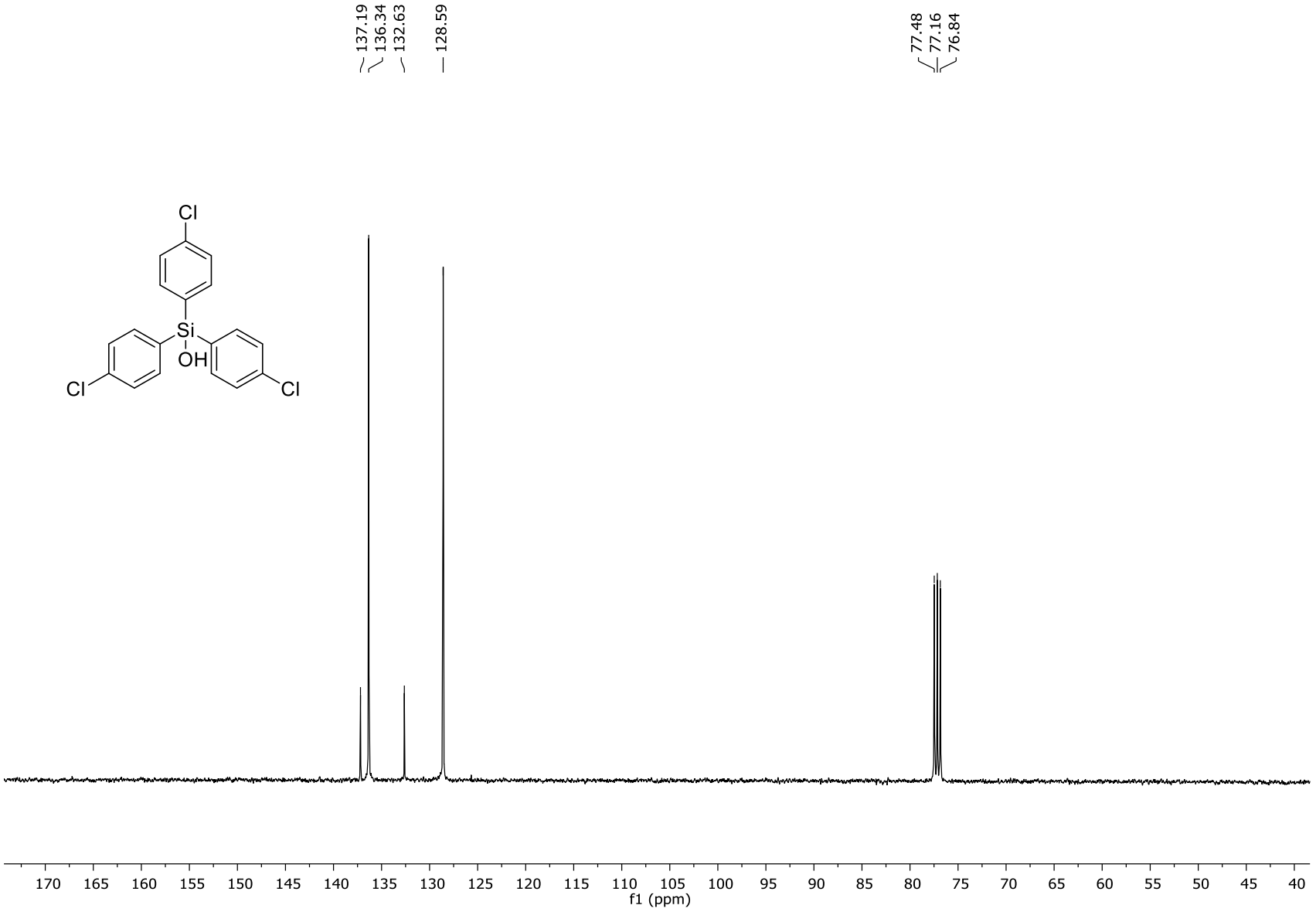
$^{29}Si\{^{1}H\}$ NMR spectrum of tris(*p*-chlorophenyl)silane **(64b)** (80 MHz, $CDCl_3$)



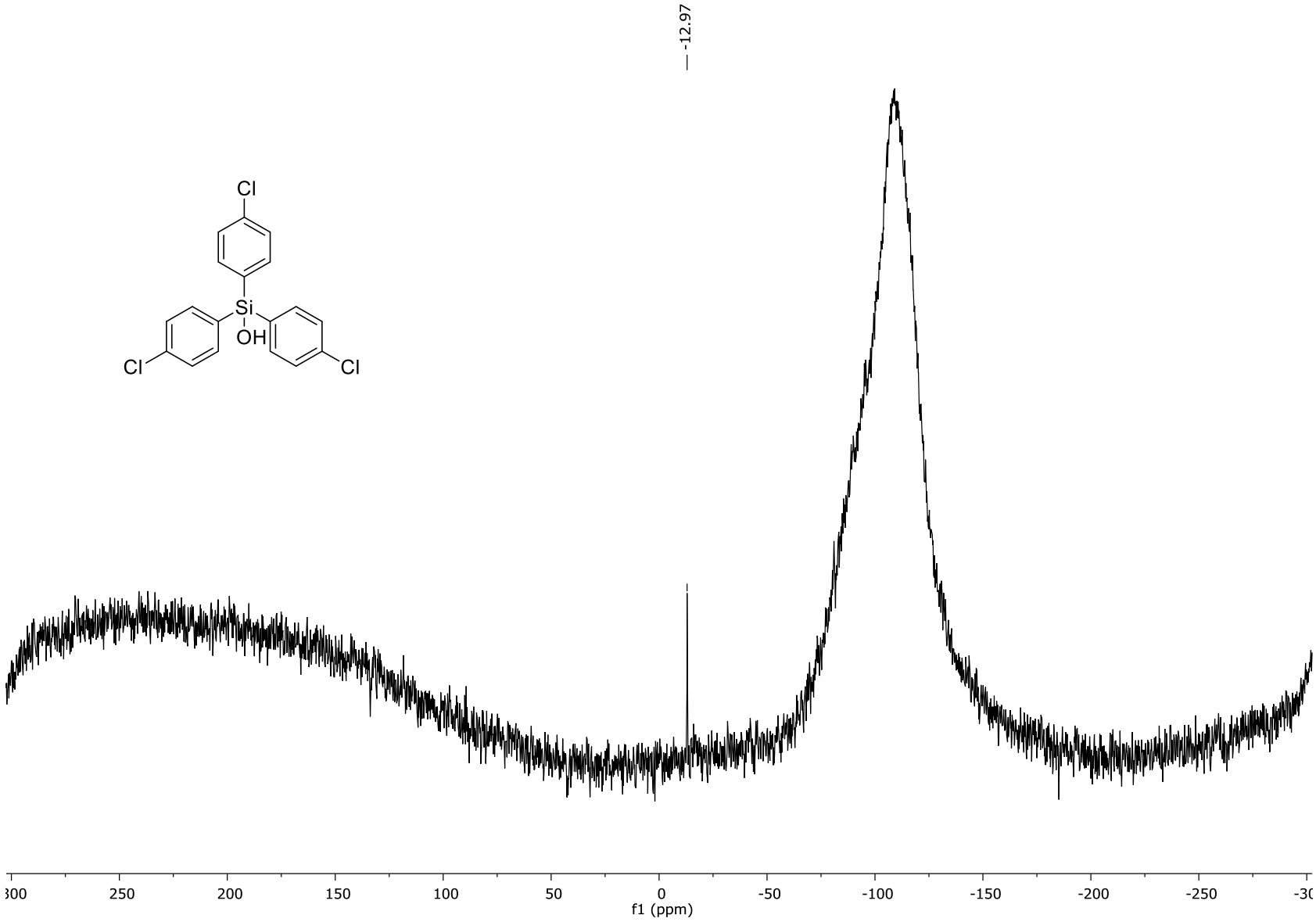
^{1}H NMR spectrum of tris(*p*-chlorophenyl)silanol **(62f)** (400 MHz, $CDCl_3$)



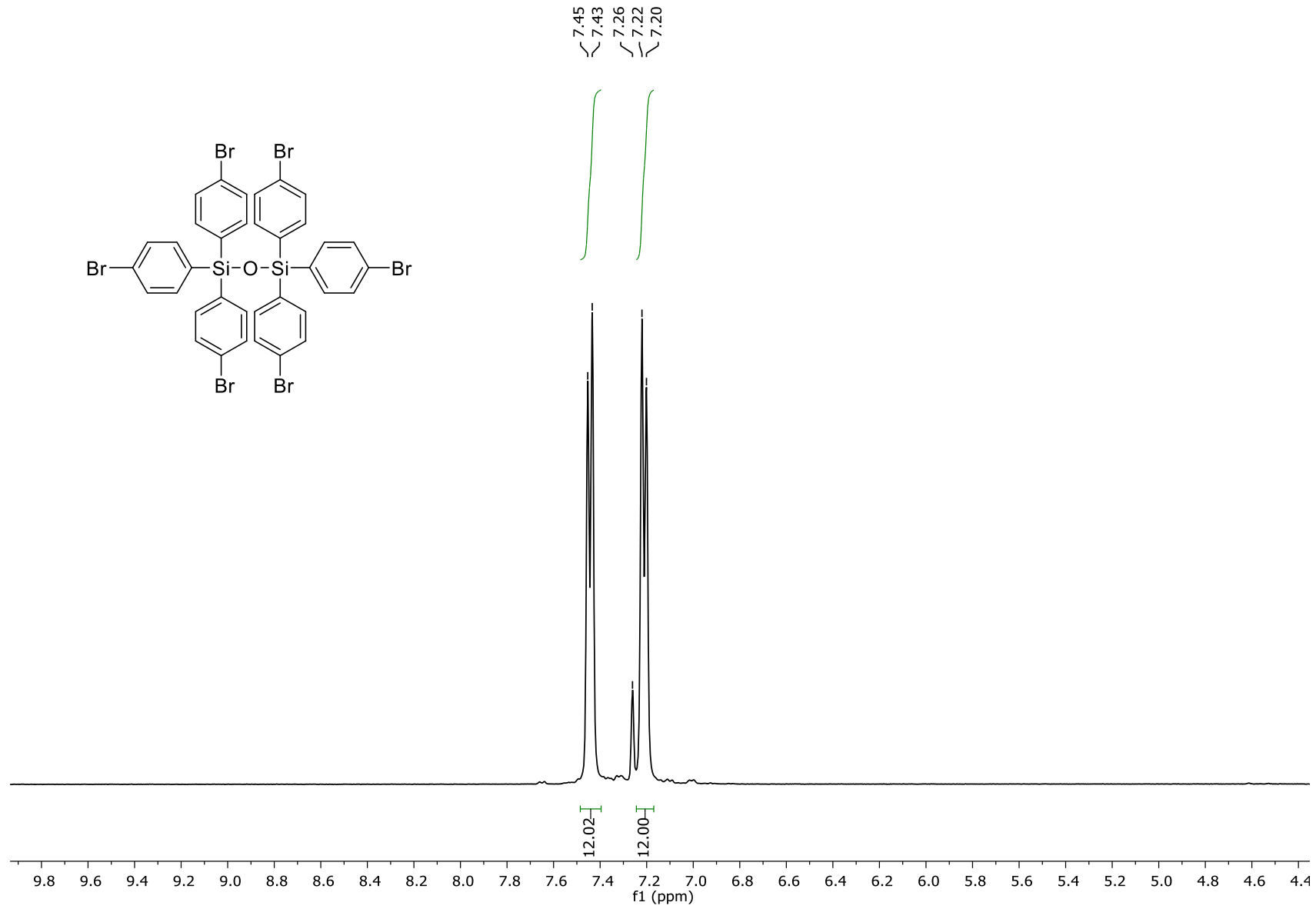
^{13}C NMR spectrum of tris(*p*-chlorophenyl)silanol **(62f)** (101 MHz, $CDCl_3$)



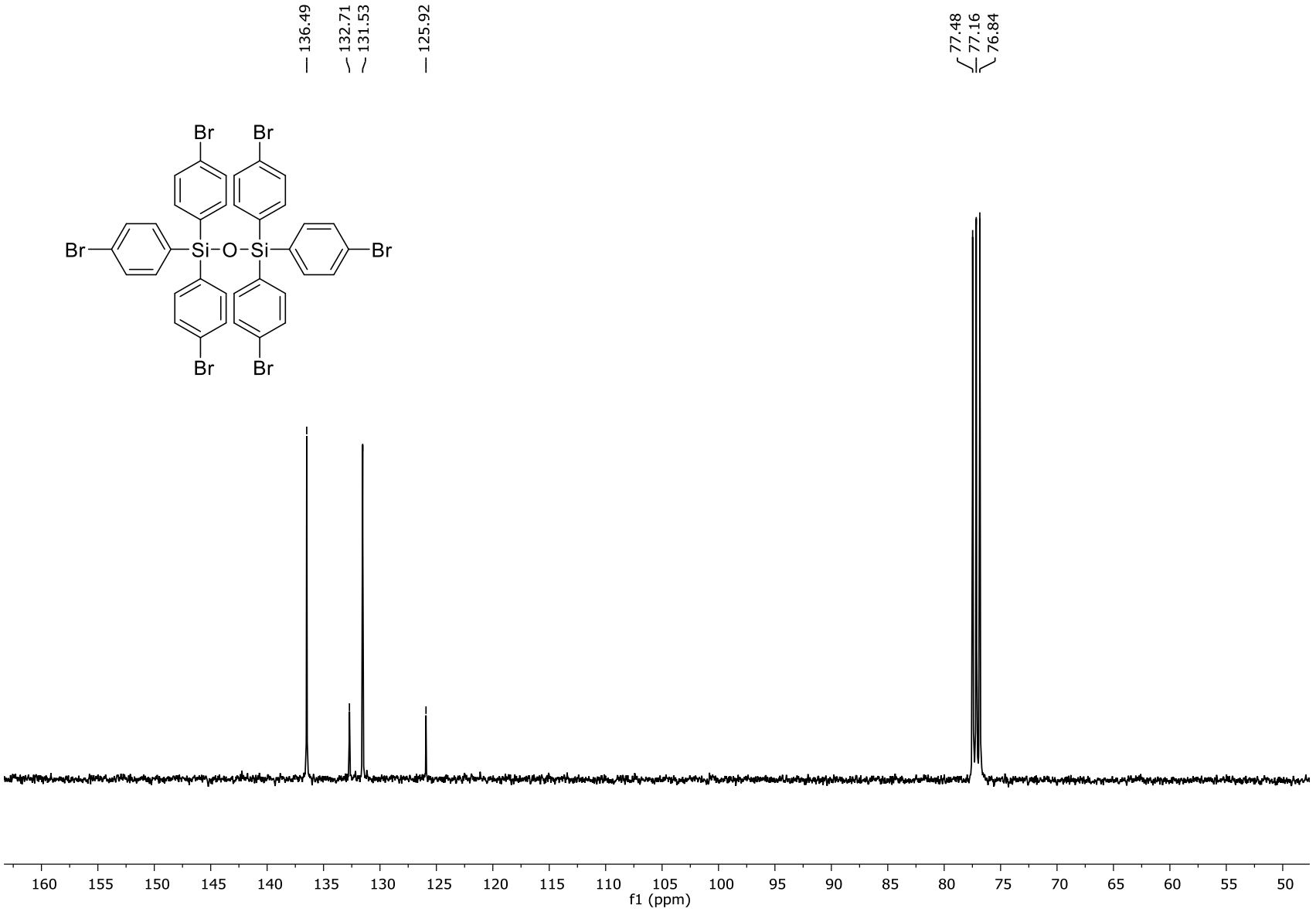
$^{29}Si\{^{1}H\}$ NMR spectrum of tris(*p*-chlorophenyl)silanol **(62f)** (80 MHz, $CDCl_3$)



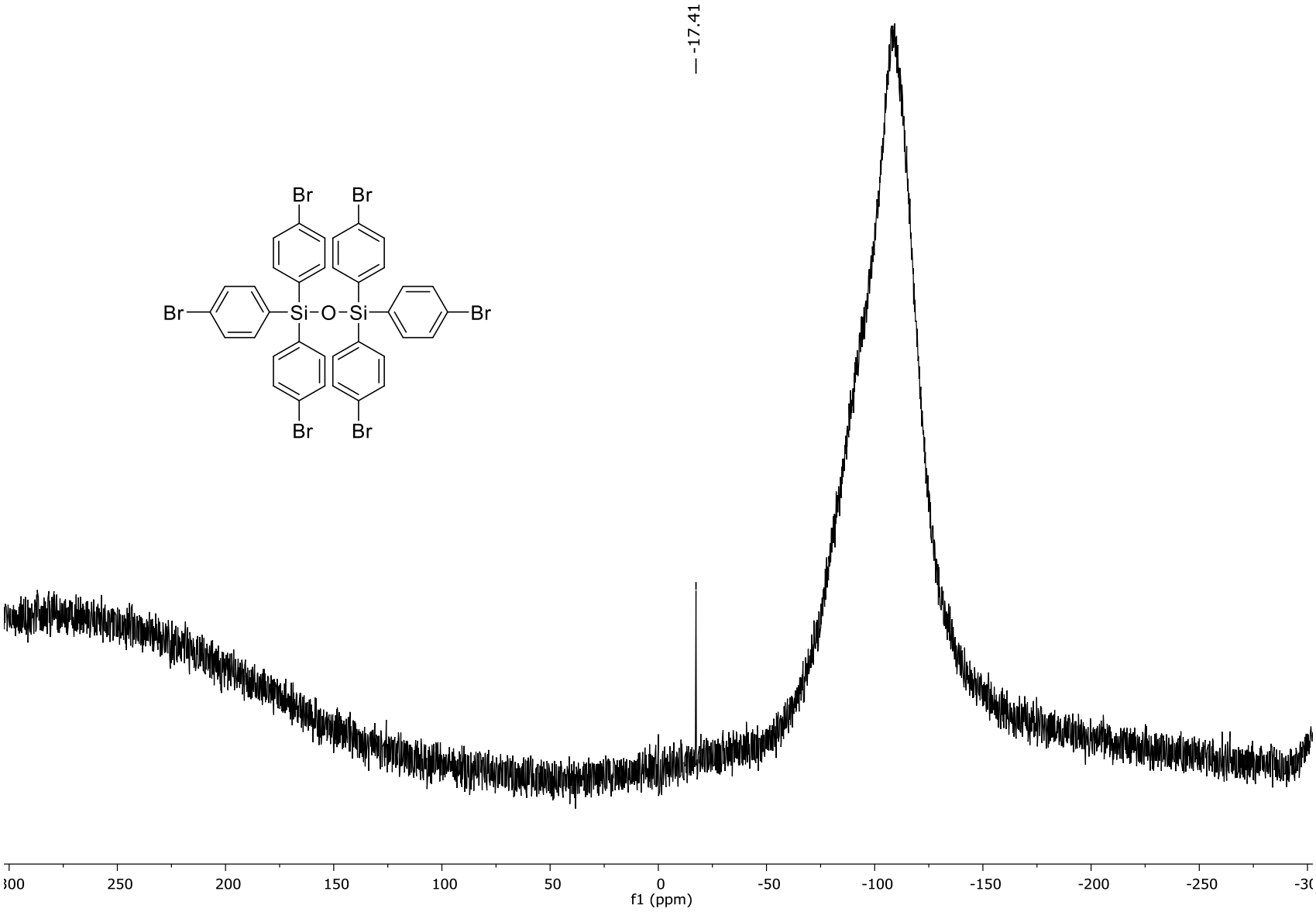
^{1}H NMR spectrum of 1,1,1,3,3,3-hexakis(*p*-bromophenyl)disiloxane **(65)** (400 MHz, $CDCl_3$)



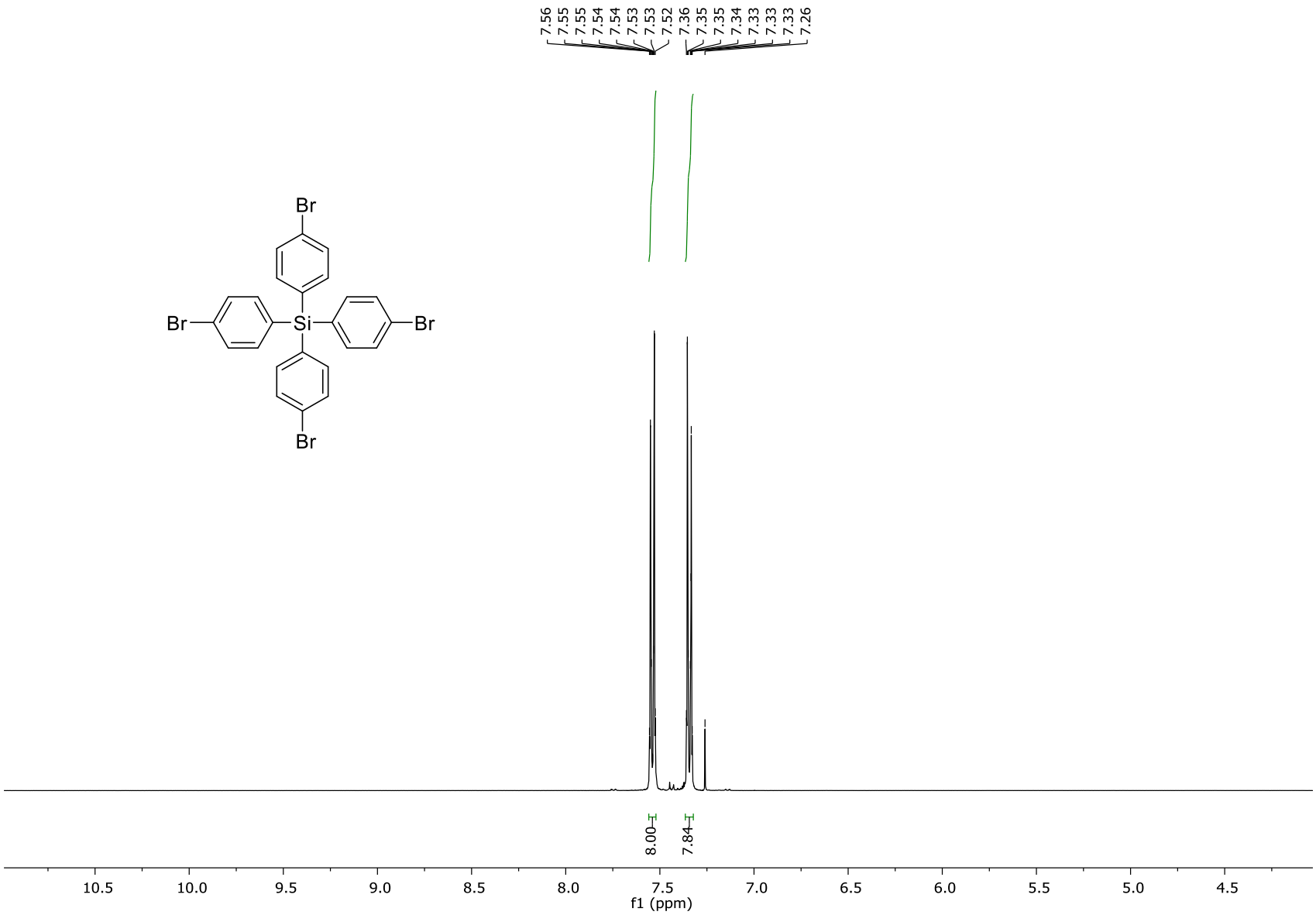
^{13}C NMR spectrum of 1,1,1,3,3,3-hexakis(*p*-bromophenyl)disiloxane **(65)** (101 MHz, $CDCl_3$)



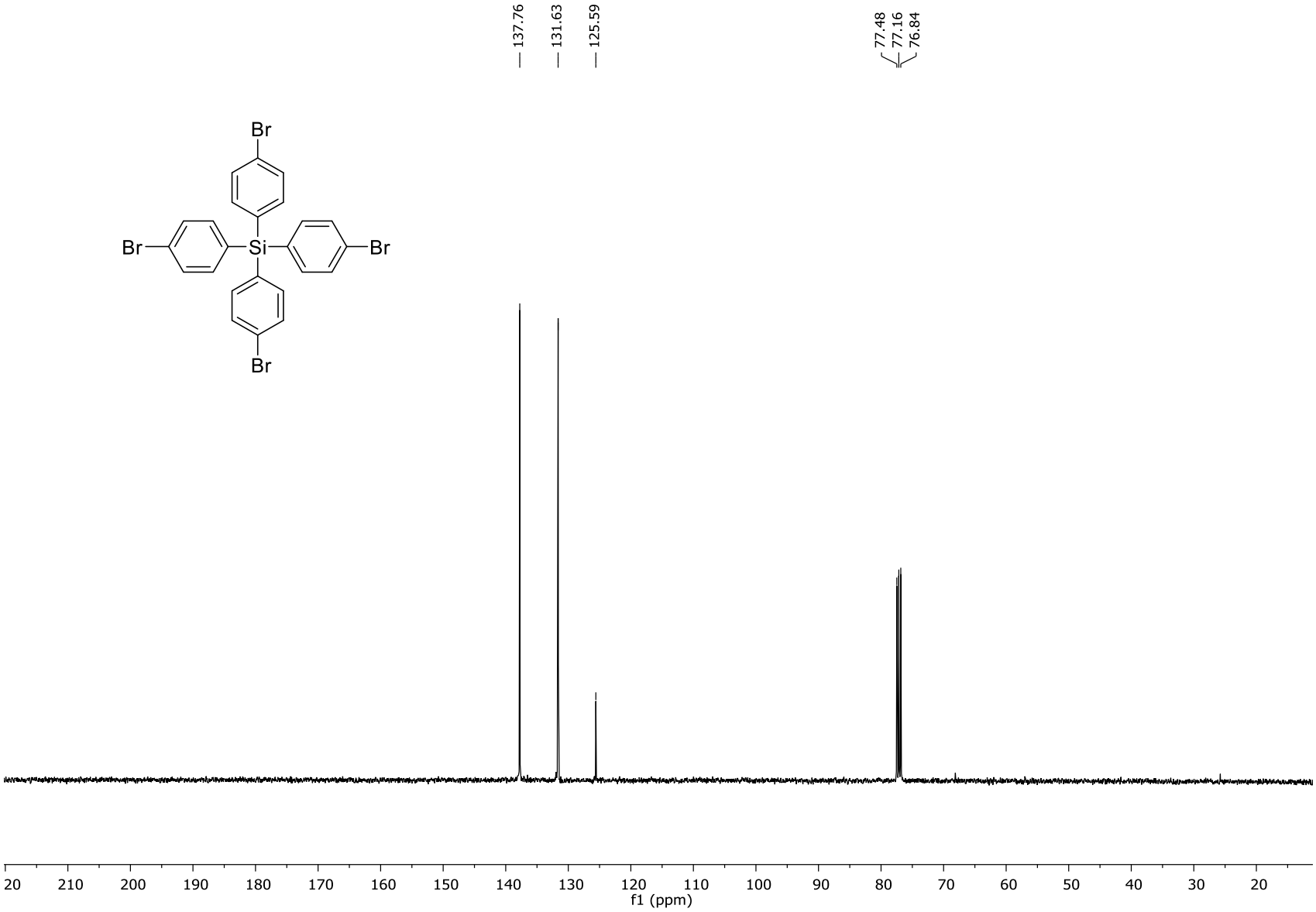
$^{29}Si\{^{1}H\}$ NMR spectrum of 1,1,1,3,3,3-hexakis(*p*-bromophenyl)disiloxane **(65)** (80 MHz, $CDCl_3$)



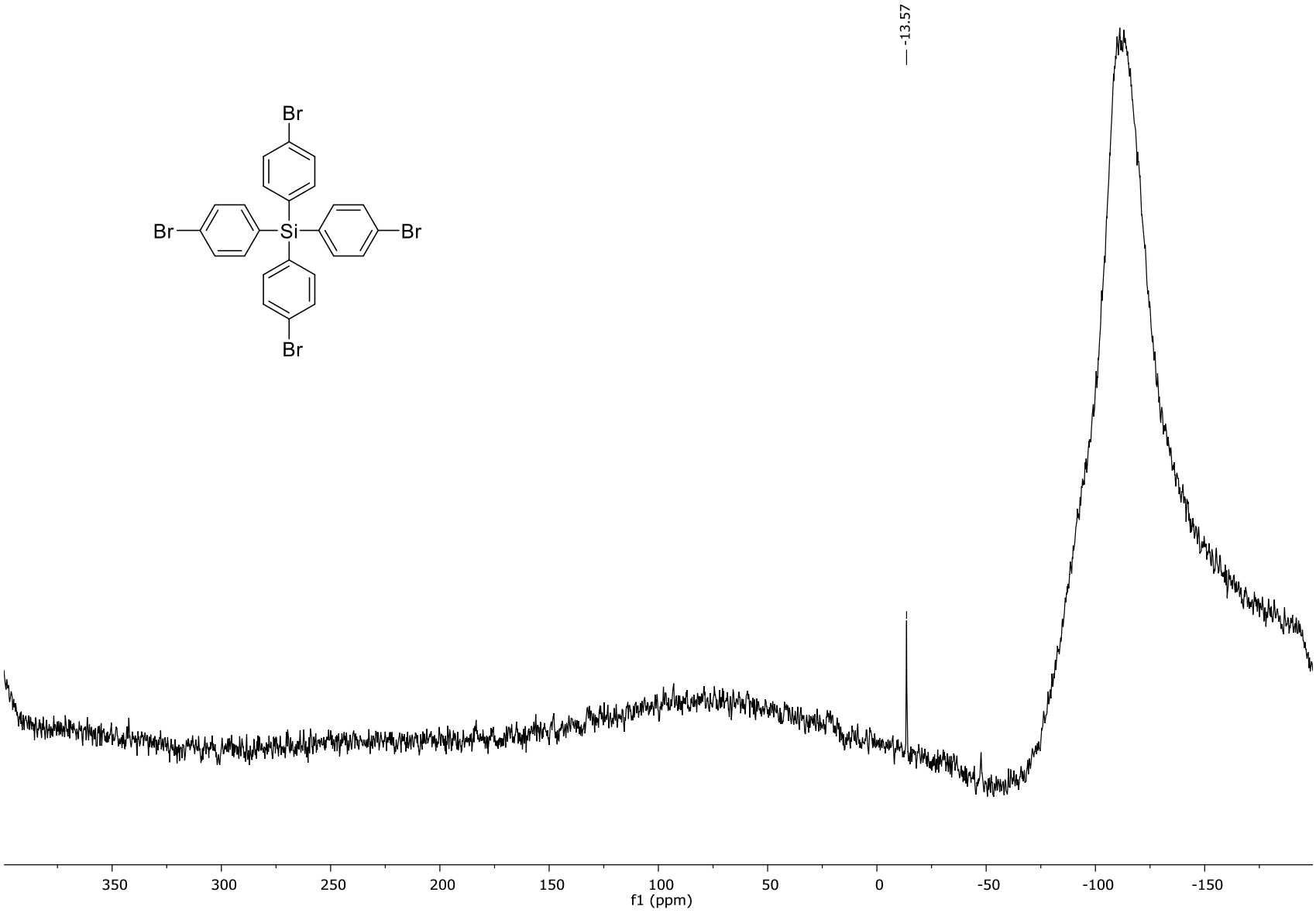
^{1}H NMR spectrum of tetrakis(*p*-bromophenyl)silane **(71a)** (400 MHz, $CDCl_3$)



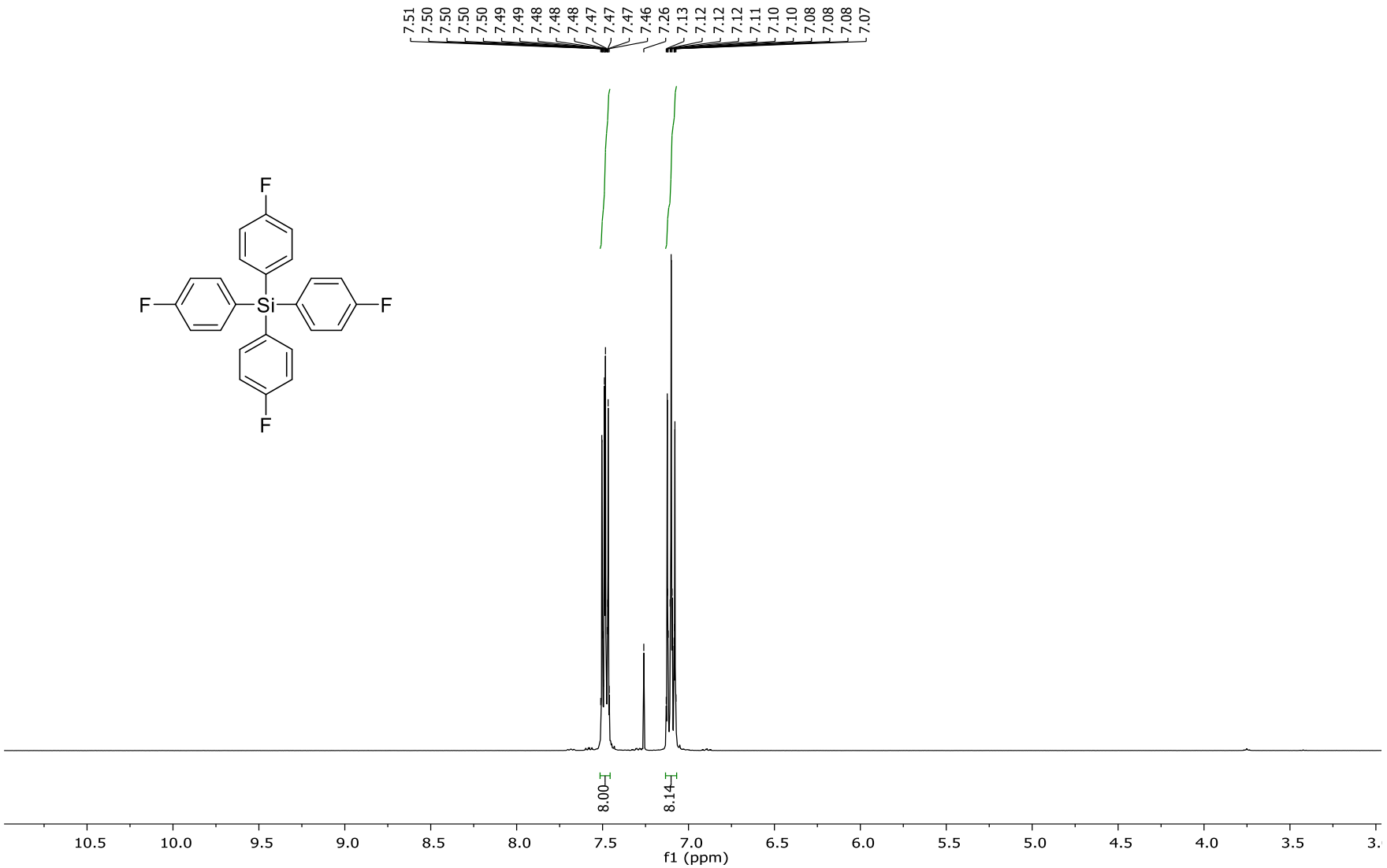
^{13}C NMR spectrum of tetrakis(*p*-bromophenyl)silane **(71a)** (101 MHz, $CDCl_3$)



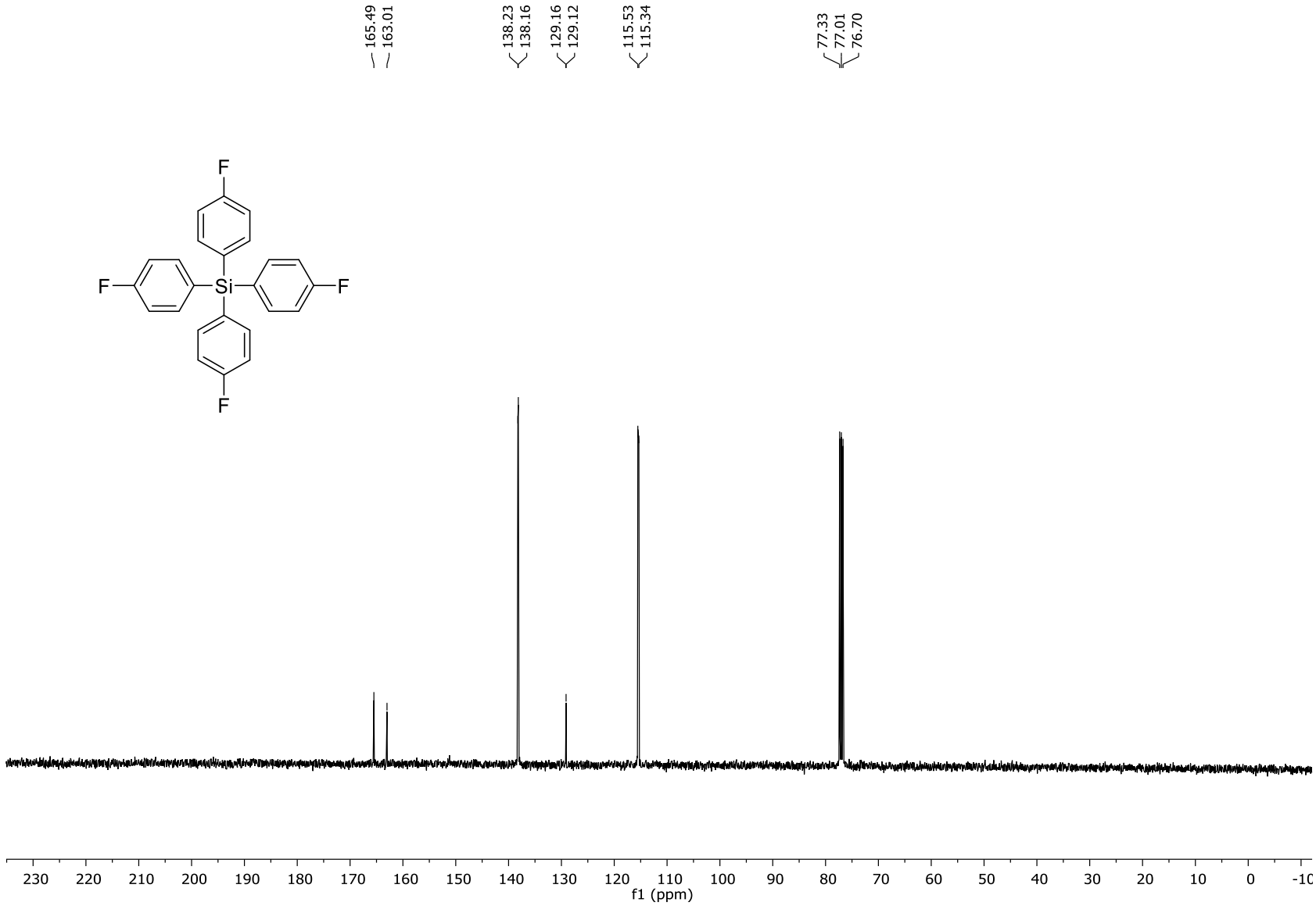
$^{29}Si\{^{1}H\}$ NMR spectrum of tetrakis(*p*-bromophenyl)silane **(71a)** (80 MHz, $CDCl_3$)



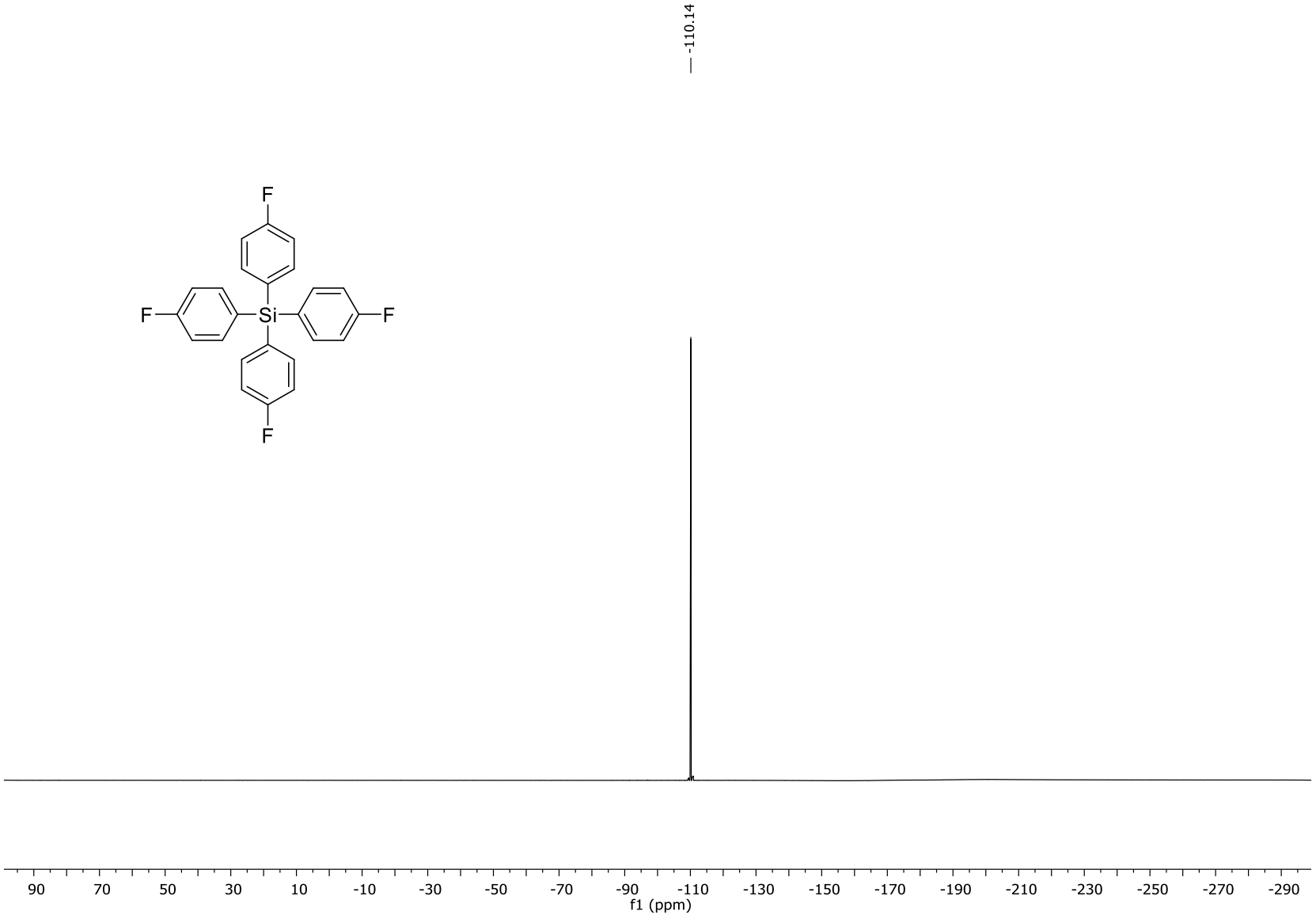
^{1}H NMR spectrum of tetrakis(*p*-fluorophenyl)silane **(71b)** (400 MHz, $CDCl_3$)



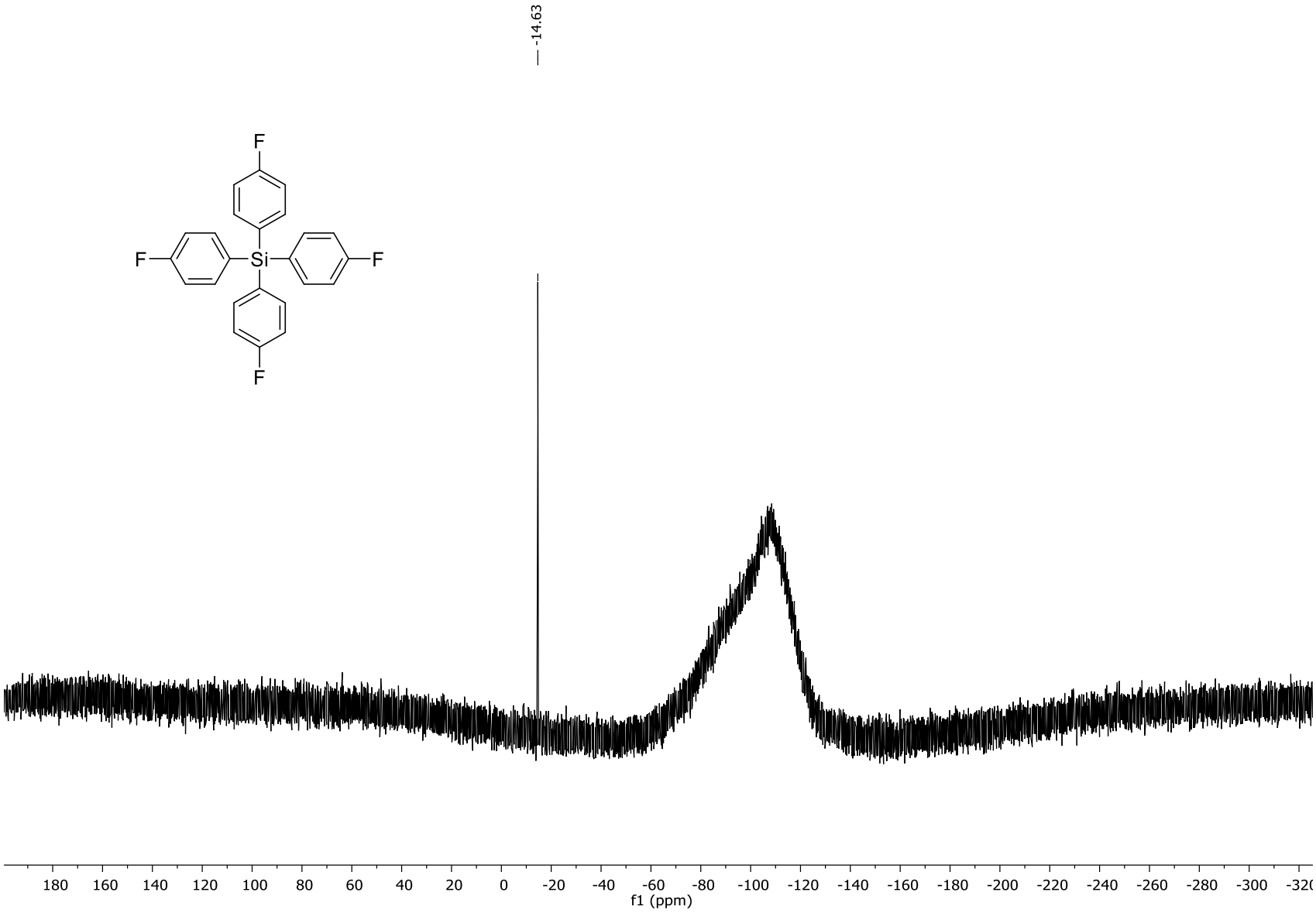
^{13}C NMR spectrum of tetrakis(*p*-fluorophenyl)silane **(71b)** (101 MHz, $CDCl_3$)



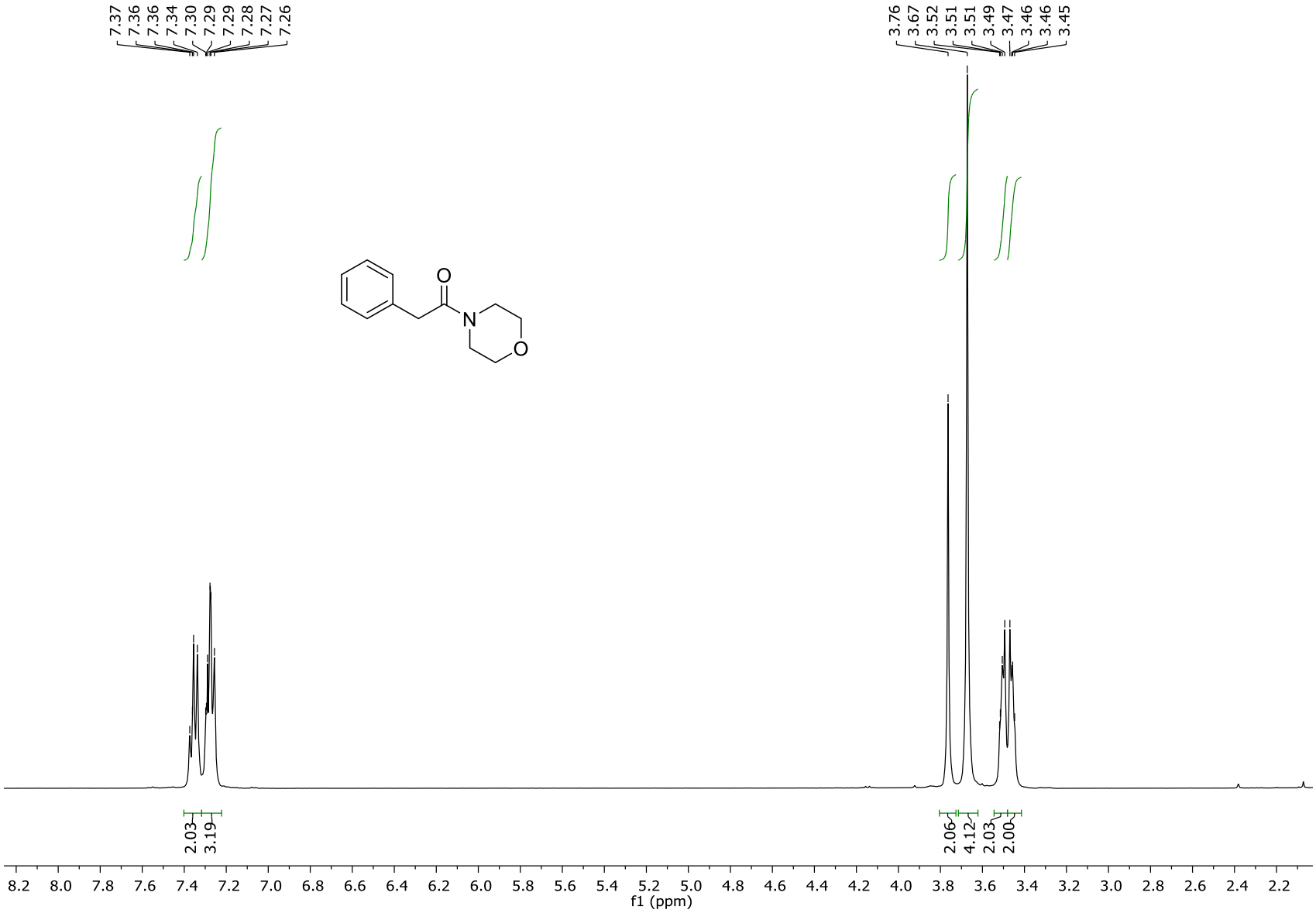
$^{19}F\{^{1}H\}$ NMR spectrum of tetrakis(*p*-fluorophenyl)silane **(71b)** (377 MHz, $CDCl_3$)



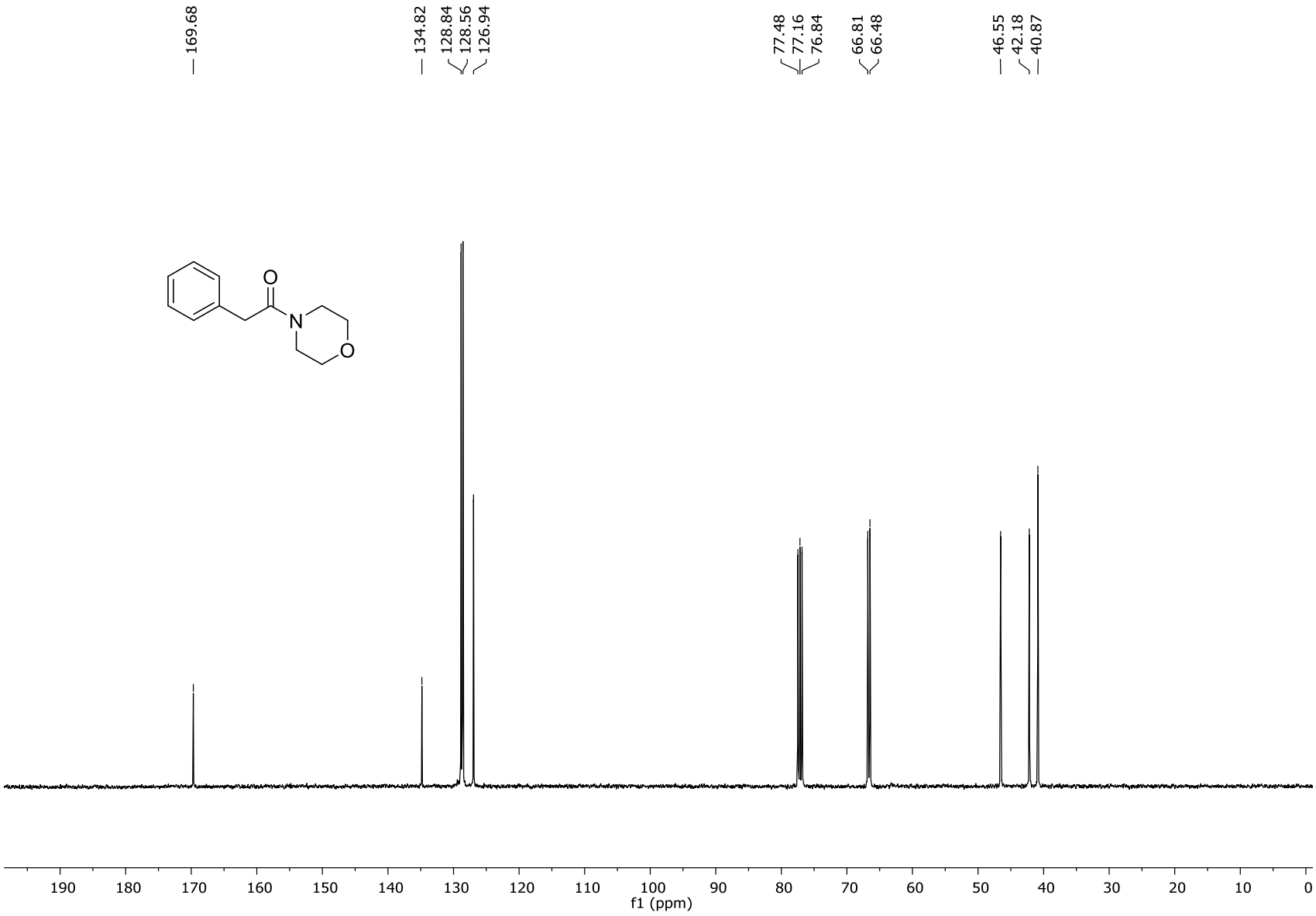
$^{29}Si\{^{1}H\}$ NMR spectrum of tetrakis(*p*-fluorophenyl)silane **(71b)** (80 MHz, $CDCl_3$)



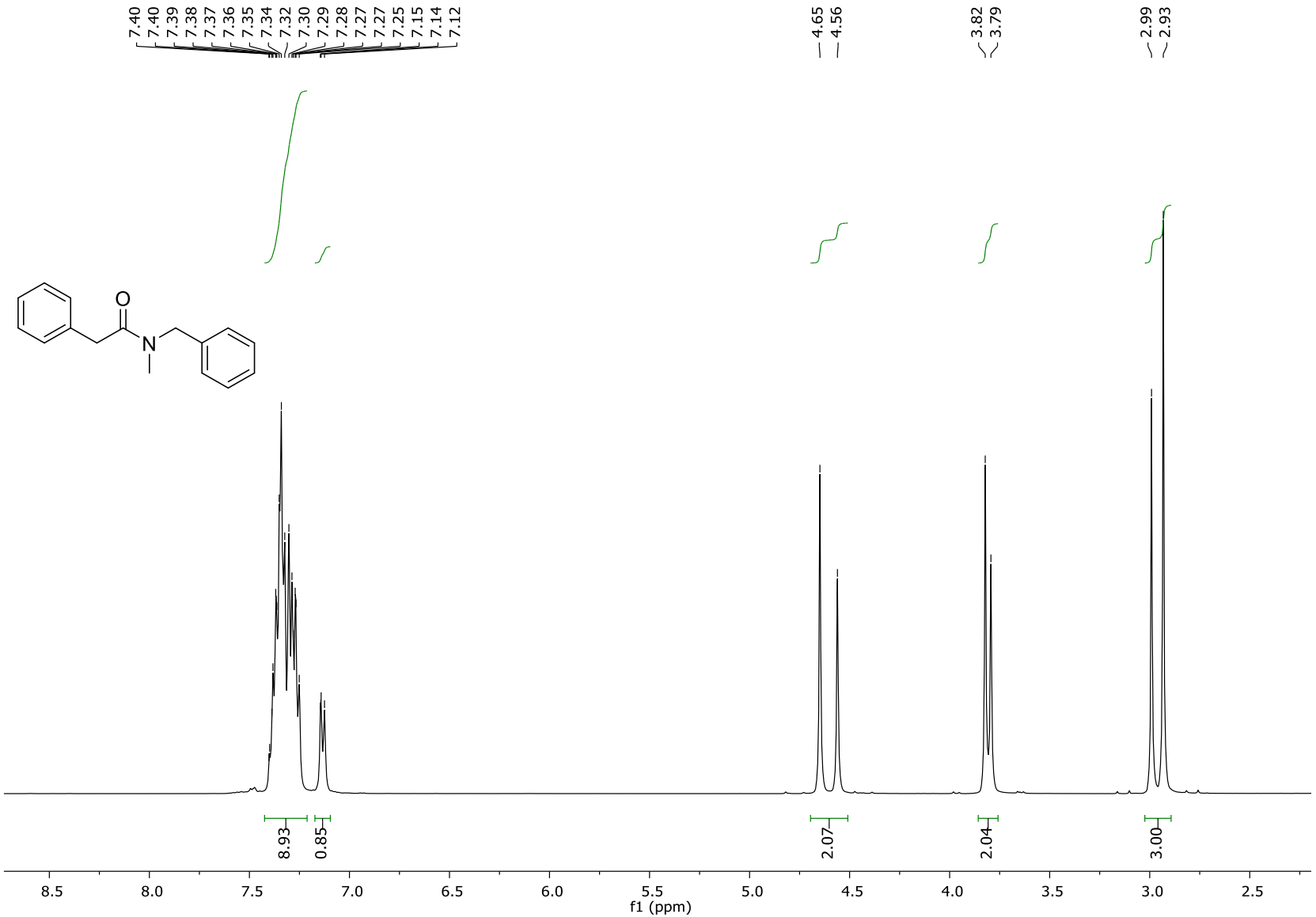
^{1}H NMR spectrum of 1-morpholino-2-phenylethan-1-one **(61b)** (400 MHz, $CDCl_3$)



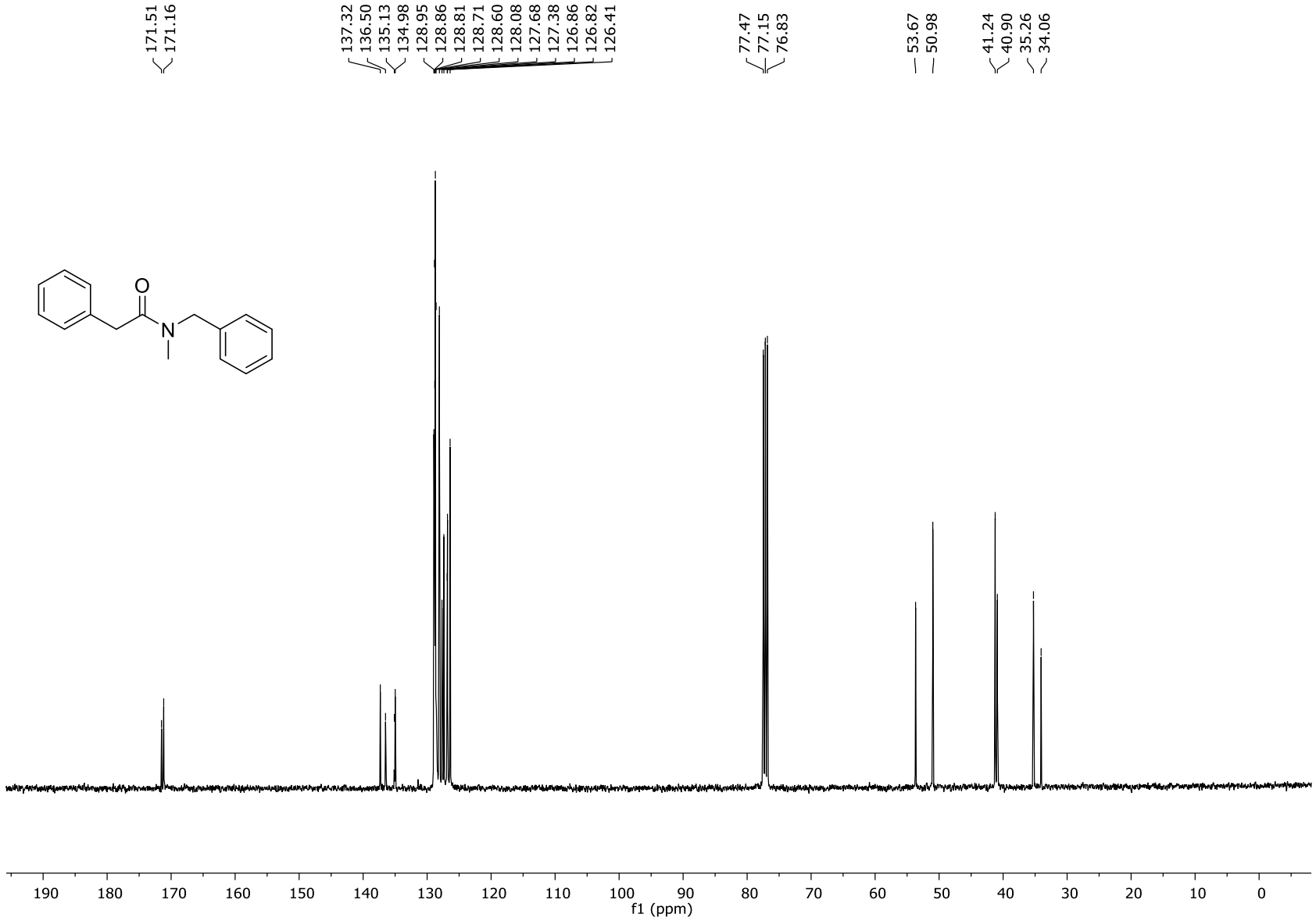
^{13}C NMR spectrum of 1-morpholino-2-phenylethan-1-one **(61b)** (101 MHz, $CDCl_3$)



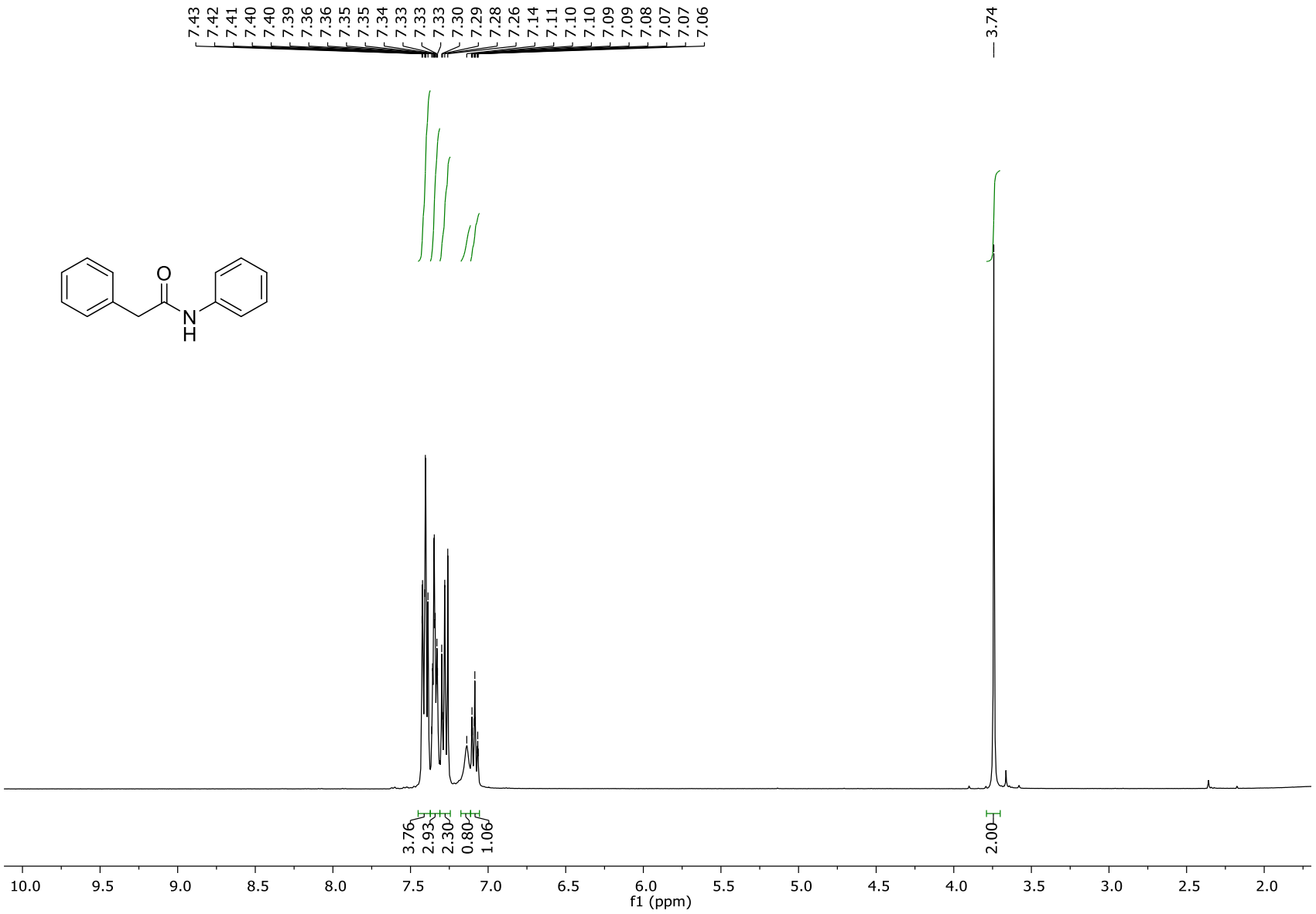
^{1}H NMR spectrum of *N*-benzyl-*N*-methyl-2-phenylacetamide **(61c)** (400 MHz, $CDCl_3$)



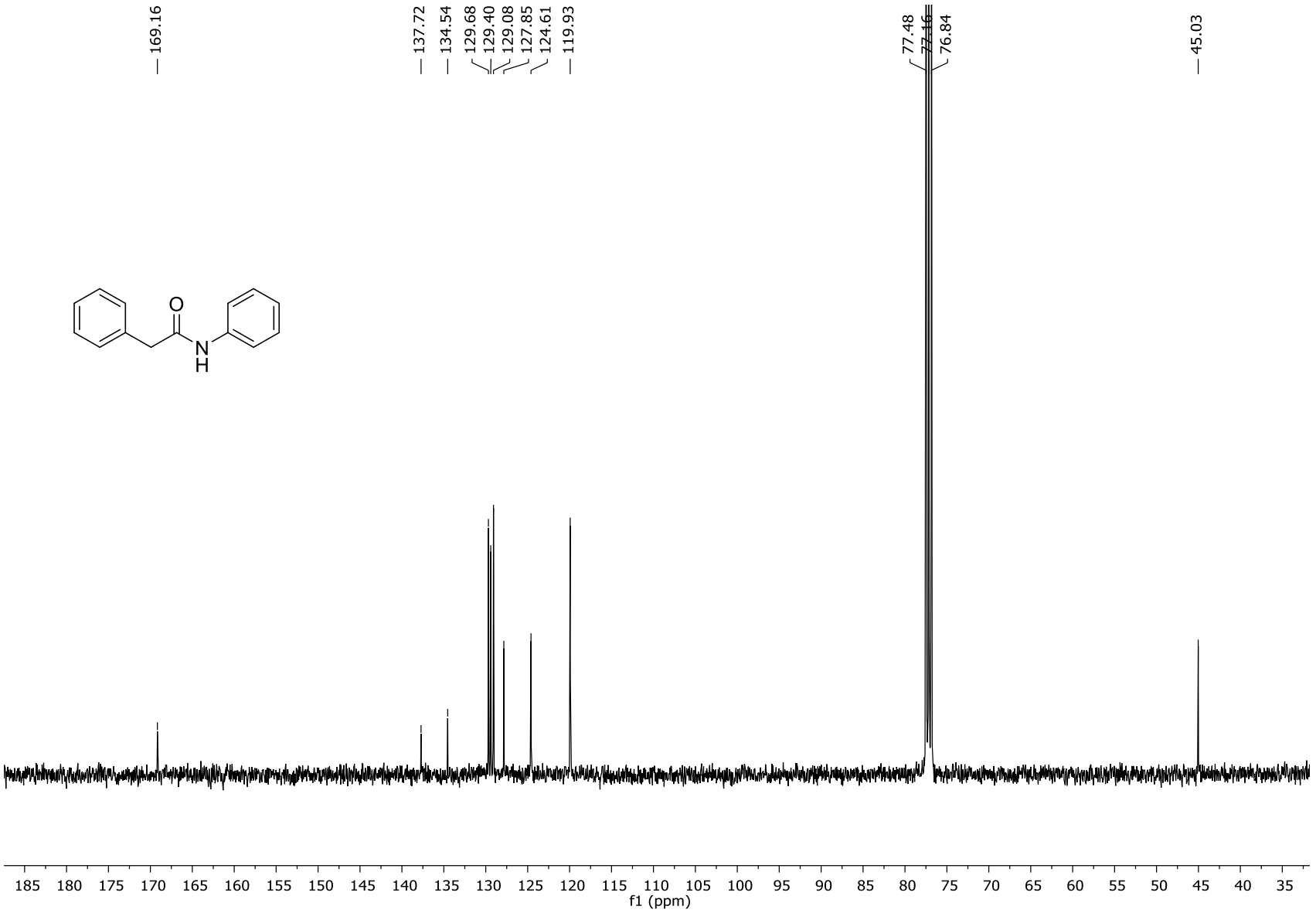
^{13}C NMR spectrum of *N*-benzyl-*N*-methyl-2-phenylacetamide **(61c)** (101 MHz, $CDCl_3$)



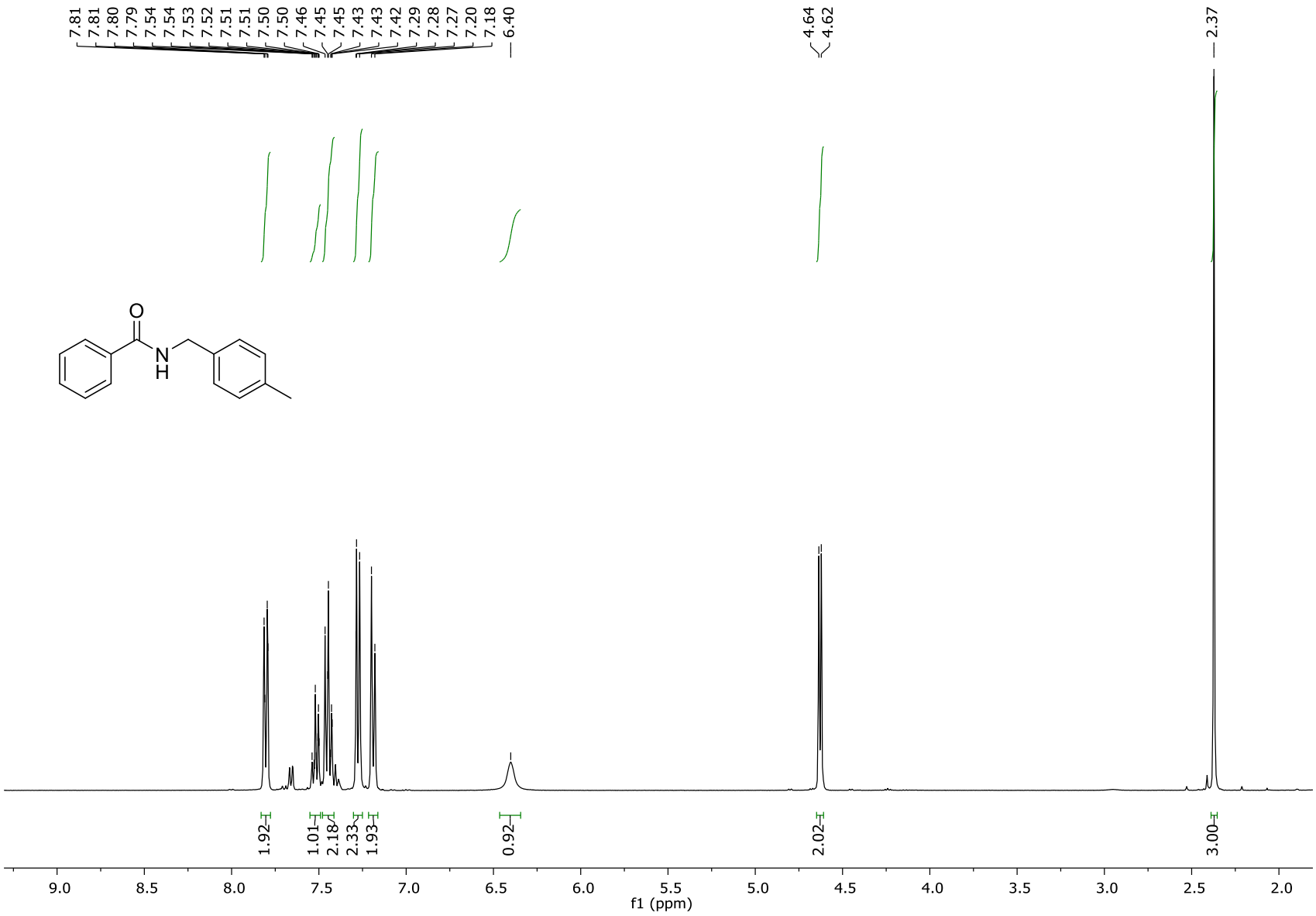
^{1}H NMR spectrum of *N*,2-diphenylacetamide **(61d)** (400 MHz, $CDCl_3$)



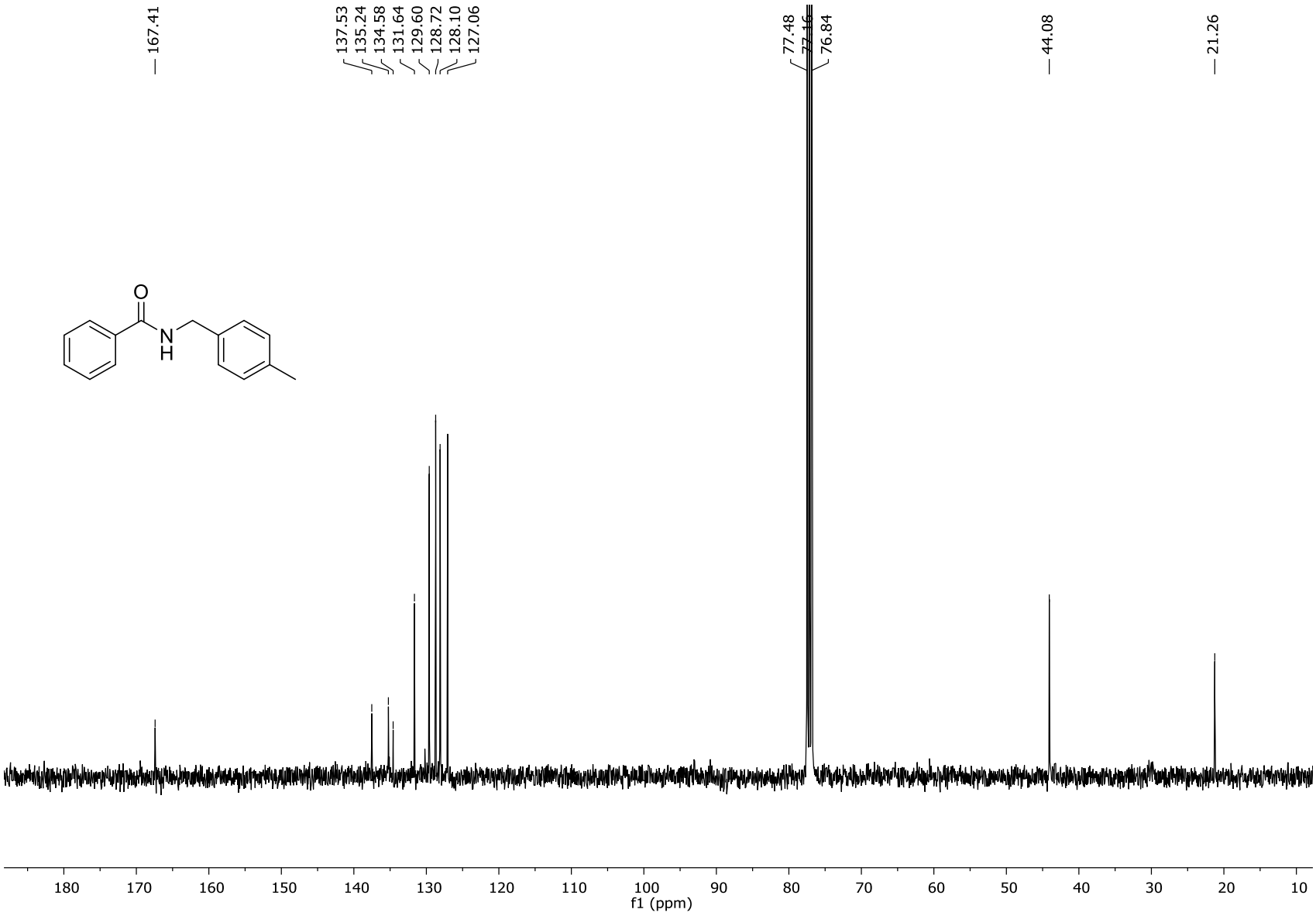
^{13}C NMR spectrum of *N*,2-diphenylacetamide **(61d)** (101 MHz, $CDCl_3$)



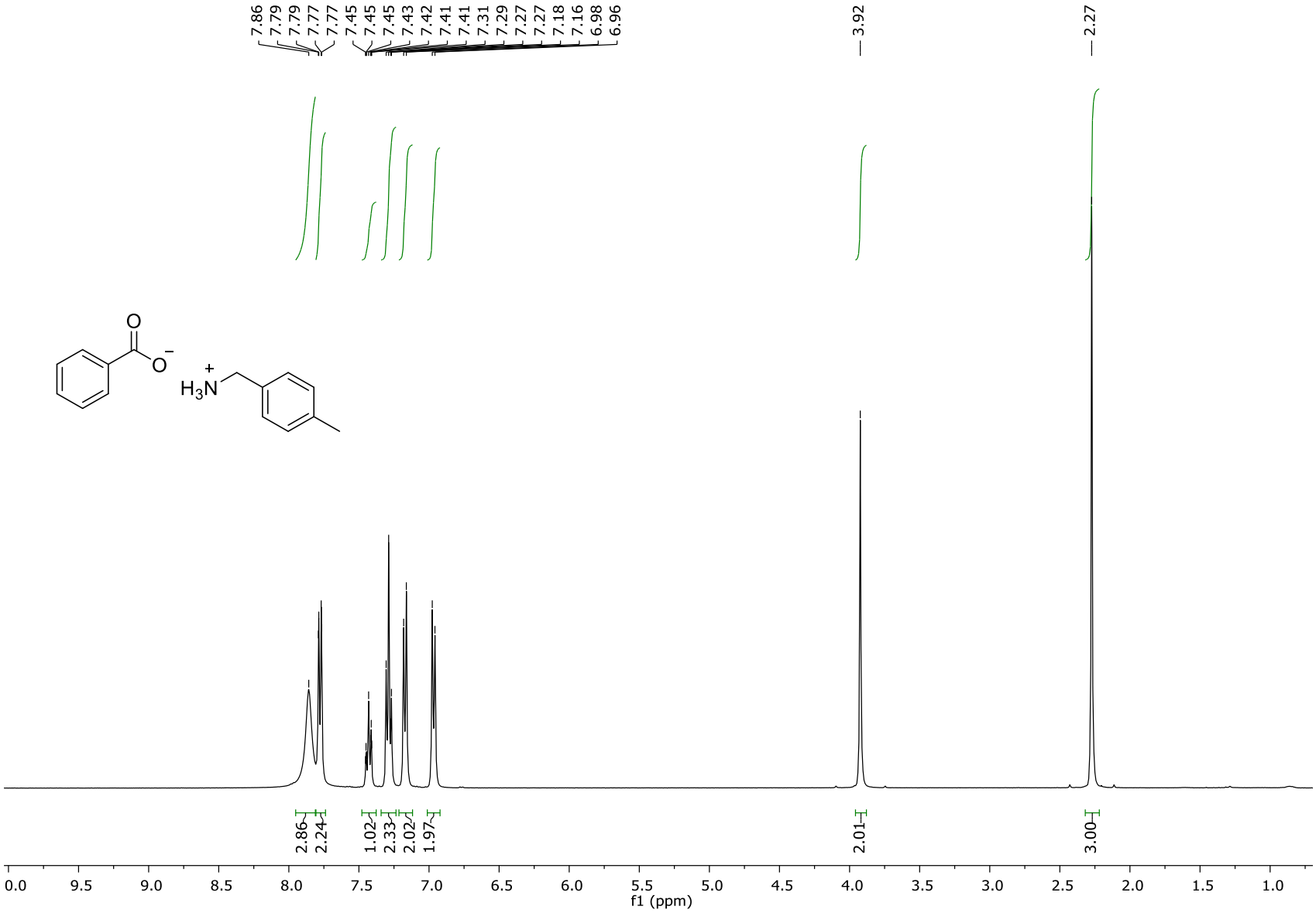
^{1}H NMR spectrum of *N*-(4-methylbenzyl)benzamide **(61e)** (400 MHz, $CDCl_3$)



^{13}C NMR spectrum of *N*-(4-methylbenzyl)benzamide **(61e)** (101 MHz, $CDCl_3$)



^{1}H NMR spectrum of ammonium benzoate salt (400 MHz, $CDCl_3$)



^{13}C NMR spectrum of ammonium benzoate salt (101 MHz, $CDCl_3$)

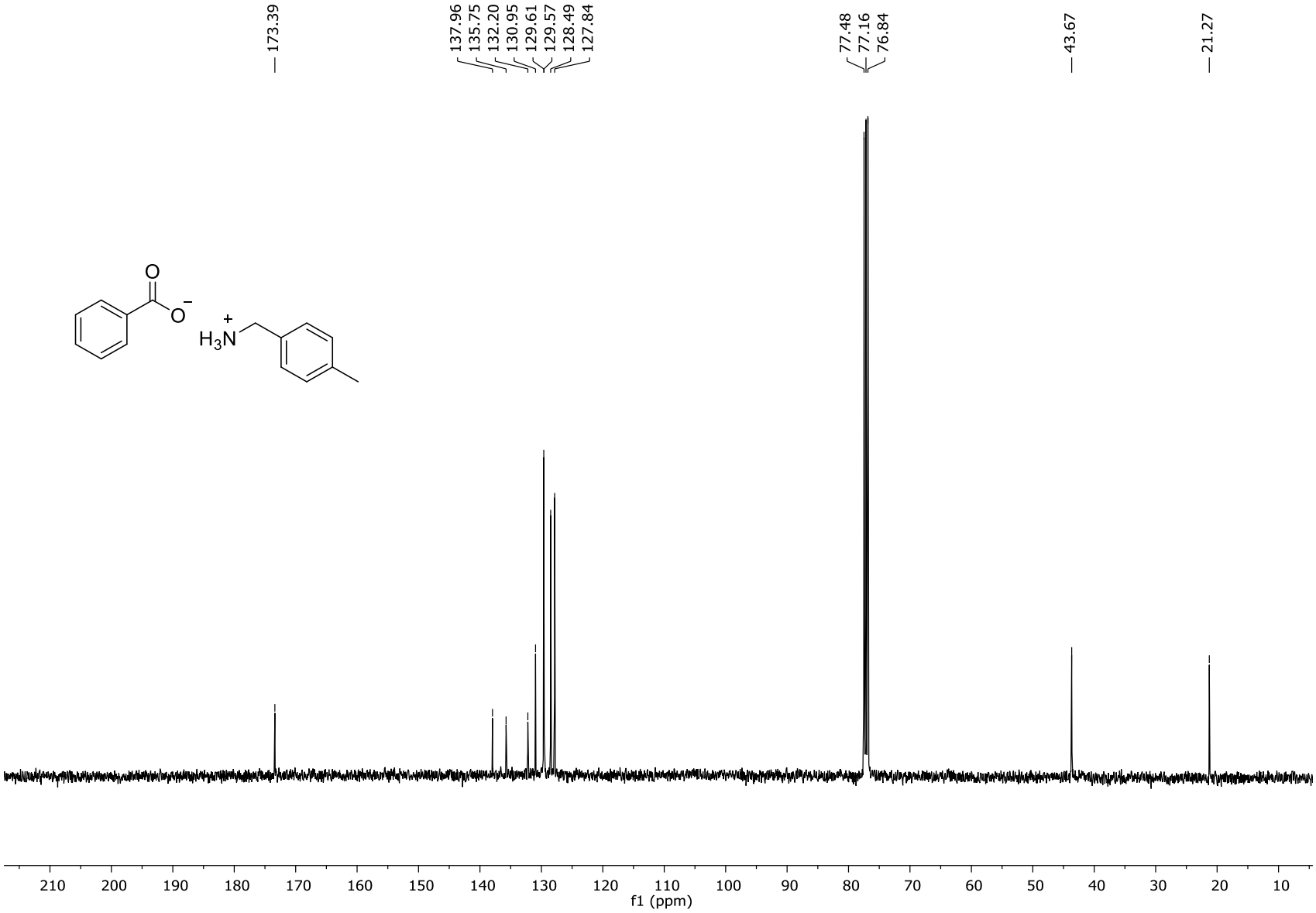


Table S1. Crystal Data, Data Collection and Refinement Parameters for the Structures of **64a-b** and **62e-f**.

Data	64a	62e	64b	62f
Formula	$C_{18}H_{13}F_3Si$	$C_{18}H_{13}F_3OSi$	$C_{18}H_{13}Cl_3Si$	$C_{18}H_{13}Cl_3OSi$
Formula weight	314.37	330.37	363.72	379.72
Colour, habit	colourless tablets	colourless blocks	colourless blocks	colourless blocks
Temperature / K	173	173	173	173
Crystal system	orthorhombic	monoclinic	orthorhombic	trigonal
Space group	*Pbca* (no. 61)	*C*2/*c* (no. 15)	$P2_12_12_1$ (no. 19)	*R*3 (no. 146)
a / Å	10.7908(4)	20.0412(7)	8.8393(2)	47.0387(10)
b / Å	8.6862(3)	16.0311(5)	11.0368(3)	47.0387(10)
c / Å	33.2183(15)	21.3364(7)	18.0391(5)	11.3591(3)
α / deg	90	90	90	90
β / deg	90	108.264(4)	90	90
γ / deg	90	90	90	120
V / Å^3	3113.6(2)	6509.7(4)	1759.84(8)	21766.2(10)
Z	8	16 [c]	4	48 [d]

D_c / gcm^{-3}	1.341	1.348	1.373	1.391
radiation used	Mo-Kα	Mo-Kα	Cu-Kα	Mo-Kα
μ / mm^{-1}	0.175	0.175	5.300	0.572
No. of unique reflns		57		
measured (R_{int})	3696 (0.0389)	6510 (0.0144)	3485 (0.0466)	21255 (0.0541)
obs, $\|F_o\| > 4\sigma(\|F_o\|)$	2946	5124	2944	13621
completeness (%) [a]	99.9	98.7	100.0	99.9
No. of variables	203	437	204	1199
R_1(obs), wR_2(all) [b]	0.0533, 0.1122	0.0462, 0.1254	0.0373, 0.0899	0.1190, 0.3303
CCDC	2247808	2247811	2247809	2247756

Table S2. Crystal Data, Data Collection and Refinement Parameters for the Structures of **62g**, **65**, and **71a-b**.

Data	62g	65	71a	71b
Formula	$C_{18}H_{13}Br_3OSi$	$C_{36}H_{24}Br_6OSi_2$	$C_{24}H_{16}Br_4Si$	$C_{24}H_{16}F_4Si$
Formula weight	513.10	1008.19	652.10	408.46
Colour, habit	colourless blocks	colourless blocks	colourless blocks	colourless blocky needles
Temperature / K	173	173	173	173
Crystal system	triclinic	Orthorhombic	Tetragonal	Monoclinic
Space group	*P*1 (no. 1)	$P2_12_12_1$	I-4	$P2_1/n$
a / Å	11.4531(9)	19.45536(12)	13.6224(5)	9.5601(3)
b / Å	13.9038(9)	19.52646(12)	13.6224(5)	20.4318(6)
c / Å	14.3428(8)	19.54344(13)	18.9771(13)	20.9010(6)
α / deg	111.169(6)	90	90	90
β / deg	107.660(6)	90	90	98.358(3)
γ / deg	102.534(6)	90	90	90
V / Å^3	1887.4(2)	7424.44(8)	3521.6(4)	4039.2(2)
Z	4 [e]	8	6	8

D_c / gcm^{-3}	1.806	1.804	1.845	1.343
radiation used	Mo-Kα	Cu-Kα	Cu-Kα	Mo-Kα
μ / mm^{-1}	6.476	8.652	6.917	0.159
measured (R_{int})	14970 (0.0590)	14967 (0.0499)	6452 (0.0372)	14290 (0.0197)
obs, $\|F_o\| > 4\sigma(\|F_o\|)$	7199	13524	2404	5991
completeness (%) [a]	99.8			
No. of variables	833	811	197	524
R_1(obs), wR_2(all) [b]	0.0699, 0.1421	0.0304, 0.0736	0.0569, 0.0876	0.0457, 0.1043
CCDC	2247757	2247765		

[a] Completeness to 0.84 Å resolution. [b] $R_1 = \Sigma||F_o| - |F_c||/\Sigma|F_o|$; $wR_2 = \{\Sigma[w(F_o^2 - F_c^2)^2] / \Sigma[w(F_o^2)^2]\}^{1/2}$; $w^{-1} = \sigma^2(F_o^2) + (aP)^2 + bP$. [c] There are two crystallographically independent molecules. [d] There are six crystallographically independent molecules, five in general positions and one adjacent to a C_3 axis. [e] There are four crystallographically independent molecules.

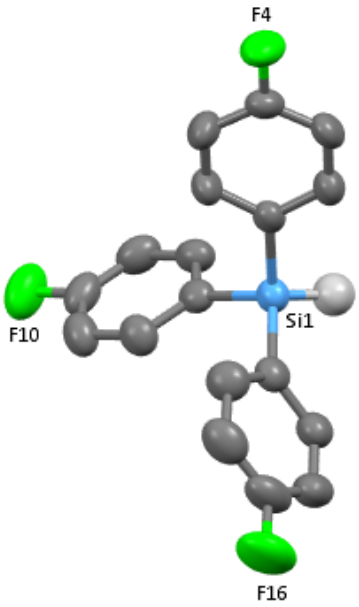


Figure S1. X-ray crystal structure of tris(*p*-fluorophenyl)silane **64a**.

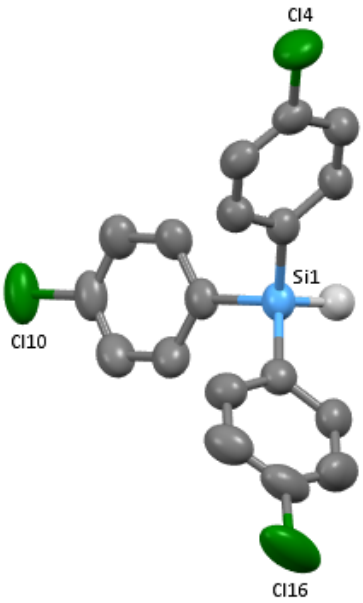


Figure S2. X-ray crystal structure of tris(*p*-chlorophenyl)silane **64b**.

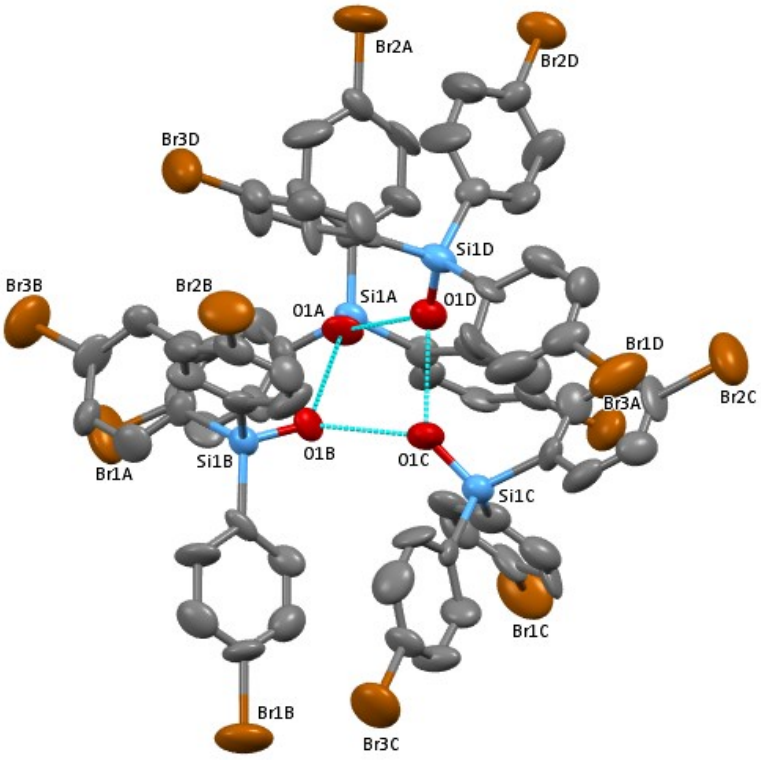


Figure S3. X-ray crystal structure of tris(*p*-bromophenyl)silanol **62g**. Hydrogen bonded tetramer (hydrogens are omitted for clarity).

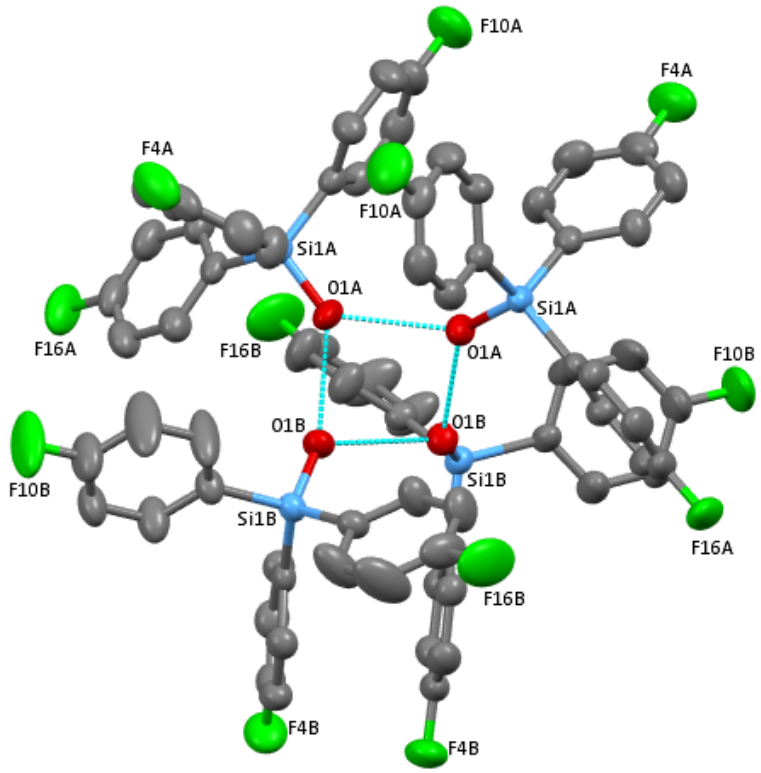


Figure S4. X-ray crystal structure of tris(*p*-fluorophenyl)silanol **62e.** Hydrogen bonded tetramer (hydrogens are omitted for clarity).

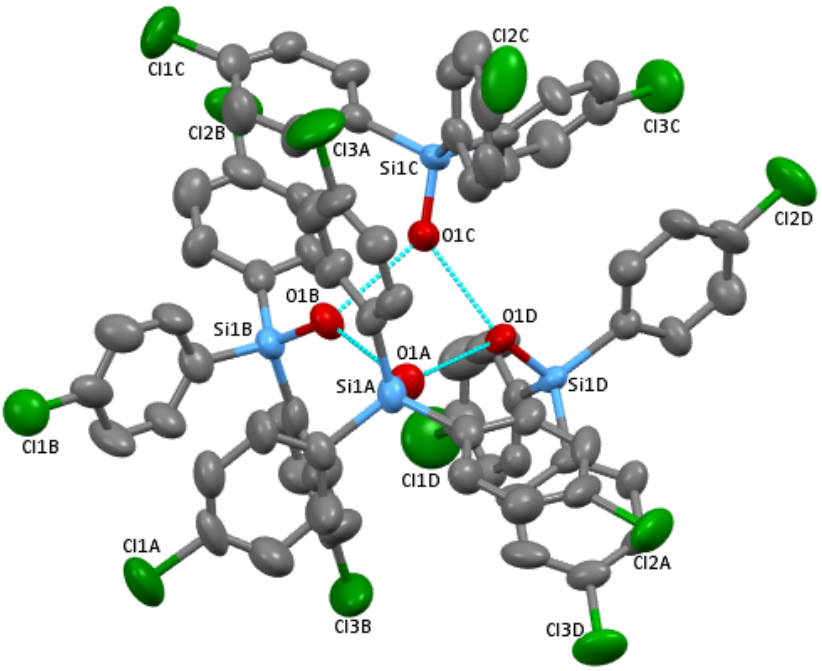


Figure S5. X-ray crystal structure of tris(*p*-chlorophenyl)silanol **62f**. Hydrogen bonded tetramer (hydrogens are omitted for clarity).

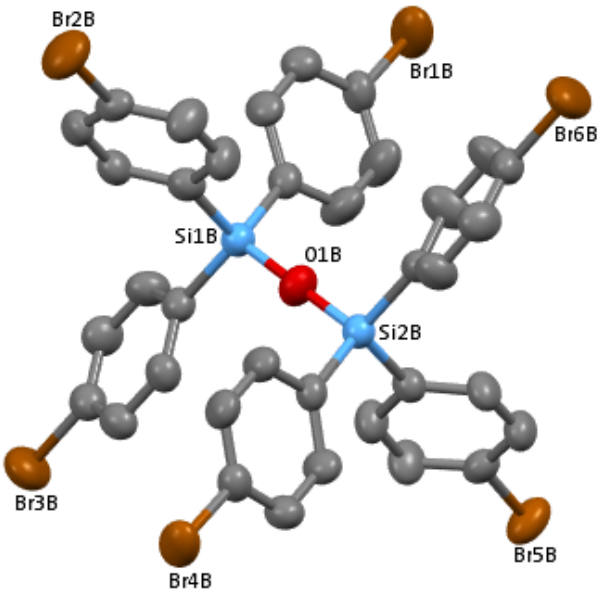
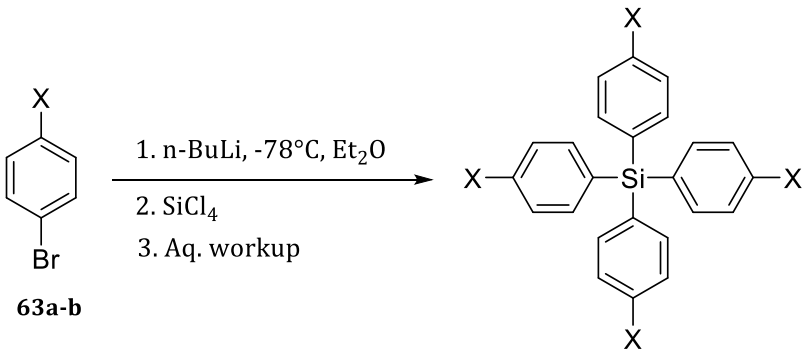


Figure S6. X-ray crystal structure of 1,1,1,3,3,3-hexakis(*p*-bromophenyl)disiloxane **65**. Hydrogens are omitted for clarity.

Appendices

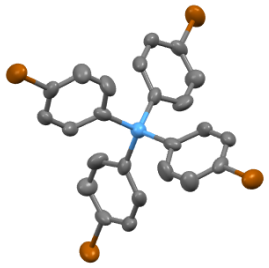
Appendix 1 – Formation of tetrakis silanes (**71a-b**).



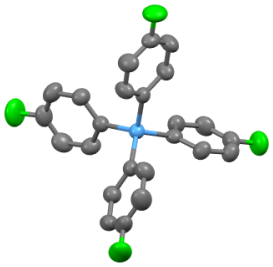
63a-b

71a, X = Br, 66%

71b, X = F, 12%

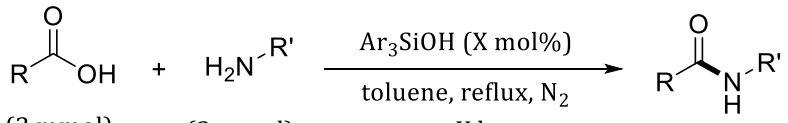


X-Ray: **71a**



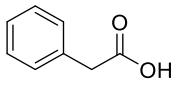
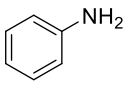
X-Ray: **71b**

Appendix 2 – Amidation reactions conducted for extended period.

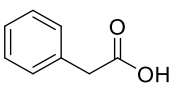
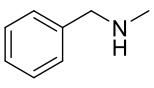


(3 mmol) (3 mmol)

(i) HPLC quantification of amide formation

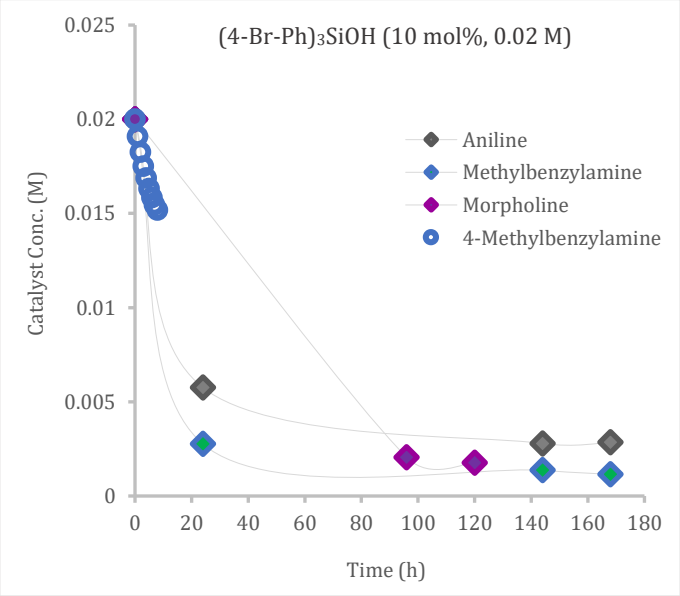
Acid	Amine	Reflux Time (h)	Catalyst (X mol%) Amide Conversion (%)
			(4-Br-Ph)$_3$SiOH (10 mol%)
		24	16
		144	35
		168	42

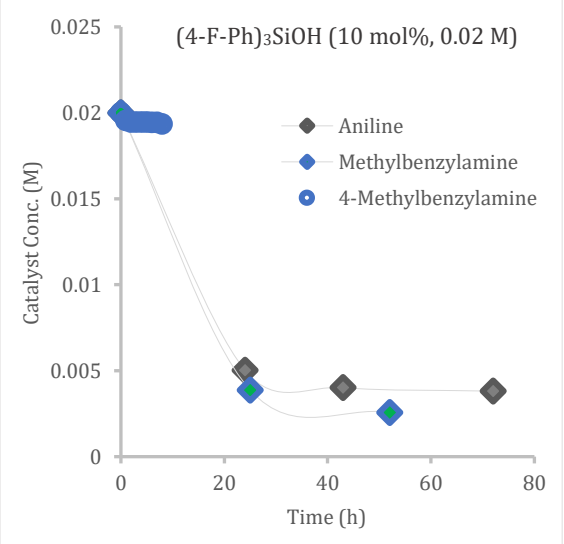
			$(4\text{-F-Ph})_3\text{SiOH}$ (10 mol%)
		24	10
		43	19
		72	28
			$(4\text{-F-Ph})_3\text{SiOH}$ (30 mol%)
		29	13
		124	63
			$(4\text{-F-Ph})_3\text{SiOH}$ (50 mol%)
		48	24
		72	39
		143	61
			$(4\text{-Cl-Ph})_3\text{SiOH}$ (30 mol%)
		49	17
		120	66

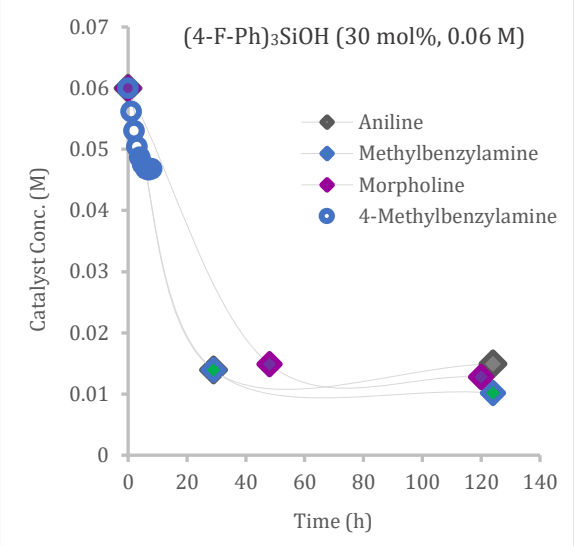
Acid	Amine	Reflux Time (h)	Catalyst (X mol%) Amide Conversion (%)
			$(4\text{-Br-Ph})_3\text{SiOH}$ (10 mol%)
		24	33
		144	100
		168	100
			$(4\text{-F-Ph})_3\text{SiOH}$ (10 mol%)

	25	35
	52	44
		$(4\text{-F-Ph})_3\text{SiOH}$ (30 mol%)
	29	47
	124	100
		$(4\text{-Cl-Ph})_3\text{SiOH}$ (30 mol%)
	49	46
	120	89

(ii) HPLC quantification of catalyst integrity







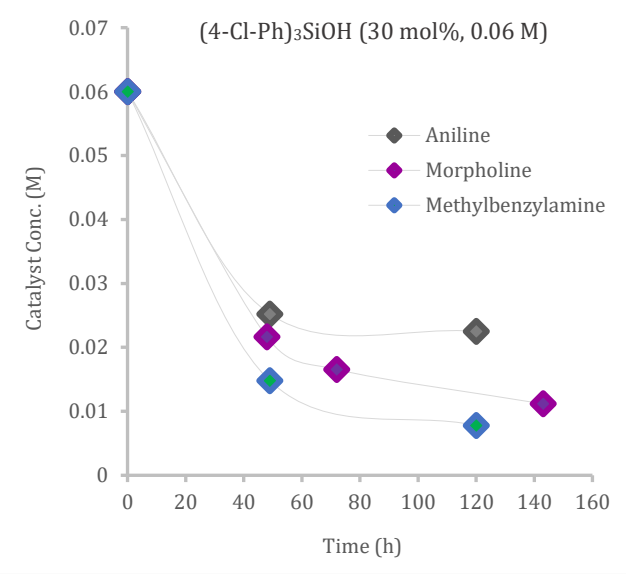


Figure S7. Catalyst integrity plots.